

Magnesium and titanium: “*The odd couple*”

Local order and the influence of stress on the
hydrogen sorption properties of Mg-Ti thin films

Andrea Baldi

Reading committee:

dr. Andreas Borgschulte, Empa (Switzerland)
prof.dr. Björgvin Hjörvarsson, Uppsala University (Sweden)
dr. Ole Martin Løvvik, University of Oslo (Norway)
dr. Tejs Vegge, Risø DTU (Denmark)
dr. Igor Zoric, Chalmers University of Technology (Sweden)

Cover: The graph on the cover is a collection of loading isotherms measured on magnesium thin films of various thicknesses and capped with Pd. It shows how the thermodynamic properties of nanosized metal-hydrides can be strongly influenced by stress effects, one of the major results described in the present thesis. The picture on the back is a Monte-Carlo simulation of a Mg-Ti alloy, characterized by an increasing amount of chemical short-range order: from a random alloy (top) to a completely segregated system (bottom).

Printed by: Ipskamp Drukkers B.V.

This work was funded by the Technologiestichting STW and carried out at:

Vrije Universiteit
Faculty of Sciences
Department of Physics and Astronomy
Condensed Matter Physics
De Boelelaan 1081
1081 HV Amsterdam
The Netherlands

ISBN 978 90 8659 440 5

VRIJE UNIVERSITEIT

Magnesium and titanium: *“The odd couple”*

Local order and the influence of stress on the
hydrogen sorption properties of Mg-Ti thin films

ACADEMISCH PROEFSCHRIFT

ter verkrijging van de graad Doctor aan
de Vrije Universiteit Amsterdam,
op gezag van de rector magnificus
prof.dr. L.M. Bouter,
in het openbaar te verdedigen
ten overstaan van de promotiecommissie
van de faculteit der Exacte Wetenschappen
op donderdag 4 maart 2010 om 11.45 uur
in de aula van de universiteit,
De Boelelaan 1105

door

Andrea Baldi

geboren te Rome, Italië

promotor: prof.dr. R.P. Griessen
copromotor: prof.dr. B. Dam

A Valentina e Lorenzo

A Enrico

Contents

1	Introduction	4
1.1	Metal hydrides	4
1.2	Optical approach to metal hydrides	7
1.2.1	Hydrogenography	9
1.2.2	A short history of switchable mirrors	9
1.3	Solar collectors	11
1.4	Electrochromic devices	12
1.5	Immiscible alloys	14
1.6	This thesis	16
2	Mg-Ti-H thin films: reversible black mirrors	18
2.1	Introduction	18
2.2	Mg-Ti-H thin films for smart solar collectors	20
2.2.1	Introduction	21
2.2.2	Experimental details	21
2.2.3	Results and discussion	21
2.2.4	Conclusions	25
2.3	Mg-Ti-H thin films as switchable solar absorbers	28
2.3.1	Introduction	29
2.3.2	Experimental details	29
2.3.3	Results and discussion	31
2.3.4	Conclusions	34
3	Chemical short-range order in Mg-Ti thin films	37
3.1	Introduction	37
3.2	Structural, optical and electrical properties of Mg-Ti-H thin films	40
3.2.1	Introduction	41
3.2.2	Experimental details	42
3.2.3	Results	43
3.2.4	Discussion	54
3.2.5	Conclusions	58
3.3	Nanoscale composition modulations in Mg-Ti-H thin film alloys	59
3.3.1	Introduction	60
3.3.2	Experimental details	61
3.3.3	Results	63

3.3.4	Discussion	69
3.3.5	Conclusions	71
3.4	Chemical short-range order probed by hydrogenography	73
3.4.1	Introduction	74
3.4.2	Experimental details	75
3.4.3	Experimental PTIs	75
3.4.4	PTI modeling: Lattice gas model for H in a multi-site solid with long-range H-H interaction	77
3.4.5	Comparison with experimental PTIs	82
3.4.6	Discussion	89
3.4.7	Conclusions	93
4	Mg/Ti multilayers: artificially engineered short-range order	94
4.1	Introduction	94
4.2	Mg/Ti multilayers: structural, optical and hydrogen absorption properties	96
4.2.1	Introduction	97
4.2.2	Experimental details	97
4.2.3	Results and discussion	99
4.2.4	Conclusions	124
5	Mg sandwiches: destabilization through elastic constraints	125
5.1	Introduction	125
5.2	Destabilization of the Mg-H system through elastic constraints .	127
5.2.1	Introduction	128
5.2.2	Experimental details	129
5.2.3	Results and discussion	129
5.2.4	Conclusions	135
5.3	Quasifree Mg-H thin films	137
5.3.1	Introduction	138
5.3.2	Experimental details	138
5.3.3	Results and discussion	139
5.3.4	Conclusions	144
6	Energy Outlook	145
6.1	Introduction	145
6.2	Elastic clamping in 3D	147
6.3	New materials	147
6.4	Surface energy	148
6.5	From optical hydrogen detectors to optical hydrogen sensors . .	149
6.6	Conclusions	151
	Appendices	153
A	Chemical short-range order	154

B Beer-Lambert Law	162
C Elastic clamping model	164
Bibliography	183
Summary	184
Samenvatting	187
List of publications	190
Acknowledgements	192
Curriculum Vitae	194

Chapter 1

Introduction

The aim of the present thesis is to study the applicability of metallic thin films with variable optical properties, as tunable smart absorbers for solar collectors. In particular we are interested in thin films capable of fast and reversible switching from a metallic reflecting state to a hydrogenated black “light-absorbing” state. Our interest lies both in their technological application and their fundamental physical properties. In the course of our investigations we discovered a new way to tune the thermodynamic properties of Mg films by elastic constraints. This opens a new route to the optimization of metal hydrogen systems for energy storage and hydrogen sensing applications.

1.1 Metal hydrides

Hydrogen is considered worldwide as an attractive energy vector of a future sustainable economy. An ideal hydrogen cycle (Fig. 1.1) is composed of three steps: 1) hydrogen production by means of water electrolysis, powered with renewable energy sources, such as hydropower, wind power, geothermal and photovoltaics [1], 2) hydrogen storage and transport and 3) hydrogen combustion in a fuel cell, to produce electricity and H_2O as the only exhaust product [2]. Due to hydrogen’s lightness and volatility its storage is one of the major technological challenges yet to be solved. Besides high gravimetric and volumetric hydrogen densities, an ideal hydrogen storage system should have an equilibrium hydrogen pressure of 10^5 Pa at room temperature and fast and reversible kinetics of hydrogen absorption and release. None of the existing materials fulfill all these requirements. Storage of molecular hydrogen (H_2), both in liquid and gas phase, requires high pressures and/or low temperatures and is therefore not energy efficient. Alternatively it is possible to store atomic hydrogen in metal- or complex-hydrides. Although these compounds typically have lower gravimetric storage densities compared to pure H_2 in liquid and gas phase, they are able to absorb hydrogen at room temperature and atmospheric pressure and have very high volumetric densities. Extensive studies are now focusing on improving their thermodynamic and kinetic properties.

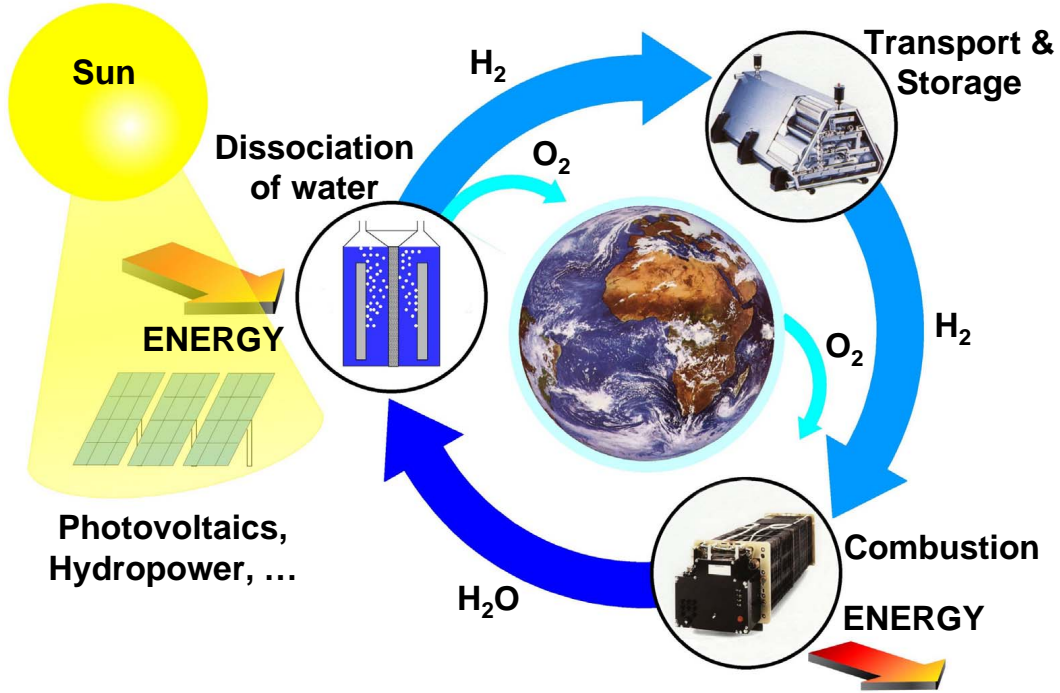


Figure 1.1: The hydrogen cycle. The figure is rearranged from [2].

In metal hydrides, on which the present thesis focuses, hydrogen (H) enters the lattice of the host metal (M) in atomic form and occupies interstitial sites, expanding the volume by about $2\text{-}3 \text{ \AA}^3$ per H atom. At low concentrations ($H/M < 0.1$) the exothermal dissolution of H atoms into the metallic host leads to a solid solution, or α phase, in which hydrogen atoms are very sparse and volume changes are proportional to the hydrogen concentration. At larger hydrogen concentrations ($H/M > 0.1$) the H-H interaction causes the nucleation and growth of a hydrogen-rich β -phase, typically characterized by large volume expansions and drastic changes in the chemical and physical properties of the material.

The thermodynamics of hydrogen absorption are described in terms of pressure composition isotherms (PCI's), in which the logarithm of the hydrogen pressure is plotted as a function of the hydrogen concentration in the metal, Fig. 1.2a. In the region of coexistence of α and β phases the isotherms show a pressure plateau analogous to the one observed for the condensation of vapors below the critical temperature. The coexistence region vanishes at temperatures higher than the critical temperature T_c . The plateau pressure, p_{eq} , is

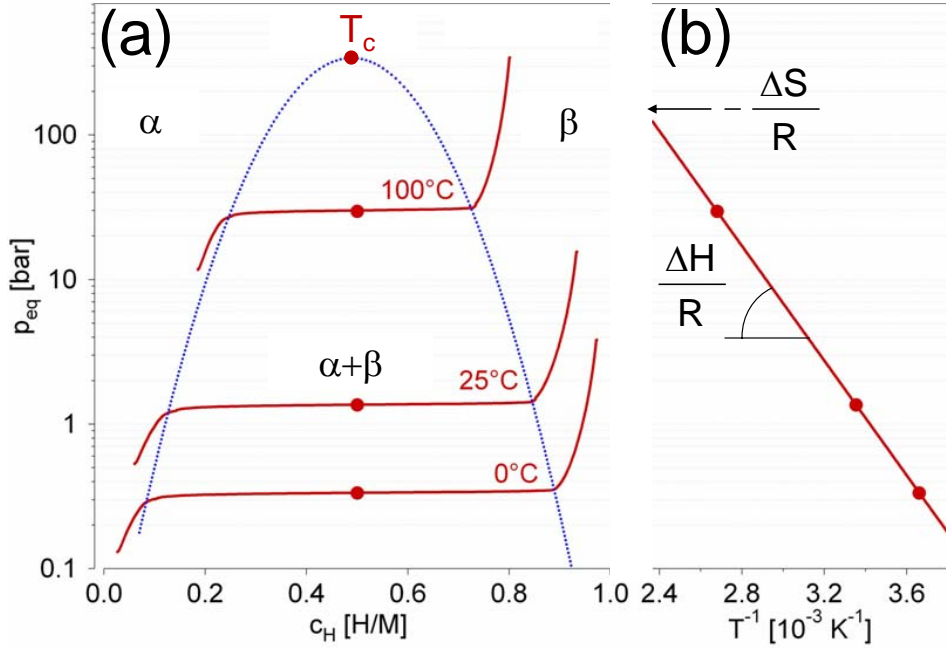


Figure 1.2: (a) Pressure composition isotherms of a typical metal-hydride. (b) Van't Hoff plot: the slope and the intercept are proportional to the enthalpy ΔH and entropy ΔS of hydride formation, respectively. R is the gas constant. The figure is rearranged from [3].

related to the temperature by the van't Hoff equation (see Fig. 1.2b):

$$\begin{aligned} \ln\left(\frac{p_{\text{eq}}}{p^0}\right) &= \frac{\Delta H_{\alpha \rightarrow \beta}}{RT} - \frac{1}{R} \left(2 \frac{S_{\beta} - S_{\alpha}}{c_{\beta} - c_{\alpha}} - S_{\text{H}_2}^0 \right) \\ \ln\left(\frac{p_{\text{eq}}}{p^0}\right) &= \frac{\Delta H}{RT} - \frac{\Delta S_0}{R} \end{aligned} \quad (1.1)$$

where p^0 is the standard pressure (standard conditions: $p = p^0 = 1.013 \times 10^5$ Pa and $T = 298$ K), ΔH is the heat of formation of the hydride phase and ΔS_0 is the difference between the partial molar entropy of the hydride and the standard entropy of hydrogen gas. The term ΔS_0 is mostly due to the entropy loss of hydrogen gas when absorbed into the metal and for most metal-hydrides we can assume $\Delta S_0 \approx -S_{\text{H}_2}^0 = -130.8 \text{ JK}^{-1}(\text{mol H}_2)^{-1}$. From the van't Hoff equation we can therefore calculate that, in order for an ideal hydrogen storage system to have an equilibrium pressure of 10^5 Pa at 298 K, we need to have $\Delta H \approx -39 \text{ kJ}(\text{mol H}_2)^{-1}$.

The physical nature of the H-H interaction, responsible for the nucleation of the hydrogen-rich β -phase, has been the subject of extensive research [4, 5, 6, 7]. Experimental studies of the pressure-composition-isotherms of metal-hydrogen systems close to the critical point suggest that this interaction is attractive and long ranged, extending to distances much larger than 1 nm.

At these separations the electronic screening is very strong: typical screening lengths in metals are of the order of 0.1 nm. This rules out the possibility of an electronic nature for the H-H interaction. Alefeld [4, 5] suggested that the attractive interaction observed between hydrogen atoms dissolved in metals is of elastic origin: when hydrogen is absorbed by a metal, the host lattice is expanded and the protons induce long-ranged strain fields whose elastic energy is equivalent to an effective H-H interaction [6]. A remarkable consequence of the long-ranged H-H interaction is that the thermodynamic properties are dependent on the boundary conditions imposed on the system (i.e. on the shape of the sample, as confirmed by Zabel and Peisl [8]). More in detail the elastic interaction is attractive for a metal with free surfaces and becomes repulsive for a perfectly “clamped” sample, as schematically shown in Fig. 1.3. As shown in chapter 5, we can exploit the dependence of the H-H interaction on the boundary conditions to effectively tune the thermodynamics of a metal-hydrogen system. The enthalpy of hydride formation, in fact, depends on the volume of the host lattice [9]:

$$\frac{d\Delta H}{d \ln V} = -B_M V_H \quad (1.2)$$

where B_M is the bulk modulus of the metal and V_H is the partial molar volume of hydrogen. Elastic constraints, by limiting the allowed volume expansion, have therefore the effect of increasing the enthalpy of hydride formation (“destabilize” the hydride) and therefore to rise the hydrogen equilibrium pressure. This effect is highly desirable in hydrogen storage applications, where one of the limiting factors preventing the use of metal hydrides is the high thermodynamic stability of their hydrides and their concomitant low equilibrium hydrogen pressure.

1.2 Optical approach to metal hydrides

Hydrogen absorption leads to drastic changes in the chemical and physical properties of the host metal, allowing to measure absorption isotherms with many different techniques. Volumetric measurements follow the decrease in hydrogen pressure occurring when a hydrogen-absorbing material is exposed to a fixed amount of H_2 gas in a closed volume. Similarly the sample weight increase can be monitored to deduce the hydrogen concentration within the material. Hydrogen absorption can also be detected by measuring the changes in electrical resistivity, magnetic susceptibility or lattice parameters. Electrochemistry allows to load samples in solution and calculate the hydrogen content by integrating in time the current flowing in the cell. Far from pretending to give an exhaustive record of all the methods of hydrogen detection, we would also like to mention more indirect techniques such as Differential Scanning Calorimetry

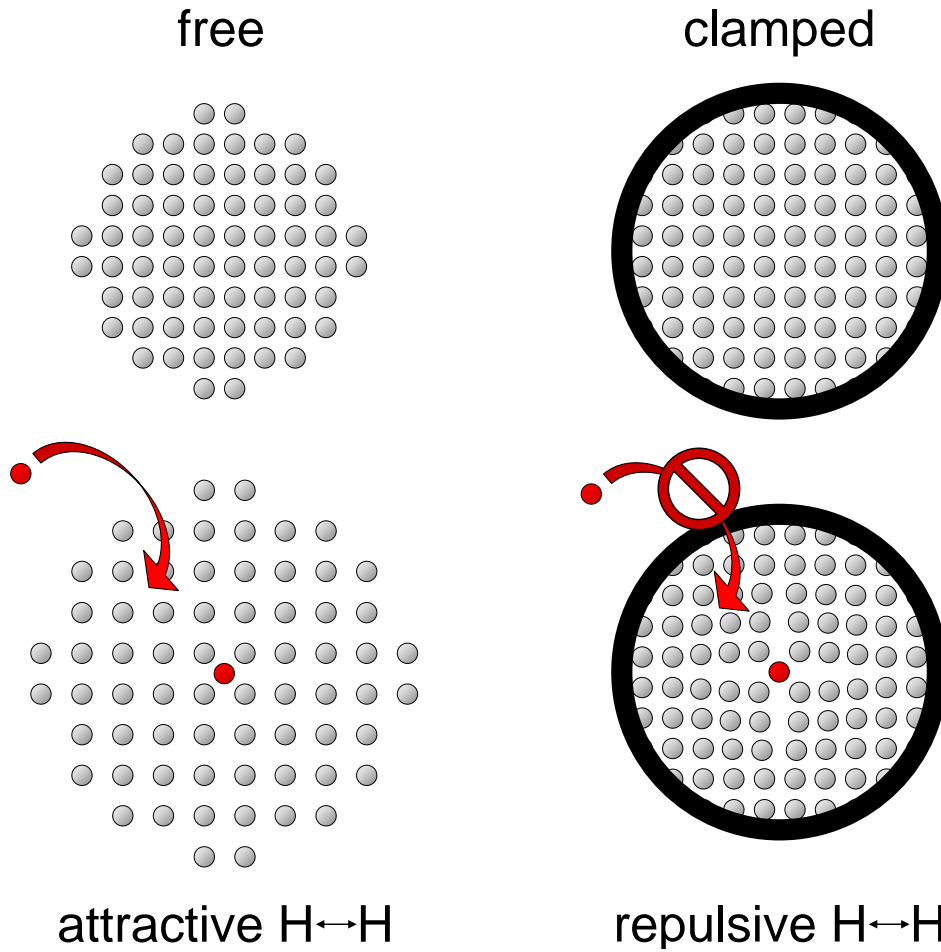


Figure 1.3: Schematic illustration of the effect of boundary conditions on the H-H interaction in metals. When a metal with free surfaces (left) absorbs hydrogen, the local volume expansion induces long-ranged strain fields leading to an attractive H-H interaction. In a perfectly constrained metal (right) the local volume expansion caused by the presence of an added proton reduces the volume available for the next hydrogen atom, effectively inducing a repulsive H-H interaction.

(DSC) that allows to measure the heat exchanged in the absorption and desorption reactions. Recently Langhammer *et al.* demonstrated how Localized Surface Plasmon Resonance (LSPR) of metallic nanoparticles, in which shifts in the wavelength of plasmon resonances are linked to the hydrogen content, allows to build Pressure-LSPR Response-Isotherms [10].

In our group in Amsterdam, since the discovery of the so-called “switchable mirror” effect [11], we follow the hydrogenation of thin metallic films by monitoring the optical changes occurring upon hydrogen uptake and release. Such optical approach recently led to the development of a combinatorial optical technique, Hydrogenography [12], that allows to measure the thermodynamic properties of hydrogen absorption in thousands of different samples at once.

1.2.1 Hydrogenography

Gremaud *et al.* recently developed Hydrogenography [12], a combinatorial technique that allows to simultaneously measure the hydrogen absorption isotherms of thousands of thin film metal-hydrides, by following the optical changes occurring upon hydrogenation. In a Hydrogenography experiment the amount of light transmitted through a thin film is recorded as a function of the hydrogen pressure in equilibrium with the sample. According to the Beer-Lambert law, the logarithm of the optical transmission is directly proportional to the hydrogen concentration in the material; the Pressure-Optical Transmission-Isotherms (PTI's) obtained with hydrogenography, in which the hydrogen pressure is plotted as a function of the logarithm of the optical transmission, are therefore equivalent to the standard Pressure-Composition-Isotherms (PCI's) measured in conventional metal-hydride research [13]. An example of a PTI measured on a 30 nm thick Mg film covered with 40 nm of Pd is shown in Fig. 1.4. The transmission in the x -axis is normalized by the transmission of the film before exposure to hydrogen and corrected by the background noise. The advantage of Hydrogenography is that it allows to measure the hydrogen absorption properties of thousands of different compositions at once, by measuring the optical transmission as a function of hydrogen pressure of a single thin film wafer [12, 14]. Furthermore the technique is not only applicable to materials undergoing metal-to-semiconductor transition upon hydrogenation but, thanks to its high sensitivity, it can also be applied to metallic hydrides such as PdH_x [13].

1.2.2 A short history of switchable mirrors

In 1996 Huiberts *et al.* [11] discovered the so called “switchable mirrors”: films of Y and La covered with Pd that, upon exposure to hydrogen gas, undergo exceptional optical transitions from shiny reflecting metals to yellowish transparent insulators (Fig. 1.5).

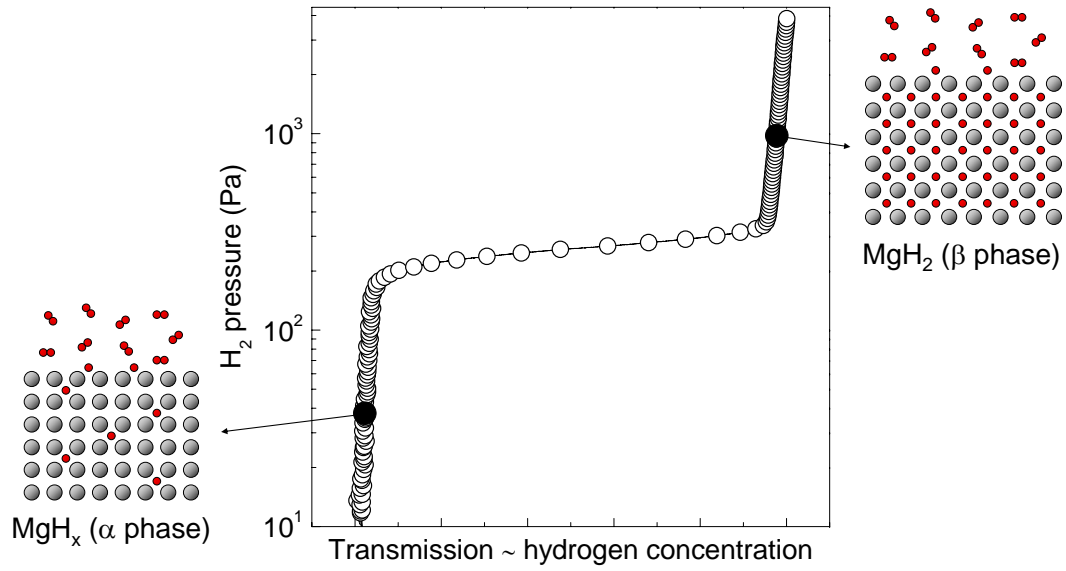


Figure 1.4: Pressure-Optical Transmission-Isotherm of a 30 nm thick Mg film covered with 40 nm of Pd measured with hydrogenography at 333 K. Only 2% of the experimental points are shown.



Figure 1.5: Appearance of a 500 nm thick Y film covered with 20 nm of Pd before (left) and after (right) exposure to 10^5 Pa of H_2 at room temperature [11].

One year later van der Sluis *et al.* [15] found similar optical switching properties in Mg-La thin films, with the advantage of a colorless transparent hydrogenated state and in 2001 Richardson and co-workers reported switchable mirror properties for magnesium-rich Mg-Ni layers [16]. These discoveries triggered extensive studies of the fundamental physical aspects of switchable mirrors and their possible technological applications.

A further boost in switchable mirrors research came in 2004, when Lohstroh *et al.* [17] showed that partially hydrogenated Mg₂Ni thin films exhibit a remarkable optical black state, which is destroyed upon complete hydrogenation of the films. This intermediate absorbing state originates from the preferential nucleation of Mg₂NiH₄ at the film/substrate interface and is due to the interference of light reflected at the substrate/Mg₂NiH₄ and at the Mg₂NiH₄/Mg₂Ni interfaces. Two years later Pasturel *et al.* showed that a stable black state can be obtained by depositing a Mg₂Ni(30 nm)/Ti(100 nm)/Pd(10 nm) film [18]: upon hydrogenation the Mg₂Ni layer becomes transparent, while Ti forms metallic TiH₂ and the interference effect is maintained.

A transient black state was also observed during loading of Mg and Mg-RE thin films [19]. Such black state, however, originates from the coexistence of metallic Mg and insulating MgH₂ particles and it is therefore not a consequence of optical interference. Borsa *et al.* have also shown that upon loading of Mg_{2+δ}Ni thin films, two hydrogenation mechanisms can take place, depending on the composition of the alloy: while hydrogenation of Mg_{2+δ}Ni films with $0 < \delta < 0.5$ proceeds by a random nucleation and growth of the Mg₂NiH₄ phase within the metallic top layer, for Mg_{2+δ}Ni films with $-0.3 < \delta < 0$ the predominant effect is the growth of the transparent Mg₂NiH₄ layer formed at the substrate interface [20].

In 2006 Borsa *et al.* reported an optical study of Mg_yTi_{1-y} thin films [21]: these films are highly reflective in the metallic state and highly absorbing in the fully hydrogenated state, showing fast and reversible kinetics of hydrogen absorption and desorption (Fig. 1.6). The advantage of the black appearance observed in Mg_yTi_{1-y} with respect to the one of Mg₂Ni is that it is reached at the end of the hydrogenation process and it is therefore an equilibrium state rather than a transient intermediate. The possibility of transforming a mirror into a black absorbing layer suggested the application of Mg-Ti thin films as optical hydrogen detectors [18, 23, 24, 25] and smart coatings for solar collectors [21, 22].

1.3 Solar collectors

In Section 1.2.2 we have suggested the idea of using Mg-Ti thin films as switchable covers for solar collectors. Solar collectors are devices capable of absorbing solar radiation to provide heat. The most common solar collector design is a flat black plate with built-in pipes, that absorbs the solar radiation arriving

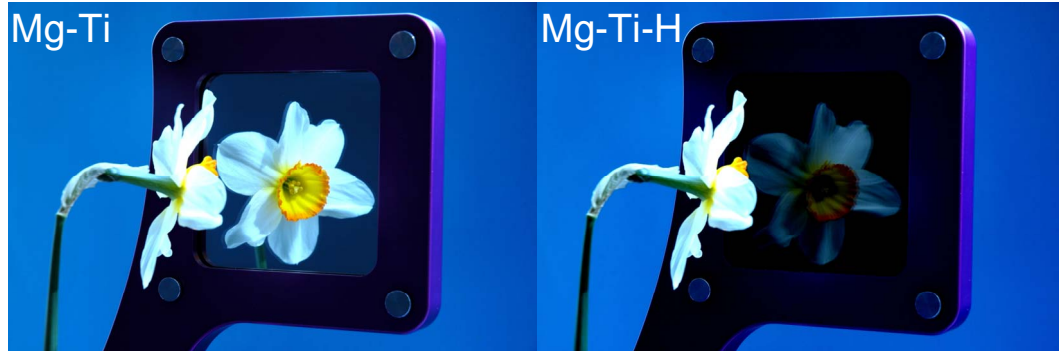


Figure 1.6: Appearance of a 200 nm thick $\text{Mg}_{0.7}\text{Ti}_{0.3}$ film covered with 10 nm of Pd before (left) and after (right) exposure to 10^5 Pa of a 4% H_2/Ar mixture at room temperature [22]. The pictures are taken from the substrate side.

on the Earth and heats a fluid (typically water) circulating into the pipes. Optimal efficiency is obtained for high solar absorptance (the convolution of the film's absorption spectrum with the solar spectrum) and low solar emissivity (the convolution of the film's absorption spectrum with the black body radiation at a given temperature) [26]. A major problem in the manufacturing of these devices is that, when not in use (in stagnation conditions), the collector can reach temperatures as high as 300°C , requiring expensive construction materials such as copper or aluminum, capable of withstanding extreme conditions. A way to reduce the stagnation temperature is to cover the solar collectors with VARIABLE REFLECTANCE MATERIALS (VAREM): by coating a solar collector with an optically active material such as Mg-Ti it is possible to tune the amount of absorbed light by changing the hydrogen concentration in the alloy [21]. By proper tuning of the Mg-Ti film thickness and composition it is in principle possible to strongly reduce the stagnation temperature of the device, without significantly lowering its efficiency [22]. The hydrogenation of thin film switchable mirrors is, however, typically obtained via gas loading, implying the use of costly equipment such as pumps, gas connectors and pressure regulators, which set severe cost limits in their use in real solar collectors. In order for VAREMs to be a viable solution their optical state has to be tuned by means of an applied voltage, by insertion into an all-solid-state electrochromic device (ECD).

1.4 Electrochromic devices

Electrochromism is the property of a material to change its optical appearance when electrochemically oxidized or reduced [27]. In an electrochromic device the optical properties are reversibly switched by means of an applied voltage [28]. An all-solid-state ECD is made of several layers sandwiched between two

glass or plastic plates. A typical device geometry is shown in Fig. 1.7. In

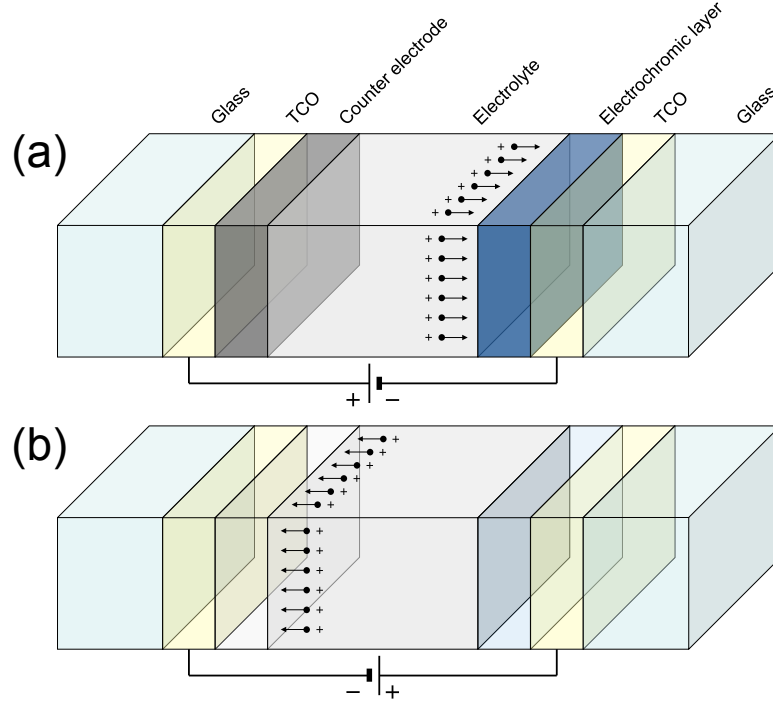


Figure 1.7: Typical electrochromic device with a proton conducting electrolyte. (a) Device in the colored opaque state. (b) Device in the bleached transparent state.

the colored (opaque) state (Fig. 1.7a) the positive ions are transported from the counter electrode to the electrochromic layer, via a potential difference applied on the transparent conductive oxide (TCO) layers. In the bleached (transparent) state (Fig. 1.7b) the polarity of the electric field is reversed. In the device depicted in Fig. 1.7 the optical properties of the electrochromic layer are complementary to the ones of the counter electrode: the former darkens upon ion intercalation (cathodic coloration) while the latter darkens upon ion deintercalation (anodic coloration). Changes in optical appearance upon intercalation of positive ions (typically protons) have been observed in many transition metal oxides [29], characterized by both cathodic (WO_3 , Ta_2O_5 , TiO_2 , Nb_2O_5 , MoO_3) and anodic (Cr_2O_3 , MnO_2 , RhO_2 , IrO_2) coloration.

Of course, many other device geometries with different optical properties are possible. In the present thesis we are interested in the use of a metal-hydride switchable mirror as electrochromic layer of an ECD. In particular we aimed at an ECD based on Mg-Ti alloys, capable of switching from a mirror-like appearance to a dark light-absorbing state, to be used as a switchable protection layer on solar collectors. The use of a metal hydride instead of a transition metal oxide, however, implies severe material demands in order

to avoid oxidation of the metallic layers. In this respect the choice of the proper electrolyte is crucial and reversible switching has been proven to occur in switchable mirror-based ECDs with both ZrO_2H_x [30, 31] and Ta_2O_5 [32] as proton conductors.

In order to build a switchable all-solid-state electrochromic device we focused our research on optimizing the proton conducting properties of Ta_2O_5 . However, although we succeeded in fabricating a half-device capable of switching optical properties by applying an electrical voltage, this was only possible in high humidity conditions and the reversible switching could not be reproduced. We therefore focused on investigating the optical properties of the Mg-Ti alloys, in order to understand the physical origin of their black hydrogenated state and their surprising structural stability.

1.5 Immiscible alloys

Magnesium and titanium are immiscible elements. The enthalpy of mixing for a $\text{Mg}_{0.50}\text{Ti}_{0.50}$ mixture is as high as $\Delta H_{mix} \approx 20$ kJ/g-atom [33]. The synthesis of Mg-Ti alloys has nevertheless been achieved both in bulk and in thin films via non-equilibrium processes such as physical vapor deposition [34], e-beam deposition [35, 36], sputtering [21, 37, 38] and mechanical alloying [39]. In our laboratory we deposit Mg-Ti thin films by means of magnetron sputtering. These films have intriguing optical properties: in their metallic state they are shiny reflecting while, when loaded with hydrogen, they turn into a “black” light-absorbing state, characterized by very low reflectivity over an unusual broad range of photon energies, from 1 to 6 eV. Furthermore they do not segregate into pure Mg and Ti upon hydrogen absorption/desorption cycles as observed for many other binary Mg-based alloys, such as YMg [40], GdMg [41, 42], LaMg [19] and MgV[43]. These remarkable properties have to originate from a non-trivial microstructure. In order to study the structural properties of immiscible alloys, however, standard X-Ray Diffraction techniques are often inadequate: immiscible elements “frozen” in a metastable mixture can develop a certain degree of order, in which atoms of the same element tend to aggregate and form small clusters within the crystal structure of the alloy [44]. The wavelength of such nanosized inhomogeneities is often much shorter than the coherence wavelength probed by X-Ray Diffraction and a partially segregated alloy can therefore be undistinguishable from one with a random distribution of atoms. In order to study these systems it is therefore necessary to probe the local environment of the atoms with techniques sensitive to the local atomic distribution of the atoms. A valuable tool in detecting local atomic arrangements is EXAFS (Extended X-ray Absorption Fine Structure), a technique that uses synchrotron radiation to measure the total number of neighbors of a particular element “X”, their chemical nature and their distance from X [45].

The partial segregation of the component of a binary alloy can be quantified

by the so-called Chemical Short-Range Order (CSRO) parameter, s [46, 47]. For a binary system of the type A_xB_{1-x} , s is defined as

$$s = 1 - \frac{n_{BA}}{(n_{BA} + n_{BB}) \cdot x} = 1 - \frac{n_{BA}}{n_c \cdot x} \quad (1.3)$$

where n_{BA} is the number of B-A bonds per B atom, n_{BB} is the number of B-B bonds per B atom and their sum is the total coordination number around each B atom, n_c . This definition is particularly handy when measuring the chemical short-range order with EXAFS, as this technique allows to measure directly the average number of bonds of a particular element. A more general definition of chemical short-range order is given in Appendix A. In figure 1.8 we show the effect of chemical short-range order on a binary alloy A_xB_{1-x} , with $x = 0.7$ and $s = 0, 0.4$ and 0.8 . The s parameter is such that, for $s = 0$,

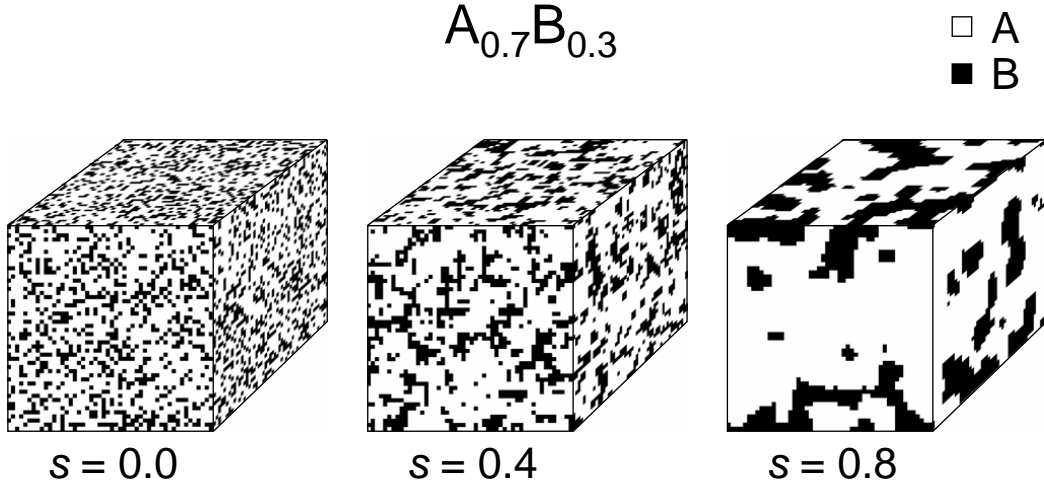


Figure 1.8: Visual representation of the atoms distributions in a binary cubic $A_{0.7}B_{0.3}$ alloy with different degrees of chemical short-range order. The images are generated by a three-dimensional Monte Carlo calculation.

the atoms distribution within the alloy is completely random while, for $s > 0$, A and B atoms cluster into small chemically homogenous domains. In this representation a CSRO parameter $s = 1$ would describe a completely segregated system, while $s = -1$ would correspond to a perfect “antiferromagnetic order”, in which each A atom is only surrounded by B atoms and viceversa.

By combining XRD and EXAFS studies we will show that in Mg_yTi_{1-y} thin films the distribution of Mg and Ti atoms is not random and that a certain level of local chemical segregation occurs, without affecting the long-range structural coherence of the film [48]. Such microstructure is responsible for the great structural stability observed in these metastable alloys, which retain their structural integrity upon multiple cycles of hydrogen loading and unloading. By applying the proper synthesis techniques one may thus aim

to stabilize crystal structures not feasible according to basic thermodynamics. This kind of microstructures are of particular technological interest in the synthesis of new metastable materials, with high hydrogen storage capacities and fast hydrogen absorption and desorption kinetics.

1.6 This thesis

As already mentioned above, at the beginning of our investigation we searched for new materials capable of switching between a reflecting metallic state and a black hydrogenated state. Our attention focused on the optical properties of Mg-Ti thin films, as described in Chapter 2. These alloys have a mirror-like appearance in the as-deposited state and, when exposed to hydrogen, undergo a fast and reversible optical transition towards a black light-absorbing state [21]. Furthermore their solar absorptances and thermal emissivities, which are key parameters in defining the thermal efficiency of a solar collector, can be readily tailored by proper choice of layer thickness and composition [22]. The reversibility and structural stability of these alloys is remarkable when considering that Mg and Ti are immiscible and do not form any thermodynamically stable alloy or compound. Their hydrogenated black appearance extends in the whole visible range and suggested also their application as optical hydrogen sensor [23, 49]. Given the broad technological interest of Mg-Ti thin films, we wanted to have a better understanding of the physical origin of their hydrogenated black state, by looking at the microstructural details of these alloys.

The structural properties of Mg-Ti thin films are described in Chapter 3. The metallic $\text{Mg}_y\text{Ti}_{1-y}$ thin films are crystalline with hexagonal symmetry and, upon hydrogenation, undergo a phase transition to a MgH_2 -like tetragonal phase for $y > 0.87$ and to a face-centered-cubic phase for $y < 0.87$ [38]. The black optical appearance of the hydrogenated state was originally interpreted as originating from the coexistence of metallic (reflecting) TiH_2 and insulating (transparent) MgH_2 nanosized domains. In order to confirm this picture we performed Ti K-edge Extended X-ray Absorption Fine Structure (EXAFS) on $\text{Mg}_y\text{Ti}_{1-y}$ thin films [48]. The advantage of EXAFS with respect to standard diffraction techniques, is that it allows to obtain detailed information about the local distribution of the atoms in the crystalline lattice. A similar microstructural information was obtained after appropriate modeling and fitting of the Pressure-optical Transmission-Isotherms (PTI's) measured with Hydrogenography, on a $\text{Mg}_y\text{Ti}_{1-y}$ thin film with a compositional gradient ($0.6 < y < 0.89$) [50]. Both techniques converge to indicate that Mg-Ti thin films are made of a crystalline fine dispersion of Mg and Ti atoms characterized by a small degree of chemical short-range order.

Given the exceptional properties observed in metastable Mg-Ti thin films, originating from the coherent coexistence of Mg-rich and Ti-rich domains, we

wanted to have a deeper understanding of the effects of chemical segregation and coherence in Mg-Ti systems. In order to do so we artificially engineered one dimensional chemical short-range order by depositing Pd-capped Mg/Ti multilayers, with several bilayer thicknesses [51]. The structural, optical and hydrogen absorbing characteristics of these multilayers are described in Chapter 4. We were particularly intrigued by the nature of the Mg/Ti interfaces: *Is it possible to obtain structurally coherent interfaces, notwithstanding the large lattice parameter mismatch existing between the crystal structures of pure Mg and Ti? How is such coherence affected by the absorption and desorption of hydrogen? How large is the out-of-plane expansion of the individual layers upon hydrogen absorption? Given the geometry of the multilayers, what hydrogen loading and unloading sequences should we expect?*

Although we have been able to answer all these questions, a new and somewhat more intriguing problem arose after measuring the thermodynamic properties of hydrogen absorption in Mg/Ti multilayers: *Are the thermodynamics of hydrogen absorption going to be affected by the nature of the Mg/Ti interfaces?* In order to address this problem we thoroughly investigated the hydrogen loading properties of Mg layers “sandwiched” between various materials, as described in Chapter 5.

We found that Mg thin films covered with Pd feel a strong elastic clamping due to the capping layer, leading to hydrogen plateau pressures significantly higher than what expected from bulk Mg. A simple elastic model allows to interpret the dependence of the plateau pressure on the Mg thickness [52]. The clamping arises as a consequence of alloying of Mg and Pd at the Mg/Pd interface. A similar effect is observed for Ni-capped Mg films. On the contrary, Mg films sandwiched between immiscible elements, such as Ti, Nb and V, do not feel significant elastic constraints, thanks to the positive enthalpy of mixing, which leads to poor interface adhesion [52, 53]. The possibility to use elastic constraints to tune the hydrogen absorption characteristics of thin metallic films opens new interesting perspectives, for the development of advanced optical hydrogen detectors and tailored hydrogen storage materials, with optimized thermodynamic properties.

Chapter 2

Mg-Ti-H thin films: reversible black mirrors

2.1 Introduction

Mg and Ti are immiscible elements in thermodynamic equilibrium. Mg-Ti alloys have nevertheless been synthesized both in thin films and in bulk, by means of high-energy techniques, such as mechanical alloying [39], physical vapour deposition [34], electron beam deposition [35, 36] and magnetron sputtering [21, 37].

In 2005 Niessen and Notten [35] characterized e-beam deposited Mg-Ti thin films by means of electrochemical loading. They found good gravimetric hydrogen storage capacity and fast and reversible kinetics of hydrogen absorption and desorption. Triggered by their findings we studied how the optical properties of co-sputtered Pd-capped Mg-Ti thin films would change, when exposed to different pressures of hydrogen gas.

Surprisingly we found that the hydrogenated state of $\text{Mg}_y\text{Ti}_{1-y}$ ($y = 0.7, 0.8$ and 0.9) thin films has a very low reflection and transmission (i.e., very high absorption) in the whole visible spectrum. This black state appeared to be a stable, final, fully hydrogenated state and not due to preferential nucleation of the hydride at the substrate/sample interface [21]. The discovery of a reversible, fast and robust system capable of switching between a mirror-like and a black appearance led to the idea of using such materials as optical hydrogen detectors [23, 24, 25] and switchable covers for solar collectors [21, 22].

Solar collectors are devices that absorb solar radiation and transfer the absorbed heat to a cooling fluid (typically water). Their disadvantage is that, when not in use, such devices can reach very high temperatures (up to $300\text{ }^\circ\text{C}$) hence requiring expensive building materials. A switchable black mirror could therefore be used to circumvent this problem: when hydrogenated the black mirror absorbs light and heats the water and when dehydrogenated it reflects the light avoiding overheating of the system.

In order to maximize the efficiency of a solar collector the solar absorptance,

given by the integral of the convolution of the film's absorption spectrum with the solar spectrum, must be maximized while its thermal emissivity, given by the integral of the convolution of the film's absorption spectrum with the black body radiation at the operating temperature, must be minimized. By accurate measurements of the optical reflection and transmission of $\text{Mg}_y\text{Ti}_{1-y}$ thin films in a broad range of energies, we determined the dielectric functions for these materials. This allowed us to make predictions about the solar absorptance and thermal emissivity of Mg-Ti thin films with various thicknesses and compositions. By implementing the optimum values obtained in a theoretical solar collector model we demonstrated the possibility to reduce the stagnation temperature, defined as the temperature at which the collector efficiency drops to zero, from ~ 180 to ~ 80 °C [22].

In Section 2.2 we measure the optical properties of $\text{Mg}_y\text{Ti}_{1-y}$ thin films ($y = 0.7, 0.8$ and 0.9) and demonstrate their cycling stability upon multiple hydrogen loading and unloading cycles.

In Section 2.3 we discuss in more detail the dependence of the solar absorptance and thermal emissivity of $\text{Mg}_y\text{Ti}_{1-y}$ thin films on film's thickness and composition, in the perspective of their implementation as a VArIable REflecting Material (VAREM) in solar collectors.

2.2 Mg-Ti-H thin films for smart solar collectors

Abstract – Mg-Ti-H thin films are found to have very attractive optical properties: they absorb 87% of the solar radiation in the hydrogenated state and only 32% in the metallic state. Furthermore, in the absorbing state Mg-Ti-H has a low emissivity; at 400 K only 10% of black body radiation is emitted. The transition between both optical states is fast, robust and reversible. The sum of these properties highlights the applicability of such materials as switchable smart coatings in solar collectors.

2.2.1 Introduction

Many metal hydrides behave as switchable mirrors (i.e. their optical properties switch from reflective in the metallic state to transparent in the hydrogenated state) [11, 15, 16, 54]. In addition, magnesium-rare-earth (Mg-RE) and magnesium-transition-metal (Mg-TM) switchable mirrors also exhibit an intermediate highly absorbing optical state on hydrogenation. The possibility to switch a film from a reflective state to an absorbing state suggests that such materials might be interesting for smart solar collectors, which absorb light in normal operation condition and switch to a reflective state to avoid overheating. Limiting the stagnation temperature of the solar collector makes it possible to use cheap materials such as plastics (generally not designed for high temperatures).

In this Letter we show that $\text{Mg}_y\text{Ti}_{1-y}$ thin films prepared by dc magnetron co-sputtering of Mg and Ti at room temperature (on quartz and CaF_2) satisfy the following requirements for a smart solar coating i) high absorption in the solar regime ($0.5 < \hbar\omega < 4$ eV), ii) low emissivity in the thermal regime ($\hbar\omega < 0.5$ eV) and iii) reversibility.

2.2.2 Experimental details

Three compositions are studied in detail: $y=0.70$, $y=0.80$ and $y=0.90$. Typical deposition rates are: $2\text{\AA}/\text{s}$ for Mg (150 W RF power), $0.1\text{-}1\text{\AA}/\text{s}$ for Ti (25-160 W DC power) and $1.3\text{\AA}/\text{s}$ for Pd (50 W DC power). All the films are covered with a Pd layer (10-50 nm) to promote dissociation of H_2 and to prevent oxidation of the underlying film. Reflection (R) and transmission (T) spectra are measured simultaneously during hydrogenation (pressures up to 1 bar H_2) in a Perkin Elmer Lambda 900 diffraction grating spectrometer ($0.495 < \hbar\omega < 6.51$ eV) and a Bruker IFS 66 Fourier transform infrared spectrometer ($0.2 < \hbar\omega < 1.1$ eV). The R-T spectra are measured through the transparent substrate at near normal incidence of the incoming beam.

2.2.3 Results and discussion

Figures 2.1(a) and 2.1(b) show the reflection and transmission spectra measured for 200 nm $\text{Mg}_y\text{Ti}_{1-y}/10$ nm Pd films ($y=0.90$, 0.80 and 0.70) in the as-prepared and hydrogenated state (in 1 bar H_2 at room temperature). In the metallic state (Fig. 2.1(a)) all the films have a relatively high and featureless reflection that decreases with increasing Ti content. After hydrogen absorption, the reflection is low for all compositions whereas significant transmission is observed only for the $y=0.90$ sample. The combination of low reflection and low transmission in the hydrogenated state ($y=0.80$ and 0.70 samples) gives rise to a highly absorbing state that extends over the entire visible range. For example $\text{Mg}_{0.80}\text{Ti}_{0.20}\text{H}_x$ absorbs $\sim 87\%$ of the solar radiation in the hydro-

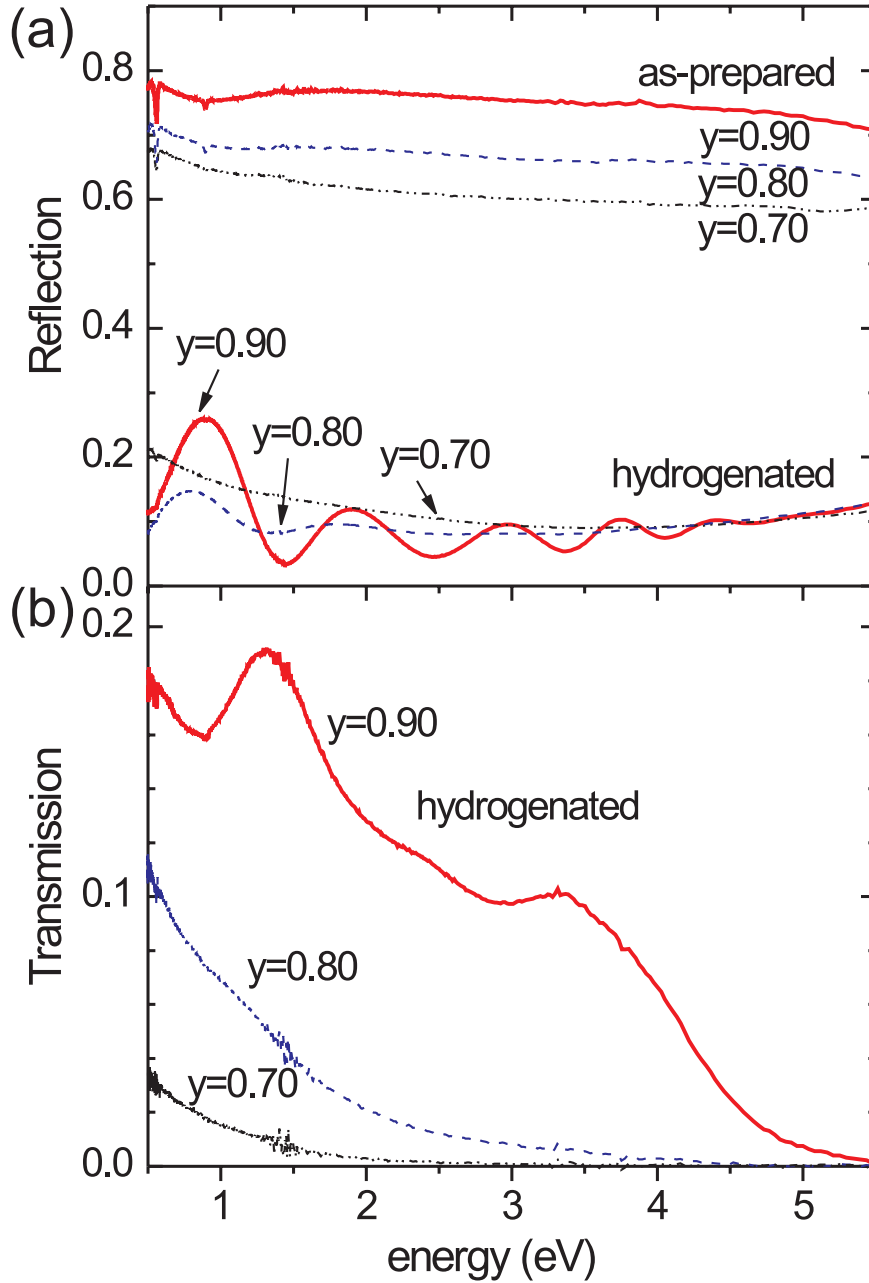


Figure 2.1: (a) Reflection spectra measured on 200 nm $\text{Mg}_y\text{Ti}_{1-y}/10$ nm Pd films with $y=0.90$, 0.80 and 0.70 in the as-prepared (metallic) and hydrogenated state (1 bar H_2 at room temperature). (b) Transmission spectra measured on the same films in the hydrogenated state. In the metallic state the transmission is below the detection limit of the spectrometer.

generated state and only $\sim 32\%$ in the reflective state. The highly absorbing state described here is a final state and not an intermediate optical state as in Mg-Ni-H [55] and is thus robust and easily tunable. The same behavior is observed when using electrochemical loading. Again the reflection and transmission vary continuously (R decreasing; T increasing) until the maximum concentration of hydrogen is reached. Thus, this material can be applied both in electrochromic and gasochromic applications.

Despite the limited solubility reported for Ti in bulk Mg, alloying of Mg and Ti is obtained by using physical vapour deposition [34], mechanical alloying [39] or e-beam deposition [35, 36]. We observe a similar crystalline Mg-Ti alloy phase (hexagonal structure) when co-sputtering Mg and Ti. In hydrogenated films the formation of a MgH_2 -like rutile phase is observed for low Ti contents ($y=0.90$) whereas in $\text{Mg}_y\text{Ti}_{1-y}$ with $y=0.80$ and $y=0.70$ a fluorite-like Mg-Ti-H phase is formed, similar to that identified by Kyoi et al. [56] in bulk samples. There are no indications that phase segregation takes place as it is the case for Mg-rare earth systems such as Mg-Gd, Mg-La, Mg-Y [15, 19]. The influence of phase composition and structure on the optical properties will be published elsewhere.

The optical properties of $\text{Mg}_y\text{Ti}_{1-y}$ ($y=0.85, y=0.73$) thin films capped with 10 nm Pd were also studied recently by Farangis *et al.* [57] and Richardson *et al.* [58]. Upon hydrogenation, the x-ray amorphous films prepared by dc magnetron co-sputtering were reported to switch from reflective to transparent similarly to other Mg-TM (TM=Co, Ni, Fe, Mn) with Ti acting primarily as a catalyst for MgH_2 formation [58]. In comparison with the films studied here, their hydrogenated films do have similar low and featureless reflection but also rather high transmission. Probably, due to the small thickness of their films (40-50 nm) the difference in the optical properties of the various hydrides does not show up.

For solar collector applications, it is desirable to have coatings that absorb as much as possible of the solar radiation while emitting as little as possible in the thermal range. A linear extrapolation to lower energies of the R-T spectra shown in Fig. 2.1 does not yield the desired low absorption. This is, however, a problem that is easily solved by choosing an appropriate thickness of the $\text{Mg}_y\text{Ti}_{1-y}$ and Pd layers. The thickness dependence of the absorption ($A=1-R-T$) calculated for a $\text{Mg}_y\text{Ti}_{1-y}\text{H}_x/\text{Pd}$ ($y=0.80$) film is shown in Fig. 2.2(a). For these calculations we use the dielectric function of $\text{Mg}_y\text{Ti}_{1-y}\text{H}_x$ derived from measurements on thick films in the 0.5-6 eV energy range. The overall reflection (from the substrate side) and transmission are then calculated by means of a transfer matrix method [59]. The quartz substrate and the Pd cap layer [60] are also taken into account. The thickness of the Pd layer is fixed to 40 nm. Such a thick layer suppresses any optical transmission and also contributes to the total reflection (measured from the substrate side). The thickness of the Mg-Ti-H layer is varied between 30 and 250 nm. As shown

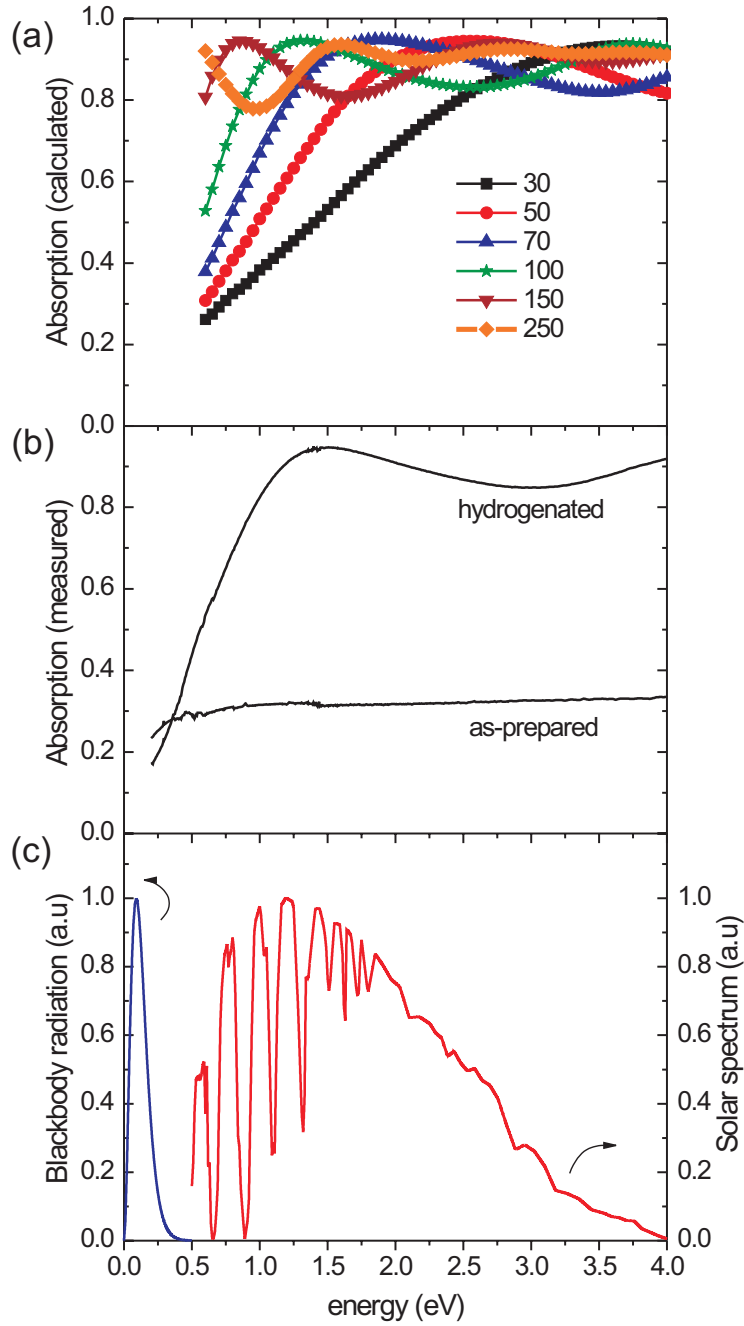


Figure 2.2: (a) Absorption spectra calculated for a $[\text{d nm}] \text{Mg}_y\text{Ti}_{1-y}\text{H}_x/40 \text{ nm Pd}$ ($y=0.80$) film; the thickness of the Mg-Ti-H layer $[\text{d}]$ is varied between 30 and 250 nm. (b) Absorption spectra measured for a 65 nm $\text{Mg}_y\text{Ti}_{1-y}/40 \text{ nm Pd}$ ($y=0.80$) film in the as-prepared and hydrogenated state (1 bar H_2 at room temperature). (c) Spectrum of the solar radiation at atmospheric mass AM 1.5 shown together with the blackbody radiation at 400 K. Both are in arbitrary units.

in Fig. 2.2(a), with increasing layer thickness, the absorption edge shifts to lower energies while the overall absorption stays very high in the solar range. Therefore, to prevent a high emissivity and still obtain a high solar absorption, we have to choose an intermediate layer thickness. The absorption spectra measured on a 65 nm $\text{Mg}_y\text{Ti}_{1-y}/40$ nm Pd ($y=0.80$) film in the as-prepared and hydrogenated state (1 bar H_2 at room temperature) are shown in Fig. 2.2(b) and compare quite well with the predicted one. In the hydrogenated state, the total solar absorption is high (87%) but low in the thermal range. The thermal emissivity of the system is calculated by extrapolating the absorption to zero energies and convoluting the data with the blackbody radiation at 400 K (spectrum shown in Fig. 2.2(c) together with the spectrum of the solar radiation at atmospheric mass AM 1.5). The result, a thermal emissivity of 0.10 is quite promising and indeed much lower than that of a thick film (~ 0.50).

A key issue for switchable coatings is the reversibility. This is tested by measuring reflection (through the transparent substrate) during gas cycling: hydrogenation with 5% H_2 in Ar (250 ml/m flow) and dehydrogenation with 20% O_2 in Ar (250 ml/m flow). Here we focus on the highly absorbing compositions ($y=0.80$ and $y=0.70$) that also show better switching properties as compared to the $y=0.90$ sample. In Fig. 2.3(a) we compare the reflection ($\hbar\omega=1.95$ eV) for the first two cycles measured on 65 nm $\text{Mg}_y\text{Ti}_{1-y}/40$ nm Pd films ($y=0.70$ and $y=0.80$). The reflective-to-absorbing transition is very fast and rather independent of composition. An increase in Ti content has a beneficial effect on the absorbing-to-reflective speed though it decreases slightly the optical contrast. A set of 15 cycles measured for the $y=0.70$ sample is shown in Fig. 2.3(b). This result illustrates both the stability and reversibility of the system: the switching time from the reflective to the absorbing state is of only a few seconds and stays rather constant similar to the optical contrast. Switching back to the reflective state is however slower and increases slightly with cycling. This effect could be related to poisoning of the Pd cap layer and/or intermixing at the interface. Appropriate coatings and/or buffer layers can improve these performances.

2.2.4 Conclusions

Summarizing, we have shown that $\text{Mg}_y\text{Ti}_{1-y}$ thin films have very attractive switchable optical properties that can be tuned by varying the composition and film thickness. In the optimal configuration, the films absorb 87% of the solar radiation in the hydrogenated state and only 32% in the metallic state improving thus the solar absorption efficiency and reducing the stagnation temperature. Furthermore, in the absorbing state Mg-Ti-H has a low emissivity; at 400 K only 10 % of black body radiation is emitted. These characteristics are comparable to that of advanced solar coatings such as ceramic-metal composite materials [61]. Mg-Ti-H however, has the great advantage of being

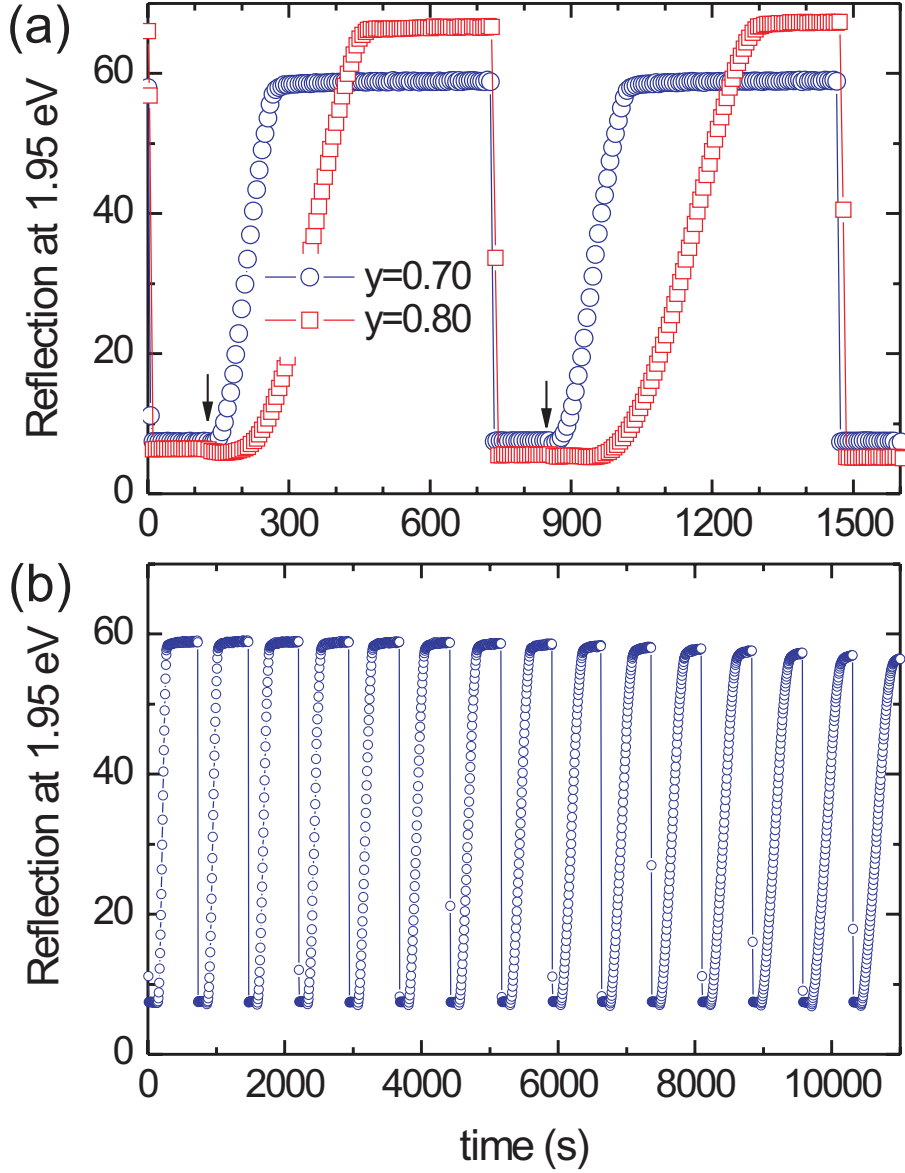


Figure 2.3: (a) Reflection at $\hbar\omega=1.95$ eV measured on 65 nm $\text{Mg}_y\text{Ti}_{1-y}/40$ nm Pd films with $y=0.70$ and $y=0.80$; the first two cycles are shown. Hydrogen is introduced in the system at: $t=0$, 730 and 1470 s; starting of the dehydrogenation period is indicated by the two arrows; loading is done with 5% H_2 in Ar flow and unloading with 20% O_2 in Ar flow. (b) Same measurements as in (a) but for more cycles.

switchable. The combination of these properties highlights the applicability of Mg-Ti-H thin films as switchable smart coatings for solar collector applications. Moreover, the fast switching together with the high optical contrast between the reflective and the absorbing state makes Mg-Ti-H films also interesting for hydrogen sensor applications. The solar collector and sensor applications of Mg-Ti-H thin films described in this Letter combined with the very large reversible hydrogen storage capacity of Mg-Ti-H thin film battery electrodes reported earlier by Notten and co-workers [35, 36] make this metal-hydride system truly remarkable.

2.3 Mg-Ti-H thin films as switchable solar absorbers

Abstract – The reflection and transmission spectra of Pd capped $\text{Mg}_y\text{Ti}_{1-y}$ thin films ($y = 0.7, 0.8$ and 0.9) are measured in the 0.5 to 5.5 eV energy range, both in the as-prepared and hydrogenated states. Upon hydrogenation these films switch reversibly from a shiny metallic state into a “black” absorbing one. The composition and thicknesses can be tailored to achieve high solar absorptance and low thermal emittance in the hydrogenated state. The combination of these two characteristics is interesting for the application of this material as switchable absorber in solar collectors. The use of a $\text{Mg}_y\text{Ti}_{1-y}$ switchable absorber in solar collectors allows to lower the stagnation temperature from 180 to 80°C. The collector efficiency is affected only minimally.

2.3.1 Introduction

In 1996 Huiberts et al. discovered that Y and La thin films exhibit drastic optical changes upon hydrogenation [11]. Shiny reflecting in the metallic state they become transparent during hydrogen loading. Richardson et al. found similar behavior in Mg_2Ni thin films [16, 54]. Besides the reflecting and the transmitting states, Mg_2Ni films also showed an intermediate absorbing state [62] due to the preferential nucleation of the hydride phase at the film-substrate interface [17]. We have recently found that an absorbing (black) state is also present when hydrogenating $\text{Mg}_y\text{Ti}_{1-y}$ thin films, Fig. 2.4. The black state in $\text{Mg}_y\text{Ti}_{1-y}\text{H}_x$ thin films is, however, a final, reversible state and offers therefore interesting possibilities for technological application as switchable absorber in solar collectors [21]. In solar collectors, the absorber must have a very high absorptance in the solar spectrum (ss) ($h\nu > 0.5$ eV), while simultaneously having a very low emittance in the infrared ($h\nu < 0.5$ eV). In this way, the conversion of solar irradiation is maximized while thermal losses are minimized. However, due to this optimization, temperatures in a solar collector can rise to above 200°C under stagnation conditions, i.e. when no heat is withdrawn from the collector. Therefore, relatively expensive materials such as copper or aluminium must be used to withstand these temperatures. This puts a fundamental lower limit on the cost of solar collectors. To structurally lower the cost, cheaper materials are needed. Polymer technology has developed several materials that can withstand temperatures up to $150\text{-}200^\circ\text{C}$ but their costs are still too high to be economically feasible for application in solar collectors. On the other hand cheap plastics cannot withstand temperatures above $\sim 100^\circ\text{C}$. We show how the use of $\text{Mg}_y\text{Ti}_{1-y}$ thin films as switchable absorbers can effectively reduce the stagnation temperature of a solar collector, without affecting the collector efficiency. We also show how it is possible to tune the solar absorptance and thermal emittance of this material, by properly tailoring alloy composition and film thickness.

2.3.2 Experimental details

200 nm thick $\text{Mg}_y\text{Ti}_{1-y}$ ($y = 0.7, 0.8$ and 0.9) films covered with 10 nm of Pd are prepared by DC/RF magnetron co-sputtering of Mg and Ti, on quartz substrates. The palladium layer is needed to prevent oxidation and to promote hydrogen dissociation. The film composition and thickness are measured *ex-situ* by Rutherford backscattering and profilometry, on samples prepared during the same deposition run, but on carbon substrates. The reflection (R) and transmission (T) spectra of the films are measured in a Perkin Elmer Lambda 900 diffraction grating spectrometer ($0.5 < h\nu < 6.5$ eV) and in a Bruker IFS 66 Fourier transform infrared spectrometer ($0.2 < h\nu < 1.1$ eV). The spectra are measured through the substrate, at near normal incidence, on films in the as-prepared state and during hydrogenation (H_2 pressures up to 1 bar).

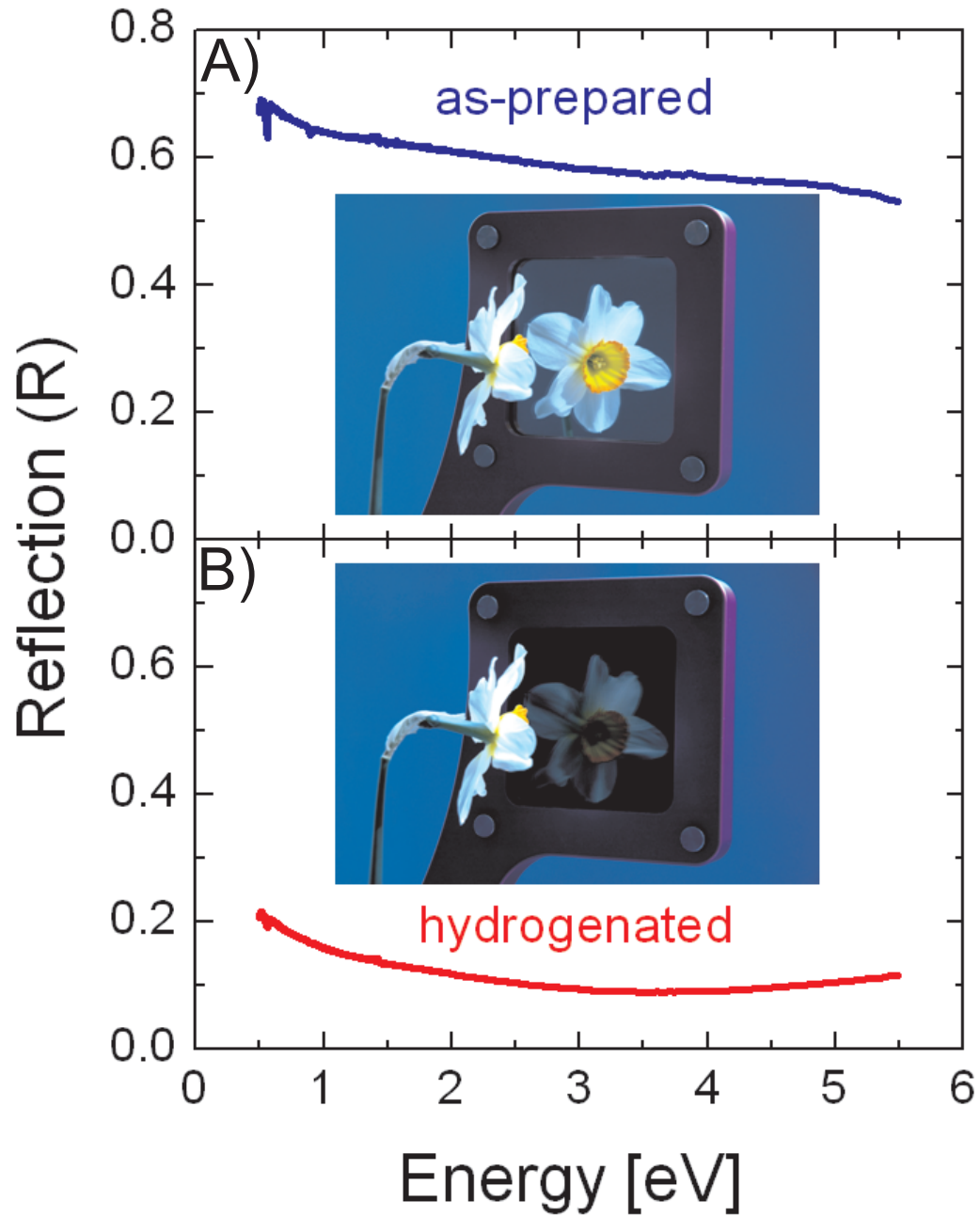


Figure 2.4: Reflection spectra and optical appearances of a 200 nm $\text{Mg}_{0.7}\text{Ti}_{0.3}$ film covered with 10 nm Pd, viewed through the glass substrate. (a) in absence of hydrogen the reflection of the $\text{Mg}_{0.7}\text{Ti}_{0.3}$ layer is mirror-like. (b) when exposed to 4% H_2/Ar mixture the reflection drops and the layer becomes black.

2.3.3 Results and discussion

Absorption ($A = 1 - R - T$) spectra of 200 nm $\text{Mg}_y\text{Ti}_{1-y}$ films covered with 10 nm Pd are shown in Fig. 2.5. In the as-prepared states the films have a

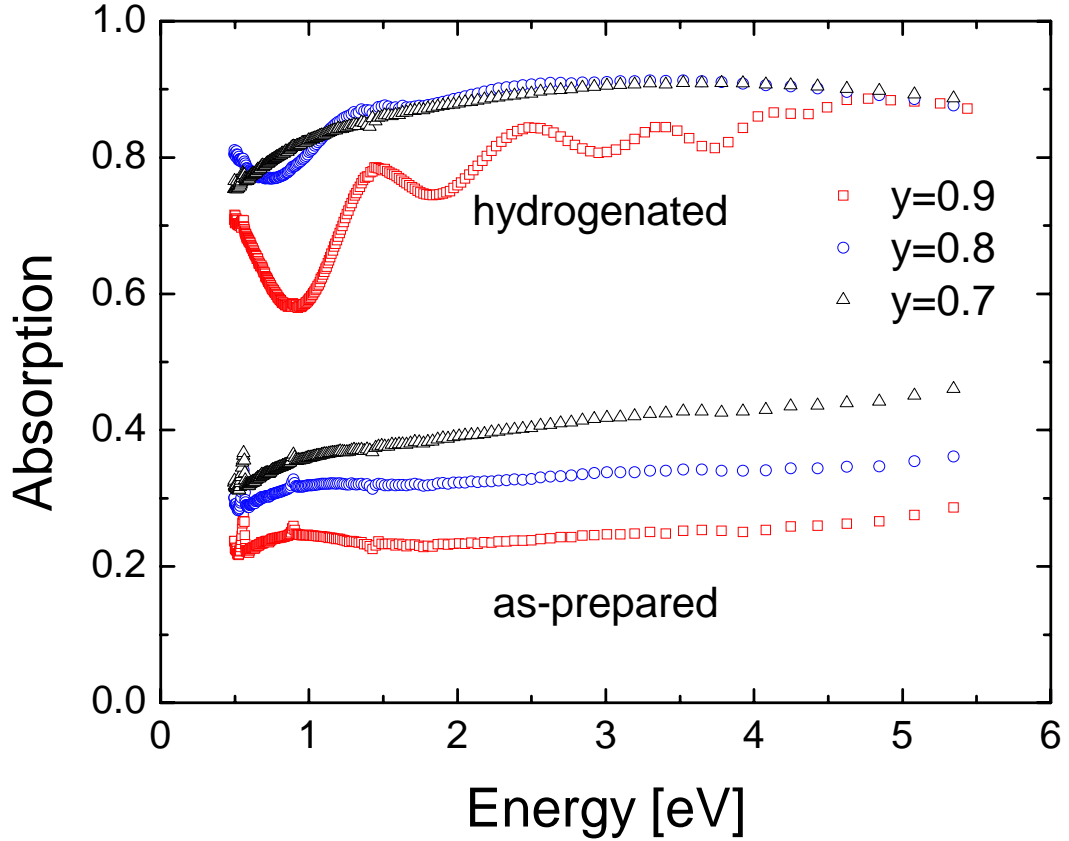


Figure 2.5: Absorption spectra of 200 nm $\text{Mg}_y\text{Ti}_{1-y}$ thin films ($y = 0.7, 0.8, 0.9$), covered with 10 nm Pd, measured in the as-prepared and hydrogenated (1 bar H_2 at room temperature) states.

high (metallic) reflection and no transmission and consequently low absorption. When exposed to 1 bar H_2 at room temperature the absorption increases for all compositions: the reflection decreases dramatically and a significant transmission is observed only for $y = 0.9$ [21]. In order to evaluate the total solar absorptance (SA) of these films we convolute the absorption spectra (A) with the solar spectrum (SS) in the 0 to 4 eV range. In addition we calculate the ratio (Z) between the SA in the hydrogenated and as-prepared states, Fig. 2.6. The maximum SA (87%) is obtained for the hydrogenated state of $\text{Mg}_{0.8}\text{Ti}_{0.2}$, while the best contrast (highest Z) is found in the $y = 0.9$ composition. However the speed of hydrogen absorption and desorption are strongly dependent on the metal ratio in the initial alloy and films with higher Ti content have the best kinetics. These layers have absorptances only slightly

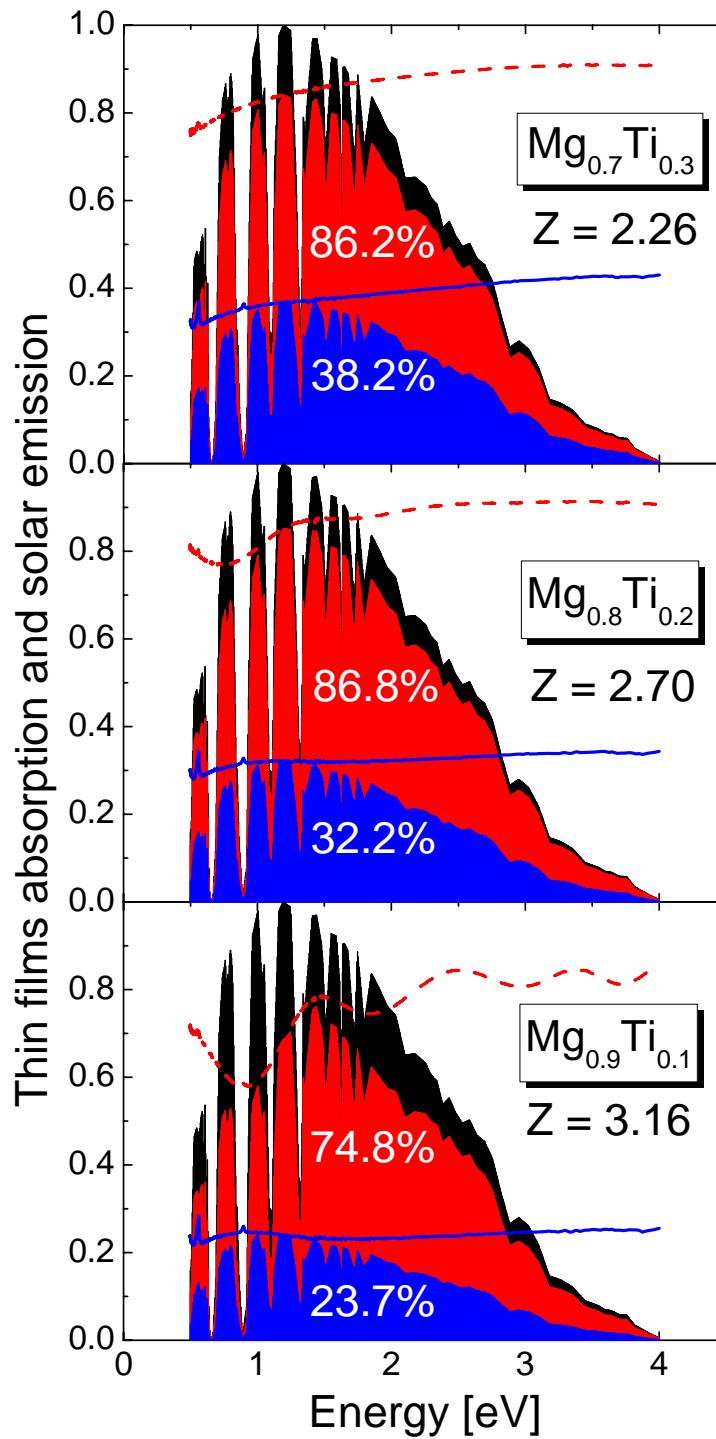


Figure 2.6: Lines: absorption spectra of the as-prepared (solid line) and hydrogenated (dotted line) states for 200 nm $\text{Mg}_y\text{Ti}_{1-y}$ thin films ($y = 0.7, 0.8, 0.9$), covered with 10 nm Pd. Areas: solar spectrum (black) and its convolution with the absorption spectra of the as-prepared and hydrogenated states.

lower than those found in commercially available absorbers (91-96%) [63], but they have the great advantage of being switchable. In order to increase the efficiency of a solar absorber, it is also necessary to reduce the thermal emittance as much as possible [64]. The thermal emittance of a layer stack can be tuned by changing the thicknesses of the layers and it depends on the dielectric functions of the materials. From the reflection and transmission measurements we have calculated the dielectric functions of our $\text{Mg}_y\text{Ti}_{1-y}$ thin films through a Drude-Lorentz parametrization [38]:

$$\varepsilon(\omega) = \varepsilon_1 + i\varepsilon_2 = \varepsilon_\infty - \frac{\omega_p^2}{\omega^2 + i\omega/\tau} + \sum_{j=1}^3 \frac{f_j}{\omega_{0j}^2 - \omega^2 - i\omega\beta_j} \quad (2.1)$$

where ε_∞ accounts for high energy excitations, the second term in the sum is the free-carrier absorption (Drude) and the last term is a sum of three Lorentz oscillators. With the dielectric functions obtained we have calculated the absorption spectra for different thicknesses of hydrogenated $\text{Mg}_y\text{Ti}_{1-y}$ films, covered with 40 nm of Pd. The thermal emittance is then derived by convoluting the calculated absorption spectra with the black body radiation at 100°C in the 0 to 0.5 eV range. The absorption spectra in this range are obtained by linearly extrapolating to zero energy the spectra obtained in the 0.5 to 5.5 eV range [21]. The results are shown in Fig. 2.7. It is clear that in order to

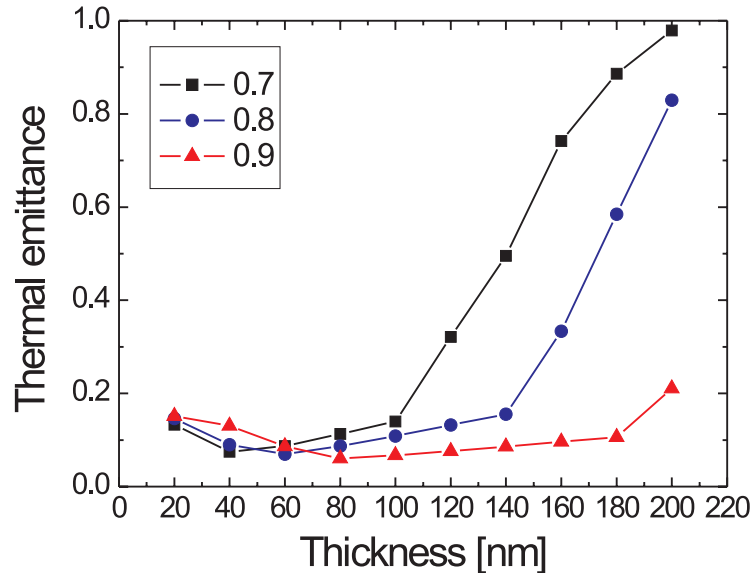


Figure 2.7: Thickness dependence of the calculated thermal emittance of hydrogenated $\text{Mg}_y\text{Ti}_{1-y}$ thin films ($y = 0.7, 0.8, 0.9$), covered with 40 nm of Pd.

reduce the thermal emittance, the film thickness should not exceed a critical value, depending on composition: in fact, from an analysis of the dielectric functions we have seen that the higher the amount of Ti in the film, the higher is the extinction coefficient (k) and therefore the lower will be the thickness at which the thermal emittance starts to increase. On the other hand a too thin layer would compromise the SA due to an increase in transmission in the visible range. A thickness of 65 nm is a good compromise for all compositions both in terms of high SA and low thermal emittance. The hydrogenation process is both fast and reversible: upon exposure to 5% H₂/Ar mixture a 65 nm Mg_{0.7}Ti_{0.3} film covered with 40 nm of Pd undergoes an optical transition from shiny metallic to black absorbing in a few seconds. By subsequent exposure to a 20% O₂/Ar mixture the films dehydrogenate in less than 200 seconds [21] recovering the initial state both from an optical and a structural point of view [38]. The reversibility has been demonstrated for over 150 cycles. In order to evaluate the applicability of a Mg_yTi_{1-y} layer as a switchable absorber in a real solar collector we consider the model collector depicted in Fig. 2.8a. The model consists of a glass cover, an air gap and the switchable absorber which is in thermal contact with the water pipes. The light shines from above onto our film, through its substrate. In order to achieve an optical switch we have either to expose our absorber to hydrogen (gasochromic loading) or to integrate it into an all-solid state electrochromic device (electrochromic loading). In our simulation, however, we consider the absorber as a single layer. We did not take into account the effects due to the substrate, the eventual hydrogen gas reservoir or the additional layers needed in an electrochromic device. This is reasonable both from an optical and a thermal point of view: the major optical changes happen at the substrate-film and film-palladium interfaces and the optical properties of the substrate do not have a significant influence on them. Furthermore the films are very thin, assuring a high thermal conduction to the water pipes even in presence of additional layers. The stagnation temperature of the whole collector is plotted as a function of the SA and thermal emittance of our absorber in Fig. 2.8b. The calculation is based on the method described by De Vries [65] and Zondag *et al.* [66]. As an example of the behavior of a Mg_yTi_{1-y} layer we have taken a 65 nm thick Mg_{0.8}Ti_{0.2} covered with 40 nm of Pd and calculated its SAs and thermal emittances both in the as-prepared and hydrogenated states. From Fig. 2.8b we see that, by switching the layer between these two states, the stagnation temperature can be lowered from ~180 to ~80°C. The calculations have also shown that the collector efficiency is affected only minimally.

2.3.4 Conclusions

We have studied the optical properties of Mg_yTi_{1-y} thin films covered with 10 nm of Pd in the 0.5 to 5.5 eV range. Highly reflecting in the as-prepared

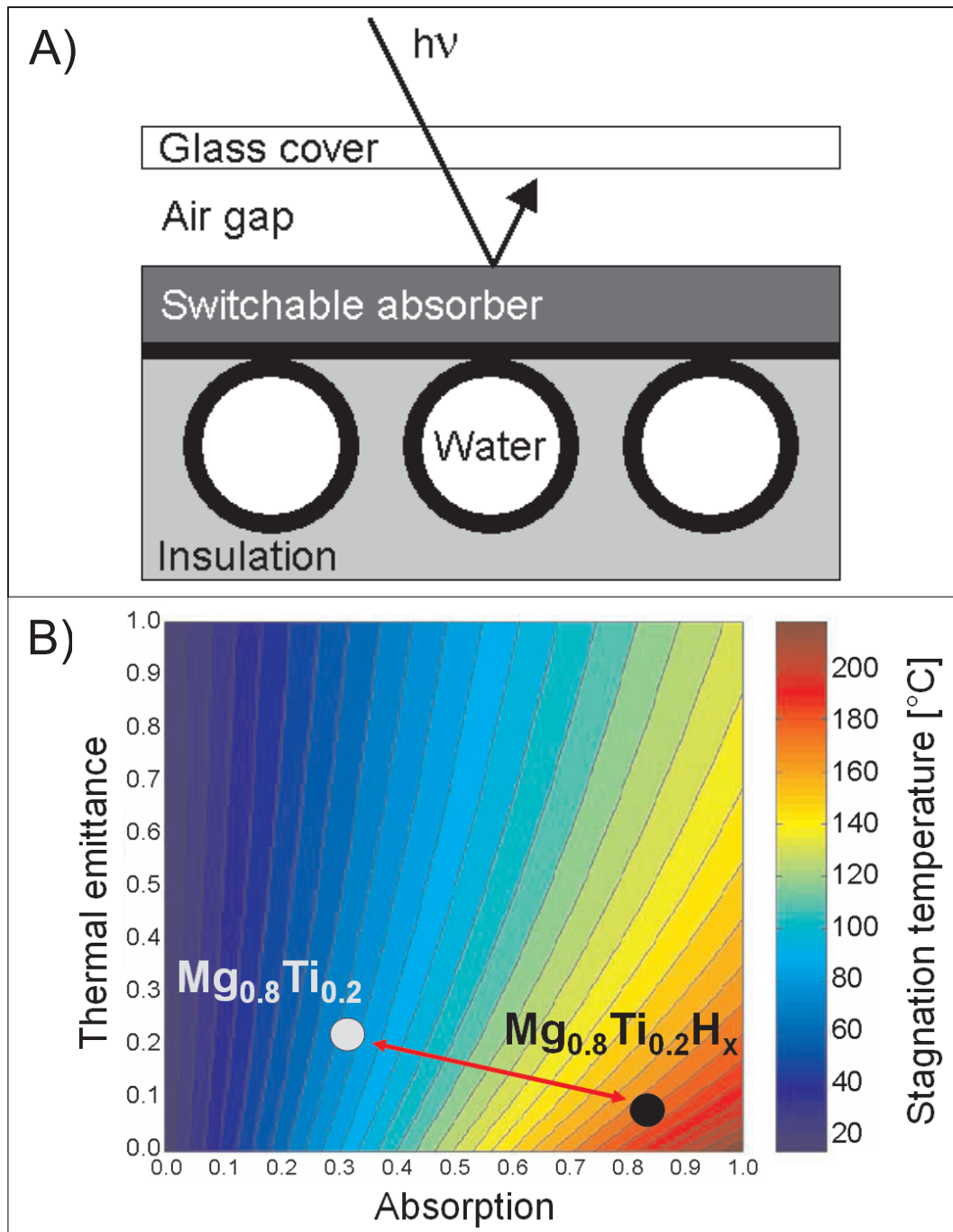


Figure 2.8: (a) Model of the solar collector. (b) Stagnation temperature map as a function of solar absorptance and thermal emittance of the absorber. The dots indicate the stagnation temperature for a 65 nm thick $\text{Mg}_{0.8}\text{Ti}_{0.2}$ covered with 40 nm of Pd, both in the as-prepared (white dot) and hydrogenated (black dot) states.

state these films become highly absorbing upon exposure to hydrogen. The hydrogenated “black” state is a final, reversible state. The SA and thermal emittance of these layers can be tailored by changing the metal ratio in the initial alloy and the thickness of the films. These optical properties are ideal to be used in a solar collector, in order to reduce the stagnation temperature, without significantly decreasing the efficiency of the device.

Chapter 3

Chemical short-range order in Mg-Ti thin films

3.1 Introduction

The optical black state observed in hydrogenated Mg-Ti thin films is not only interesting from the point of view of its technological applications, but it also raises questions on its physical origin. Such a black appearance is commonly observed in cermet materials, dispersions of metallic particles in a ceramic matrix, in which strong light absorption occurs due to localized surface plasmon resonance (LSPR): light induced collective excitation of the conduction electrons at the surface of the metallic nanoparticles. This analogy suggested the possibility that Mg-Ti-H thin films might be composed of metallic TiH₂ nanoparticles dispersed into an insulating MgH₂ matrix. To verify such hypothesis we performed thorough investigation of the optical, structural and electrical properties of Mg_yTi_{1-y} ($0.55 < y < 0.95$) thin films [38].

These metastable alloys are crystalline, with a hexagonal-closed-packed structure in the metallic state. The alloys follow closely Vegard's law [67], suggesting a high degree of atomic intermixing. The crystal structure of the hydrogenated state depends on the composition of the parent alloy. For Mg_yTi_{1-y} films with $y > 0.87$ the structure is tetragonal, similar to pure MgH₂. For $y < 0.87$ a face-centered-cubic phase is observed, similar to the TiH₂ fluorite phase. The films are structurally reversible upon hydrogen loading/unloading cycles. This is in strong contrast with the behavior observed for many Mg-based binary alloys (such as YMg [40], GdMg [41, 42], LaMg [19] and MgV [43]), which undergo severe phase segregation upon hydrogen absorption and desorption.

In order to test the hypothesis of a composite microstructure we tried to simulate the optical reflection and transmission of the hydrogenated state of several Mg-Ti thin films by using effective medium approximations (EMA). These approximations allow to calculate the dielectric response of a composite material A_xB_{1-x}, by assuming spherical inclusions of element A into a matrix of B (Bruggeman [68]) or spherical particles of A covered with a skin of

material B (Maxwell-Garnett [69]). However, neither of the above approximations succeeded to reproduce the experimental spectra, indicating a non-trivial distribution of the Mg and Ti atoms in the crystalline lattice.

We therefore argued that, given also the positive enthalpy of mixing of Mg and Ti, the microstructure of Mg-Ti thin films could be composed of coherently coupled mixtures of Mg-rich and Ti-rich regions. As we have seen in Section 1.5, however, standard XRD characterization of the films is not sufficient to confirm the presence of partial segregation within our Mg-Ti alloys and we characterized their microstructure by means of EXAFS. Investigating $\text{Mg}_y\text{Ti}_{1-y}$ ($0.53 < y < 0.90$) thin films in the metallic, hydrogenated and dehydrogenated state, we were able to confirm that the distribution of Mg and Ti atoms is not random: a certain degree of local chemical segregation occurs, without affecting the long-range structural coherence of the film. The amount of segregation depends weakly on composition and it is stable upon cycling with hydrogen, with $s \approx 0.3$ for all compositions. This degree of ordering is not unusual in immiscible binary alloys [70, 71] and a visual representation of its effect on the microstructure of a binary alloy is given in Fig. 1.8.

Similar microstructural informations can be obtained by proper modeling of the pressure–transmission–isotherms obtained by hydrogenography. By developing a multi-site lattice gas model, we were able to fit the measured isotherms by varying only one fit parameter: the chemical short-range order, s . The model assumes that hydrogen is absorbed into tetrahedral interstitial sites. In a binary Mg-Ti alloy there are 5 different sites: Mg_4 , Mg_3Ti , Mg_2Ti_2 , MgTi_3 and Ti_4 . Each site has a different energy for hydrogen absorption and their abundance depends on the alloy composition and on the degree of chemical ordering: in a highly segregated system the Mg_4 and Ti_4 sites will be more probable than in a completely random one. The model takes also into account the local lattice deformations due to alloying of Mg and Ti and assumes the existence of a long range elastic H-H interaction between hydrogen atoms dissolved into the metal. The s values obtain by fitting the PTIs are in good agreement with the ones obtained by EXAFS.

The “spinodal-like” distribution of atoms observed in Mg-Ti thin film alloys allows to understand the robustness of these systems: the coexistence of Mg-rich and Ti-rich nanosized domains and the accidental equality in molar volumes of Mg and TiH_2 , allow the Mg-Ti alloys to go through a structurally stable intermediate Mg-TiH₂ state, both upon hydrogenation and dehydrogenation. This kind of microstructure, originating from the rapid cooling of an immiscible mixture of Mg and Ti atoms during sputtering, is of particular technological interest in the synthesis of new materials with high hydrogen storage capacities and fast hydrogen absorption and desorption kinetics. By applying the proper synthesis techniques one may in fact aim to stabilize crystal structures not feasible according to basic thermodynamics. Our work shows that the possibilities to optimize the properties of hydrogen storage materials

are more abundant than previously envisaged.

In Section 3.2 we present a detailed study of the structural, optical and electrical properties of $\text{Mg}_y\text{Ti}_{1-y}$ thin films ($0.55 < y < 0.95$), both in their metallic and hydrogenated states. The aim is to reveal the microstructural details laying underneath the exceptional optical properties described in Chapter 2. As previously mentioned, however, standard X-Ray Diffraction is sometimes inadequate to reveal very short ranged inhomogeneities and local probe techniques, such as EXAFS, have to be used instead.

Section 3.3 describes the results obtained by measuring EXAFS on several Mg-Ti thin films in the as-deposited, hydrogenated and de-hydrogenated states, revealing how these films are characterized by a small degree of chemical short-range order: the Mg and Ti atoms are clustered in chemically homogeneous nanosized domains. Similar results can be obtained by fitting the loading isotherms obtained by hydrogenography.

Section 3.4 describes the theoretical approach used to model the Pressure-optical Transmission-Isotherms measured by Hydrogenography on thin films, characterized by a certain degree of chemical short-range order. The model is then applied to the PTI's measured on a $\text{Mg}_y\text{Ti}_{1-y}$ thin film with a compositional gradient. The values of chemical short-range order parameter s thus obtained agree very well with those measured with EXAFS, demonstrating the validity of the model.

3.2 Structural, optical and electrical properties of Mg-Ti-H thin films

Abstract – The structural, optical and electrical transformations induced by hydrogen absorption/desorption in Mg-Ti thin films prepared by co-sputtering of Mg and Ti are investigated. Highly reflective in the metallic state, the films become highly absorbing upon H-absorption. The reflector-to-absorber transition is fast, robust and reversible over many cycles. Such a highly absorbing state hints at the coexistence of a metallic and a semiconducting phase. It is however, not simply a composite material consisting of independent MgH₂ and TiH₂ grains. By continuously monitoring the structure during H uptake, we obtain data that are compatible with a coherent structure. The average structure resembles rutile MgH₂ at high Mg content and is fluorite otherwise. Of crucial importance in preserving the reversibility and the coherency of the system upon hydrogen cycling is the accidental equality of the molar volume of the Mg and TiH₂. The present results point towards a rich and unexpected chemistry of Mg-Ti-H compounds.

3.2.1 Introduction

Recently, Notten and coworkers [35, 36] reported on the excellent hydrogen storage capacity of Mg-Ti-H thin films which is approx. 5 times larger than that of conventional metal hydride electrodes in NiMH-batteries. Rather surprisingly, we found that the same material has also remarkable optical properties [21]. Highly reflective in the metallic state, the films become strongly absorbing upon hydrogen absorption. For example, fully hydrogenated $\text{Mg}_{0.80}\text{Ti}_{0.20}\text{H}_{\sim 1.7}$ thin films combine a high absorption (87% of the solar spectrum) with a low thermal emissivity (only 10%), while after removal of hydrogen $\text{Mg}_{0.80}\text{Ti}_{0.20}$ absorbs no more than 1/3 of the solar spectrum. The energy conversion performance of fully hydrogenated $\text{Mg}_{0.80}\text{Ti}_{0.20}\text{H}_{\sim 1.7}$ is comparable to those of advanced solar coatings such as ceramic-metal composite materials [61]. Mg-Ti-H however, has the great advantage of being switchable. The switching between the two optical states is fast, robust and reversible. The combination of these properties highlights the applicability of Mg-Ti-H thin films as switchable smart coatings for solar collector applications [21]. Moreover, the fast switching together with the high optical contrast between the reflective and absorbing states makes Mg-Ti-H films also interesting for hydrogen sensor applications [23]. One of the most surprising properties of Mg-Ti-H films is their structural stability. We show here that this is due to the accidental equality of the molar volume of TiH_2 and Mg.

Little is presently known and understood about the structure, stability, bonding and electronic properties of Mg-Ti alloys or Mg-Ti hydrides. The binary phase diagram of Mg with Ti indicates that no stable bulk compounds are formed. However, based on X-ray diffraction results, it was reported that alloying of Mg and Ti does take place in mechanically alloyed bulk samples [39] and in thin films (physical vapour deposition [34], e-beam deposition [35, 36] and sputtering [21, 37]). On the other hand, the only Mg-Ti-H phase identified so far is Mg_7TiH_x , obtained in bulk alloys by Kyojima et al. [56] This phase was synthesized in a high-pressure anvil cell by compressing a mixture of MgH_2 and $\text{TiH}_{1.9}$ at 8GPa and 873 K. However, no Mg_7Ti phase was left after high temperature dehydrogenation.

In this paper we investigate the structural, optical and electrical properties of $\text{Mg}_y\text{Ti}_{1-y}\text{H}_x$ thin films obtained by co-sputtering of Mg and Ti at room temperature. Quite remarkably, the crystallinity (as deduced from x-ray diffraction) of the films is preserved during hydrogenation at all intermediate steps. The optical properties vary continuously with metal composition. The structure on the other hand, is rutile MgH_2 for high Mg content compositions ($y > 0.87$) and fluorite otherwise. Combining optical, electrical and structural data we find that $\text{Mg}_y\text{Ti}_{1-y}\text{H}_x$ is a system made of coherently coupled $\text{MgH}_2/\text{TiH}_2$ grains with in addition some x-ray amorphous regions made of insulating MgH_2 and unreacted or partially oxidized Mg and Ti. The structure

and the reversibility of Mg-Ti-H make it an unique and interesting material to study the effect of coherency on the reversibility of the hydrogenation process.

3.2.2 Experimental details

Mg_yTi_{1-y} thin films are prepared by dc/rf magnetron co-sputtering of Mg and Ti on quartz substrates. Various compositions in the 0.55 < y < 0.95 range are studied. Typical deposition rates are: 2 Å/s for Mg (150 W RF power), 0.1-1 Å/s for Ti (25-160 W DC power) and 1.3 Å/s for Pd (50 W DC power). All the films are covered in-situ with a Pd layer (5-10 nm) to prevent oxidation of the Mg-Ti film and to promote dissociation of H₂ [11, 72]. A detailed account of the dissociation mechanism is given by Borgschulte *et al.* [72]. Homogeneous composition and thickness over the entire substrate area are ensured by continuously rotating the substrates during sputtering. In addition, we prepared Mg_yTi_{1-y} (0.55 < y < 0.95) gradient thin films to study the concentration dependent properties in a continuous way. The composition of the films is investigated by Rutherford Backscattering spectrometry on samples grown in the same deposition run but on carbon substrates. Optical reflection (R) and transmission (T) spectra are measured simultaneously during hydrogenation (pressures up to 1 bar H₂) in a Perkin Elmer Lambda 900 diffraction grating spectrometer (0.495 < ħω < 6.51 eV) and a Bruker IFS 66 Fourier transform spectrometer (0.72 < ħω < 3.5 eV). The R-T spectra are measured through the transparent substrate at near normal incidence of the incoming beam. As an indication of hydrogen uptake in the films, the electrical resistivity of the films is measured in a van der Pauw [73] configuration together with the R-T spectra. The structural properties of the films are investigated by means of x-ray diffraction (XRD) in a Bruker D8 Discover x-ray diffractometer equipped with a two-dimensional (2D) detector which can perform real-time diffraction data collection over a large area with high speed, high sensitivity and low background. A Be dome allows in-situ x-ray measurements upon hydrogenation. XRD patterns are also measured during dehydrogenation (in air, at room temperature). The dehydrogenation time (few minutes for a 50 nm Mg_{0.70}Ti_{0.30}/30 nm Pd film) depends on the thickness of the film and can be improved by decreasing the thickness and/or increasing the temperature [21, 23]. All the measurements are done using the Cu-Kα radiation (λ=1.5418 Å). Additionally, TEM plan-view and cross-sectional images were recorded using a JEOL 2010F working at 200 kV (point resolution 0.23 nm and information limit 0.11 nm). This TEM is also equipped with an Energy Dispersive X-Ray Spectrometer and a Gatan Imaging Filter (GIF 2000). The plan-view samples were obtained by directly depositing the films on silicon nitride membranes (30 nm thick). Hydrogenated samples were prepared using a 1 nm Pd cap layer. Cross-section samples were made by cutting, polishing and ion milling with 4 kV Ar-ions with an Gatan PIPS. To measure the hydrogen content, electrochemical mea-

measurements (loading/unloading) are done in a standard three electrode setup containing a Hg/HgO reference electrode and a Pt counter electrode in a 1 M KOH electrolyte. The reflection and the transmission at $\lambda=635$ nm (1.95 eV) can be measured simultaneously in the electrochemical setup [74].

3.2.3 Results

Optical and electrical properties

Hydrogen uptake in $\text{Mg}_y\text{Ti}_{1-y}$ thin films is fast and induces a gradual change in optical appearance for all alloy compositions. The color of the fully hydrogenated films changes from dark grey to yellowish with increasing Mg fraction. The kinetics of hydrogen uptake improves with increasing Ti content in the alloy [21] and compositions with only a few percents of Ti are already far superior to pure Mg. Reflection and transmission spectra are measured on 200 nm $\text{Mg}_y\text{Ti}_{1-y}/10$ nm Pd films ($y=0.90, 0.80$ and 0.70) during hydrogenation in 1 bar H_2 at room temperature. In the metallic state (not shown), all the films have zero transmission and a relatively high and featureless reflection that decreases with increasing Ti content. After hydrogen absorption, the reflection is low for all compositions whereas significant transmission is observed only for the $y=0.90$ sample. The combination of low reflection and low transmission in the hydrogenated state ($y=0.80$ and 0.70 samples) gives rise to a highly absorbing state that extends over the entire visible range. In Fig.3.1, the experimental spectra are shown together with calculated spectra using a Drude-Lorentz parametrization scheme. The good agreement shows that the optical properties are consistent with a homogeneous layer. Additional measurements are done on similar compositions but much thinner layers (50 nm) capped with 5 nm Pd. The R,T spectra measured on hydrogenated films are shown in Fig.3.2(a),(b). In comparison with the thick films, we measure the same low reflection but much more transmission. These results are similar to those obtained by Farangis et al. [57] on amorphous Mg-Ti-H thin films and show that the absorption ($A=1-R-T$) of a Mg-Ti-H layer can be tuned just by varying the film thickness. Some insight into the optical transitions can be gained from the energy dependence of the absorption coefficient α . This is calculated from the R,T data measured on thin films and corrected for the Pd cap layer as follows:

$$\alpha = -\frac{1}{d} \left[\ln \left(\frac{T}{1-R} \right) + \alpha_{Pd} d_{Pd} \right] \quad (3.1)$$

with $\alpha_{Pd} = 2k\omega/c$ where k is the extinction coefficient of Pd [60]. The results are shown in Fig.3.2(c). For comparison, also the absorption coefficient of MgH_2 is shown. All Mg-Ti-H compositions have a similar dependence: an absorption edge at high energies and significant absorption below this edge. An effective band gap E_g is tentatively estimated by linearly extrapolating the

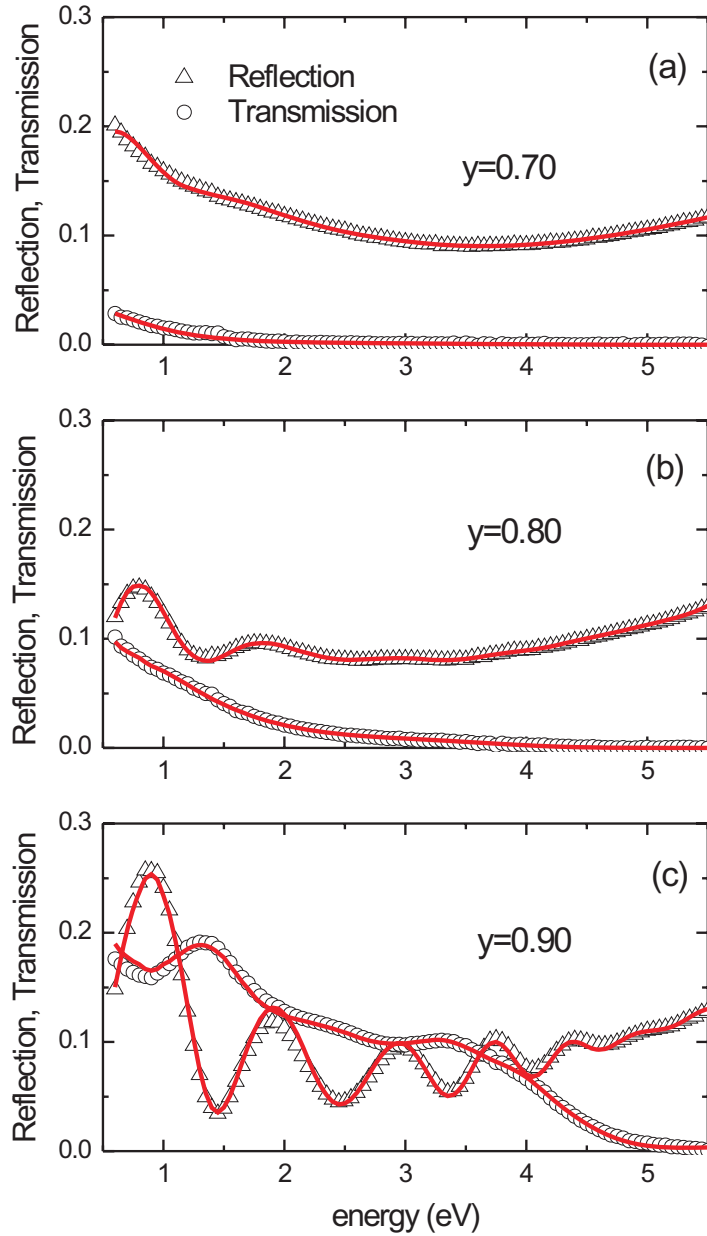


Figure 3.1: Optical reflection (measured through the substrate) and transmission spectra measured on 200 nm $\text{Mg}_y\text{Ti}_{1-y}/10$ nm Pd films ($y=0.70$, $y=0.80$ and $y=0.90$) after hydrogenation in 1 bar H_2 at room temperature. The solid lines are calculations using a Drude-Lorentz parametrization scheme.

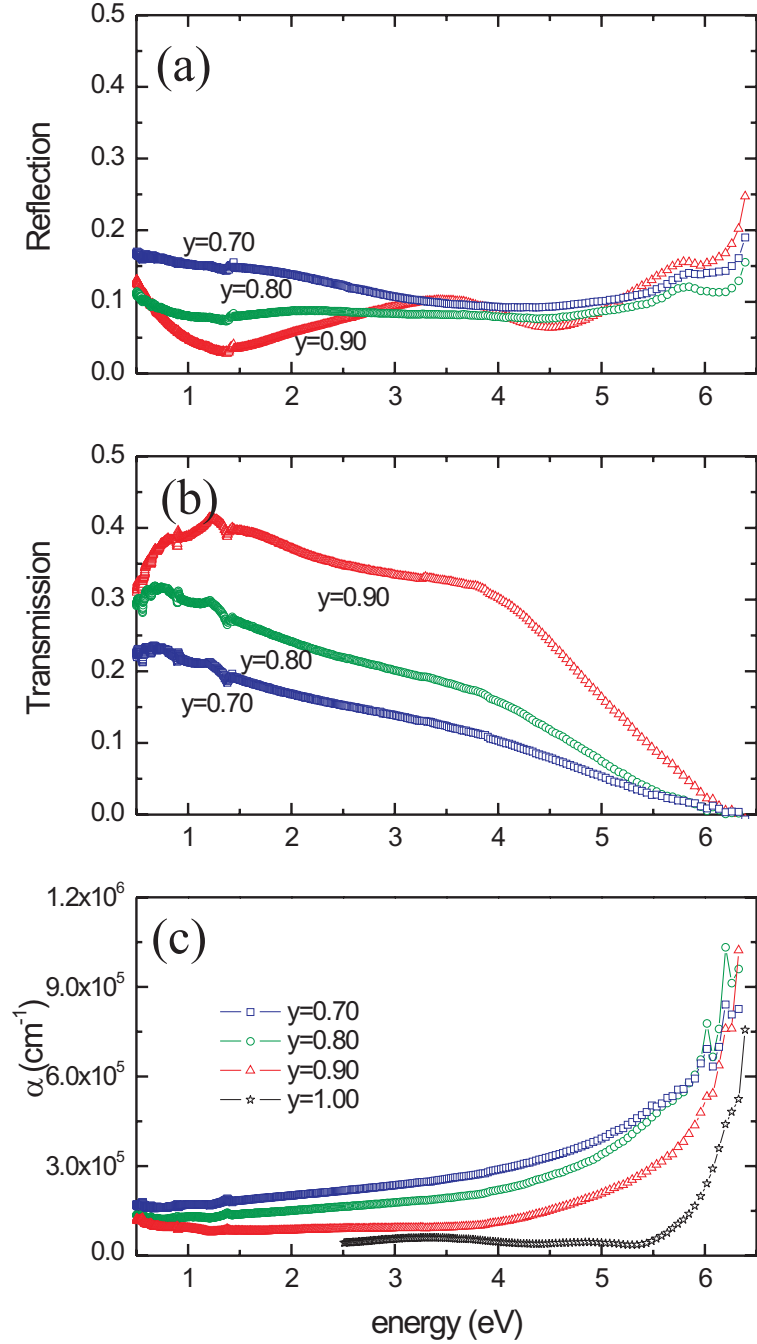


Figure 3.2: Optical reflection (a) and transmission (b) spectra measured on 50 nm $\text{Mg}_y\text{Ti}_{1-y}/5$ nm Pd ($y=0.70, 0.80$ and 0.90) films after hydrogenation in 1 bar H_2 at room temperature. (c) Absorption coefficient α for $\text{Mg}_y\text{Ti}_{1-y}\text{H}_x$ ($y=0.70, 0.80, 0.90$ and 1).

absorption edge to zero. This extrapolation is however not unique, making the value of E_g only approximate. The dependence of absorption coefficient on energy is also common to other Mg-based systems such as Mg-Pd-H [75], Mg-Y-H [76] or Mg-Ni-H [77], but the mechanism responsible for this effect is often different. Whereas in Mg-Pd-H it was understood by considering Pd as a deep donor in semiconducting MgH_2 , in Mg-Y-H it was attributed to quantum confinement effects. However, such an absorption edge could be seen as the signature of MgH_2 or a phase with a similarly large energy gap.

To get a qualitative understanding of the optical properties we analyze the optical data within the framework of an effective medium approximation. We assume a two phase system consisting of a metallic and a dielectric phase. This method was successfully applied previously [19] to the Mg- MgH_2 system to explain that the highly absorbing state found at intermediate hydrogen compositions was due to the coexistence of nanoscale grains of metallic Mg and insulating MgH_2 (with a gap $E_g=5.6$ eV). The Bruggeman effective medium approximation [68] can be used if the particle size is smaller than the wavelength of light, a criterium generally valid for metal hydride thin films. As a first approximation of the Mg-Ti-H system, we assume a medium consisting of spherical grains of metallic TiH_2 and insulating MgH_2 (volume fraction $f(\text{MgH}_2)$). The effective dielectric function of such a medium is calculated from the dielectric functions of TiH_2 and MgH_2 , determined in separate runs. Subsequently, the transfer matrix method [59] is used to calculate the reflection and transmission of the total sample also taking into account the quartz substrate and a 6 nm PdH_x cap layer [60]. A comparison with spectra measured on 60 nm $\text{Mg}_y\text{Ti}_{1-y}\text{H}_x/6$ nm PdH_x films is shown in Fig.3.3. The $f(\text{MgH}_2)$ volume fractions used are: 0.75, 0.85 and 0.92 for $y=0.70$, 0.80 and 0.90, respectively. As shown here, the agreement is reasonable below 4 eV, but the calculated data deviate considerably from the measured spectra at high energies. We also considered a non-spherical shape of the grains or even a different effective medium approximation (e.g. Maxwell-Garnet). In this case, the deviation between the calculated and the measured spectra was even bigger. The failure of an effective medium approximation to reproduce in detail the measured optical properties indicates a more complex phase composition and/or interaction on an atomic level between the components. However, this analysis indicates unambiguously that the hydrogenated films contain a significant fraction of an insulating material such as MgH_2 . This conclusion is further substantiated by electrical resistivity measurements.

As-prepared films have electrical resistivity (ρ) values typical for metals (50-100 $\mu\Omega\text{cm}$). Upon hydrogenation ρ increases gradually to final values that are more than a factor five higher than in the as-prepared state. Typical values measured on fully hydrogenated films are 1.32 m Ωcm and 1.9 m Ωcm for $y=0.70$ and $y=0.90$ samples, respectively (all the values are corrected for the Pd cap layer by assuming a parallel resistor model and $\rho_{\text{Pd}}=0.75$ $\mu\Omega\text{cm}$ [19]). These

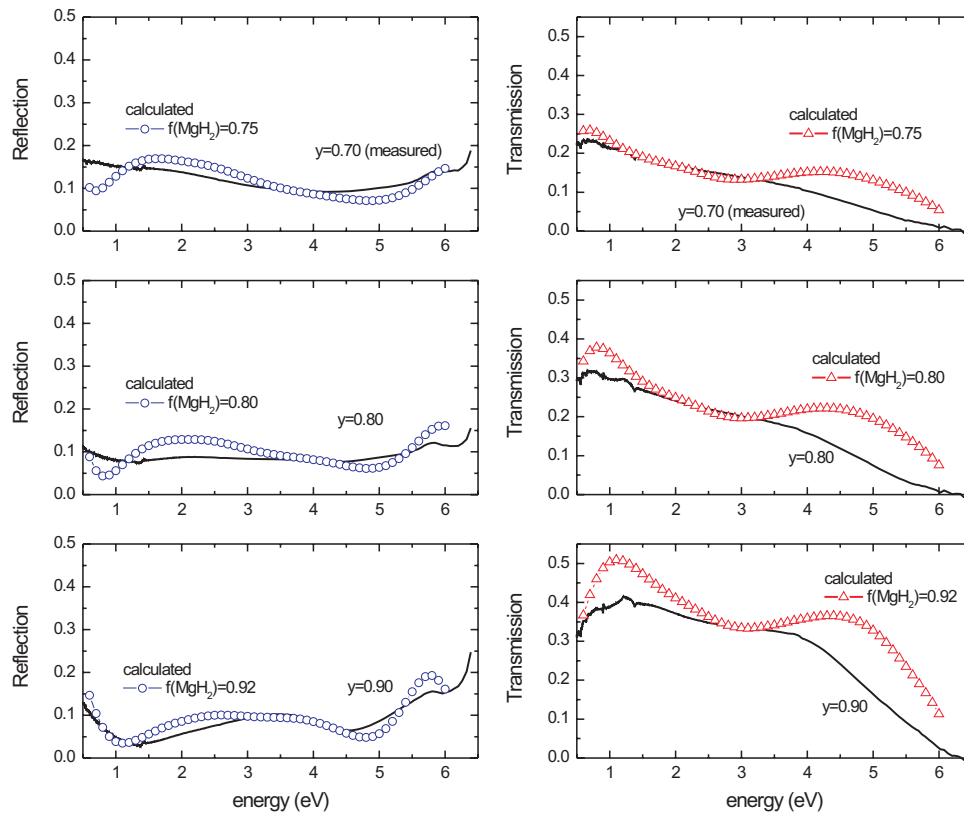


Figure 3.3: Comparison between reflection and transmission spectra measured on 60 nm $\text{Mg}_y\text{Ti}_{1-y}\text{H}_x/6$ nm PdH_x films and spectra calculated assuming a mixture of spherical particles of metallic TiH_2 and semiconducting MgH_2 (volume fraction $f(\text{MgH}_2)$).

values point to a decrease in the number of free carriers in the films. Temperature dependent resistivity measurements done on a 200 nm $\text{Mg}_{0.70}\text{Ti}_{0.30}/1$ nm Pd sample in the fully hydrogenated state are shown in Fig.3.4. Such a thin Pd cap layer is sufficient for hydrogenation of the film but consist of disconnected islands. It is thus possible to measure the intrinsic electrical resistivity of the Mg-Ti layer. Upon cooling, the electrical resistivity increases, pointing to a non-metallic behavior. The logarithmic temperature dependence of the resistivity between $35 \text{ K} < T < 298 \text{ K}$ is similar to that reported for granular niobium nitride cermet films [78]. A similar dependence was also reported for $\text{YH}_{3-\delta}$ [79] and discussed in terms of 2D weak electron localization or Kondo scattering. Although the microscopic origin of the $\log T$ dependence in Fig.3.4 has not been identified yet, the data implies clearly that $\text{Mg}_{0.70}\text{Ti}_{0.30}\text{H}_{1.55}$ is neither a metal nor a semimetal.

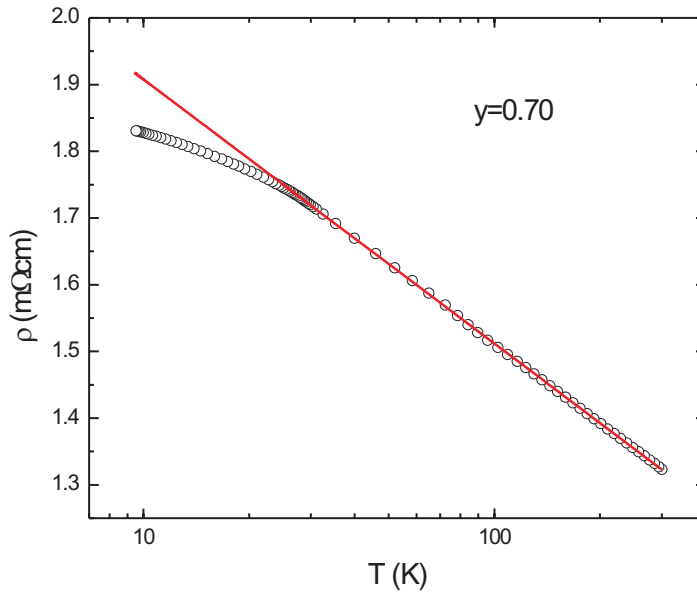


Figure 3.4: Resistivity versus T (on a logarithmic scale) measured for a 200 nm $\text{Mg}_{0.70}\text{Ti}_{0.30}/1$ nm Pd film in the fully hydrogenated state (in 1 bar H_2). The solid line is a guide to the eye.

The hydrogen concentration dependence of the optical properties can be obtained from measurements in an optical-electrochemical cell. In this case, reflection and transmission at 1.95 eV are measured simultaneously with the hydrogen content. The results obtained for a 100 nm $\text{Mg}_{0.70}\text{Ti}_{0.30}/10$ nm Pd film in a constant current mode ($I = -133.3 \mu\text{A}/\text{cm}^2$) are shown in Fig. 3.5. With increasing amount of hydrogen in the sample, the reflection decreases

while the transmission increases gradually. Such a behavior is typical for a homogeneous nucleation and growth of a hydride phase within the whole volume of the sample as was observed in Mg-MgH₂ thin films [19]. For $[H]/[M] < 0.5$ (dashed line in Fig.3.5), the measured transmission falls below the detection limit of the instrument. Above $[H]/[M] > 0.5$, the logarithm of the transmission increases linearly as expected from Lambert-Beers's law. The total amount of hydrogen that can be incorporated is $[H]/[M] \sim 1.55$. This value is below the theoretical limit of $[H]/[M] = 2$ expected for an alloy of two metals forming the dihydrides TiH₂ and MgH₂. Our results are in agreement with the results of Vermeulen et al. [36] measured on e-beam deposited thin films. They moreover showed that the H-content decreases with increasing the amount of Ti for all alloy compositions measured.

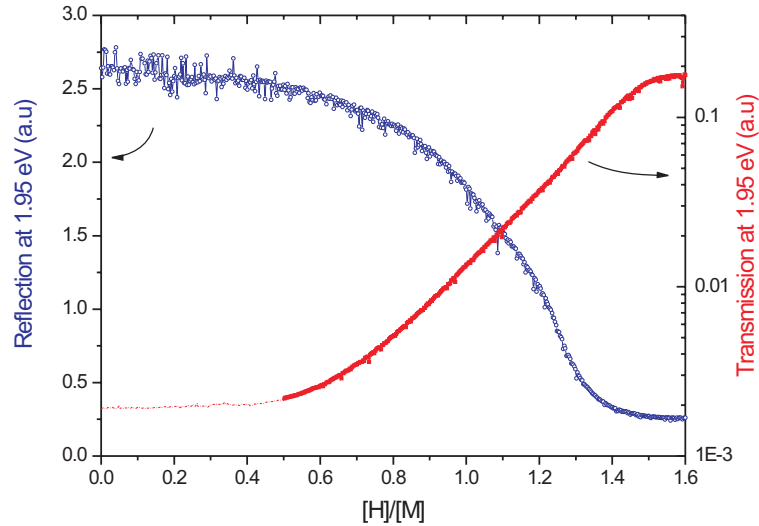


Figure 3.5: Optical reflection and transmission of a 100 nm Mg_{0.70}Ti_{0.30} film capped with 10 nm Pd measured in-situ during galvanostatic loading (current $I = -133.3 \mu\text{A}/\text{cm}^2$). $[H]/[M]$ corresponds to the number of hydrogen atoms per metal atom. In the region indicated by the dashed line, the measured transmission falls below the sensitivity limit of the instrument.

Structural properties

Structural data obtained from x-ray diffraction measurements are summarized in Fig.3.6. X-ray $\theta-2\theta$ scans measured on $y=0.70$ and $y=0.90$ samples are shown in Figs.3.6 (a) and (b), respectively. Here we compare spectra corresponding to the as-prepared (initial), fully hydrogenated (at room temperature in 1 bar H₂) and dehydrogenated (after exposure to air) state.

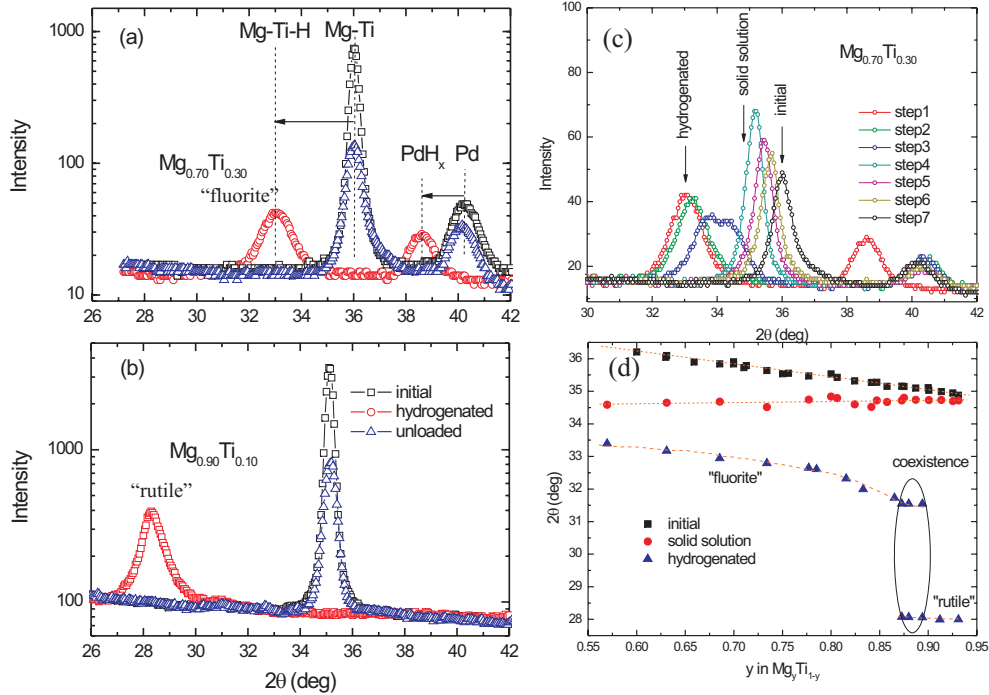


Figure 3.6: (a),(b) $\theta-2\theta$ x-ray scans measured on 200 nm Mg_yTi_{1-y}/10 nm Pd films ($y=0.70$ and $y=0.90$) in the as-prepared (initial), fully hydrogenated (at room temperature in 1 bar H₂) and fully dehydrogenated states. (c) Intermediate steps during dehydrogenation measured on a $y=0.70$ sample. (d) Composition dependence of 2θ measured on a Mg_yTi_{1-y} gradient thin films with $0.55 < y < 0.95$. Data corresponding to as-prepared (initial), solid solution (intermediate) and hydrogenated (final) states as defined in Fig.3.6(c), are shown.

In the XRD spectra there are reflections from the Mg-Ti layer and from the Pd cap layer. The peak at $\sim 40.1^\circ$ corresponds to the (111) reflection of Pd. Upon hydrogenation, the peak shifts to lower scattering angles, indicating thus the formation of PdH_x . The reflection of Pd is absent for samples with a composition $y=0.90$, even though the presence of Pd was confirmed by RBS. A similar result was obtained for e-beam deposited Mg-Ti films [35] or pure Mg films [19]. Therefore, on Mg rich surfaces, the Pd appears not to have a preferential orientation, which is necessary for these thin films to produce an XRD reflection. Very likely, this is related to the morphology of the Mg-Ti and Mg layers.

For as-prepared $y=0.70$ and $y=0.90$ samples, (Fig.3.6(a),(b)) there is only one reflection peak that is assigned to the Mg-Ti layer. The 2θ position of this peak depends on the Mg/Ti ratio and is between the (002) reflection of Mg ($2\theta = 34.4^\circ$; hexagonal structure) and the (002) reflection of Ti ($2\theta = 38.52^\circ$; hexagonal structure). This suggests the formation of a Mg-Ti random alloy on deposition with the same hexagonal symmetry as the metal constituents. The formation of a random alloy is however, highly unlikely given the large positive enthalpy of mixing calculated for such an alloy (> 30 kJ/g-atom [33]). Instead we argue that in fact a coherently coupled mixture of Mg and Ti is formed. The hexagonal symmetry is confirmed by additional TEM plan-view measurements. A typical result measured on a 50 nm $\text{Mg}_{0.70}\text{Ti}_{0.30}/5$ nm Pd film is shown in Fig.3.7(a). The reflections from the Pd cap layer (diffuse rings due to very small crystallites in the order of 5 nm) can easily be distinguished from those of the $\text{Mg}_y\text{Ti}_{1-y}$ film (well defined rings with individual spots due to crystallites in the order of 50 nm). The reflections from the film are consistent with a $\text{P6}_3/\text{mmc}$ structure (the same as for Mg and Ti) with lattice spacings ($a=3.11$ Å, $c=4.98$ Å) in close agreement with the XRD results.

After hydrogenation, we find a reflection at $2\theta=28.1^\circ$ for the $y=0.90$ sample whereas for the $y=0.70$ sample the hydride peak appears at $2\theta=32.8^\circ$. The difference in peak position suggests a difference in structure of the hydride phase. The peak at $2\theta=28.1^\circ$ we can clearly identify as the (110) reflection of a rutile MgH_2 phase ($2\theta=27.91^\circ$ for pure MgH_2). The small shift can be due either to small Ti doping in MgH_2 or strain in the thin film. On the other hand, the peak at $2\theta \approx 32.8^\circ$ is more difficult to identify. We assume this hydride to have fcc symmetry ("fluorite" phase) as its peak position is close to the (111) reflection of fcc TiH_2 and almost coincides with high-pressure fcc MgH_2 [80]. Assuming a fluorite phase, the corresponding lattice spacing is $a=4.729$ Å. TEM plan-view measurements on hydrogenated $\text{Mg}_{0.70}\text{Ti}_{0.30}$ films confirm the fcc symmetry (where the (111), (200), (220), (311) and (222) reflections can be identified) and indicate a structural homogeneity at least on a scale above 20 nm (Fig.3.7(b)). The lattice spacing obtained from these measurements is $a=4.55$ Å. This value is slightly lower than the data obtained from XRD on similar compositions, indicating a partial dehydrogenation due to electron

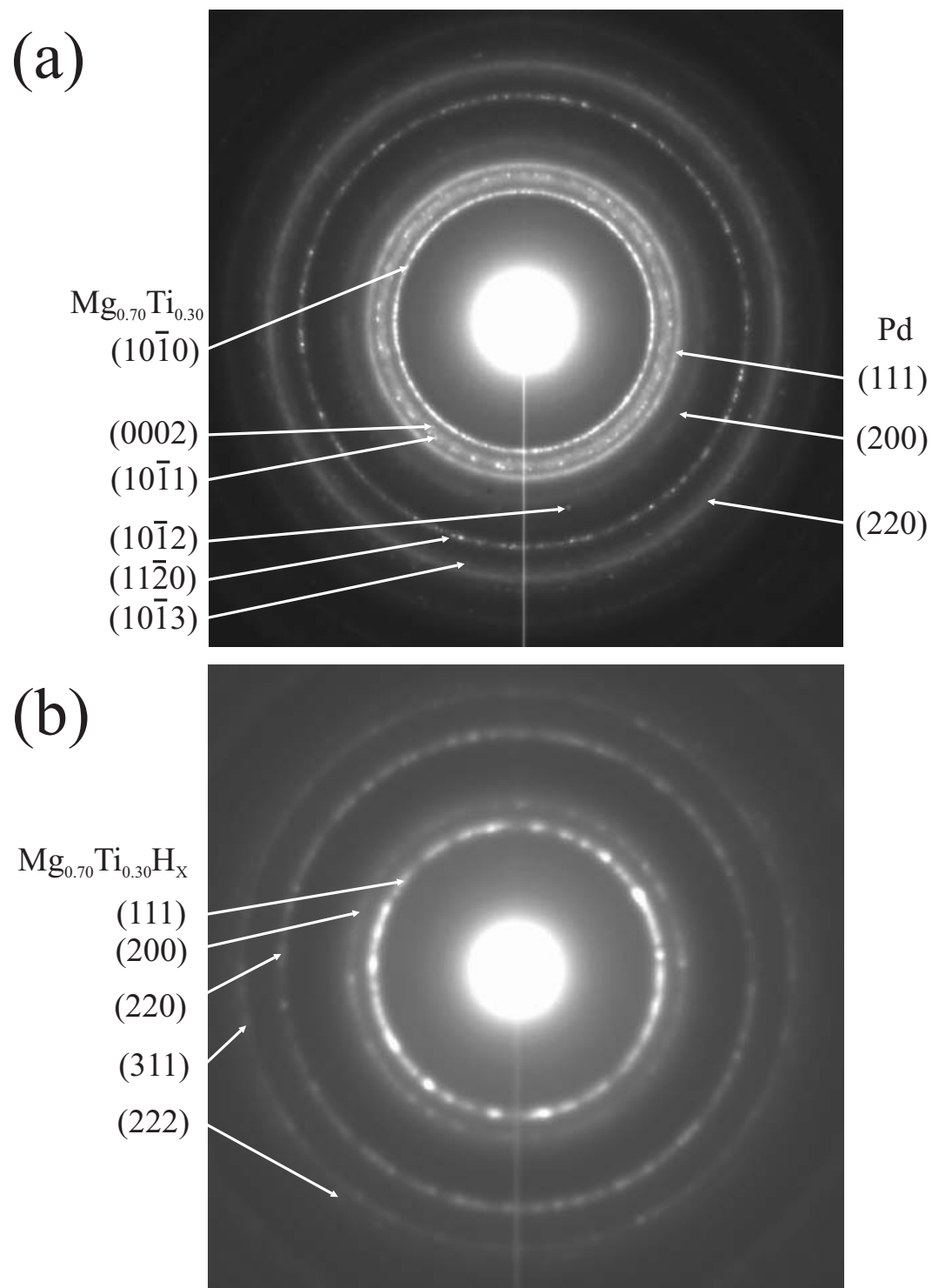


Figure 3.7: Selected area electron diffraction patterns: (a) of a $\text{Mg}_{0.70}\text{Ti}_{0.30}/5$ nm Pd thin film and (b) of a $\text{Mg}_{0.70}\text{Ti}_{0.30}\text{H}_x/1$ nm Pd thin film. Arrows identify reflections from the film (Mg-Ti or Mg-Ti-H) and the Pd cap layer (only visible in (a); in (b) the layer is too thin).

beam bombardment during the TEM measurements.

The reflection at $2\theta \approx 32.8^\circ$ is also close to the 222 reflection reported for the Mg_7TiH_x phase [56] (Ca_7Ge type structure; $a=9.532 \text{ \AA}$) synthesized in a high-pressure anvil cell by mixing MgH_2 and $\text{TiH}_{1.9}$ at 8GPa and 873 K. The structure of this phase was argued to be similar with that of $\text{TiH}_{1.9}$ (fcc) but with most of the Ti atoms substituted by Mg in an ordered way, resulting in a superstructure with a doubled unit cell.

As shown in Figs.3.6(a) and 3.6(b), after full dehydrogenation, the peak shifts back to its initial position which is evidence for the structural reversibility of the system and the absence of phase segregation. This is a surprising result since hydrogen cycling in Mg-based systems is in general accompanied by a large scale phase segregation [15, 19]. Also remarkable is the fact that the films remain crystalline during hydrogenation and subsequent dehydrogenation. However, the crystallinity of the films decreases upon hydrogen cycling. This has however little effect on the switching time and the optical response [21, 23] and therefore we conclude no major structural changes to take place apart from a reduction in grain size.

To understand the structural transformations and its composition dependence we performed XRD measurements at intermediate stages during hydrogenation (dehydrogenation) on homogeneous samples and also on a $\text{Mg}_y\text{Ti}_{1-y}$ gradient sample with $0.55 < y < 0.95$. In Fig.3.6(d) we have summarized results as measured on the gradient sample. We find that the position of the Mg-Ti peak varies linearly with Mg/Ti ratio (Fig.3.6(d)) for the entire composition range. This is in accordance with Vegard's law [67]. A small reflection from Ti is only found for $y < 0.65$ compositions but no signs of crystalline Mg is present for all $0.55 < y < 0.95$ compositions. The XRD data suggest that the alloy has always the hexagonal symmetry which was confirmed by TEM plan-view measurements on one composition. The results in Fig.3.6(d) suggest three distinct structural regimes for the hydrogenated state as a function of composition: (I) single phase fluorite for $y < 0.87$, (II) single phase rutile for $y > 0.90$ and (III) two phase coexistence for $0.87 < y < 0.90$. Within the fluorite regime, the structure varies continuously with composition. At intermediate compositions, coexistence of both phases is found. For all compositions, the FWHM indicates very small crystallites in the order of 10-20 nm. As shown in Fig.3.6(c), for a $y=0.70$ sample, the transformation between the initial and the hydrogenated state is almost continuous and fully reversible. The intermediate steps shown here are measured during H-desorption. Assuming an hcp structure in the as-prepared state and fcc structure in the final state, the intermediate steps should reveal an hcp-fcc phase transformation. Upon H uptake, first the lattice expands continuously (step 4-7). We define as the solid solution state, the whole range of 2θ values which are attained continuously starting from the metallic state. At intermediate hydrogen concentrations (step 3), the double-peak structure of the XRD spectrum points to coexistence of two phases: an

fcc phase and an hcp phase. Subsequent H-uptake leads to a further expansion of the fcc phase.

Similar intermediate steps can be defined for all compositions in the $0.55 < y < 0.95$ range. Interestingly, the minimum 2θ angle in the metal solid solution phase is the same for all compositions and corresponds to the scattering angle of both TiH_2 (111 reflection) and Mg (002 reflection). This results suggests strongly a hydrogenation sequence where hydrogen occupies first Ti-related sites in the Mg-Ti lattice. An indication in favor of this scenario is also the increase in peak intensity in the beginning of the hydrogenation process. The lattice expands and becomes more ordered since the molar volume of TiH_2 (13.3 cm^3) equals almost exactly that of pure Mg (13.98 cm^3). The data in Fig.3.6(d) also suggest that the amount of hydrogen that can be dissolved as a solid solution increases with increasing Ti concentration.

Additional information on the phase composition of hydrogenated films is obtained from combined structural and electrical resistivity measurements. Results measured on a $y=0.70$ sample are shown in Fig.3.8. In the beginning of the hydrogenation process, the electrical resistivity varies only slightly while 2θ decreases continuously, up to the solid solution state. An increase in electrical resistivity is measured only on further hydrogenation ($t > 3000 \text{ s}$) while 2θ decreases further. However, for $t > 4000 \text{ s}$, 2θ remains constant whereas the electrical resistivity varies almost by a factor 2. This result suggest the presence of a non-crystalline component that takes up hydrogen. The origin of this phase is not yet clear. It could be related to x-ray amorphous material formed at grain boundaries. A precise estimate of the amount of this phase is also rather difficult. A rough estimation can be obtained by assuming a linear increase of electrical resistivity with hydrogen content and combine the results in Fig.3.8 with hydrogen content measurements (see Fig.3.5). In this way, the fraction of amorphous phase is $\sim 45\%$ of the total for a $y=0.70$ sample. This fraction is quite high and is probably overestimated since TEM plan-view measurements on as-prepared films do not show evidence of an amorphous phase. Only on a hydrogen cycled sample, TEM cross-section and XRD indicate clearly an increase in disorder in comparison to the as-prepared state.

3.2.4 Discussion

As suggested in the previous section, the formation of a Mg-Ti random alloy on deposition is very unlikely given the large positive enthalpy of mixing. The occurrence of a single hcp Bragg pattern is not sufficient to prove the alloy formation on an atomic scale [81, 82] but it suggest a certain local order. The reversibility of the hydrogenation process suggests that this ordering remains intact on cycling. The optical and electrical data on fully hydrogenated films suggest the presence of an insulating MgH_2 -like phase for all metal alloy compositions. Besides the insulating component, a second phase with a metallic

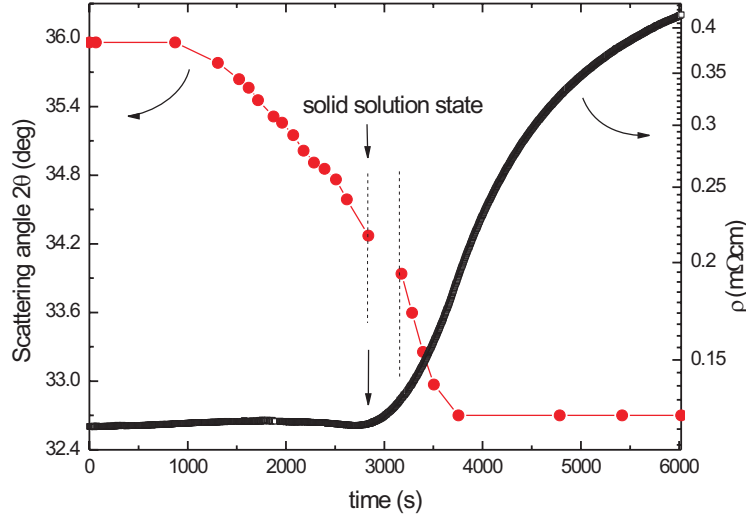


Figure 3.8: Scattering angle 2θ and electrical resistivity ρ evolution in time during hydrogenation measured simultaneously on a 200 nm $\text{Mg}_{0.70}\text{Ti}_{0.30}/10$ nm Pd sample. Hydrogenation is done at room temperature in 100 mbar H_2 .

character should be present to account for the highly absorbing state. For example, for a $y=0.70$ sample, the volume fraction of the insulating component is $\sim 75\%$, corresponding thus to the entire Mg fraction in the metal alloy. In a homogeneous random alloy, the amount of Mg_4 clusters is only $\sim 20\%$, much lower than what is needed to explain the optical and electrical properties. Also on the basis of XRD data, large scale segregation is excluded. Clear structural indications of a rutile MgH_2 phase are found only for Mg-rich compositions ($y > 0.87$). For $y < 0.87$ compositions, the XRD data point to a structure with cubic symmetry and a lattice parameter that varies continuously with metal composition in the parent alloy.

Recent theoretical calculations on $\text{Mg}_{0.75}\text{Ti}_{0.25}\text{H}_2$ [83] structures with a cubic symmetry reveal a metallic character in disagreement with our temperature dependent resistivity measurements and the optical data. From this and the continuous dependence of structure on metal alloy composition we conclude that the $\text{Mg}_y\text{Ti}_{1-y}\text{H}_x$ films with $y < 0.87$ are neither single phase nor phase separated. Instead, the experimental evidence suggests the formation of insulating MgH_2 and metallic TiH_2 regions that form a coherent crystalline structure. This conclusion is consistent with a hydrogenation sequence where hydrogen occupies first Ti-related sites. A schematic representation of a coherent crystalline grain consisting of a Mg and Ti region is shown in Fig.3.9(a). The local deformation is only schematic and might deviate from reality. The

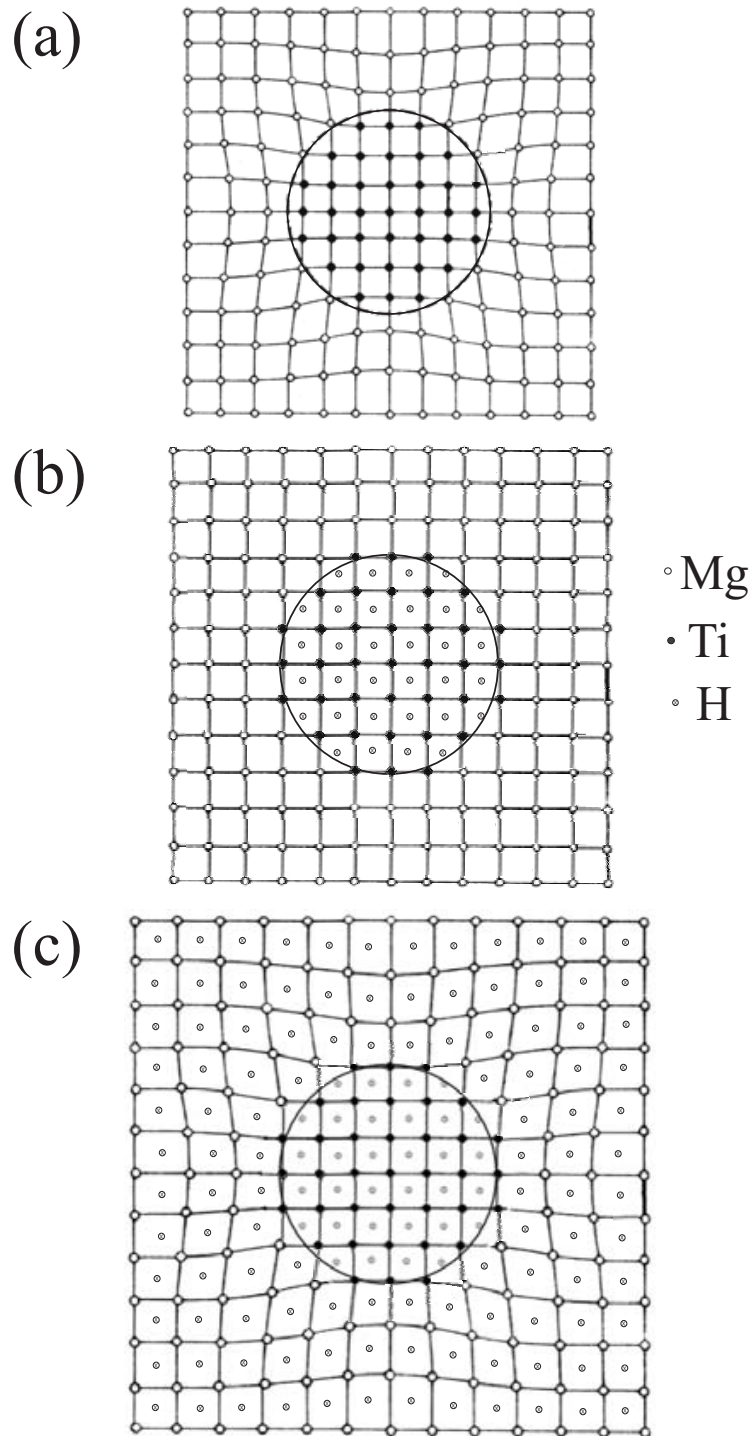


Figure 3.9: (a) Schematic representation of a coherent crystalline grain consisting of a Mg and Ti region; (b) the same crystalline grain after hydrogen uptake in the Ti-related sites; (c) full hydrogenation state. The accidental equality of the molar volumes of TiH_2 and Mg leads to an almost perfect crystal in situation (b).

same crystalline grain after hydrogen uptake in the Ti-related sites and in the fully hydrogenation state is shown in Fig.3.9(b) and Fig.3.9(c), respectively. This peculiar hydrogenation sequence is related to the more negative enthalpy of formation of TiH_2 ($-70 \text{ kJ}(\text{mol H})^{-1}$) as compared to MgH_2 ($-32 \text{ kJ}(\text{mol H})^{-1}$). Very likely, hydrogenation of Ti-related sites in the beginning of the hydrogenation process reduces the mobility of atoms during further hydrogen uptake and thus prevents the large scale segregation, observed in many other Mg-based systems.

In a scenario based on a coherent mixture of MgH_2 and TiH_2 , the structural data for $y < 0.87$ compositions can be understood by assuming that both components have a cubic structure. This is expected for TiH_2 . On the other hand, at normal pressures and temperatures, MgH_2 crystallizes in a rutile structure. A cubic MgH_2 phase was reported to be formed only at high pressures (4GPa) [80]. The theoretical calculations of Vajeeston [84] confirm a similar cubic phase as being the most stable structure if the unit-cell volume is reduced to $27.5 \text{ \AA}^3/\text{f.u}$ (equivalent to $a = 4.79 \text{ \AA}$). The formation of a cubic MgH_2 phase in our thin films, at normal pressures and temperatures is not entirely clear. Very likely, it is related to the coherent coupling to Ti/TiH_2 and the local stress induced. Using the pressure vs. volume dependence calculated by Vajeeston [84], the lattice constant of cubic MgH_2 at normal pressures should be $a(\text{MgH}_2) = 4.839 \text{ \AA}$. With this value, the average lattice spacing of fully hydrogenated $\text{Mg}_y\text{Ti}_{1-y}$ films with $y < 0.80$ is well reproduced by the weighted average of the two components, as follows:

$$a_{\text{Mg}_y\text{Ti}_{1-y}\text{H}_x} = y a_{\text{MgH}_2} + (1 - y) a_{\text{TiH}_2} \quad (3.2)$$

Then, on average, the hydrogen-to-metal ratio of the crystalline coherent structure is 2. This value corresponds to a higher hydrogen content than what we measured electrochemically ($[\text{H}]/[\text{M}] = 1.55$), and therefore supports the conclusion that an x-ray amorphous component is present which reacts only partly with hydrogen. Since the optical data suggest a high fraction of insulating material, part of this amorphous component must be insulating with properties similar to that of MgH_2 . The rest is likely to remain metallic as unreacted or partially oxidized Mg and Ti. Very likely, this amorphous component does not play an active role in maintaining the coherency of the system.

Structural coherence was reported for several systems with positive energy of mixing, such as Ag-Cu [85], Cu-Cr [81] or Cu-Fe [86], but the mechanism responsible for this effect is still a subject of controversy [87, 88, 89, 90]. Experimental results from nm-resolution methods such as APFIM (atom probe field ion microscopy) [82] or EXAFS could shed more light on the subject. It is though quite remarkable that in Mg-Ti, the coherent structure is preserved at all intermediate states during hydrogenation. This is likely to be related to the similarities in molar volume between Mg and TiH_2 .

Recently, the thermodynamic properties of $\text{Mg}_y\text{Ti}_{1-y}$ thin films were studied with hydrogenography [12]. In this method, the equilibrium pressure and the enthalpy of formation of $\text{Mg}_y\text{Ti}_{1-y}\text{H}_x$ is determined by following the changes in optical transmission upon hydrogenation. In the $0.65 < y < 0.90$ range, no significant dependence on composition was observed. Moreover, the thermodynamic properties indicate the formation of a MgH_2 -like phase for all compositions. These results support our model that considers a coherent structure made of MgH_2 and TiH_2 .

3.2.5 Conclusions

Hydrogenation of $\text{Mg}_y\text{Ti}_{1-y}$ thin films prepared by co-sputtering of Mg and Ti is monitored continuously optically, electrically and with x-ray diffraction. All the properties are found to depend on the metal ratio in the parent alloy. Structurally, as-prepared films show only one crystalline phase over a wide composition range ($0.55 < y < 0.95$) that corresponds to a hexagonal Mg-Ti alloy. Hydrogenation induces a reversible phase transformation. The structure of the hydride depends on the metal ratio in the parent alloy. From XRD, the average structure resemble the rutile MgH_2 phase for high Mg content samples ($y > 0.87$) and is fluorite otherwise ($y < 0.87$). At intermediate composition, coexistence of both phases is found. Highly reflective in the metallic state, the films are highly absorbing in the fully hydrogenated state (87% of the solar spectrum for $\text{Mg}_{0.80}\text{Ti}_{0.20}\text{H}_x$). Such a highly absorbing state hints at the coexistence of a metallic and a semiconducting phase. It is however, not simply a composite material consisting of independent MgH_2 and TiH_2 grains. By continuously monitoring the structure during H uptake, we obtain data that are compatible with a coherent structure. The complete reversibility of the system and the structural coherence are probably related to the equality of the molar volumes of TiH_2 and Mg. The present results point towards a rich and unexpected chemistry of Mg-Ti-H compounds.

3.3 Nanoscale composition modulations in Mg-Ti-H thin film alloys for hydrogen storage

Abstract – A detailed structural analysis of Mg-Ti-H thin films reveals the presence of a chemically partially segregated but structurally coherent metastable phase. By combining X-Ray Diffraction and Extended X-ray Absorption Fine Structure (EXAFS) spectroscopy on $\text{Mg}_y\text{Ti}_{1-y}\text{H}_x$ thin films we find non-zero Chemical Short-Range Order (CSRO) parameters for all the compositions measured. Despite the positive enthalpy of mixing of Mg and Ti the degree of ordering does not increase upon loading and unloading with hydrogen. The robustness of this system and the fast and reversible kinetics of hydrogen loading and unloading are caused by the formation of nanoscale compositional modulations in the intermetallic alloy. This microstructure is responsible for the exceptional properties of $\text{Mg}_y\text{Ti}_{1-y}\text{H}_x$ thin films. It also shows that reversible metastable metal-hydrides offer new possibilities for hydrogen storage, beyond the limits imposed by thermodynamic equilibrium.

3.3.1 Introduction

The Mg-Ti-H system is currently attracting a lot of attention, with potential applications in very different fields. Niessen et al. [35] proposed the use of Mg-Ti thin films as high-capacity hydrogen storage materials for batteries. By means of electrochemical loading of $\text{Mg}_{0.8}\text{Ti}_{0.2}$ thin films they found a gravimetric storage capacity of 6.53 wt% H: ~ 4 times higher than the commercially available NiMH batteries. In our group we demonstrated the possibility of gas loading of Pd-capped $\text{Mg}_y\text{Ti}_{1-y}$ thin films. These films, when exposed to hydrogen gas exhibit fast and reversible transitions from the metallic to the hydrogenated state. The Ti doping of Mg greatly enhances the kinetics of hydrogen uptake and release. A 65 nm thick film of $\text{Mg}_{0.7}\text{Ti}_{0.3}$, exposed to 5% H_2 in Ar at room temperature, hydrogenates completely in ~ 10 sec; if it is then exposed to 20% O_2 in Ar, it fully desorbs in less than 3 minutes, returning to its original metallic state [21]. The role of Ti is to favor the formation of a face-centered cubic hydride phase of $\text{Mg}_y\text{Ti}_{1-y}\text{H}_x$ (for $y < 0.87$ [38]) instead of the tetragonal MgH_2 -like phase.

The hydrogenation of $\text{Mg}_y\text{Ti}_{1-y}$ thin films is also accompanied by dramatic optical changes, which make them suitable for application as hydrogen sensors [23] and smart coating for solar collectors [22]: when exposed to hydrogen gas, they exhibit fast and reversible (> 100 cycles) optical transitions from a shiny metallic state to a black, strongly light-absorbing, hydrogenated state [21].

In order to explain these properties and eventually to control and tailor them, we need to fully understand the microstructure of these materials. Mg and Ti are immiscible elements in thermodynamic equilibrium, as their enthalpy of mixing, ΔH_{mix} , is positive. For a $\text{Mg}_{0.50}\text{Ti}_{0.50}$ mixture $\Delta H_{mix} \approx 20$ kJ/g-atom [33]. The synthesis of Mg-Ti alloys has nevertheless been achieved both in bulk and in thin films via non-equilibrium processes such as physical vapor deposition [34], e-beam deposition [35, 36], sputtering [21, 37, 38] and mechanical alloying [39].

In a previous work we measured the optical, structural and electrical properties of $\text{Mg}_y\text{Ti}_{1-y}\text{H}_x$ ($y = 0.7, 0.8$ and 0.9) thin films [38]. The XRD patterns and the TEM plane-view and cross-sectional images of the as-deposited metallic films showed crystalline hexagonal close-packed structures for all compositions, with an almost perfect Vegard's law [67] dependence of the average lattice spacing. This suggests at first sight a microstructure made of a single-phase supersaturated solid solution of randomly dispersed Mg and Ti atoms. However, the optical and electrical properties of these films hint to a more complex microstructure, consisting of partially segregated Mg-rich and Ti-rich nanosized domains, within large structurally coherent grains [38].

Standard x-ray diffraction techniques are however not sufficient to prove the validity of this model [44]: nanoscale short-range deviations from a random solid solution would also produce a Vegard's law dependence, provided that

the coherence is maintained [81]. Such deviations can arise because of incipient phase separation during the synthesis of the alloy.

In the present work we study the local atomic ordering in sputtered $\text{Mg}_y\text{Ti}_{1-y}\text{H}_x$ thin film by means of X-Ray Diffraction (XRD), Extended X-ray Absorption Fine Structure (EXAFS) spectroscopy and X-Ray Absorption Near Edge Structure (XANES) spectroscopy. EXAFS spectra of $\text{Mg}_y\text{Ti}_{1-y}$ thin films with various compositions are measured both for the as-deposited state and for the samples after one cycle of loading and unloading with hydrogen. XANES spectra are measured continuously during hydrogenation and de-hydrogenation of the films, in order to follow the phase transitions that occur during these processes.

From the analysis of the EXAFS data of $\text{Mg}_y\text{Ti}_{1-y}$ thin films with different compositions we derive the coordination shells for Ti and the corresponding chemical short-range order parameter, s . All the measured compositions have positive s values, indicating that partial chemical segregation has occurred during the film deposition. The degree of ordering is maintained upon cycling with hydrogen. Such reversibility is particularly unexpected considering the positive enthalpy of mixing of Ti and Mg and the hydrogen-induced phase separation observed in many other Mg-based binary systems [19, 15].

Similar metastable structures with short-range compositional modulations can in general be obtained in bulk via non-equilibrium processes such as mechanical alloying and liquid quenching [44]. A metastable Mg_7TiH_x powder with gravimetric hydrogen storage capacity of 5.5 wt% has been prepared by high-pressure synthesis [56]. However, the microstructure of this compound, an atomically ordered Ca_7Ge -like superstructure, is very different from the one found in $\text{Mg}_y\text{Ti}_{1-y}$ thin films. High-pressure Mg_7TiH_x releases 4.7 wt% of hydrogen at 332 °C decomposing in Mg and $\text{TiH}_{1.9}$, but the process is not reversible, although several attempts to produce destabilized bulk Mg-Ti-H alloys, with reversible hydrogen sorption properties, are currently under way [91]. Our study on thermodynamically metastable but reversible $\text{Mg}_y\text{Ti}_{1-y}$ thin film alloys shows the existence of a new class of hydrogen storage systems that is not restricted by conventional thermodynamic equilibrium considerations and has excellent kinetic properties.

3.3.2 Experimental details

$\text{Mg}_y\text{Ti}_{1-y}$ films are deposited in a UHV system (base pressure = 10^{-8} mbar) by DC/RF magnetron co-sputtering of Mg and Ti targets in argon atmosphere, on glassy carbon SIGRADUR® substrates of 100 μm thickness, kept at room temperature. The films are covered with 20 nm of Pd to prevent oxidation and promote hydrogen dissociation. Typical deposition rates are 0.22 nm/s for Mg at 150 W (RF), 0.02-0.18 nm/s for Ti at 60-400 W (DC) and 0.11 nm/s for Pd at 50 W (DC). In order to obtain a homogenous composition the substrates

are continuously rotated during sputtering. The characteristics of the films used in this work are given in Table 3.1.

Table 3.1: Alloy composition, film thickness and deposition rates of the samples used.

Sample Number	Composition	Thickness (nm)	Mg rate (nm/sec)	Ti rate (nm/sec)
1	Mg _{0.53} Ti _{0.47}	250	0.22	0.18
2	Mg _{0.59} Ti _{0.41}	310	0.22	0.13
3	Mg _{0.70} Ti _{0.30}	360	0.22	0.09
3a	Mg _{0.72} Ti _{0.28}	2000	0.36	0.12
4	Mg _{0.81} Ti _{0.19}	410	0.22	0.05
5	Mg _{0.90} Ti _{0.10}	460	0.22	0.02

Film composition and thickness are measured *ex-situ* by Rutherford Backscattering Spectrometry (RBS) and profilometry, respectively. X-ray diffraction patterns are measured in a $\theta - 2\theta$ configuration, with a Bruker D8 Discover diffractometer equipped with a two-dimensional detector for real-time data collection over a large area with high sensitivity and low background. A typical diffraction pattern is recorded in 1 hour. A beryllium dome allows *in-situ* diffraction measurements during hydrogenation of the films at room temperature in a hydrogen pressure of 10^5 Pa.

Titanium K-edge (4966 eV) EXAFS spectra are recorded at beamline E4 of the DORIS III storage ring at the Deutsches Elektronen-Synchrotron (DESY), Hamburg. The beamline is equipped with a Si(111) double-crystal monochromator, which is detuned to 60% of the Bragg peak intensity to suppress higher harmonics, and two mirrors: a Au coated toroidal mirror and a plane Ni mirror for optimum higher order harmonics reduction at the energies used. Samples are measured in transmission at room temperature, in He flow (for as-deposited and de-hydrogenated films) or in a 5% H₂/He mixture flow (for hydrogenated films). XANES spectra are recorded while loading the films in 5% H₂/He mixture at room temperature and unloading in 20% O₂/He mixture between room temperature and 100 °C, depending on film's composition. In each measurement a pile of 8-12 films, with the same composition and deposited in the same run, are inserted in the beam, in order to obtain sufficient absorption and a high signal to noise ratio. Three consecutive ionization chambers allow to simultaneously measure the absorption spectra of both the sample and a reference Ti foil.

In order to calibrate the Ti-Ti and Ti-Mg references we use a 5 μ m thick Ti foil (99.99%) and TiAl₃ (99.5%) powder, respectively.

The EXAFS data are extracted from the measured absorption spectra with XDAP [92]. At least five scans for each sample are averaged together. The edge energy is determined from the maximum of the first derivative of the

spectrum and calibrated with the reference Ti foil. A smooth atomic background function, represented by a cubic spline, is used to extract the EXAFS oscillation from the absorption spectrum [93]. The obtained data are normalized by the background height 50 eV after the edge. Experimental data are fitted in k -space with k^3 weighting, using the difference file technique in real space [94].

3.3.3 Results

X-ray diffraction patterns are measured for the as-deposited, hydrogenated and de-hydrogenated states of samples 1, 2, 3, 4 and 5. As previously reported [38], in the as-deposited state $\text{Mg}_y\text{Ti}_{1-y}$ thin films have a hexagonal close-packed structure with an almost perfect Vegard's law dependence of the interplanar distances, while upon hydrogenation the alloys undergo phase transitions to a fluorite ($y < 0.87$) or a rutile ($y > 0.90$) structure (Figure 3.10a).

In Fig. 3.10b the XRD patterns for sample 3 in the as-deposited, hydrogenated and de-hydrogenated states are shown. The only visible metallic peak is the 002 reflection arising from the hexagonal Mg-Ti alloy. In the as-deposited states of the Ti-rich compositions (samples 1, 2 and 3) a much smaller peak, similar to the 002 reflection for pure Ti ($2\theta = 38.42^\circ$; hexagonal), is also present. This peak is not recovered after one hydrogenation/de-hydrogenation cycle and it is likely to be a satellite peak, rising from the coexistence of Ti and Mg domains with coherent boundaries [81]. The diffraction peaks at higher 2θ 's are the 111 reflections of Pd and PdH_x , due to the palladium cap layer, in the metallic and hydrogenated states, respectively.

Figure 3.11 shows the k^1 -weighted background-subtracted EXAFS signal $\chi(k)$ for the as-deposited states of samples 1, 2, 3, 4 and 5, measured in He at room temperature. In all cases the measured edge-energy is equal to the edge-energy for the Ti reference (4966 eV), indicating a pure metallic state of the films. The inset in Fig. 3.11 shows the raw absorption data for sample 1, before background subtraction.

An example of fitted data is shown in Fig. 3.12 for sample 1 ($\text{Mg}_{0.53}\text{Ti}_{0.47}$). For all the samples the fits are optimized with $\Delta k = 3-11 \text{ \AA}^{-1}$ and $\Delta R = 2.0-3.4 \text{ \AA}$. Table 3.2 summarizes the fit parameters obtained for all the compositions measured in the as-deposited state. The number of independent parameters used in the fit are in all cases lower than the maximum value set by the Nyquist theorem [95]. The coordination shell of Ti is composed of both Ti and Mg atoms. For all $\text{Mg}_y\text{Ti}_{1-y}$ thin films the total coordination number, given by the sum of the Ti-Ti and Ti-Mg coordination numbers, is close to the ideal value for an hexagonal geometry ($N=12$). However their relative amount changes with composition and is different from what would be expected for a completely random solid solution. From the Ti-Ti and Ti-Mg coordination numbers in a $\text{Mg}_y\text{Ti}_{1-y}$ alloy, the Chemical Short-Range Order

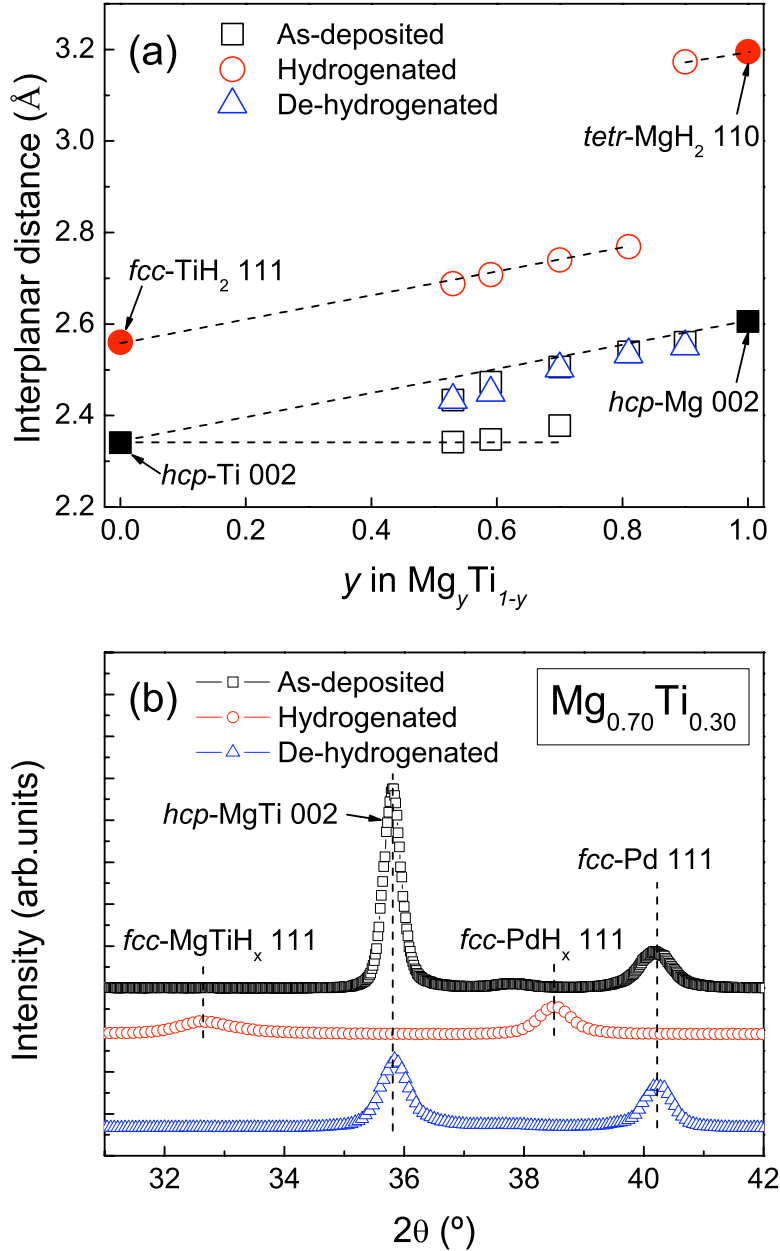


Figure 3.10: (a) Interplanar distances obtained from x-ray diffraction patterns for samples 1, 2, 3, 4 and 5 in the as-deposited (squares), hydrogenated (circles) and de-hydrogenated (triangles) states. Full squares and circles are literature values for Mg, Ti, MgH_2 and TiH_2 . The dashed lines are a guide to the eye. (b) X-ray diffraction patterns for sample 3 in the as-deposited (squares), hydrogenated (circles) and de-hydrogenated (triangles) states.

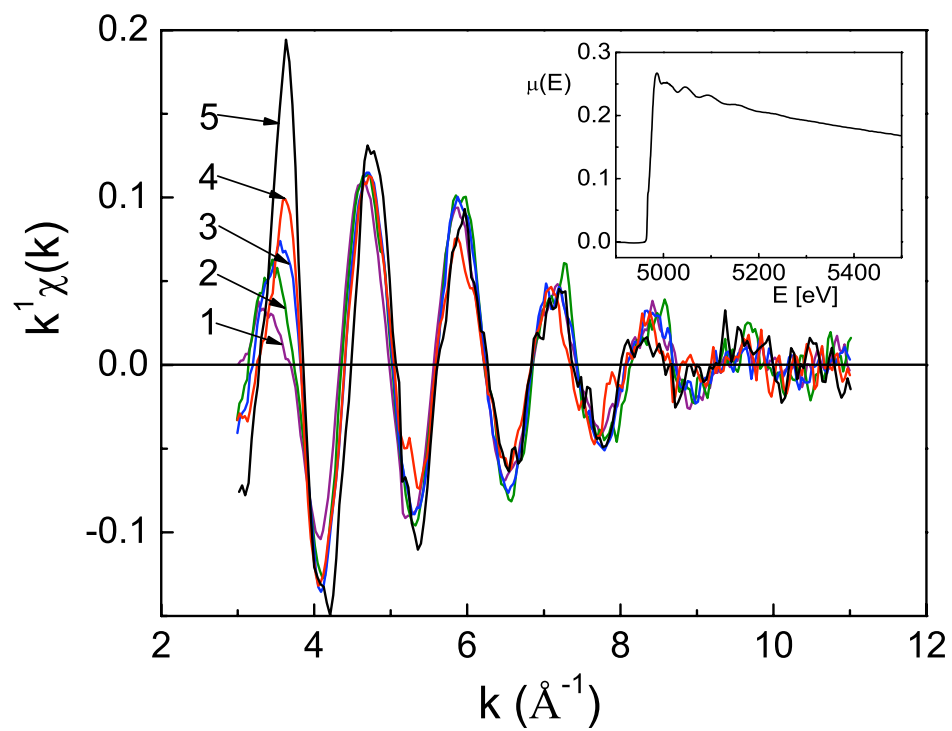


Figure 3.11: k^1 -weighted background-subtracted $\chi(k)$ for samples 1, 2, 3, 4, and 5 (see Table 3.1) in the as-deposited states. All spectra are measured in He at room temperature. In the inset the absorption spectrum around the K-edge for sample 1 is shown.

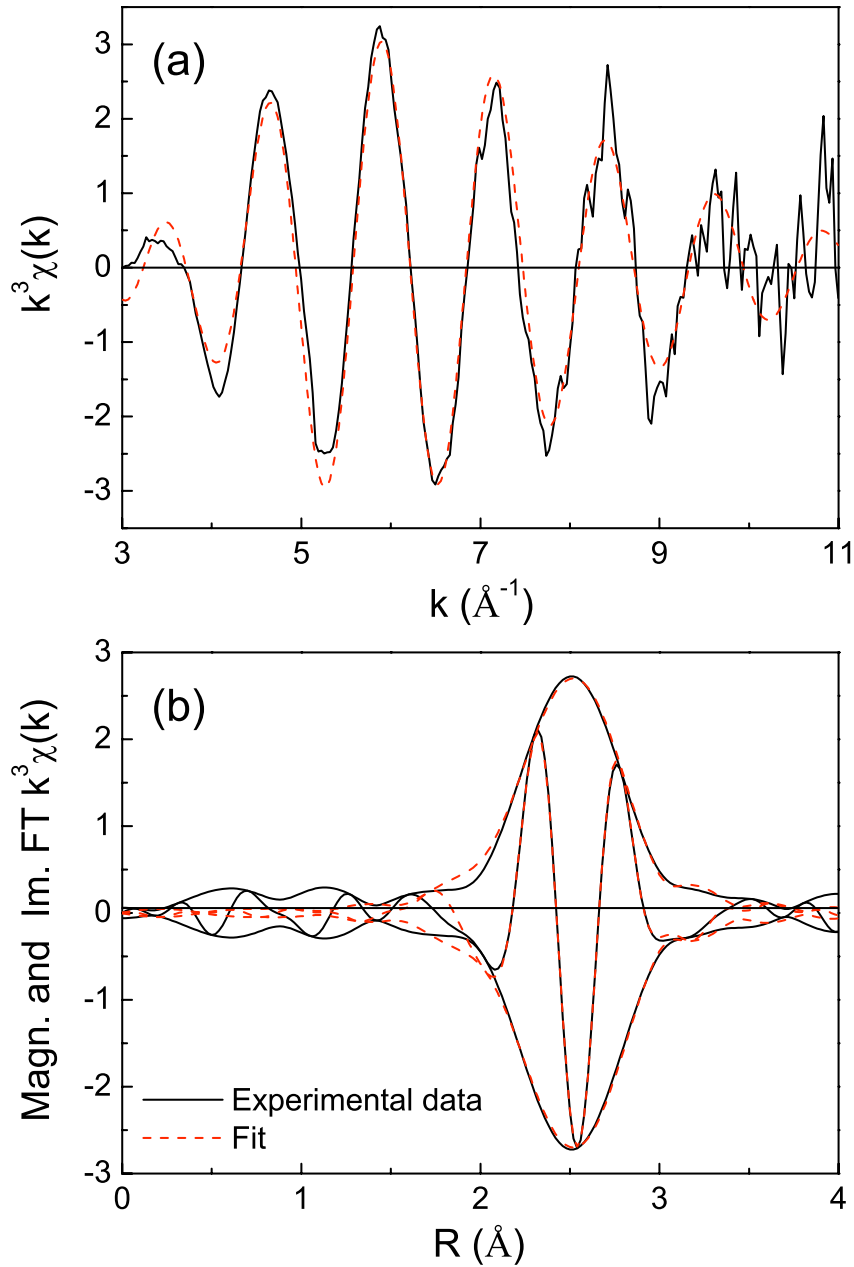


Figure 3.12: (a) k^1 -weighted background-subtracted $\chi(k)$ and (b) Magnitude and Imaginary part of the phase-uncorrected Fourier transformed $\chi(k)$ for sample 1. The fit (dashed line) is optimized with $\Delta k = 3 - 11 \text{\AA}^{-1}$ and $\Delta R = 2.0 - 3.4 \text{\AA}$.

Table 3.2: Fit parameters for the samples in the as-deposited and de-hydrogenated states: coordination number N , Debye-Waller factor $\Delta\sigma^2$, distance R and inner potential correction ΔE_0 .

Sample	Shell	N	$\Delta\sigma^2$ (10^{-3} \AA^2)	R (\AA)	ΔE_0 (eV)	y	CSRO, s
1 as-dep.	Ti-Ti	7.7	12.6	2.90	1.97	0.53	0.18±0.05
	Ti-Mg	5.9	9.6	3.02	-1.02		
2 as-dep.	Ti-Ti	7.5	12.2	2.89	2.61	0.59	0.27±0.05
	Ti-Mg	5.7	8.1	3.02	-0.31		
3 as-dep.	Ti-Ti	6.7	12.1	2.89	1.87	0.70	0.32±0.04
	Ti-Mg	6.1	12.7	3.03	-0.47		
3a as-dep.	Ti-Ti	6.1	11.0	2.89	2.11	0.72	0.38±0.04
	Ti-Mg	5.0	10.1	3.03	-0.17		
4 as-dep.	Ti-Ti	5.0	15.9	2.90	4.73	0.81	0.29±0.03
	Ti-Mg	6.8	12.7	3.09	1.50		
5 as-dep.	Ti-Ti	5.0	18.3	2.93	2.24	0.90	0.35±0.03
	Ti-Mg	7.1	8.9	3.09	1.76		
1 de-hydr.	Ti-Ti	6.8	13.4	2.89	3.44	0.53	0.16±0.05
	Ti-Mg	5.5	10.3	2.96	1.52		
3a de-hydr.	Ti-Ti	6.4	13.8	2.89	3.42	0.72	0.33±0.04
	Ti-Mg	5.9	10.6	3.03	0.61		
5 de-hydr.	Ti-Ti	5.8	22.1	3.00	2.88	0.90	0.37±0.03
	Ti-Mg	7.7	8.2	3.11	3.30		

(CSRO) parameter, s , can be calculated as follows [47]

$$s = 1 - \frac{N_{\text{Ti-Mg}}}{(N_{\text{Ti-Ti}} + N_{\text{Ti-Mg}}) y} \quad (3.3)$$

where $s = 0$ would correspond to a random distribution of Mg and Ti atoms, while $s = 1$ to a complete segregation into pure phases of Mg and Ti.

The measured s values are reported in Table 3.2. The error in s is calculated assuming a $\pm 10\%$ error in the coordination numbers [96] while the error on the composition y , as measured with RBS, is negligible.

XANES spectra are continuously recorded during the hydrogenation and de-hydrogenation of the films. For all the compositions the Ti absorption edge is identical to the one measured for the reference Ti foil, indicating a purely metallic state of the as-deposited samples. Fully hydrogenated films are obtained by exposure of the as-deposited films to a 5% H_2/He mixture for few minutes at room temperature, the end of the hydrogenation being indicated by a stable XANES spectrum. Upon exposure to a 20% O_2/He mixture for ~ 1 hour at temperatures between room temperature and 100°C , depending on film composition, the hydrogenated films release hydrogen and return to a metallic state. The comparison between the as-deposited and the de-hydrogenated metallic states, for three different compositions, is shown in Fig. 3.13, together with the fitted s values. The slight differences between

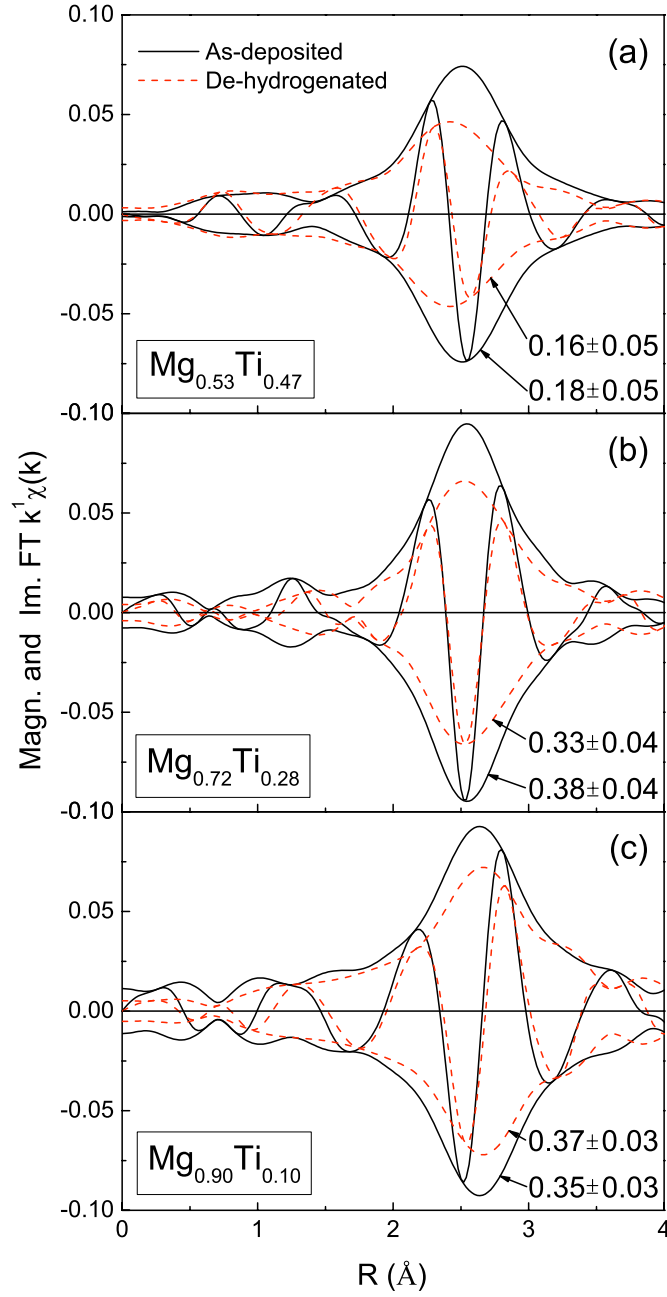


Figure 3.13: Magnitude and Imaginary part of the phase-uncorrected Fourier transformed $\chi(k)$ for $\text{Mg}_{0.53}\text{Ti}_{0.47}$, $\text{Mg}_{0.72}\text{Ti}_{0.28}$ and $\text{Mg}_{0.90}\text{Ti}_{0.10}$ both in the as-deposited (solid line) and de-hydrogenated (dashed line) states. The numerical values indicate the chemical short-range order parameters obtained upon fitting.

the two metallic states (before and after hydrogenation) are mainly due to small changes in the coordination numbers and to an increase in the amount of disorder of the Ti-Ti shells.

3.3.4 Discussion

EXAFS data show that $\text{Mg}_y\text{Ti}_{1-y}$ thin films do not form random solid solutions and that a certain degree of atom rearrangement is already present in the as-deposited films. The amount of rearrangement does not depend strongly on composition: a chemical short-range order of $s \sim 0.3$ is found for a broad range of compositions. The slightly lower s values obtained for the Ti-richer compositions are probably due to the higher total deposition rates during sputtering (Table 3.1).

As shown in Figure 3.14 the non-zero chemical short-range order leads to “spinodal-like” structures in the $\text{Mg}_y\text{Ti}_{1-y}$ alloys. Experimental evidence of

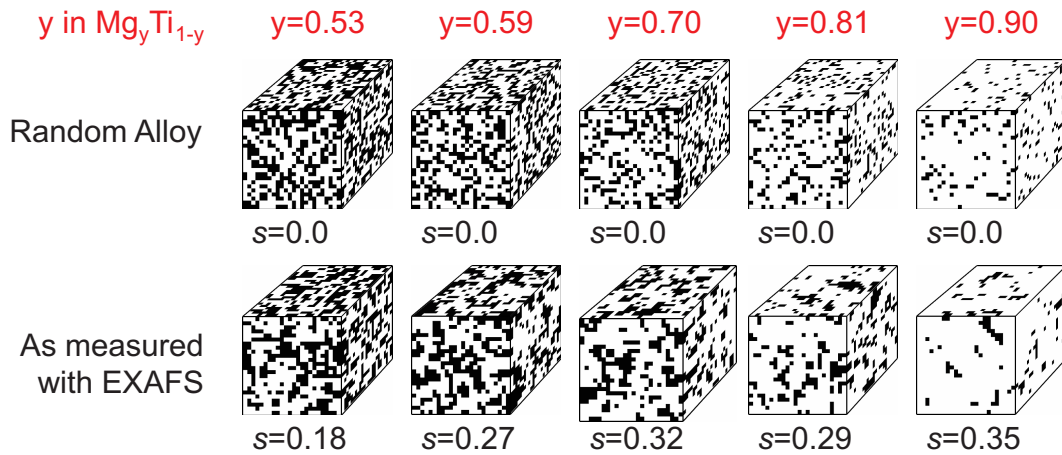


Figure 3.14: 3D-representation of $\text{Mg}_y\text{Ti}_{1-y}$ alloys with compositions as in samples 1, 2, 3, 4 and 5 and chemical short-range order parameters, s , as measured with EXAFS. For comparison the same compositions are shown for completely random distribution of Mg and Ti atoms ($s = 0$).

such “spinodal-like” structures, characterized by compositional modulations with nanometer wavelengths [47], with similar values for the chemical short-range order parameters, has been reported both for amorphous [70] and crystalline [71] immiscible binary systems. The pictures in Figure 3.14 are indicative of the degree of decomposition that occurs during films deposition and are generated via 3D Monte Carlo simulations, assuming only nearest-neighbors interactions and including periodic boundary conditions.

The chemical short-range order arises during the high-energy non equilibrium deposition process, resulting in the partial segregation into Mg-rich and Ti-rich domains which is driven by the positive enthalpy of mixing of the

two elements. Such ordering is also responsible for the fast kinetics and the exceptional robustness of these systems.

Comparison between the EXAFS spectra measured on the as-deposited and the de-hydrogenated films indicate a high structural reversibility of the $\text{Mg}_y\text{Ti}_{1-y}$ alloys, even at an atomic level. This result is particularly unexpected given the strong segregating effect of hydrogen on many Mg-based alloys, such as Mg-V [43], Mg-Sc [97], Mg-Y, Mg-La, Mg-Ce, and Mg-Gd [19]. Furthermore RBS results and the analysis of the absorption edge energies in the EXAFS spectra rule out the hypothesis that the stability upon hydrogen cycling of the $\text{Mg}_y\text{Ti}_{1-y}$ films, is due to the presence of impurities in the alloys or to partial oxidation of the films.

The structural model developed to interpret the optical and electrical properties of $\text{Mg}_y\text{Ti}_{1-y}\text{H}_x$ thin films [38] hypothesized the coexistence of Mg-rich and Ti-rich nanosized domains, within large coherent grains. This model is nicely and quantitatively confirmed by the positive chemical short-range order parameters measured by means of EXAFS (see Fig. 3.15).

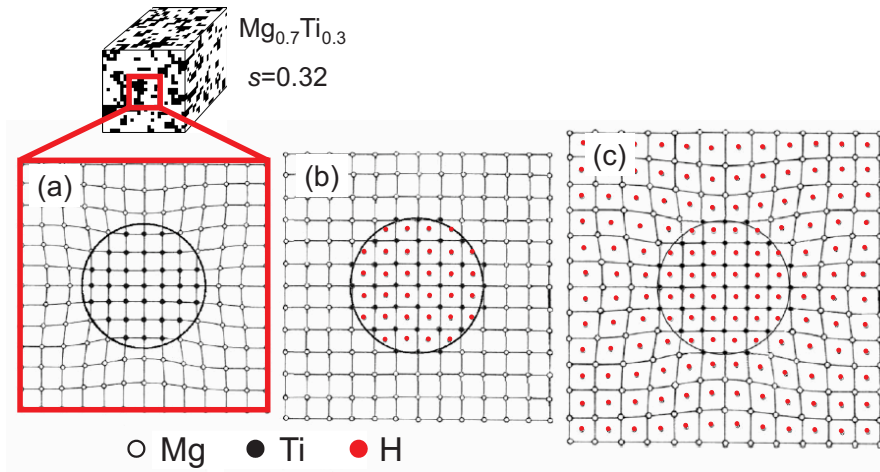


Figure 3.15: Enlargement of the $\text{Mg}_{0.7}\text{Ti}_{0.3}$ sample in Figure 5, highlighting the “cluster-like” structure of the $\text{Mg}_y\text{Ti}_{1-y}$ thin films. (a) Schematic representation of a coherent crystalline grain consisting of a Mg and a Ti region; (b) the same crystalline grain after hydrogen uptake in the Ti sites, at low hydrogen pressures; (c) and in the fully hydrogenated state [38]. Note that the cartoons are only meant as an illustration of the stress-releasing intermediate state (b), when Ti has formed TiH_2 but Mg is still in its metallic state.

As already suggested by Borsa et al. [38], once a spinodal coherent microstructure is formed upon film deposition, a key ingredient for its stability is the similarity in the molar volumes of Mg ($13.97 \text{ cm}^3/\text{mole}$) and TiH_2 ($13.30 \text{ cm}^3/\text{mole}$). Ti has a more negative enthalpy of hydride formation than Mg,

thus forming a hydride at lower pressures. Given the presence of chemical short-range order, the hydrogenation of our films proceeds in the following way (see Fig. 3.15): at very low hydrogen pressures a hydrogen solid solution forms in the $\text{Mg}_y\text{Ti}_{1-y}$ alloy producing a small expansion of the host lattice; with increasing pressure the Ti-rich parts hydrogenate and the internal lattice strains are substantially *released* by the coexistence of Mg and TiH_2 domains, thanks to the accidental equality of the molar volumes of the two components; a further increase of hydrogen pressure eventually causes Mg-rich areas to form the di-hydride, MgH_2 . The coherency with the fcc TiH_2 forces the MgH_2 to form in the fcc instead of the rutile phase. The same steps are followed in reverse order during unloading. As evidenced by XRD data the coherence of the alloy is maintained in the whole process.

Hydrogen atoms in a $\text{Mg}_y\text{Ti}_{1-y}$ alloy can occupy different tetrahedral $\text{Mg}_j\text{Ti}_{4-j}$ interstitial sites, with $0 \leq j \leq 4$. Taking into account the different site energies and including the effect of both short-range ordering and lattice distortions, Gremaud et al. [50] have successfully fitted the pressure–optical-transmission–isotherms measured by hydrogenography [12] on $\text{Mg}_y\text{Ti}_{1-y}$ thin films. The fitted values of the chemical short-range order parameter are in excellent agreement with the values measured in the present work with EXAFS and confirm the reversibility of these systems upon several hydrogen loading/unloading cycles.

Our measurements neatly confirm the structural picture which was deduced on the basis of the optical transition observed on hydrogenation. Note, that the thermodynamics of the hydrogenation of Mg is hardly affected [12]. This can be understood from the fact that the energy difference between the fcc and rutile phases is small [84]. The advantage for storage applications is that the fcc crystal structure allows for a favorable kinetics of hydrogen diffusion [98].

The nanoscale short-range deviations from a random solid solution measured in $\text{Mg}_y\text{Ti}_{1-y}\text{H}_x$ thin films make it possible to understand quantitatively the hydrogen loading and unloading mechanisms. They also provide an interpretation of the non-trivial optical black state observed in the hydrogenated state of $\text{Mg}_y\text{Ti}_{1-y}\text{H}_x$ thin films: the origin of this black state cannot be explained within a simple effective medium approximation. Recent *ab initio* density functional theory calculations by van Setten *et al.* [99] reproduce the observed optical reflection and transmission spectra, taking into account a certain degree of ordering in the distribution of atoms in $\text{Mg}_y\text{Ti}_{1-y}\text{H}_2$ super cells and including both inter band and intra band contributions to the dielectric function.

3.3.5 Conclusions

As standard x-ray diffraction techniques alone are inadequate for systems of immiscible elements [44], we combined XRD and EXAFS to study the local

structure of Mg-Ti-H alloys. We show that in $\text{Mg}_y\text{Ti}_{1-y}$ thin films the distribution of Mg and Ti atoms is not random and that a certain level of local chemical segregation occurs, without affecting the long-range structural coherence of the film. The amount of segregation depends weakly on composition and is stable upon cycling with hydrogen. The “spinodal-like” distribution of atoms, suggested by Monte-Carlo simulations, allows to understand the robustness of the system in terms of an accidental equality in the molar volumes of Mg and TiH_2 . This kind of microstructure is of particular technological interest in the synthesis of new metastable materials, with high hydrogen storage capacities and fast hydrogen absorption and desorption kinetics. By applying the proper synthesis techniques one may thus aim to stabilize crystal structures not feasible according to basic thermodynamics. Our work shows that the possibilities to optimize the properties of hydrogen storage materials are more abundant than previously envisaged.

3.4 Chemical short-range order and lattice deformations in $\text{Mg}_y\text{Ti}_{1-y}\text{H}_x$ thin films probed by hydrogenography

Abstract – A multi-site lattice gas approach is used to model pressure–optical-transmission–isotherms (PTI) recorded by hydrogenography on $\text{Mg}_y\text{Ti}_{1-y}\text{H}_x$ sputtered thin films. The model reproduces the measured PTIs well and allows to determine the chemical short-range order parameter s . The s values are in good agreement with those determined from extended X-ray absorption fine structure (EXAFS) measurements. Additionally the PTI multi-site modeling yields a parameter L that accounts for the local lattice deformations with respect to the average $\text{Mg}_y\text{Ti}_{1-y}$ lattice given by Vegard’s law. It is thus possible to extract two essential characteristics of a metastable alloy from hydrogenographic data.

3.4.1 Introduction

Mg and Ti are considered as immiscible, as their enthalpy of mixing is positive ($\Delta H_{\text{mix}} > 30$ kJ/g atom) [33]. Alloying of Mg and Ti does however take place in mechanically alloyed bulk samples [39], in physical vapor deposition [34], e-beam deposition [35, 36] and sputtering of thin films [21, 37, 38].

In general, understanding the degree of mixing achievable in immiscible systems is of considerable scientific and technological interest [44, 47, 70, 71]. In particular, the fact that reproducible and reversible switching from metal to hydride without noticeable segregation of the metal constituents occurs in Mg-Ti thin films [38] makes it an even more fascinating model system to study.

Continuous monitoring of the structure during H uptake by X-ray diffraction (XRD) hints at a persistent coherent structure during the whole (de)hydrogenation process. Additional electrical and spectrophotometric measurements suggest that Mg-Ti films are structurally coherent at the XRD scale but locally partially chemically segregated [38]. It is thus of interest to probe how much decomposition has occurred and on what spatial scale.

Thanks to their peculiar structural properties, Mg-Ti-H thin films are also of interest for application as optical switchable devices, e.g. for solar collectors [21, 22] and fiber optic hydrogen sensors [49]. While metallic in the as-deposited state (high optical reflectance and very low optical transmittance), the films become highly absorbing (low reflectance and transmittance) upon hydrogen uptake. The high degree of mixing between Mg and Ti in sputtered films is directly responsible, via a lowering of the plasma frequency [99], for an unusual "black" optical state. The optical change in optical transmission upon hydrogen absorption makes $\text{Mg}_y\text{Ti}_{1-y}\text{H}_x$ thin films also ideally suited for hydrogenography, a high-throughput combinatorial method for the search of new light-weight hydrogen storage materials [12, 13]. This technique makes it possible to measure pressure–*optical-transmission*–isotherms (PTI) on hydrides with a metal-to-semiconductor transition [12] as well as on hydrides that remain metallic upon hydrogenation [13]. From Lambert-Beer's law, $\ln(T/T_M)$, the logarithm of the optical transmission T in a film of initial transmission T_M , is expected to vary linearly with the hydrogen concentration [100]. This is confirmed by joint electrochemical and optical measurements [38]. The obtained PTIs are therefore fully analogous to pressure-concentration-isotherms (PCI) obtained with standard volumetric or gravimetric methods [13].

The formation enthalpy of bulk TiH_2 ($\Delta H = -130$ kJ(mol H_2)⁻¹) is almost twice as negative as the one of bulk MgH_2 ($\Delta H = -76$ kJ(mol H_2)⁻¹) [101]. In a fully segregated sample, one would therefore expect Ti to form a hydride at lower pressures than Mg in the film, resulting in two well-defined plateaus in the PTIs. However, both PTIs [12] and electrochemical isotherms [37] of $\text{Mg}_y\text{Ti}_{1-y}$ thin films present an unusual shape that is not compatible with a sequential formation of TiH_2 and MgH_2 .

In this article, we present a multi-site lattice gas model for optical isotherms and apply it on PTIs measured by hydrogenography on $\text{Mg}_y\text{Ti}_{1-y}\text{H}_x$ sputtered thin films. The model reproduces the measured PTIs well and allows to derive experimental values of the chemical short-range order parameter (CSRO) s which are in good agreement with the local surrounding of Ti and s values determined by EXAFS [48]. Furthermore, the model gives information on the local lattice's departures from the average lattice given by Vegard's law.

3.4.2 Experimental details

Sample preparation

$\text{Mg}_y\text{Ti}_{1-y}$ thin films with a compositional gradient are prepared in a 7-gun ultra-high-vacuum dc/rf magnetron co-sputtering system (base pressure 10^{-7} Pa) at room temperature on $70 \times 5 \text{ mm}^2$ quartz substrates. Mg and Ti are facing each other in tilted off-axis sputtering guns. By adjusting the power applied to each gun the desired compositional region of the binary phase diagram is obtained. The local composition of the gradient films is determined by Rutherford Backscattering Spectrometry on films grown in the same deposition run on amorphous carbon substrates. The Mg atomic fraction y along the length of the sample varies between 0.6 and 0.89. All the films with thickness 30-100 nm are covered *in-situ* with a 20 nm Pd caplayer to promote H_2 dissociation and to prevent oxidation of the underlying film.

Data collection

After deposition, metallic films are transferred into an optical cell to monitor their optical transmission during hydrogenation [100]. The whole cell is placed in an oven to control temperature up to 300 °C. A 150 W diffuse white light source illuminates the sample from the substrate side, and a 3-channel (RGB) SONY XC-003 charged-coupled device (CCD) camera continuously monitors the transmitted light as a function of hydrogen pressure. The 3-channel transmission intensities are added, resulting in a 1.1 to 3.3 eV photon energy bandwidth. More information about the PTI acquisition can be found in Ref. [12].

For the determination of optical absorption coefficients, spectrophotometric reflection and transmission measurements of Mg and Ti in the metallic and hydrogenated states are performed in a Perkin Elmer Lambda 900 diffraction grating spectrometer with an energy range from 0.495 to 6.19 eV (wavelength $\lambda = 2500 - 200 \text{ nm}$).

3.4.3 Experimental PTIs

Figure 3.16 shows various PTIs of $\text{Mg}_y\text{Ti}_{1-y}$ with $0.61 \leq y \leq 0.85$ at temperature $\mathcal{T} = 363 \text{ K}$. The average coherent structure determined by XRD and plan view TEM is hcp in the metallic state and fcc in the hydrided state [38].

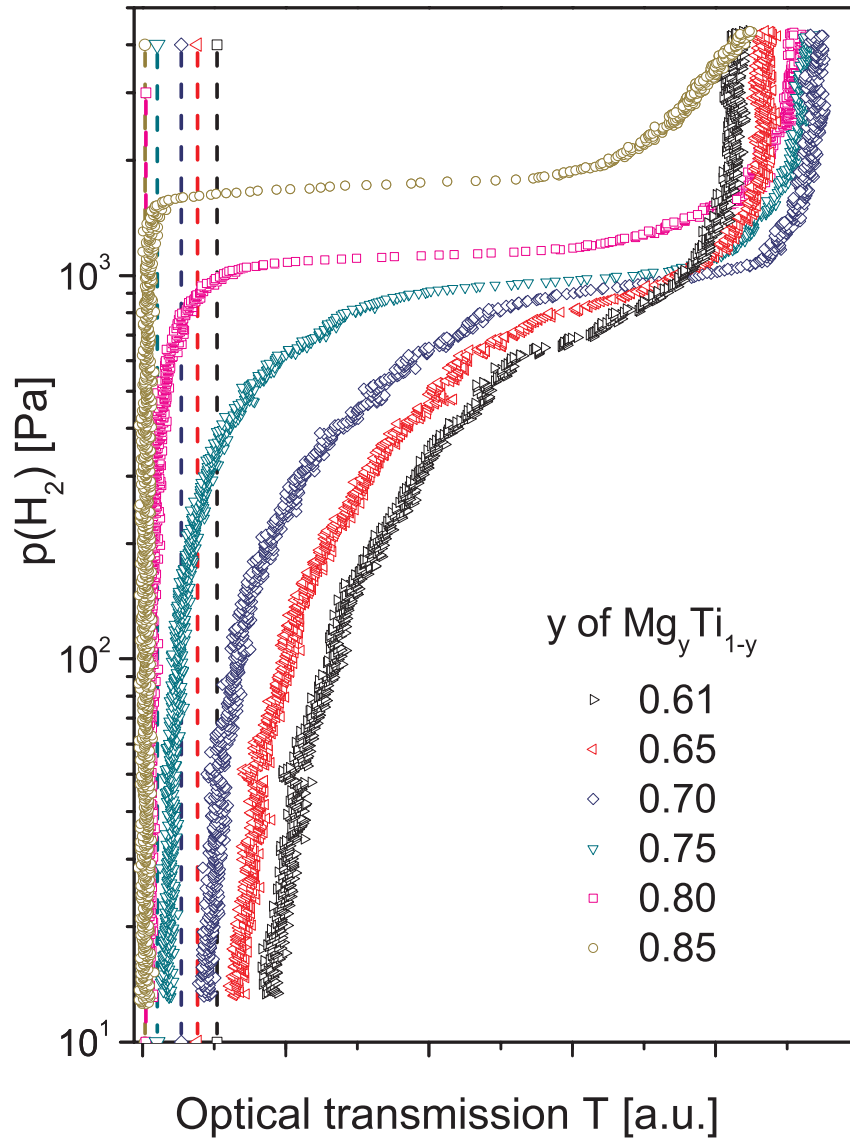


Figure 3.16: Pressure–optical–transmission–isotherms at $\mathcal{T} = 363$ K of a thin $\text{Mg}_y\text{Ti}_{1-y}$ film with a continuous gradient in alloy composition. Dashed lines indicate the transmission in the metallic state T_M .

Compositions with $y > 0.85$ are not considered here because of the presence of rutile MgH_2 that coexists with the fcc structure. Dashed lines indicate the transmission in the metallic state T_M for the various compositions. For all compositions, the optical transmission T increases with increasing hydrogen pressure. Starting from low pressures, the transmission first increases gradually, and then a sloping plateau develops at higher pressure. The plateau shifts towards higher pressures and widens with increasing Mg atomic fraction y . Conversely, the gradual transmission increase with pressure is the dominant feature in the isotherms for the Ti-richest compositions ($0.61 \leq y < 0.7$). We show in the following that this PTIs shape evolution with Mg fraction y is neither compatible with randomly distributed Mg and Ti atoms, nor with completely phase segregated Mg and Ti (hydride) phases.

3.4.4 PTI modeling: Lattice gas model for H in a multi-site solid with long-range H-H interaction

In this section, we show that a multi-site lattice gas model [102, 103, 104] with tetrahedral interstitial sites $\text{Mg}_j\text{Ti}_{4-j}$ ($0 \leq j \leq 4$) including chemical short-range order [105, 106] is suitable to model the PTIs. The six essential ingredients of the multi-site lattice gas model are the:

1. types and fractions of the various interstitial sites,
2. local lattice deformation of the host lattice due to alloying of Mg and Ti,
3. enthalpy of hydrogen solution for each site type,
4. degree of occupation of interstitial sites at thermodynamic equilibrium with the surrounding H_2 gas,
5. long-range H-H interaction in the lattice gas and the
6. relation between the total hydrogen concentration and the optical transmission.

Mg-Ti interstitial sites: types and fractions

The as-deposited $\text{Mg}_y\text{Ti}_{1-y}$ films are neither perfectly random nor fully segregated [48]. To characterize their overall degree of chemical segregation as a function of composition y we use the chemical short-range order (CSRO) parameter defined as [46]:

$$s = 1 - \frac{N_{\text{BA}}}{Ny} \quad (3.4)$$

for a A_yB_{1-y} system where N_{BA} is the nearest neighbor coordination number of A atoms around a B atom (here $\text{A}=\text{Mg}$, $\text{B}=\text{Ti}$), N is the total coordination

number in the nearest neighbor shell, and y is the atomic fraction of A. Positive, zero, and negative CSRO parameters indicate clustered, random, and ordered spatial distributions of atoms, respectively.

We assume that H in a $\text{Mg}_y\text{Ti}_{1-y}$ alloy can occupy tetrahedral interstitial sites $\text{Mg}_j\text{Ti}_{4-j}$ with $0 \leq j \leq 4$. There are N_j sites of type j and the total number of sites is $N = \sum_j N_j$. Using a cluster model [105] to calculate the fraction $g_j = N_j/N$ of each hydrogen site type, we obtain the following relations:

$$g_0 = (1 - y)(1 - y + ys)^3 \quad (3.5)$$

$$g_1 = 2(1 - y)(1 - y + ys)^2y(1 - s) + 2(1 - y)^2(1 - y + ys)y(1 - s)^2 \quad (3.6)$$

$$g_2 = 2(1 - y)(1 - y + ys)y(1 - s)(y + (1 - y)s) + 2(1 - y)^2y^2(1 - s)^3 \quad (3.7)$$

$$+ (1 - y)^2y(1 - s)^2(y + (1 - y)s) + y^2(1 - y + ys)(1 - s)^2(1 - y)$$

$$g_3 = 2(1 - y)y(1 - s)(y + (1 - y)s)^2 + 2y^2(1 - s)^2(1 - y)(y + (1 - y)s) \quad (3.8)$$

$$g_4 = y(y + (1 - y)s)^3 \quad (3.9)$$

for Ti_4 , MgTi_3 , Mg_2Ti_2 , Mg_3Ti , and Mg_4 sites respectively, with of course $\sum_j g_j = 1$.

Local lattice deformations due to alloying

Magnesium has a larger molar volume than Ti ($V_{\text{Mg}} = 13.97 \text{ cm}^3/\text{mol}$, $V_{\text{Ti}} = 10.64 \text{ cm}^3/\text{mol}$). This implies that a titanium inclusion in a Mg matrix is somewhat expanded while the Mg matrix is compressed compared to their pure metals volumes [107]. The same applies to clusters of type j . The volume V_j^e of a cluster *embedded* in the alloy matrix is related to the volume V_j^f of a *free* cluster as [105]:

$$V_j^e(y) = (1 - L)V_{\text{metal}}(y) + LV_j^f \quad (3.10)$$

where

$$V_j^f = \frac{jV_{\text{Mg}} + (4 - j)V_{\text{Ti}}}{4}, \quad (3.11)$$

$$V_{\text{metal}}(y) = yV_{\text{Mg}} + (1 - y)V_{\text{Ti}} \quad (3.12)$$

and V_{Mg} , V_{Ti} are the molar volumes of the elements. The parameter L accounts for the degree of local deformation of a cluster embedded in an alloy. The

meaning of the parameter L is best explained by taking the perfect average crystal with a molar volume $V_{\text{metal}}(y)$ given by Vegard's law (see Eq. 3.12). In this hypothetical perfect lattice all clusters have the same volume. This corresponds to $L = 0$. A positive value for L implies that a Mg-rich cluster is slightly compressed while a Ti-rich cluster is slightly expanded with respect to the $L = 0$ case in an alloy with a coherent lattice but locally modulated lattice spacings. To illustrate the effect of extreme L values, we consider the case of a Mg_4 cluster: In the rigid limit, $L = 1$, a Mg_4 cluster keeps the same volume as in pure Mg, while for $L = 0$, it is compressed according to the overall composition of the $\text{Mg}_y\text{Ti}_{1-y}$ metal alloy. Note that Vegard's law still applies to the long-range average lattice for all L values.

Site dependent enthalpies of hydrogen solution

In the simplest approximation, the enthalpies of hydrogen solution (i.e. for hydrogen concentrations $c \rightarrow 0$) $\Delta H_j^{0,\text{f}}$ for isolated *free* $\text{Mg}_j\text{Ti}_{4-j}$ clusters are taken as the weighted averages of the hydrogen solution enthalpies ΔH_{Mg}^0 and ΔH_{Ti}^0 in pure Mg and Ti [103]:*

$$\Delta H_j^{0,\text{f}} = \frac{j\Delta H_{\text{Mg}}^0 + (4-j)\Delta H_{\text{Ti}}^0}{4} \quad (3.13)$$

For a $\text{Mg}_j\text{Ti}_{4-j}$ cluster embedded in a $\text{Mg}_y\text{Ti}_{1-y}$ matrix, $\Delta H_j^{0,\text{f}}$ needs to be corrected for local deformations due to alloying.

Thermodynamically the volume dependence of the enthalpy of hydride formation is given by [9]:

$$\frac{d\Delta H}{d \ln V} = -B(y)V_{\text{H}}(y) \quad (3.14)$$

where $B(y)$ is the bulk modulus of the alloy,

$$V_{\text{H}}(y) = \frac{V_{\text{dihydride}}(y) - V_{\text{metal}}(y)}{2} \quad (3.15)$$

the partial molar volume of H in the alloy,

$$V_{\text{dihydride}}(y) = yV_{\text{MgH}_2} + (1-y)V_{\text{TiH}_2}, \quad (3.16)$$

and V_{MgH_2} and V_{TiH_2} the molar volumes of the dihydrides.

Using eq. 3.14, the enthalpy of hydrogen solution for *embedded* clusters becomes:

$$\Delta H_j^{0,\text{e}} \simeq \Delta H_j^{0,\text{f}} + \frac{d\Delta H^0}{d \ln V} \frac{(V_j^{\text{e}} - V_j^{\text{f}})}{V_j^{\text{f}}} = \Delta H_j^{0,\text{f}} - B(y)V_{\text{H}}(y) \frac{V_j^{\text{e}}(y) - V_j^{\text{f}}}{V_j^{\text{f}}} \quad (3.17)$$

The bulk modulus $B(y)$ is taken as the weighted average of the bulk moduli of the metal constituents:

$$B(y) = yB_{\text{Mg}} + (1-y)B_{\text{Ti}}. \quad (3.18)$$

*If available, theoretical values obtained, for example, by means of density functional theory can be used instead of those given by Eq. 3.13

Occupation of the interstitial sites

With increasing hydrogen pressure, hydrogen fills gradually interstitial sites in the $\text{Mg}_y\text{Ti}_{1-y}$ alloy, starting with sites with the lowest enthalpy, in our case Ti_4 sites. The total number of hydrogen atoms absorbed at a certain hydrogen gas pressure p and temperature \mathcal{T} is denoted by N^{H} , and the number of hydrogen atoms occupying a given site type by N_j^{H} . Consequently the fraction x_j of interstitial site j occupied by hydrogen atoms is

$$x_j = \frac{N_j^{\text{H}}}{N_j} \quad (3.19)$$

and the normalized total hydrogen concentration c ($0 \leq c \leq 1$) is

$$c = \frac{N^{\text{H}}}{N} = \sum_{j=0}^4 \frac{N_j}{N} \frac{N_j^{\text{H}}}{N_j} = \sum_{j=0}^4 g_j x_j \quad (3.20)$$

Thermodynamic equilibrium between hydrogen gas and hydrogen at each interstitial site requires that

$$\frac{1}{2}\mu_{\text{H}_2}(p, \mathcal{T}) = \mu_{\text{H}}^j(p, \mathcal{T}, x_j, c) \quad j = 0, \dots, 4 \quad (3.21)$$

where the chemical potential of H_2 gas is [108]

$$\mu_{\text{H}_2} = RT \left[\ln \left(\frac{p}{p^0} \right) - \frac{S_{\text{H}_2}^0}{R} \right] + E_{\text{H}_2} \quad (3.22)$$

with $S_0 = 130.68 \text{ JK}^{-1}(\text{mol H}_2)^{-1}$ the entropy of H_2 gas at standard pressure $p^0 = 1.013 \times 10^5 \text{ Pa}$, E_{H_2} the binding energy of the H_2 molecule and R the gas constant. The chemical potential of H at each interstitial site type can be written as

$$\mu_{\text{H}}^j = RT \ln \left(\frac{x_j}{1 - x_j} \right) + E_j(c) \quad j = 0, \dots, 4 \quad (3.23)$$

where the energy $E_j(c)$ of H at the interstitial site $\text{Mg}_j\text{Ti}_{4-j}$ depends in general on the *total* hydrogen concentration c . This is a direct consequence of the infinite range of the elastic H-H interaction in metal-hydrides [8].

Solving eq. (3.21) for x_j , one obtains. together with eq. (3.20)

$$c = \frac{N^{\text{H}}}{N} = \sum_{j=0}^4 g_j x_j = \sum_{j=0}^4 \frac{g_j}{\exp \left\{ \frac{\Delta H_j(c)}{RT} - \frac{1}{2} \left[\ln \left(\frac{p}{p^0} \right) - \frac{S_{\text{H}_2}^0}{R} \right] \right\} + 1} \quad (3.24)$$

with

$$\Delta H_j(c) = E_j(c) - \frac{1}{2}E_{\text{H}_2} \quad (3.25)$$

the concentration dependent enthalpy for H absorption in a site j . Equation (3.24) is a self-consistent equation for $p = p(c)$ that is solved numerically to determine the PCI at temperature \mathcal{T} .

H-H interaction

In order to calculate $\Delta H_j(c)$, the H-induced lattice expansion has to be taken into account. Increasing the H concentration makes all interstitial sites more favorable for hydrogen [109], and results in an infinite range attractive H-H interaction [4, 110]. The contribution of this H-H interaction to the enthalpy of formation is to lowest order given by (see Eq. (3.14)) [106].

$$\Delta H_j(c) \simeq \Delta H_j^{0,e} + \frac{d\Delta H}{d\ln V} \frac{d\ln V}{dc} c = \Delta H_j^{0,e} - B(y, c) V_H(y) \frac{V_{\text{dihydride}} - V_{\text{metal}}}{2V_{\text{metal}}} c \quad (3.26)$$

with

$$B(y, c) = y [cB_{\text{MgH}_2} + (1 - c)B_{\text{Mg}}] + (1 - y) [cB_{\text{TiH}_2} + (1 - c)B_{\text{Ti}}]. \quad (3.27)$$

Together with eq. (3.17), the enthalpy of hydride formation at a site j becomes:

$$\Delta H_j(c) \simeq \Delta H_j^{0,f} - B(y, 0) V_H(y) \frac{V_j^e(y) - V_j^f}{V_j^f} - B(y, c) \frac{V_H(y)^2}{V_{\text{metal}}} c \quad (3.28)$$

The second and third terms in Eq. 3.28 describe the influence on the enthalpy of formation of local lattice deformations at zero hydrogen concentration and of the filling of sites with hydrogen, respectively.

Optical transmission

Lambert-Beer's law is used to calculate the optical transmission T :

$$T = T_0 \prod_{j=0}^4 \exp \{ [-\alpha_j^{\text{M}}(1 - x_j) - \alpha_j^{\text{MH}} x_j] g_j \} \quad (3.29)$$

where T_0 is the light intensity in the absence of the sample and $\alpha_j^{\text{M(H)}}$ are the optical absorption coefficients of the metallic and hydrided $\text{Mg}_j\text{Ti}_{1-j}$ clusters averaged over the measured photon-energy $\hbar\omega$ bandwidth, respectively. According to Eq. 3.29, the transmission in the metallic state T_{M} is:

$$T_{\text{M}} = T_0 \prod_{j=0}^4 \exp(-\alpha_j^{\text{M}} g_j) \quad (3.30)$$

Combining Eqs. (3.29) and (3.30), the logarithm of the optical transmission normalized by the transmission in the metallic state is

$$\ln \left(\frac{T}{T_{\text{M}}} \right) = - \sum_{j=0}^4 (\alpha_j^{\text{MH}} - \alpha_j^{\text{M}}) x_j g_j \quad (3.31)$$

If the optical change $\alpha_j^{\text{MH}} - \alpha_j^{\text{M}}$ was independent of j , i.e. of the cluster composition, then

$$\ln\left(\frac{T}{T_{\text{M}}}\right) \propto c \quad (3.32)$$

This is however certainly not the case, as MgH_2 is a transparent insulator and TiH_2 a metal. The simplest approximation would be to neglect the optical change of the metal and take

$$\alpha_j^{\text{MH}} - \alpha_j^{\text{M}} \cong j \cdot (\alpha_{\text{MgH}_2} - \alpha_{\text{Mg}}), \quad (3.33)$$

then

$$\ln\left(\frac{T}{T_{\text{M}}}\right) \cong -(\alpha_{\text{MgH}_2} - \alpha_{\text{Mg}}) \sum_{j=0}^4 j x_j g_j. \quad (3.34)$$

This shows that Mg-rich clusters have a predominant contribution to the optical transmission.

The last step is to combine Eqs. (3.24) and (3.31) to obtain

$$\ln\left(\frac{T}{T_{\text{M}}}\right) = \sum_{j=0}^4 \frac{(\alpha_j^{\text{M}} - \alpha_j^{\text{MH}}) g_j}{\exp\left\{\frac{\Delta H_j(c)}{RT} - \frac{1}{2} \left[\ln\left(\frac{p}{p^0}\right) - \frac{S_{\text{H}_2}^0}{R}\right]\right\} + 1} \quad (3.35)$$

This is the central result of our model, used to calculate the PTIs.

3.4.5 Comparison with experimental PTIs

The present model is applied to pressure–optical–transmission–isotherms measured on $\text{Mg}_y\text{Ti}_{1-y}\text{H}_x$ gradient thin films. This ensures a reliable comparison of the isotherms, as all compositions y are measured simultaneously under exactly the same pressure and temperature conditions.

The determination of the optical absorption coefficients of the pure Mg and Ti metals is done on separately deposited Pd capped Mg and Ti thin films [111]. The consistency of the results is checked with data from Palik [60]. The absorption coefficient of the hydrides MgH_2 and TiH_2 are then determined on the same films exposed to 10^5 Pa H_2 pressure. The absorption coefficients of the intermediate $\text{Mg}_j\text{Ti}_{4-j}$ clusters ($j = 1, 2, 3$) are to first order the weighted average of values for pure metals (hydrides).^{*} We make use of *ab initio* calculations of the optical properties of Mg-Ti supercells [99] to interpolate more precisely the absorption coefficients (see Fig. 3.17).

We use the standard molar volumes $V_{\text{Mg}} = 13.97 \text{ cm}^3 (\text{mol})^{-1}$ and $V_{\text{Ti}} = 10.64 \text{ cm}^3 (\text{mol})^{-1}$ for the metals. For the hydrides, 32% and 25% volume

^{*}The weak curvature of the absorption coefficients difference in Fig. 2 shows that if first principles calculation had not been available, a simple linear interpolation would have induced only minor errors. This observation is important for the applicability of our model to alloy system for which experimental (or theoretical) values are not available.

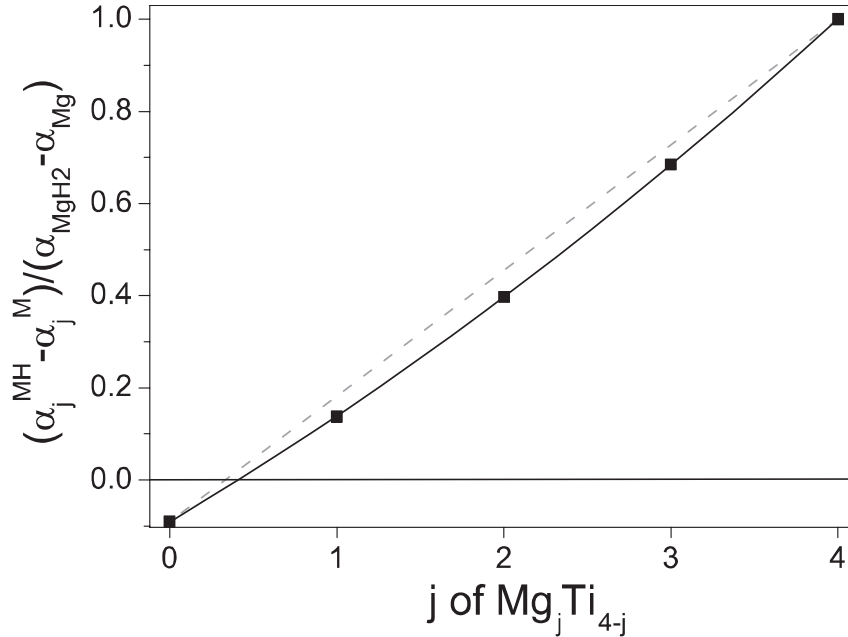


Figure 3.17: *Squares*, normalized absorptions coefficient differences of the Mg_jTi_{4-j} clusters obtained by density functional theory [99] used in the PTI simulations. Dashed line, linear interpolation between the Mg and Ti values. The black line is a guide to the eye.

expansion is assumed for MgH_2 and TiH_2 , respectively [101]. Bulk moduli values for the metals are taken as $B_{Mg} = 35.4$ GPa, $B_{Ti} = 105.1$ GPa [112], and $B_{MgH_2} = 50$ GPa [113], $B_{TiH_2} = 161$ GPa for the hydrides [114].

Figure 3.18a displays a calculated PCI and its corresponding PTI obtained with the multi-site lattice gas model with a realistic set of parameters for a wide range of pressure. In the PCI, the wide distribution of sites energies and site fractions results in a gradual increase of the hydrogen concentration with pressure. In comparison, most of the optical transmission change occurs in a narrower pressure range in the PTI than in the PCI. The high optical absorption coefficient difference of Mg-rich clusters is responsible for this behavior, giving extra weight in transmission to the filling of Mg_4 and Mg_3Ti sites. Similarly, the filling of Ti_4 sites results in an initial decrease of the optical transmission as a consequence of the negative absorption coefficient difference for these sites (See Fig. 3.17). To put in evidence the contribution of the different sites to the isotherms, the derivative of the concentration and of the optical transmission with respect to the logarithm of the pressure are calculated and plotted in Fig. 3.18b). Five peaks corresponding to the five interstitial sites are clearly seen in the derivatives. Due to the predominant Mg fraction ($y = 0.61$) and the positive CSRO parameter ($s = 0.4$) chosen for this example, Mg-rich sites are contributing most. This effect is even more

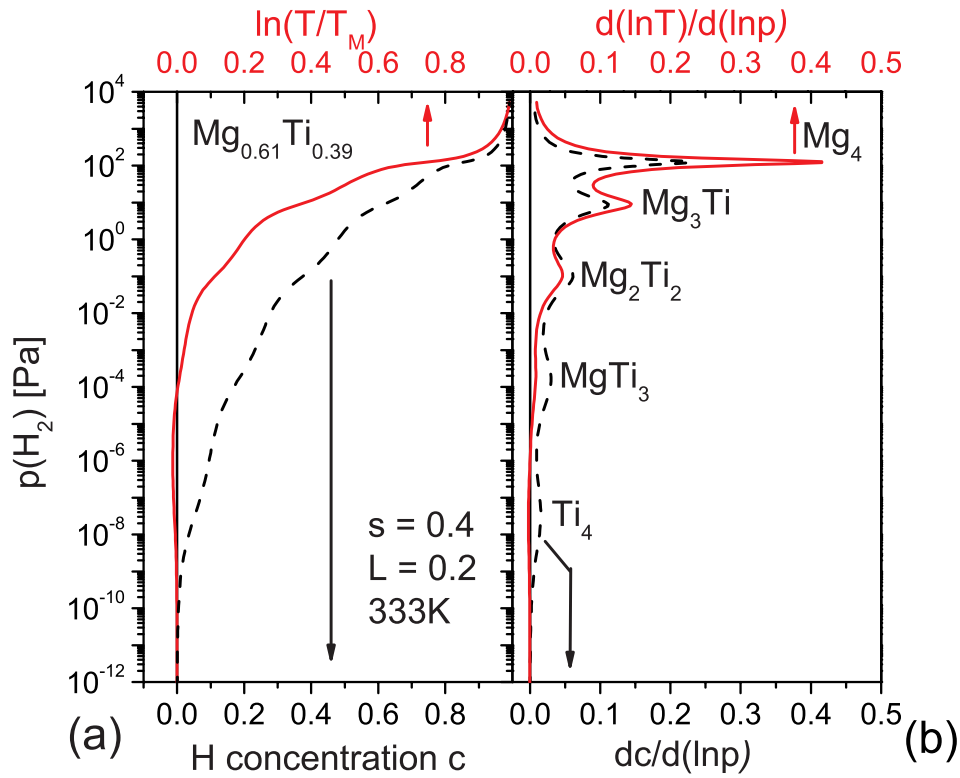


Figure 3.18: (a) Comparison between PCI (dashed line) and PTI (full line) of $\text{Mg}_{0.61}\text{Ti}_{0.39}\text{H}_x$ at $T = 333\text{ K}$ as calculated with the multi-site lattice gas model with $s = 0.4$ and $L = 0.2$ (Model described in Sec. 3.4.4). (b) Derivatives of the H concentration c (dashed line) and of $\ln(T)$ (full line) with respect to $\ln(p)$.

pronounced in the $\ln(T)$ derivative because of the high transparency of MgH_2 (See Sec. 3.4.4).

The comparison between modeled and experimental PTIs for 5 different compositions and 3 different temperatures is shown in Fig. 3.19. The solution

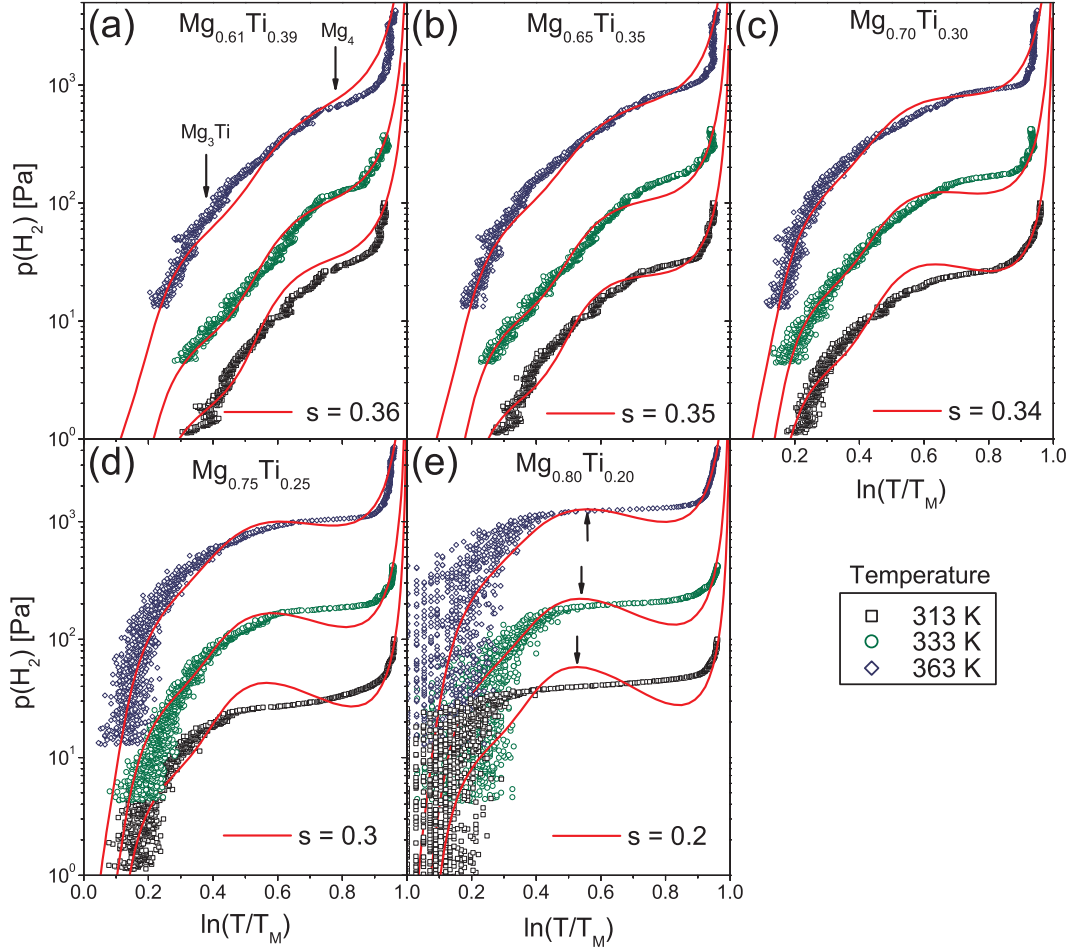


Figure 3.19: *Symbols*, (a)-(e) experimental pressure–optical–transmission–isotherms of $\text{Mg}_y\text{Ti}_{1-y}\text{H}_x$ at temperatures $T = 313, 333$ and 363 K and various Mg fraction y . Lines, Multi-site lattice gas PTI simulations for fixed $L = 0.2$. The chemical short-range order parameter s used for each alloy composition is indicated in the figure. Note that s is independent of temperature. The arrows indicate: in (a), the transmission at which half of the Mg_3Ti and Mg_4 sites are filled, and in (e) the transmission at the first spinodal concentration (See text).

enthalpies for free Mg_4 , respectively Ti_4 clusters are kept constant for all compositions and temperatures at $\Delta H_{\text{Mg}}^0 = -36.6 \text{ kJ}(\text{mol H}_2)^{-1}$ and $\Delta H_{\text{Ti}}^0 = -85.6 \text{ kJ}(\text{mol H}_2)^{-1}$ (See Table 3.3).

From XRD measurements, the average $\text{Mg}_y\text{Ti}_{1-y}\text{H}_x$ lattice is coherent, with no evidence for large-scale phase segregation [38]. Furthermore, since the molar volumes of Mg and TiH_2 are similar, the hydrogenation of Ti-rich

Table 3.3: Input parameters of the multi-site model, valid for all compositions y of $\text{Mg}_y\text{Ti}_{1-y}$ and temperatures. The L parameter is 0.2.

	Molar volume, V (cm^3/mol)	Bulk modulus, B (GPa)	Enthalpy, ΔH^0 ($\text{kJ}(\text{mol H}_2)^{-1}$)
Mg	13.97	35.4 [112]	-36.6
Ti	10.64	105.1 [112]	-86.6
MgH_2	18.44 [101]	50 [113]	
TiH_2	13.30 [101]	162.0 [114]	

sites reduces the differences in volume between clusters and even increases the structural coherence at intermediate hydrogenation stages. The L parameter, that characterizes the local rigidity of embedded clusters with respect to the average lattice, is therefore expected to take a small value: a constant value of $L = 0.2$ gives satisfactory results for all isotherms. The only free parameter for each composition is then the CSRO parameter s .

For every composition $y < 0.85$, there is a well-defined positive short-range order parameter value that reproduces the experimental data well for the 3 temperatures considered. The observed plateau corresponds to the hydrogenation of Mg_4 sites, while the gradual increase of transmission at lower pressure is due to the gradual filling of Ti-containing sites. For high Mg fractions ($y \geq 0.75$), the PTIs are reproduced best if assuming a plateau starting near the spinodal concentration, i.e. near the local maximum in the simulated isotherm (See the *arrows* in Fig. 3.19e). A plateau pressure higher than the one derived using the Maxwell construction is expected in solid-gas systems where the metal-to-hydride transformation generates coherency strain and therefore adds an additional energy barrier for the phase transformation to proceed [115, 116]. The fractions of interstitial sites g_j and the embedded site energies $\Delta H_j^{0,e}$ obtained by modeling as a function of compositions are plotted in Fig. 3.20. The fraction g_4 of Mg_4 interstitial sites is the largest at all concentrations considered, but for Ti-rich compositions, a significant fraction of all other sites is also present.

It is counterintuitive that for a given temperature, the modeled and experimental plateau pressures *increase* with the Mg fraction y . Indeed, as seen in Fig. 3.21, the enthalpy of Mg_4 sites decreases with increasing Mg fraction for any fixed H concentration in the hydride, and the plateau pressure should decrease accordingly. However, due to the changing amount of Ti, the minimum concentration $c_{\min} = 1 - g_4(y)$ at which the Mg_4 site occupation starts is *not* constant. The Mg_4 plateau pressure is thus essentially determined by the enthalpy of Mg_4 sites $\Delta H_4(c_{\min})$ (*stars* in Fig. 3.21), and increases slightly with increasing Mg fraction. This weak dependence of the Mg_4 site enthalpy

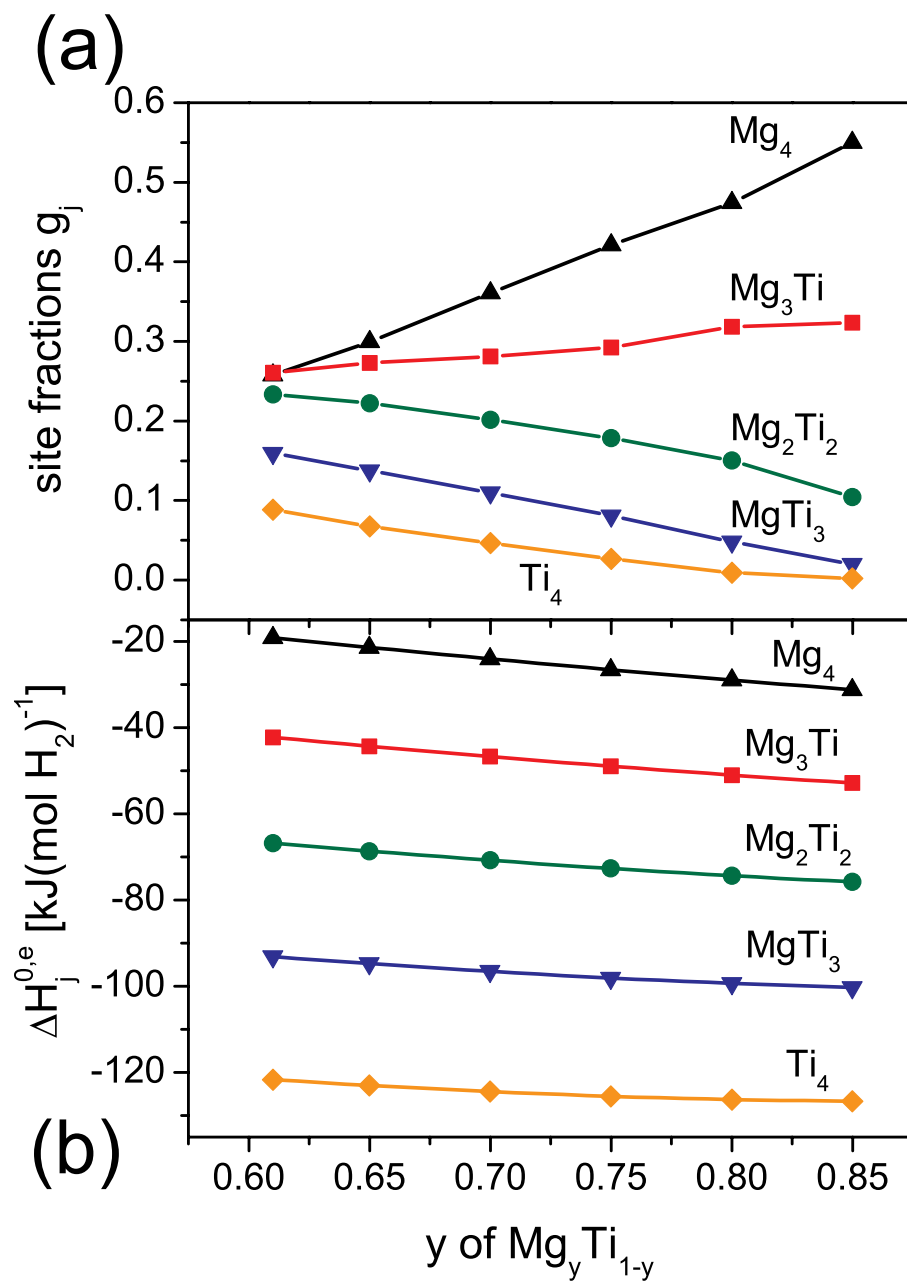


Figure 3.20: Symbols (a) fractions g_j of $\text{Mg}_j\text{Ti}_{4-j}$ sites and (b), enthalpies of solution per site $\Delta H_j^{0,e}$ derived from the experimental PTIs using the multi-site model described in Sec. 3.4.4.

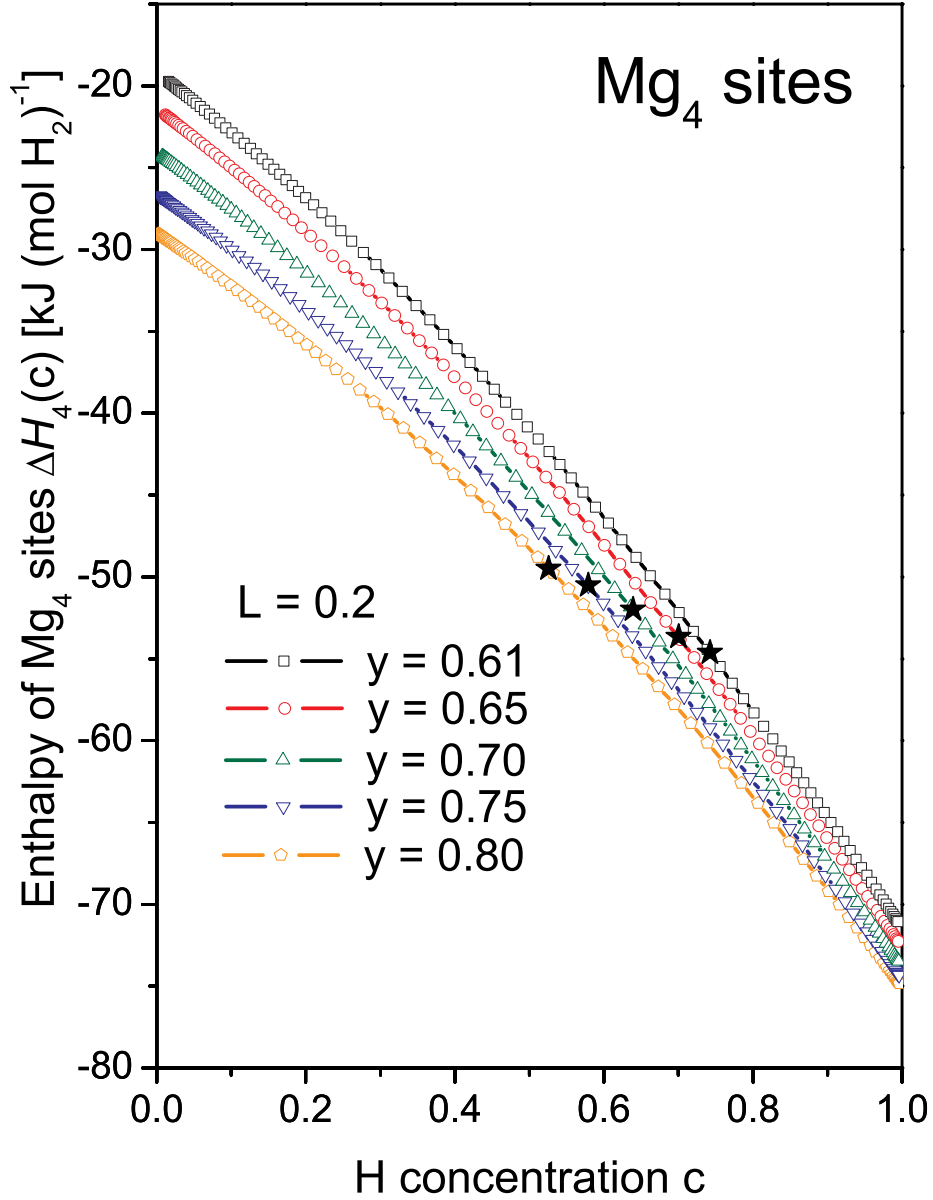


Figure 3.21: Open symbols, enthalpy of the Mg₄ sites $\Delta H_4(c)$ as a function of H concentration c for various Mg fractions y . Filled Stars, enthalpy $\Delta H_4(c_{\min})$ of the Mg₄ sites at the minimum concentration for Mg₄ site occupation c_{\min} as a function of Mg fraction.

on Mg fraction originates from the counteracting effect of the second and third terms in Eq. 3.28: Due to the small size of the Ti atom relatively to Mg, alloying makes the second term positive and reduces the stability of Mg₄ sites towards hydrogen. However, adding Ti also increases c_{\min} , and therefore destabilizes the hydrogenation of Mg₄ sites via a strengthening of the H-H interaction (third term). These theoretical considerations are consistent with our previous experimental work [12], where we concluded from the temperature dependence of the Mg₄ sites plateau pressure that the Mg₄ enthalpy does not depend significantly on Mg_yTi_{1-y} composition.

3.4.6 Discussion

The input energies used in the modeling ($\Delta H_{\text{Mg}}^0 = -36.6 \text{ kJ}(\text{mol H}_2)^{-1}$, $\Delta H_{\text{Ti}}^0 = -85.6 \text{ kJ}(\text{mol H}_2)^{-1}$) are H solution enthalpies and seem at first sight not negative enough. To compare directly the energies used in the modeling with measured hydride (MgH₂ and TiH₂) enthalpies from literature, we need to calculate the enthalpy of an hypothetical material containing only Mg₄ (or Ti₄) sites at half the hydrogen filling ($c = 0.5$). For this we use equation Eq. 3.28 with $y = 1, j = 4$ (Mg₄ sites) and $y = 0, j = 0$ (Ti₄ sites). The obtained enthalpies are $\Delta H_4(0.5) = -52.2 \text{ kJ}(\text{mol H}_2)^{-1}$ and $\Delta H_0(0.5) = -108.6 \text{ kJ}(\text{mol H}_2)^{-1}$ for Mg₄ and Ti₄ sites respectively. These values are $\sim 20 \text{ kJ}(\text{mol H}_2)^{-1}$ less negative than those determined on bulk MgH₂ ($\Delta H = -76 \text{ kJ}(\text{mol H}_2)^{-1}$) and TiH₂ ($\Delta H = -130 \text{ kJ}(\text{mol H}_2)^{-1}$) [101]. Such a discrepancy is not unusual for thin hydride films: Due to the hydrogen-induced lattice expansion, films, that are clamped to the substrate, get strained. Although at high H concentrations dislocations and a complex rearrangement of nanograins reduce clamping effects [117], the remaining compressive strain reduces the hydride stability in a similar way as alloying does in Eq. 3.17. For example, experiments on pure Mg thin films report an enthalpy for hydrogen absorption of $\Delta H = -60.7 \text{ kJ}(\text{mol H}_2)^{-1}$ [118]. Additionally to the clamping to the substrate, the nanostructure of the films can also influence the enthalpy [14].

To show the sensitivity of the model to the L and s parameters, the isotherms of Mg_{0.61}Ti_{0.39} and Mg_{0.75}Ti_{0.25} at temperature $\mathcal{T} = 333 \text{ K}$ are compared with simulations in Fig. 3.22 with the optimal s parameter and varying L values from completely "soft" ($L = 0$) to completely "rigid" clusters ($L = 1$) (Fig. 3.22(a) and (c)) and with a $L = 0.2$, for varying s parameters, from random ($s = 0$) to completely segregated Mg₄H _{x} and Ti₄H _{x} sites ($s = 1$) (Fig. 3.22(b) and (d)).

- For constant s and low L values ($L < 0.4$), the multi-site modeling reproduces the PTIs' shape reasonably well.
- For constant s and high L values, the cluster volume goes towards that of free clusters (See Eq. (3.10)), and the second alloying term in eq. 3.28,

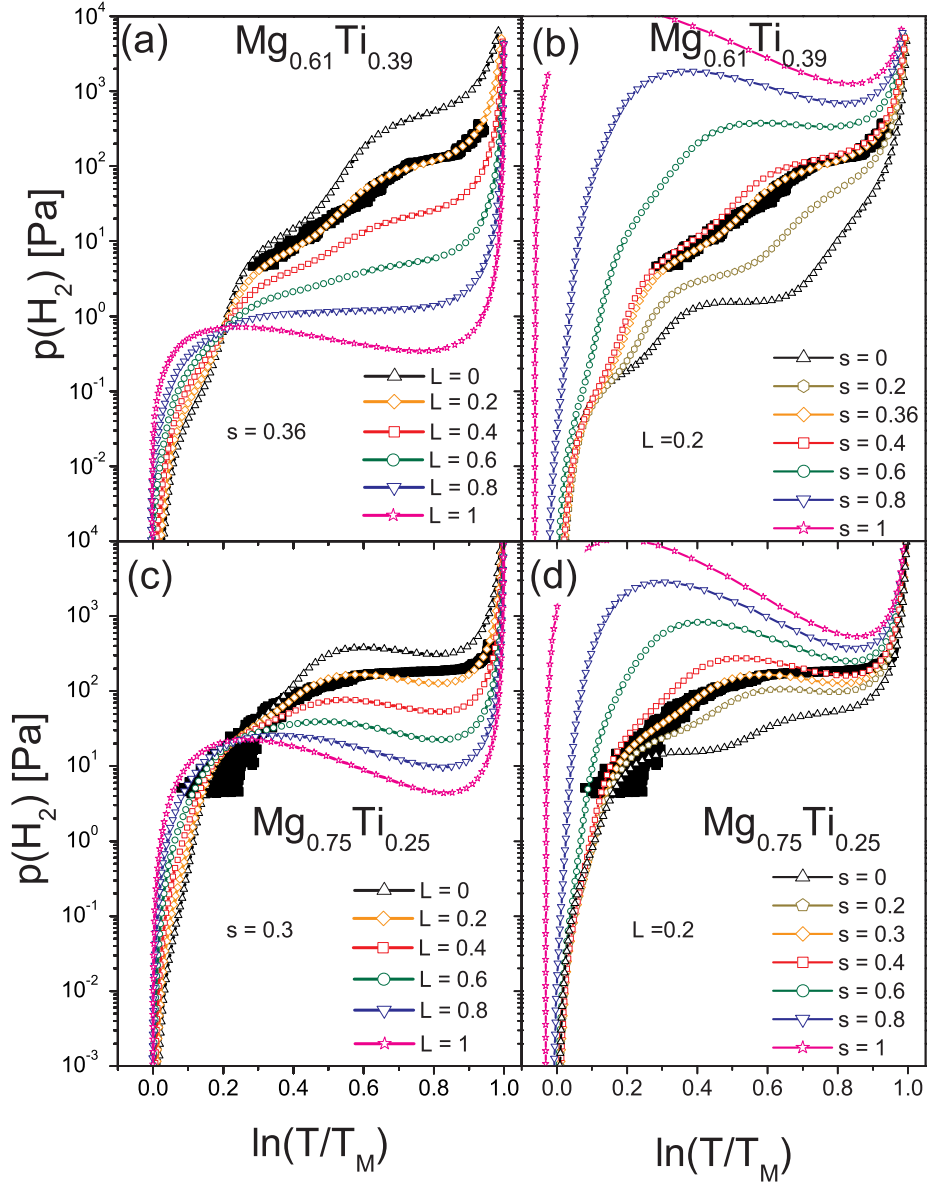


Figure 3.22: Empty symbols, PTI simulations for $\text{Mg}_{0.61}\text{Ti}_{0.39}$ with (a) varying L and $s = 0.36$, (b) $L = 0.2$ and varying s , and for $\text{Mg}_{0.75}\text{Ti}_{0.25}$ with (c) varying L and $s = 0.36$ and (d) $L = 0.2$ and varying s . Filled squares, corresponding experimental pressure-optical-transmission-isotherms at temperature $T = 333$ K. The orange diamond symbols are the best simulations as shown in Fig. 3.19.

that effectively separate the site enthalpies $\Delta H_j^{0,e}$ from each other, goes to zero. Consequently, the $\Delta H_j^{0,e}$ values are too close from each other to be discriminated in the isotherms, which therefore exhibit only one large plateau. The gradual increase of pressure with optical transmission observed experimentally is therefore also not reproduced.

- For constant L and a fully random alloy ($s = 0$), the Mg_3Ti fraction becomes preponderant and, besides the Mg_4 plateau, a second plateau at lower pressures should be seen in the isotherms. This is not the case in the $\text{Mg}_{0.75}\text{Ti}_{0.25}$ isotherm and indicates that some local chemical separation occurs in Mg-Ti.
- For constant L and a fully segregated phases ($s = 1$), in this case, only two types of sites exist: Mg_4 and Ti_4 . The calculated Mg_4 plateau is the only one in the vicinity of the experimental isotherm and cannot reproduce its sloping behavior.

These examples show that modeling PTIs with a simple multi-site lattice gas model is powerful enough to determine s and L parameters and therefore discriminate between different possible microstructures in Mg-Ti-H. A certain degree of chemical segregation ($s > 0$) must be introduced in the simulated isotherms to reproduce the experimental data properly. Moreover, while the material remains X-ray coherent, the non-zero L parameter shows that the volume of interstitial sites still depends on the local chemical composition, and therefore indicates the presence of local lattice size modulations. This is consistent with Michaelsen [81], who showed that coherent inhomogeneities must be larger than several nanometers before they can be detected by conventional XRD.

According to the model, the successive filling of sites with increasing pressure should result in a modulated isotherm slope (See Fig. 3.18b), and not in a gradual decrease of the isotherm slope as observed in the experiments (See all panels of Fig. 3.19). Within the measured pressure range, two interstitial sites, Mg_3Ti and Mg_4 , contribute to the isotherms (See arrows in Fig. 3.19a). Due to stress and/or microstructural defects, these two interstitial sites most probably have a certain energy distribution for H occupation. This leads to a smearing of the isotherms and consequently to a monotonously decreasing isotherm slope.

The values of the CSRO parameter s as a function of composition are summarized in Fig. 3.23, together with s values obtained from Ti K-edge EXAFS measurements [48]. It is remarkable that the values derived from PTI modeling are in such good agreement with those calculated from the first coordination number around Ti atoms determined by EXAFS. In both cases, s is around 0.2 to 0.4 for Mg fraction $0.6 < y < 0.8$, with little variation upon composition. This confirms that a certain degree of chemical segregation does

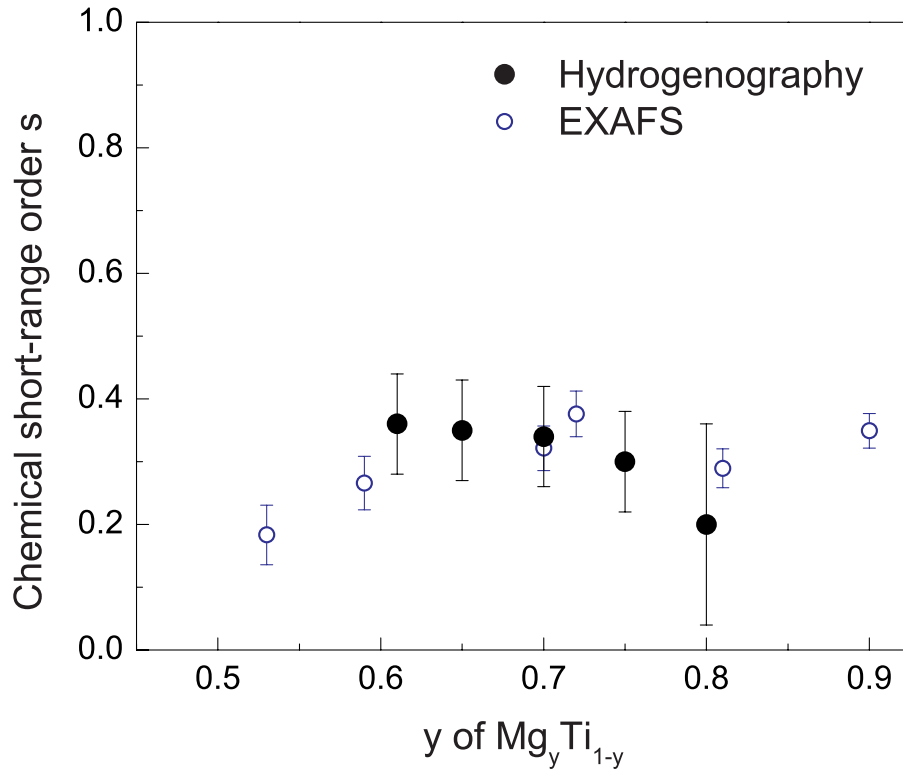


Figure 3.23: Filled circles, Chemical short-range order (CSRO) parameter s for various $\text{Mg}_y\text{Ti}_{1-y}$ compositions derived from hydrogenography data by means of the multi-site model described in Sec. 3.4.4. The increased error bar at $y = 0.80$ originates from a larger error in the metallic state transmission T_M at this composition. Empty circles, CSRO parameters from EXAFS measurements (as-deposited state, data from Baldi *et al.* [48]).

occur in systems with a positive enthalpy of mixing, even if a rapid quenching technique such as sputtering is used.

3.4.7 Conclusions

We use hydrogen as a probe for tracking the degree of chemical segregation in the immiscible $\text{Mg}_y\text{Ti}_{1-y}\text{H}_x$ alloy system through the recording and modeling of pressure–optical-transmission–isotherms. The unusual shape of the experimental PTIs and the plateau pressures at various Mg atomic fractions y and temperatures are well reproduced by the multi-site lattice gas model, assuming the chemical short-range order parameter s as only free varying parameter. We find that the sloping behavior in the isotherms is reproduced assuming the gradual filling with pressure of Ti-containing tetrahedral sites (mainly Mg_3Ti sites in the pressure range measured), while the plateaus are due to the hydrogenation of Mg_4 sites. The CSRO s values derived from the multi-site modeling of hydrogenography data agree well with s values determined from EXAFS measurements. The non-zero L parameter shows that the volume of interstitial sites depends on the local chemical composition, and therefore indicates the presence of local modulations of the crystal lattice size.

The ability to model optical isotherms is a significant step in understanding the hydrogenography results from the microstructural point of view and adds a valuable tool in the combinatorial search for new light-weight hydrogen storage materials. More generally, this multi-site lattice-gas model, by determining two essential characteristics of an alloy microstructure that are the CSRO parameter s and the lattice modulation parameter L , is complementary to experimental local-environment probes such as EXAFS or more elaborate modeling approaches using Reverse Monte Carlo simulation and Molecular Dynamics [44] to characterize alloys created between immiscible elements.

Chapter 4

Mg/Ti multilayers: artificially engineered short-range order

4.1 Introduction

In Chapter 3 we have studied the microstructural origin of the exceptional optical, structural and electrical properties of co-deposited Mg-Ti thin films. These metastable alloys derive much of their appeal from a non-trivial distribution of the Mg and Ti atoms, characterized by a small degree of chemical short-range order. In order to study the effect of short-range order and structural coherence in Mg-Ti thin films we deposited Mg/Ti multilayers with different periodicities. In this way we are able to control the degree of segregation and to study its effects on the structural and hydrogen absorption properties of these thin film alloys. The “period” of a multilayer Λ (often referred to as the bilayer thickness) indicates the thickness of the repeating Mg/Ti unit. In all the 6 samples studied (see Fig. 4.1), the Mg layers are twice as thick as the Ti ones and the total thickness is 60 nm:

$$N \times [\text{Ti}(\frac{20}{N} \text{ nm})\text{Mg}(\frac{40}{N} \text{ nm})]$$

with $N = 40, 20, 10, 5, 2$ and 1 . All the samples are covered with Pd to prevent oxidation and catalyze hydrogen absorption. The metallic samples show partial structural coherence across the Mg/Ti interfaces. Upon exposure to H_2 the multilayers absorb hydrogen in a two step process: first only the Ti layers form the dihydride TiH_2 , while Mg remains in the metallic form; when all the Ti layers are hydrogenated the Mg layers begin to absorb hydrogen themselves. This is reasonable as TiH_2 is much more stable (i.e., has a much lower enthalpy of hydride formation) than MgH_2 and it forms at lower equilibrium hydrogen pressures. The hydrogenation of both Mg and Ti layers induces lattice expansions in the out-of-plane direction much larger than expected for an elastic deformation. In order to justify such a thickness increase we have therefore to assume that material rearrangement and pile-up occurs, leading to reduced coherence at the Mg/Ti interfaces. Upon exposure

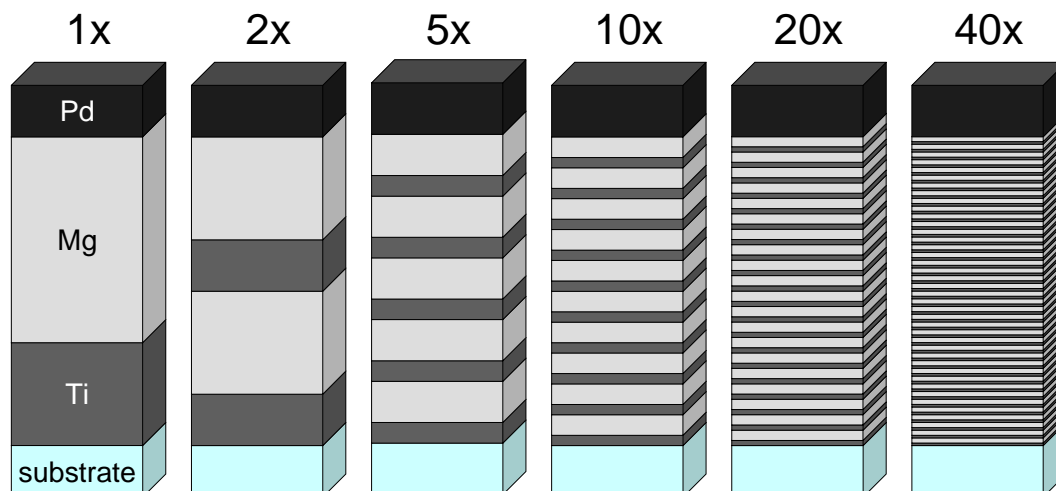


Figure 4.1: Architecture of $N \times [\text{Ti}(\frac{20}{N} \text{ nm})\text{Mg}(\frac{40}{N} \text{ nm})]$ multilayers with different periodicities ($N = 40, 20, 10, 5, 2,$ and 1) and constant total thickness.

to air at room temperature hydrogen desorbs from the Mg layers but it remains trapped in the Ti ones and a complete metallic state is only recovered upon heating in air at 160°C . Both loading and unloading sequences can be qualitatively reproduced by a simple diffusion model for a multilayered system, taking into account only the different thermodynamic properties of the metals in the multilayer. The Pressure–optical Transmission–Isotherms measured by Hydrogenography exhibit interesting features that can be interpreted on the basis of a few assumptions, the discussion of which is given in Chapter 5:

- Mg films capped with Mg-alloy-forming elements (such as Pd and Ni) feel an elastic constraint which leads to higher hydrogen absorption pressure with respect to bulk Mg.
- Mg films “sandwiched” between immiscible elements (such as Ti, Nb and V), thanks to the poor interface adhesion, behave as quasifree and have hydrogen plateau pressures similar to bulk Mg.

Furthermore, the PTIs measured on the Mg/Ti multilayers suggest that, for Mg thicknesses below 10 nm, surface energy effects play a role in destabilizing the formation of MgH_2 .

4.2 Mg/Ti multilayers: structural, optical and hydrogen absorption properties

Abstract – Mg-Ti alloys have uncommon optical and hydrogen absorbing properties, originating from a “spinodal-like” microstructure with a small degree of chemical short-range order in the atoms distribution. In the present study we artificially engineer short-range order by depositing Pd-capped Mg/Ti multilayers with different periodicities and characterize them both structurally and optically. Notwithstanding the large lattice parameter mismatch between Mg and Ti, the as-deposited metallic multilayers show good structural coherence. Upon exposure to H₂ gas a two-step hydrogenation process occurs, with the Ti layers forming the hydride before Mg. From *in-situ* measurements of the bilayer thickness Λ at different hydrogen pressures, we observe large out-of-plane expansions of the Mg and Ti layers upon hydrogenation, indicating strong plastic deformations in the films and a consequent shortening of the coherence length. Upon unloading at room temperature in air, hydrogen atoms remain trapped in the Ti layers due to kinetic constraints. Such loading/unloading sequence can be explained in terms of the different thermodynamic properties of hydrogen in Mg and Ti, as shown by diffusion calculations on a model multilayered systems. Absorption isotherms measured by hydrogenography can be interpreted as a result of the elastic clamping arising from strongly bonded Mg/Pd and broken Mg/Ti interfaces.

This paper is under review: A. Baldi, G. K. Pálsson, M. Gonzalez-Silveira, H. Schreuders, M. Slaman, J. H. Rector, G. Krishnan, B. J. Kooi, G. S. Walker, M. W. Fay, B. Hjörvarsson, R. J. Wijngaarden, B. Dam, and R. Griessen, <http://arxiv.org/abs/0911.5666>

4.2.1 Introduction

Magnesium and titanium are immiscible. Metastable Mg-Ti alloys have nevertheless been successfully prepared in thin films by high energy processes, such as electron beam deposition [35] and magnetron sputtering [21, 119]. These films have gravimetric hydrogen storage capacities up to 6.5 wt% [35] and fast and reversible kinetics of hydrogen absorption and desorption [21]. The structural reversibility of Mg-Ti alloys is particularly surprising when considering the strong segregation occurring in many Mg-based binary systems [19, 43]. Furthermore, when exposed to H₂, Pd-capped Mg-Ti thin films switch from a reflecting metallic state to a black, light-absorbing, hydrogenated state [21]. This reversible optical black state can be applied in hydrogen sensors [23] and smart absorbers for solar collectors [21, 22]. As also suggested by first principle calculations [99], the black appearance of the hydride is due to the formation of a face-centered-cubic phase, in which Mg and Ti atoms are distributed among the lattice sites with a certain degree of chemical short-range order [50, 48], leading to the coexistence of Mg-rich and Ti-rich regions with structurally coherent boundaries. Such “spinodal-like” microstructure is not uncommon in immiscible binary alloys [44, 70] and it is a key ingredient in understanding the exceptional reversibility of Mg-Ti thin films [38, 48]. In order to achieve a deeper understanding of the role of chemical segregation on the structural, optical and hydrogen absorbing properties of these systems, we engineered one dimensional short-range order by depositing several Mg/Ti multilayers with different periodicities. By means of optical and structural studies we are able to reconstruct the hydrogen loading sequence, measure the out-of-plane expansion of the individual layers and detect the breaking of structural coherence occurring at the Mg/Ti interfaces upon formation of TiH₂. Such removal of coherence is responsible for the “scissor” effect observed in Ti-sandwiched Mg thin films [53]: when a thin Mg film is sandwiched between Ti layers it absorbs hydrogen at pressures close to bulk Mg, effectively behaving as quasifree. This is due to the fact that Mg and Ti, thanks to their positive enthalpy of mixing, form interfaces with poor adhesion, which become even more disconnected when Ti expands upon hydrogen absorption. On the contrary, in Mg films capped with Pd, alloying occurs at the Mg/Pd interface and Mg feels an elastic constraint due to the presence of the cap layer that leads to higher equilibrium pressures of hydrogen absorption [52].

4.2.2 Experimental details

Mg/Ti multilayers covered with Pd are deposited in a ultra-high vacuum (UHV) compatible system (base pressure = 10⁻⁶ Pa) equipped with a computer controlled shutter system, by DC and RF magnetron sputtering of Mg (99.95%), Ti (99.999%) and Pd (99.98%) targets in 0.3 Pa of Ar, on substrates kept at room temperature. The substrates used are 10x10x1 mm polished

single-crystal Si(100) for XRD, XRR and HRTEM, silicon nitride membranes for in-plane TEM, 20x10x1 mm quartz for optical spectroscopy and 10x10x0.5 mm float glass for hydrogenography measurements. In order to obtain homogeneous films the substrates are continuously rotated during sputtering. The films are covered with Pd to prevent oxidation and promote hydrogen dissociation and absorption. The Pd thickness varies between 1 and 10 nm depending on the experimental technique used to analyze the samples. Typical deposition rates are 0.22 nm/s for Mg at 150 W (RF), 0.08 nm/s for Ti at 200 W (DC) and 0.11 nm/s for Pd at 50 W (DC). In each Mg/Ti sample the Mg layers are twice as thick as the Ti ones, giving, after correcting for the molar volumes ($\bar{V}_{\text{Mg}} = 13.97 \text{ cm}^3/\text{mol}$, $\bar{V}_{\text{Ti}} = 10.64 \text{ cm}^3/\text{mol}$), an overall composition of $\text{Mg}_{0.60}\text{Ti}_{0.40}$. The total multilayer thickness is 60 nm with 6 different bi-layer thicknesses Λ , ranging from 1.5 to 60 nm: $N \times [\text{Ti}(\frac{20}{N} \text{ nm})\text{Mg}(\frac{40}{N} \text{ nm})]$, with $N = 40, 20, 10, 5, 2$ and 1. These samples characteristics allow us to have fast and comparable kinetics of hydrogen absorption and desorption in all the multilayers. A sketch of the samples geometry is shown in Fig. 4.2.

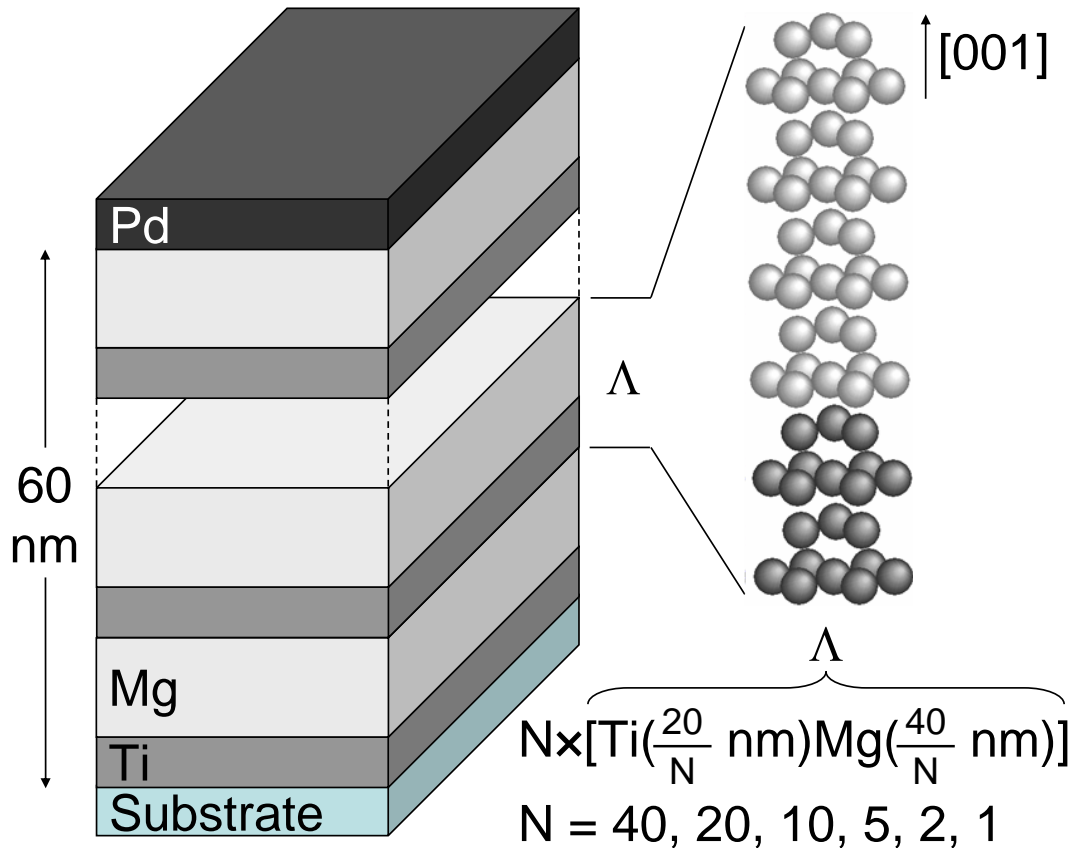


Figure 4.2: Sample geometry. The total multilayers thickness is 60 nm and, in every sample, Mg layers are twice as thick as Ti ones: $N \times [\text{Ti}(\frac{20}{N} \text{ nm})\text{Mg}(\frac{40}{N} \text{ nm})]$, with $N = 40, 20, 10, 5, 2$ and 1.

XRD patterns are measured in a $\theta - 2\theta$ configuration, with a Bruker D8 Discover diffractometer equipped with a two-dimensional detector for real-time data collection over a large area with high sensitivity and low background. A beryllium dome allows *in-situ* diffraction measurements during hydrogenation/dehydrogenation of the films in hydrogen pressures up to 10^5 Pa and temperatures between room temperature and 473 K.

XRR measurements are performed on the 10x sample in a specially designed UHV chamber mounted on a Bruker Discover D8 X-ray diffractometer equipped with a parallel X-ray beam ($\text{CuK}\alpha_1$ $\lambda = 0.15406$ nm), that allows *in-situ* hydrogen loading in a wide range of temperatures and pressures [120]. The sample is measured at 333 K both in the as-deposited metallic state and during hydrogen uptake at different H_2 pressures. The temperature is high enough to promote fast kinetics of hydrogen absorption but low enough to avoid severe alloying at the Mg/Pd interface. In-plane resistance measurements are used to determine whether the dissolved hydrogen is in equilibrium with the surrounding H_2 atmosphere.

HRTEM was performed on a JEOL 2100F FEG-TEM, equipped with Digital STEM, Gatan Orius imaging system, and Gatan DigiScan. Cross section samples were prepared by ion beam milling using an FEI Quanta 200 ED FIB-SEM and transferred to the TEM using a Gatan HHST 4004 environmental cell and vacuum transfer holder to minimise oxidation.

Hydrogen loading isotherms are measured at 333 K by means of Hydrogenography [12], an optical technique that allows to detect the amount of light transmitted through a thin film, while slowly increasing the hydrogen pressure at constant temperature. The Pressure-Optical transmission-Isotherms (PTIs) obtained by hydrogenography can be directly related to the standard Pressure-Composition-Isotherms (PCIs) measured for metal hydrides [13]. Details of the hydrogenography experimental setup can be found in Gremaud *et al.* [12].

Optical spectra are measured with a Perkin Elmer Lambda 900 diffraction grating spectrometer ($0.5 < \hbar\omega < 6.5$ eV). Reflection and transmission spectra of the as-deposited and hydrogenated films are measured through the transparent quartz substrate at 333 K in vacuum and in 10^5 Pa H_2 , respectively.

4.2.3 Results and discussion

Structural characterization: XRD, XRR and TEM

As-deposited multilayers The uncorrected diffraction patterns measured for the as-deposited samples in vacuum at room temperature are shown in Fig. 4.3. Both Mg and Ti have hexagonal-closed-packed structures in their elemental form and, as will be shown below, the Mg/Ti multilayers grow with the (001) plane parallel to the substrate surface. For the 1x sample the Ti and Mg layers are thick enough to give the reflections of pure elements, while

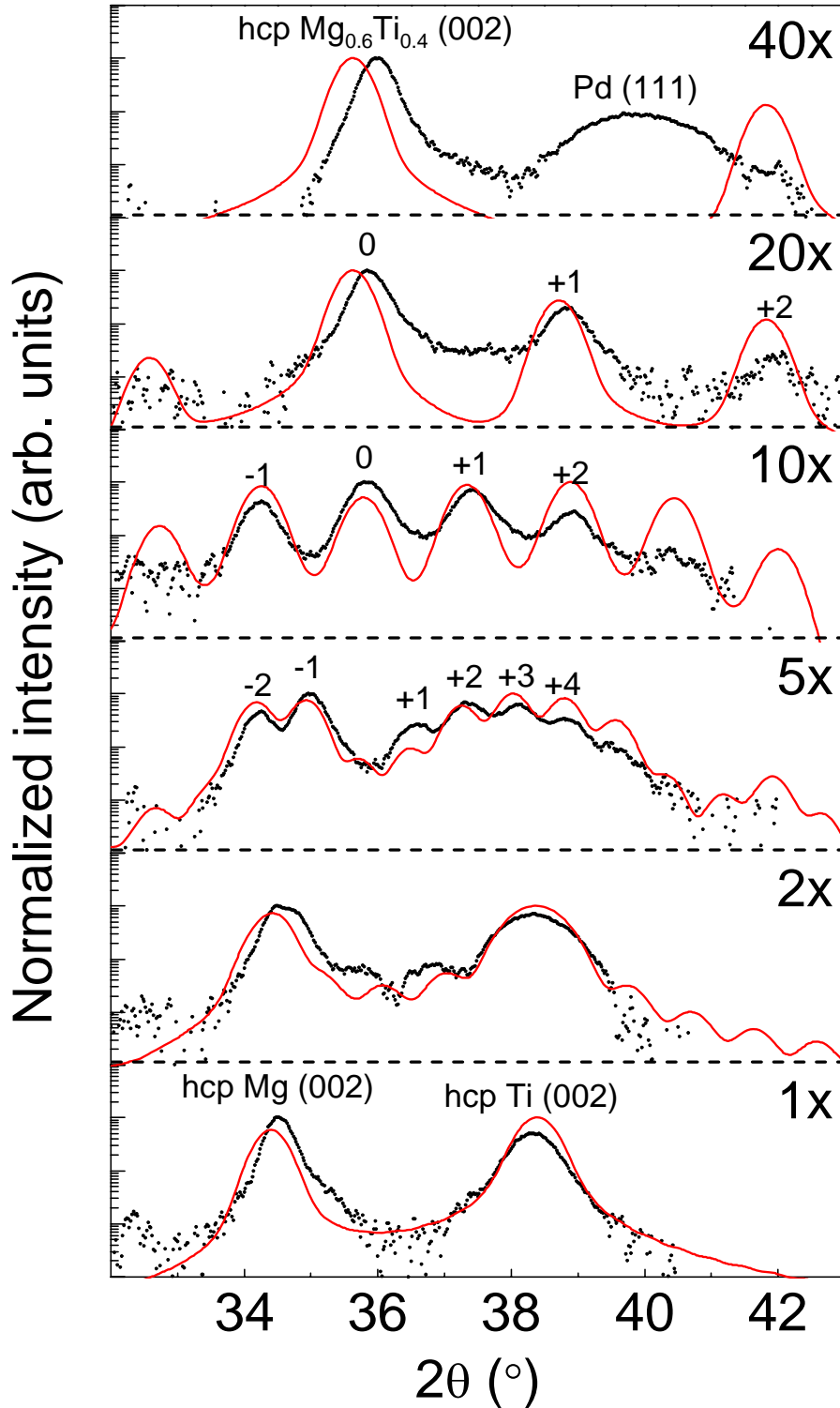


Figure 4.3: Measured (dots) and simulated (lines) XRD patterns of $N_x[\text{Ti}(\frac{20}{N} \text{ nm})\text{Mg}(\frac{40}{N} \text{ nm})]$ multilayers with $N = 40, 20, 10, 5, 2$ and 1 , covered with 5 nm of Pd. The simulations are based on idealized step model, not capturing the influence of defects and other imperfections.

already for the 5x sample superlattice peaks (satellite peaks) begin to appear, due to the repetitions of the bi-layer thickness Λ . The broad peak appearing at $\sim 40^\circ$ for the 40x sample is the (111) reflection from the face-centered cubic Pd. The absence of any Pd reflection in the patterns of the other multilayers is not surprising when considering that Pd is deposited on top of the uppermost Mg layer. Pd deposited on $\text{Mg}_y\text{Ti}_{1-y}$ thin films, in fact, does not produce any diffraction signal for $y > 0.9$, although its presence is confirmed by Rutherford Backscattering Spectrometry (RBS) [38]. This peak disappearance is most likely due to the increase in lattice mismatch between Pd and $\text{Mg}_y\text{Ti}_{1-y}$ with increasing magnesium content, suggesting that for the 40x sample the Ti and Mg layers are thin enough to undergo lattice deformations similar to the ones expected in a $\text{Mg}_{0.6}\text{Ti}_{0.4}$ alloy. In Fig. 4.3 we also show the simulated patterns obtained with an ideal step model, which assumes perfect superlattices with a square-wave composition modulation along the growth direction, and coherent Mg/Ti interfaces [121, 81]. In the model the diffracted intensity I is given by:

$$I = I_N (I_{\text{Mg}} + I_{\text{Ti}} + I_{\text{MgTi}}) \quad (4.1)$$

where I_N is a term due to the N bilayer repetitions in the multilayers, I_{Mg} and I_{Ti} are the intensities of the constituent materials and I_{MgTi} is a mixed term arising from the structural coherence [81]. In incoherent multilayers the mixed term disappears leading to a different distribution of intensities in the satellite peaks. The scattering powers of the elements are approximated with their atomic numbers and the patterns are filtered with a Gaussian distribution, with a full width at half maximum (fwhm) of 0.47° , to take into account the instrumental broadening and the possible deviations from a perfect geometry. These deviations include random variations in the number of atomic layers, interface roughness or interdiffusion, variations in the lattice spacings due to in-plane elastic coherency strain, distribution of sizes in in-plane grains and random orientations of the growth direction of each grain. Several models have been developed to include corrections to the ideal step model and take into account deviations from a perfect geometry [121, 122]. In our XRD measurements, however, the experimental broadening is very high, of the order of 0.3° , due to the use of a two-dimensional detector that has a finite grid and requires a rather large beam spot on the sample in order to produce a high signal-to-noise ratio. Such a large experimental broadening hinders any attempt to obtain more detailed informations from the XRD patterns. Nevertheless, the simulations shown in Fig. 4.3 qualitatively reproduce all the features observed experimentally, showing that upon deposition Mg and Ti form well defined layers with partially coherent interfaces. The structural coherence in Mg/Ti multilayers is rather surprising given the 8.7% lattice mismatch between the in-plane cell parameter of Mg ($a_{\text{hcp}} = 0.3209$ nm) and Ti ($a_{\text{hcp}} = 0.2951$ nm). The rocking curve measured over the fundamental peak ($s = 0$) of the 10x sample has a fwhm of 5.7° , indicating a moderately textured multilayer.

For a multilayer the Bragg law can be written as [120]:

$$\frac{\sin \theta_s}{\lambda_{\text{CuK}\alpha_1}} = \frac{1}{2d_{\text{Mg/Ti}}} \pm \frac{s}{2\Lambda} \quad (4.2)$$

where s is the index of the satellite peak with respect to the fundamental peak ($s = 0$), as shown for samples 20x, 10x and 5x in Fig. 4.3, $d_{\text{Mg/Ti}}$ is the average interplanar distance of a Mg/Ti bilayer and Λ is the bilayer thickness. In Fig. 4.4 we plot the ratio $\sin \theta_s / \lambda_{\text{CuK}\alpha_1}$ versus s , for the satellite peaks of the 20x, 10x and 5x samples. Using Eq. 4.2, from the fitted slopes, S , and intercepts, I ,

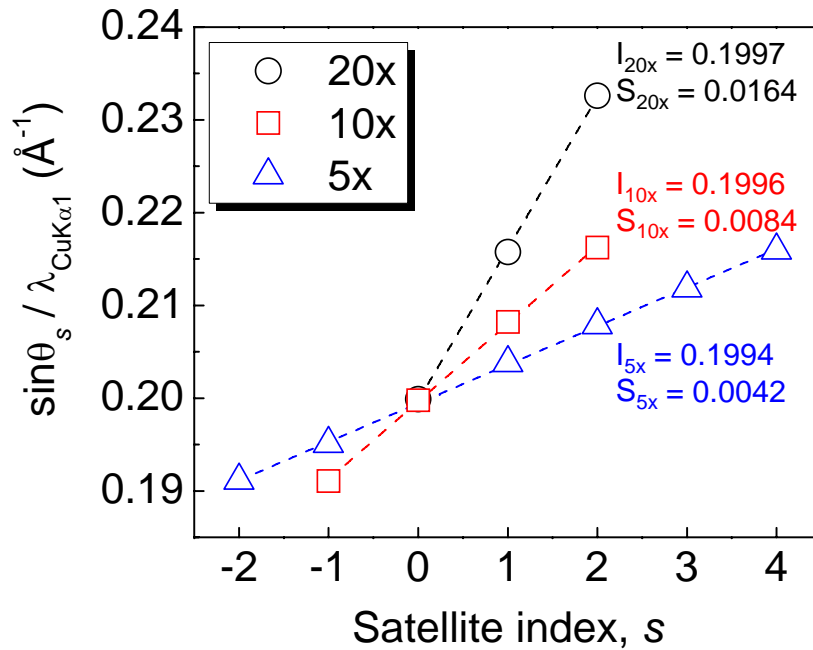


Figure 4.4: Measured linear dependence of the ratio $\sin \theta_s / \lambda_{\text{CuK}\alpha_1}$ on the satellite index s for the 20x (circles), 10x (squares) and 5x (triangles) samples as indicated in Fig. 4.3. The dashed lines are linear fits to the data with slopes S and intercepts I .

I , we obtain the bilayer thicknesses Λ and the average interplanar distance $d_{\text{Mg/Ti}}$, see Table 4.1. The excellent agreement between experiment and model indicates that the textured regions of our Mg/Ti multilayers correspond closely to their ideal geometries.

A rough estimate of the average coherence length ξ , defined as the distance over which the atomic positions are quantitatively correlated [122], can be obtained with Scherrer's formula: $\xi = (K \cdot \lambda_{\text{CuK}\alpha_1}) / (\beta \cdot \cos \theta)$, where K is the shape factor (K ranging between 0.9 and 1, depending on the grains shape) and β is the fwhm expressed in radians. For the fundamental peak ($s = 0$) of the 10x sample we have $\beta \approx 0.5^\circ = 8.7 \cdot 10^{-3}$ rad and $\theta = 17.92^\circ$, corresponding to a coherence length $\xi \approx 17$ nm, assuming spherical grains. Given the very high

Table 4.1: Comparison between the experimental and nominal values for the bilayer thickness Λ and the average interplanar distance $d_{\text{Mg/Ti}}$ obtained from eq. 4.2 for samples 20x, 10x and 5x.

Sample	$\Lambda(\text{nom})$ nm	$\Lambda(\text{exp})$ nm	$d_{\text{Mg/Ti}}(\text{nom})$ nm	$d_{\text{Mg/Ti}}(\text{exp})$ nm
20x	3.0	3.0	0.2518	0.2504
10x	6.0	6.0	0.2518	0.2505
5x	12.0	11.9	0.2518	0.2508

experimental broadening in our XRD measurements, this value has to be taken only as a lower limit. Considering that for the 10x sample the bilayer thickness is $\Lambda = 6$ nm we conclude that, in the textured regions of the multilayer, the crystal registry is maintained at least for few Mg/Ti bilayer repetitions and that the Mg/Ti interfaces are therefore partially coherent, as already suggested by the comparison between experimental and simulated XRD patterns (Fig. 4.3).

The 10x sample, 10x[Ti(2 nm)Mg(4 nm)], has been explored in more detail by means of *in-situ* X-Ray Reflectivity at different hydrogen pressures. The XRR measurement of the as-deposited state of sample 10x, covered with 10 nm of Pd, is shown in Fig. 4.5a: the measurement is conducted in vacuum (base pressure = 10^{-7} Pa) at 333 K and the sample is deposited on a Si substrate with (100) orientation. From the satellite peaks positions in the XRD pattern measured at high angles on a sample deposited in the same run (inset in Fig. 4.5a) we obtain $\Lambda = 5.63$ nm and $d_{\text{Mg/Ti}} = 0.2500$ nm. The XRR curve is simulated with GenX [123] using the model in Fig. 4.2 to obtain the individual thicknesses of the constituent layers and the roughnesses at the interfaces. The software uses a dynamic optical model that incorporates effects arising from refraction, x-ray absorption, multiple scattering, instrumental resolution and instrumental geometry. In the fit all the layer thicknesses and the interface roughnesses are varied. A layer of 1.7 nm of SiO₂ is added to the simulation on top of the Si (100) substrate to take into account the substrate surface oxidation. The results for the as-deposited state of sample 10x are summarized in the third column of Table 4.2. The agreement between the Λ values obtained from the satellite peaks position and from the simulation of the XRR pattern is excellent. The layers are flat with interface roughnesses of the order of one unit cell (assuming hcp Mg with $c = 0.521$ nm and hcp Ti with $c = 0.469$ nm). Fig. 4.5b shows the real part of the Scattering Length Density (SLD) profile corresponding to the simulation in Fig. 4.5a. The SLD, which is given by the mass density profile times the scattering lengths of the elements, gives an idea of the deviations from a perfect square-wave model that we have to introduce in the simulation, in order to accurately reproduce the experimental

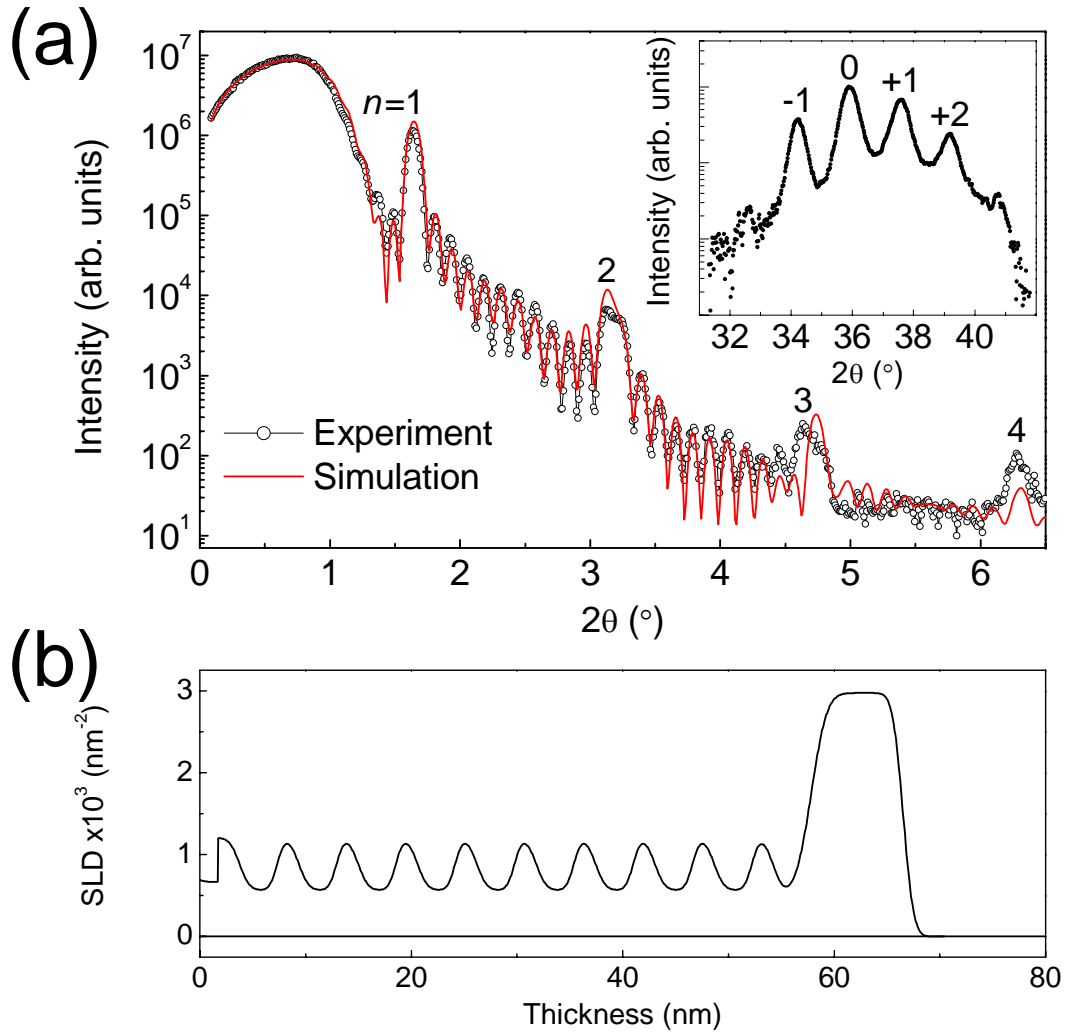


Figure 4.5: (a) X-Ray Reflectivity pattern of the 10x sample, $10x[\text{Ti}(2 \text{ nm})\text{Mg}(4 \text{ nm})]\text{Pd}(10 \text{ nm})$, taken at 333 K in vacuum (base pressure = 10^{-7} Pa). The red solid line is a simulation of the multilayer using GenX [123]. The inset shows the XRD pattern measured at high angles on a 10x sample deposited in the same run. (b) Real part of the Scattering Length Density (SLD) profile corresponding to the simulation in Fig. 4.5a.

Table 4.2: Nominal and measured structural parameters of the 10x sample, 10x[Ti(2 nm)Mg(4 nm)]Pd(10 nm), as obtained from fitting the XRR patterns measured in vacuum (as-deposited) and in 10^3 Pa of H_2 (fully hydrogenated): bi-layer thickness Λ , layers thickness d and roughness σ .

	Nominal nm	XRR (vacuum) nm	XRR ($p_{H_2} = 10^3$ Pa) nm
Λ	6	5.6	6.9
d_{SiO_2}	–	1.7	2.0
d_{Ti}	2	2.0	2.3
d_{Mg}	4	3.6	4.6
d_{Pd}	10	8.7	8.7
$\sigma_{Ti/Mg}$	0	0.74	1.0
$\sigma_{Mg/Ti}$	0	0.55	1.2
$\sigma_{Mg/Pd}$	0	1.2	1.3
$\sigma_{Pd/vacuum}$	0	0.78	1.1

measurement.

Another method to determine the bilayer thickness Λ , in the limit of a kinematic approximation, is by looking at the position of the reflectivity peaks at low angles. We have [124]:

$$\sin^2 \theta_n = \left(\frac{\lambda_{CuK\alpha_1}}{2\Lambda} \right)^2 n^2 + 2\delta \quad (4.3)$$

where n is the order of the reflectivity peaks, as shown in Fig. 4.5a, and δ is the deviation from unity of the real part of the average refractive index and, in first approximation, can be neglected [122, 120]. From a linear fit of the plot $\sin^2 \theta_n / \lambda_{CuK\alpha_1}^2$ versus n^2 we calculate $\Lambda = 5.64$ nm, in agreement with the values obtained both from the XRR simulation and from the satellite peak positions in the XRD pattern.

In Fig. 4.6a we show the cross-section bright-field Scanning Transmission Electron Microscopy (STEM) image of a 20x[Ti(2 nm)Mg(4 nm)] multilayer, deposited on a Si(100) substrate and covered with 10 nm of Pd. The sample is well layered with slightly wavy Mg/Ti interfaces. Due to cumulative roughness, only 16 out of 20 bilayer repetitions are visible. Figure 4.6b shows the intensity profile of the area delimited by the white dashed line in Fig. 4.6a. The maxima in the profile correspond to the bright Mg layers, except for the first peak on the bottom, which is attributed to the SiO_2 film covering the Si substrate. The effect of cumulative roughness is clearly visible in the intensity profile, where the peak-to-valley ratio decreases with increasing film thickness. Note that the sample measured in TEM is twice as thick as all the other investigated samples, in which the cumulative roughness effect is therefore going to be much

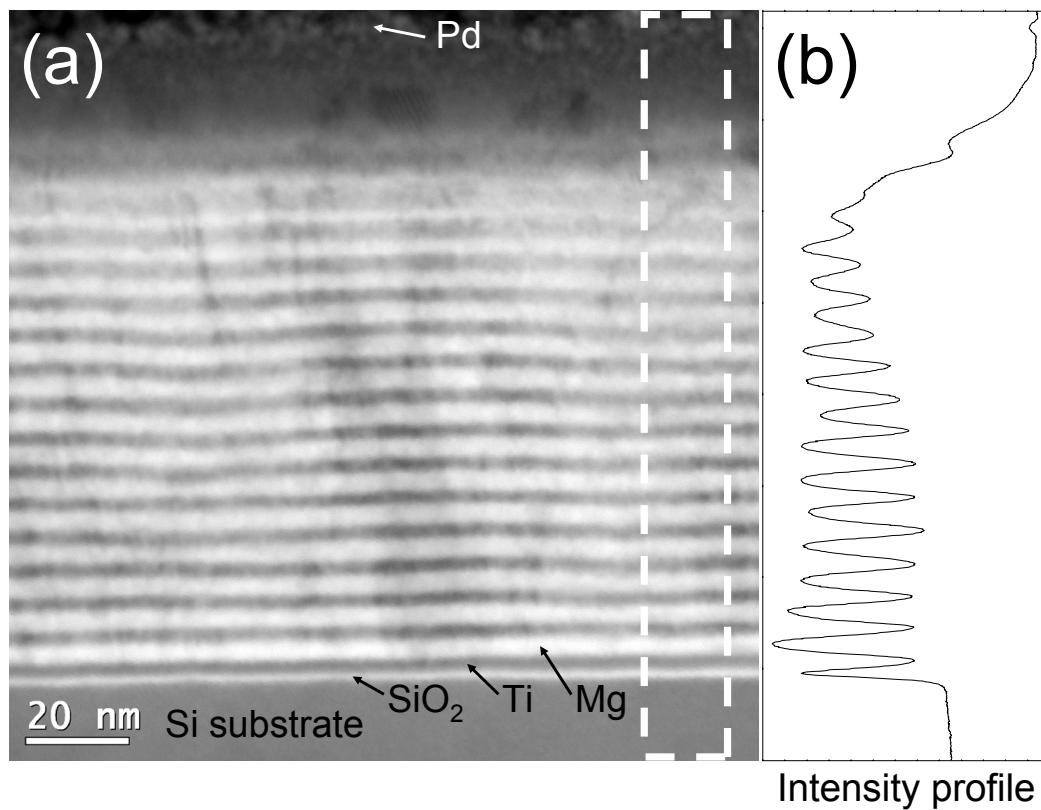


Figure 4.6: (a) Cross-section bright-field STEM image of a $20\times[\text{Ti}(2\text{ nm})\text{Mg}(4\text{ nm})]$ multilayer deposited on a Si(100) substrate and covered with 10 nm of Pd. (b) Intensity profile of the area delimited by a white dashed line. The maxima correspond to the Mg bright layers, except for the first (bottom) peak, which is attributed to SiO₂ at the substrate/film interface.

smaller. Figure 4.7a shows a cross-section image of the same sample, in which it is clearly visible how the film is partially crystalline, with grains extending for several Mg/Ti repetitions, as already suggested by X-Ray Diffraction results. Figures 4.7b and 4.7c show a High Resolution TEM (HRTEM) image of the $20\times[\text{Ti}(2\text{ nm})\text{Mg}(4\text{ nm})]$ multilayer and its Fourier transform, respectively. As expected, the multilayer has hexagonal closed-packed structure and grows along to the [001] direction. Although a slight decrease in crystallinity is observed with increasing thickness (not shown here), the crystal structure and orientation shown in Figure 4.7b are visible across the multilayer from the substrate up to the Pd cap.

Hydrogen loading When exposed to H_2 gas at room temperature, the Pd-capped Mg/Ti multilayers hydrogenate in two consecutive steps: (i) at lower H_2 pressures only the Ti layers form a hydride while Mg remains in its metallic state, (ii) at higher H_2 pressures also Mg absorbs hydrogen forming MgH_2 . Such loading sequence is due to the lower (more negative) enthalpy of hydride formation of TiH_2 ($-65\text{ kJ}(\text{mol H})^{-1}$) [101] with respect to MgH_2 ($-37.2\text{ kJ}(\text{mol H})^{-1}$) [125] and can be detected from XRD, XRR and optical spectroscopy measurements.

Figure 4.8 exhibits the XRD patterns measured during loading and unloading of sample 10x. Upon loading the sample is exposed to 1 bar H_2 pressure at room temperature. The loading sequence shows an intermediate step in which only one peak is visible. This intermediate peak is similar to what is expected for a perfect hcp-(002) Mg / fcc-(111) TiH_2 multilayer, (dashed lines in Fig. 4.8), although it is shifted to slightly lower angles, suggesting that Mg layers might also be partially hydrogenated. The final hydrogenated state shows poor crystallinity with a broad reflection at $2\theta \approx 34^\circ$. When unloading the multilayer in air at room temperature the intermediate peak is recovered, suggesting that, due to kinetic limitations, hydrogen does not desorb from the Ti layers in the sample. In order to recover the initial metallic state the sample has to be heated in air at 433 K. Although the satellite peaks in the final de-hydrogenated state are broader than in the as-deposited initial sample, it is remarkable that crystallinity appears again, after the large changes in volume upon hydrogenation and dehydrogenation of the Mg and Ti layers.

An intermediate state, similar to the one observed upon desorption in air at room temperature for the 10x sample, corresponding to a hcp-(002) Mg / fcc-(111) TiH_2 multilayer, is obtained for the desorbed state of all the multilayers explored in the present work, Fig. 4.9. The lines are simulations based on the ideal step model, in which we assume that the samples have an ideal geometry and that only the Ti layers are hydrogenated. The agreement between measured and simulated patterns is good. Significant discrepancies in the peaks positions only occur for the 20x and 40x samples, for which the measured peak lies at higher angles with respect to the simulated one, indicating

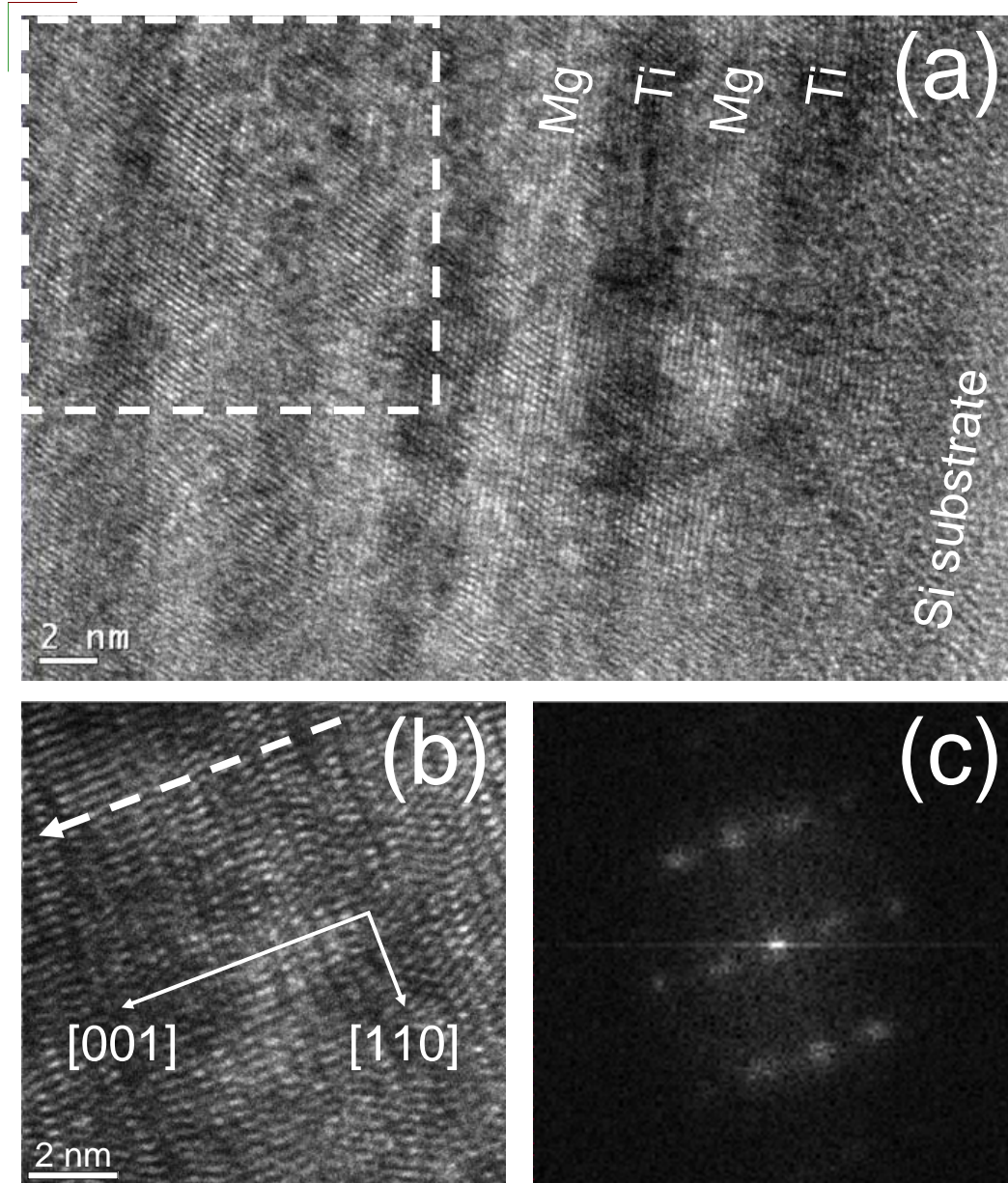


Figure 4.7: (a) Cross-section TEM image of the 20x sample shown in Fig. 4.6. The dashed area highlights a region in which structural coherence is maintained across multiple Mg/Ti interfaces. (b) HRTEM image of sample 20x, taken approximately in the middle of the multilayer. The dashed arrow, parallel to the [001] direction of the hcp structure, indicates the growth direction of the multilayer. (c) Fourier transform of Fig. 4.7b.

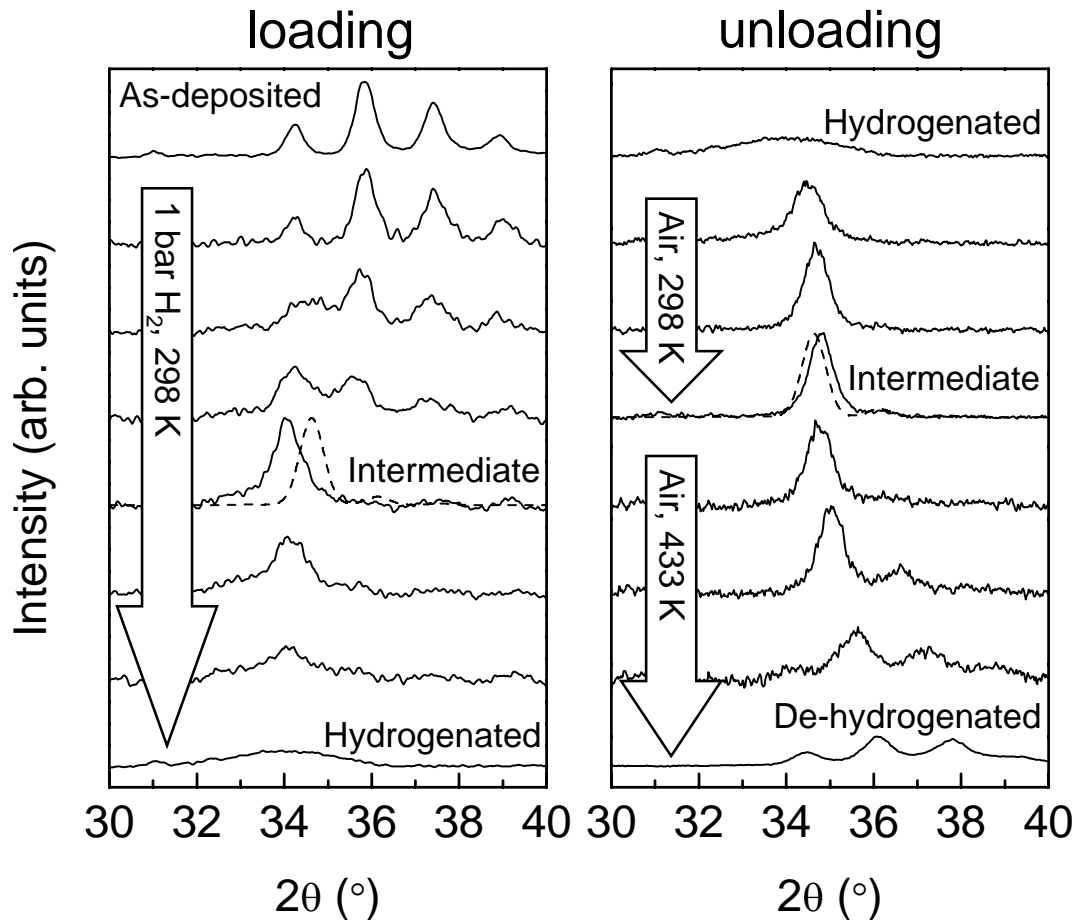


Figure 4.8: XRD patterns measured during loading (left) and unloading (right) of the 10x sample, 10x[Ti(2 nm)Mg(4 nm)]Pd(10 nm). The intensities are normalized by the measuring time. The dashed lines are simulations of a perfect hcp-(002) Mg / fcc-(111) TiH₂ 10x multilayer.

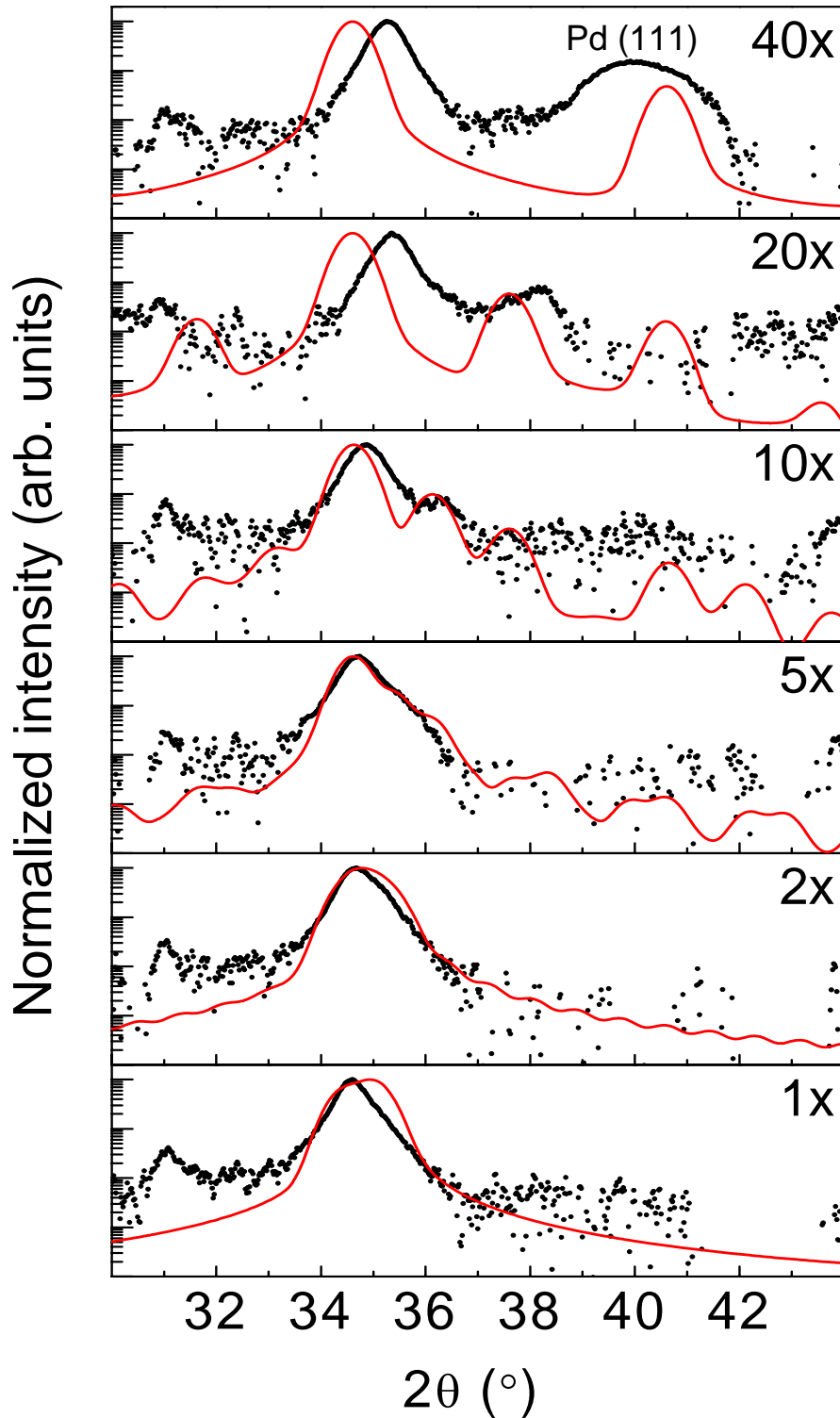


Figure 4.9: Measured (dots) and simulated (lines) XRD patterns for the partially desorbed, “intermediate” states of the samples described in the present work. The simulations assume samples geometries identical to the original multilayers but with fcc-(111) TiH_2 instead of hcp-(002) Ti.

that partial release of hydrogen has already occurred from the Ti layers. This is not surprising as the 20x and 40x samples have Ti layers as thin as 1 and 0.5 nm, respectively. In the simulations of Fig. 4.9 the gaussian distribution fwhm is increased to 0.6° to account for reduced crystallite size. Significantly, while the fwhm value reproduces well the width of the fundamental peak for the 40x, 20x, 10x and 5x Mg/TiH₂ multilayers, it is too high for the 2x and 1x samples. In the latter the coherence length must therefore be larger, thanks to the reduced amount of Mg/Ti interfaces.

The intermediate state, characterized by the loading of the Ti layers only, has been explored in detail by measuring XRR on a 10x sample exposed to ~ 6 Pa of hydrogen at 333 K. Such a low pressure is enough to induce hydrogen absorption in Ti but not in Mg. Figure 4.10 shows the change in electrical resistance occurring upon loading of the 10x sample in the *in-situ* XRR setup at 333 K under ~ 6 Pa of hydrogen. The resistance decreases as a confirmation

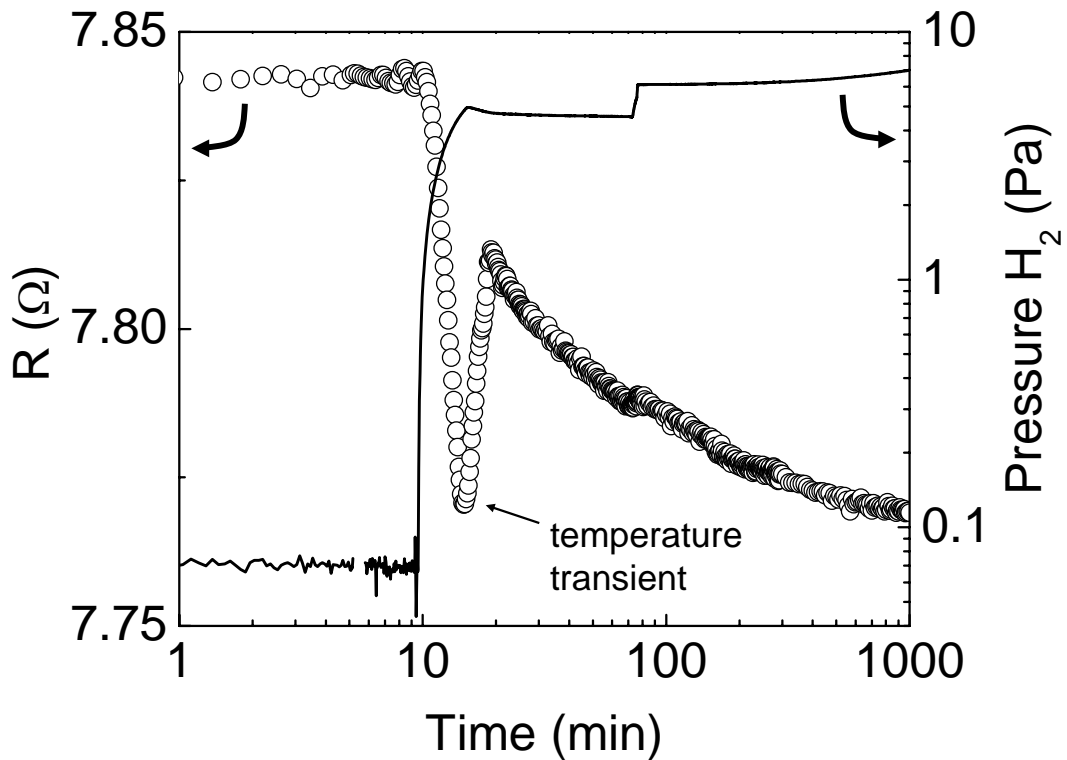


Figure 4.10: Time evolution of the electrical resistance of sample 10x, 10x[Ti(2 nm)Mg(4 nm)]Pd(10 nm), while loading in ~ 6 Pa of hydrogen at 333 K in the *in-situ* XRR setup.

that only the Ti layers are loaded: unlike MgH₂, which is an insulator, TiH₂ is a metal with a higher electrical conductivity than Ti [126]. The temperature transient highlighted in Fig. 4.10 is due to the injection of hydrogen gas at room temperature, in the sample chamber at 333 K. Figure 4.11 shows the

XRR pattern measured on the 10x sample at 333 K in ~ 6 Pa of hydrogen. From the position of the reflectivity peaks and applying eq. 4.3, we calculate

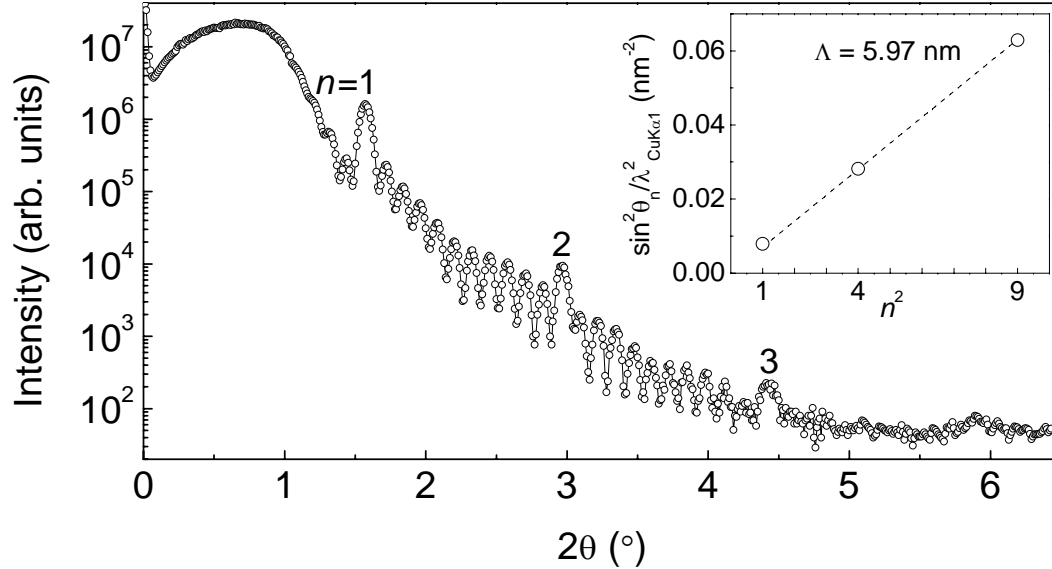


Figure 4.11: XRR from the partially loaded 10x multilayer at $p_{\text{H}_2} = 6$ Pa and $T = 333$ K. The inset shows the measured linear dependence of the ratio $\sin^2 \theta_n / \lambda_{\text{CuK}\alpha 1}^2$ versus n^2 .

a period expansion of about 5.9%, with respect to the as-deposited metallic state (see inset in Fig. 4.11). According to the literature values for the molar volumes of Ti ($\bar{V}_{\text{Ti}} = 10.64$ cm 3 /mol) and TiH $_2$ ($\bar{V}_{\text{TiH}_2} = 13.3$ cm 3 /mol), the hydrogenation of titanium should expand the lattice of the host metal by 25%. Given the 3.6:2 thickness ratio of Mg and Ti measured by XRR (Table 4.2) on the as-deposited sample, a uniaxial vertical expansion of the period Λ of 5.9%, due to the hydrogenation of Ti only, implies a vertical expansion of the Ti layers of 16.5%. This can only be understood taking into account strong plastic deformations and out-of-plane material pile up, due to the hydrogen-induced in-plane coherency stress in the titanium layers [127]. This dramatic material movement is likely to remove the structural coherence at the Mg/Ti interfaces and to be at the origin of the “scissor” effect observed in Mg layers sandwiched between Ti thin films [52, 53].

After measuring the XRR of the intermediate state in ~ 6 Pa of H $_2$ at 333 K, we slowly increased the hydrogen pressure up to 10^3 Pa at constant temperature, while measuring the electrical resistance of the film (see Fig. 4.12). The abrupt increase of electrical resistance between 100 and 300 Pa is due to hydrogen absorption in the Mg layers. After reaching equilibrium in 10^3 Pa of H $_2$ we measured the XRR pattern for the fully hydrogenated state, as shown in Fig. 4.13. The fit parameters used in the simulation in Fig. 4.13a are given in the fourth column of Table 4.2. Upon hydrogenation the bilayer

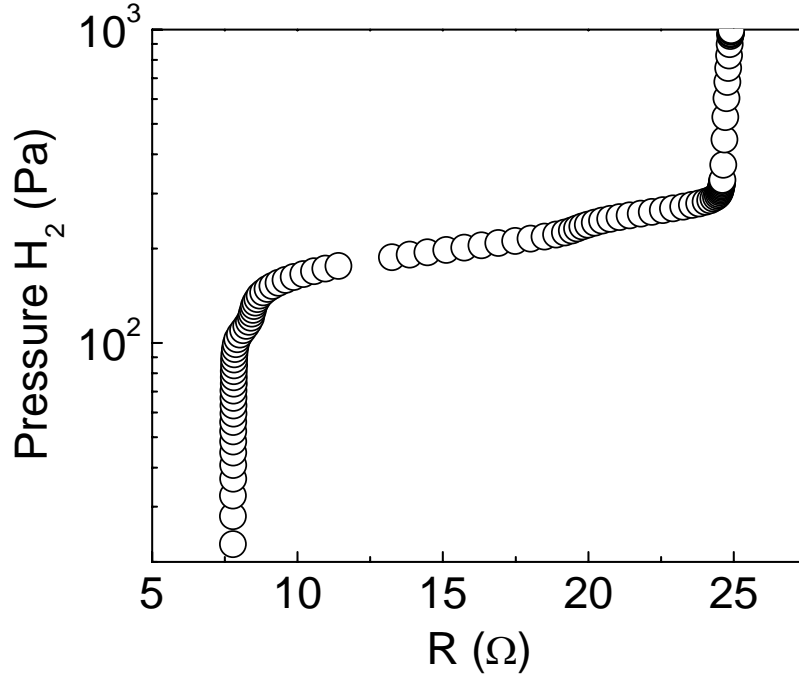


Figure 4.12: Pressure-resistance-isotherm measured during loading of the 10x sample, $10x[\text{Ti}(2 \text{ nm})\text{Mg}(4 \text{ nm})]\text{Pd}(10 \text{ nm})$, at 333 K in the *in-situ* XRR setup.

thickness Λ increases by 23%, from 5.6 nm in the as-deposited state to 6.9 nm in the fully hydrogenated state. Titanium layers expand by 15%, from 2.0 to 2.3 nm, in good agreement with the value obtained from the period expansion observed upon hydrogenation at 6 Pa (16.5%). Magnesium layers expand by $\sim 28\%$, from 3.6 to 4.6 nm. In the hydrogenation of bulk Mg the molar volume increases by 30%, going from $13.97 \text{ cm}^3/\text{mol}$ in Mg to $18.2 \text{ cm}^3/\text{mol}$ in MgH_2 : a vertical expansion of the Mg layers of 28% is therefore an indication of strong plastic deformations. Fig. 4.14 shows the rocking curves measured over the second order reflectivity peak, for the as-deposited, intermediate and fully hydrogenated sample. The pattern consists of two components, one narrow with a fwhm of 0.023° and one much broader. The narrow peak is the specular reflectivity and the width is what would be expected from an optically flat sample. The broader component comes from off-specular scattering which includes scattering from roughness at the interfaces. As can be seen in the figure, the off-specular contribution increases during loading, indicating an increase in interfacial roughness [128, 129]. This is consistent with the reflectivity simulations which also showed a roughness increase upon loading. This roughness increase could in principle also be attributed to atomic interdiffusion, however, since interdiffusion causes a lateral roughness with no particular length scale, it contributes zero or a constant amount to the off specular scattering. The increase in the off-specular scattering observed in Fig. 4.14 is therefore due to

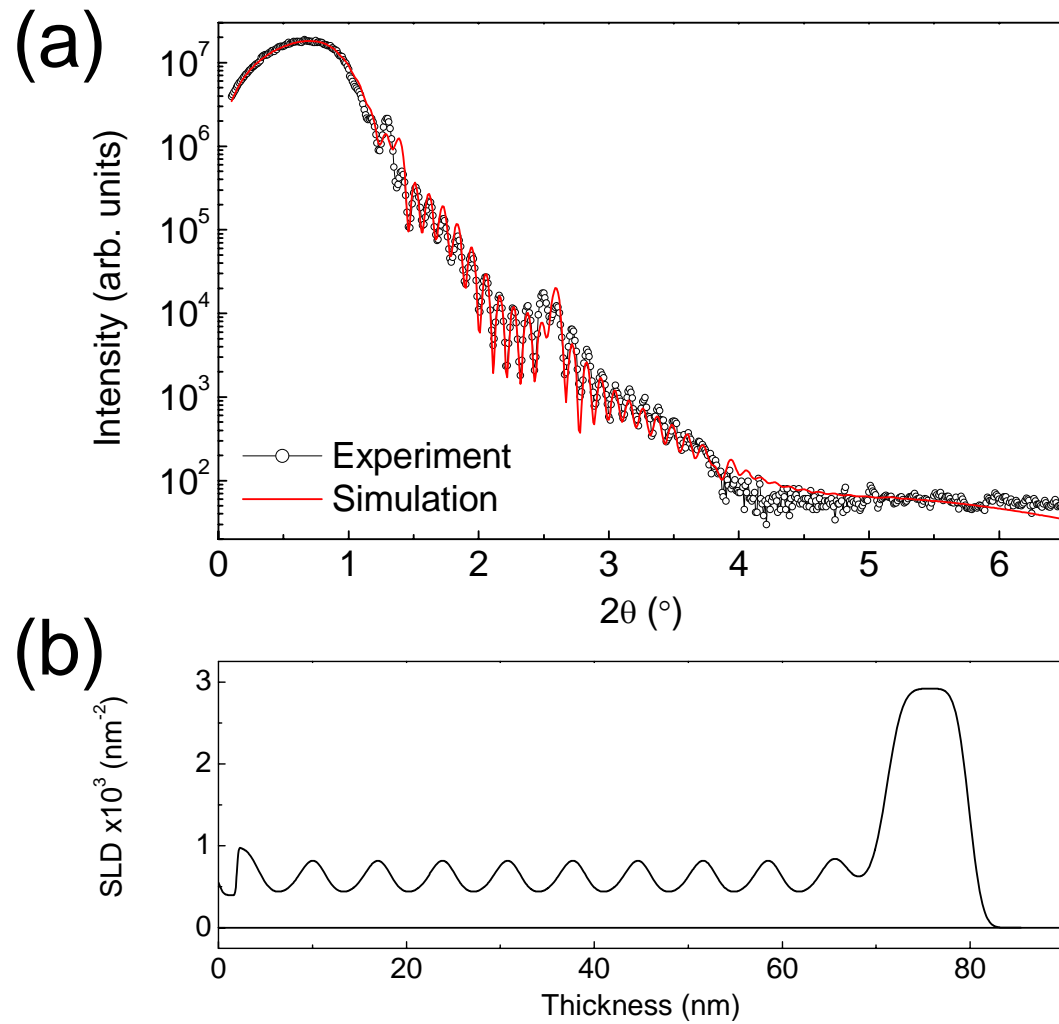


Figure 4.13: XRR pattern of the fully loaded 10x sample at $p_{\text{H}_2} = 10^3$ Pa and $T = 333$ K. The solid red line is a simulation of the multilayer using GenX [123]. (b) Scattering Length Density (SLD) profile corresponding to the simulation in Fig. 4.13a.

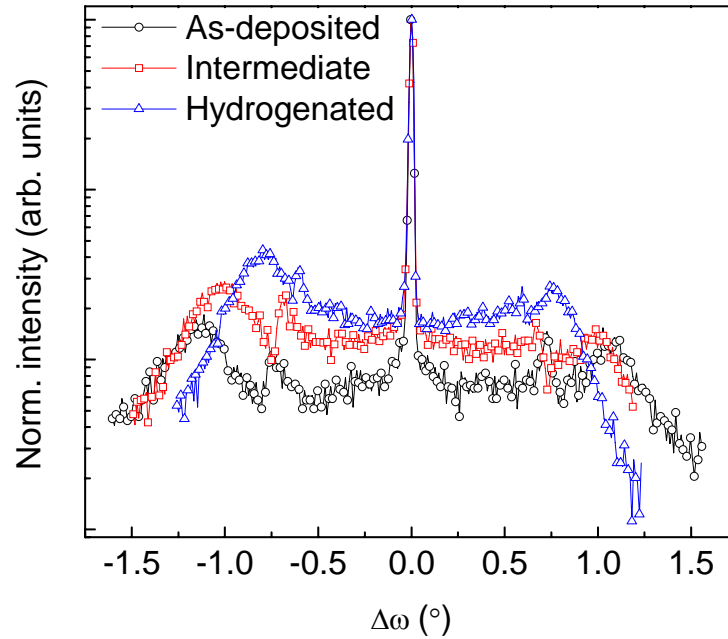


Figure 4.14: Rocking curves measured over the second order reflectivity peak, for the as-deposited, intermediate and fully hydrogenated 10x sample. The scans are offset and only 50% of the experimental points are shown for clarity.

an increase in roughness in the form of thickness variations. The small peaks at either side of the specular reflections are likely to be due to off-specular scattering from the first order reflectivity peaks and not to correlations in the roughness.

Due to the poor crystallinity of the fully loaded samples a detailed structural characterization of the hydrogenated state cannot be achieved with XRD only. In order to measure the crystal phases present in the hydrogenated multilayers we performed selected area electron-diffraction patterns of a 10x sample covered with only 1 nm of Pd. Such small amount of Pd allows loading of the sample but its catalytic activity is rapidly suppressed by strong metal-support interaction (SMSI) effects [130] and it is not enough to promote significant hydrogen desorption [38]. The measurements were performed both for few seconds and for 10 minutes of electron beam exposure. In the former case both tetragonal MgH_2 and face-centered-cubic TiH_2 peaks are observed, while in the latter hydrogen desorption from the MgH_2 layers occurs due to electron irradiation and reflections from hexagonal-closed-packed Mg are visible, Fig. 4.15. It is noteworthy that in the hydrogenated state no signs of cubic MgH_2 are present: in codeposited $\text{Mg}_y\text{Ti}_{1-y}$ thin films, the hydrogenated state is tetragonal for $y > 0.87$ and face-centered-cubic for $y < 0.87$ [38]. This fcc phase is similar to the one proposed for high pressure $\beta\text{-MgH}_2$ [84] and originates from the structurally coherent dispersion of Mg-rich and Ti-rich

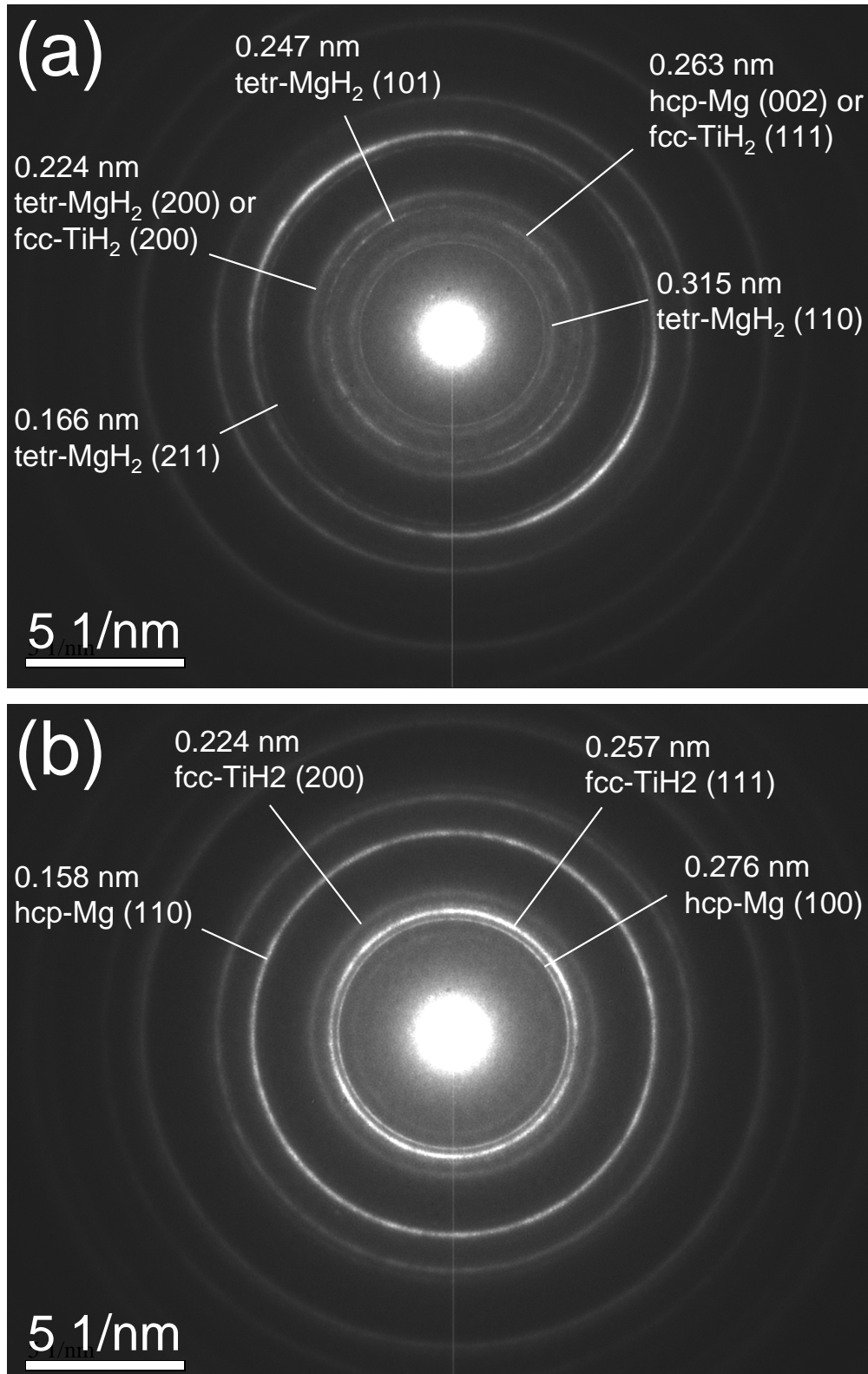


Figure 4.15: Selected area electron diffraction patterns for the hydrogenated state of a 10x Mg/Ti multilayer. (a) Short and (b) long beam exposure.

nanosized domains in Mg-Ti thin film alloys [50, 48]. The multilayers studied in the present work contain 40 at.% of Ti and one would therefore expect a similar cubic structure to occur upon hydrogenation. Apparently, however, the cubic hydride phase can only be stabilized by a very fine 3D dispersion of Mg and Ti atoms. A 10x multilayer, consisting of repetitions of 2 nm of Ti and 4 nm of Mg, is already too “segregated” and leads to standard tetragonal MgH₂. This result is consistent with the “scissor” effect observed in Ti-sandwiched Mg film, according to which no elastic interaction exists between adjacent Mg and Ti layers [53].

Optical spectroscopy

The loading sequence is further investigated by optical spectroscopy measurements. An example is given for sample 2x in Fig. 4.16, where the measured optical reflection of the multilayer, deposited on a quartz substrate and covered with 10 nm of Pd, is shown for different stages of hydrogenation. Comparison with simulated optical spectra obtained with SCOUT [131] shows that the disappearance of the reflection hump at ~ 4 eV at the beginning of the hydrogenation process is due to the formation of TiH₂ (see white arrow in Fig. 4.16a and 4.16b). In the simulations shown in Fig. 4.16 the thickness increase of the individual Ti and Mg layers has been taken according to the variations observed by means of XRR, $\sim 15\%$ for Ti and 28% for Mg, leading to an excellent agreement with the measured spectra.

Hydrogenography

In order to interpret the Pressure-optical Transmission-Isotherms (PTIs) measured by hydrogenography on the Pd-capped Mg/Ti multilayers we make use of the following assumptions: 1) Mg layers in direct contact with Pd feel an elastic constraint, due to the formation of Mg-Pd alloys at the interface, which leads to plateau pressures higher than what expected from bulk Mg ($p_{\text{bulk Mg}}^{333 \text{ K}} = 12$ Pa [118])[52]; 2) in the process of Mg-Pd alloy formation typically 6 nm of Mg are “lost” and do not contribute to the optical change occurring upon hydrogen absorption [52]; 3) Mg films surrounded by Ti layers, on the contrary, do not feel significant elastic constraints, thanks to the positive enthalpy of mixing of Mg and Ti which leads to poor interface adhesion. Furthermore Ti absorbs hydrogen at lower pressures than Mg and the consequent lattice expansion removes the partial lattice coherence at the Ti/Mg interfaces and leads to quasifree Mg layers [53]. The PTIs measured at 333 K for the multilayers studied in the present work are shown in Fig. 4.17. The PTI for the 1x sample, Ti(20 nm)Mg(40 nm)Pd(10 nm), shows a relatively high plateau pressure with respect to bulk Mg ($p_{\text{bulk Mg}}^{333 \text{ K}} = 12$ Pa) [118], due to the elastic

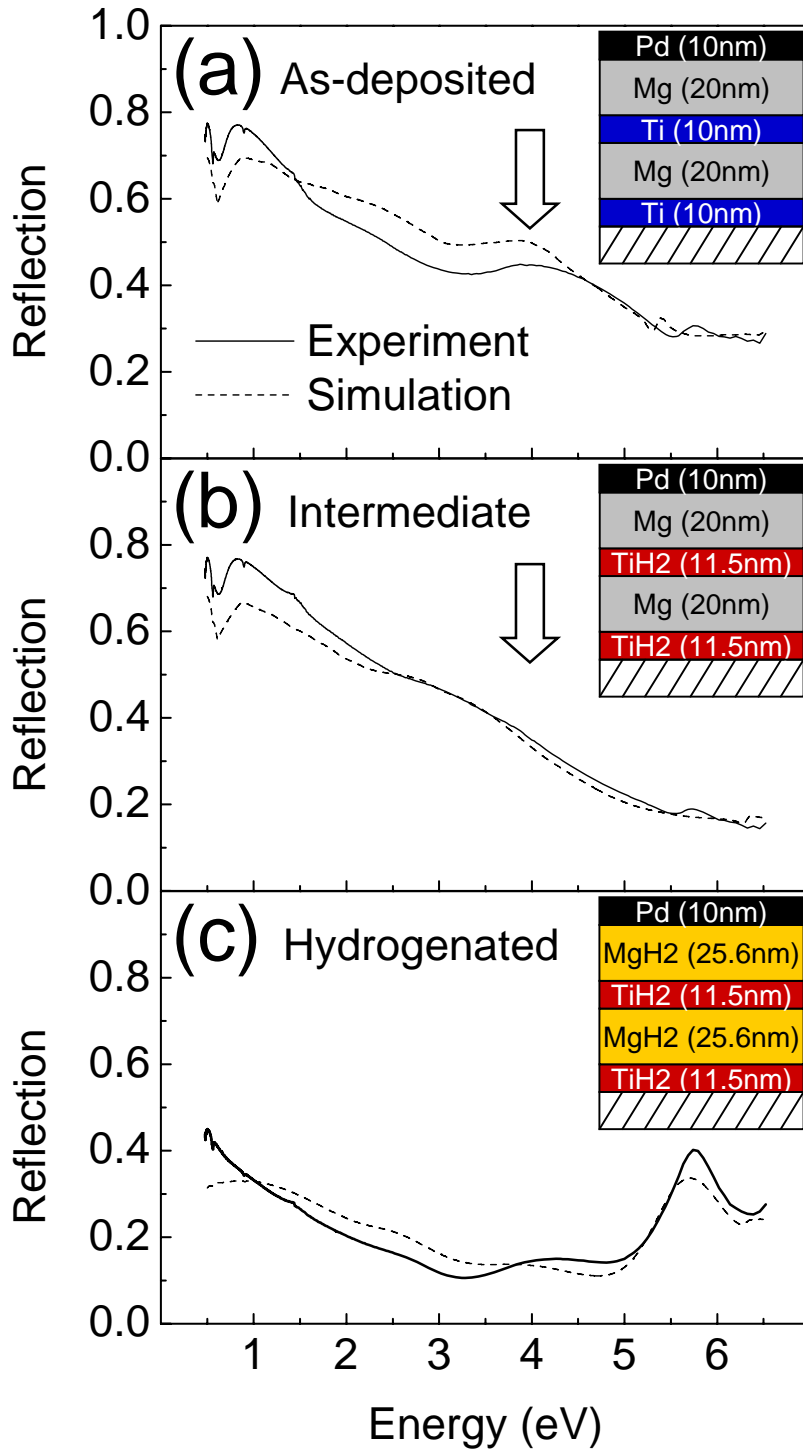


Figure 4.16: Experimental (lines) and simulated (dots) reflection spectra measured through the quartz substrate for the 2x sample, $2x[\text{Ti}(10 \text{ nm})\text{Mg}(20 \text{ nm})]\text{Pd}(10 \text{ nm})$, exposed to slowly increasing pressures of a 6% H_2/Ar mixtures at room temperature. (a) As-deposited, (b) intermediate and (c) hydrogenated state. The dielectric functions of Ti, Mg, TiH_2 , MgH_2 and Pd used in the simulations are the same used in Ref. 14.

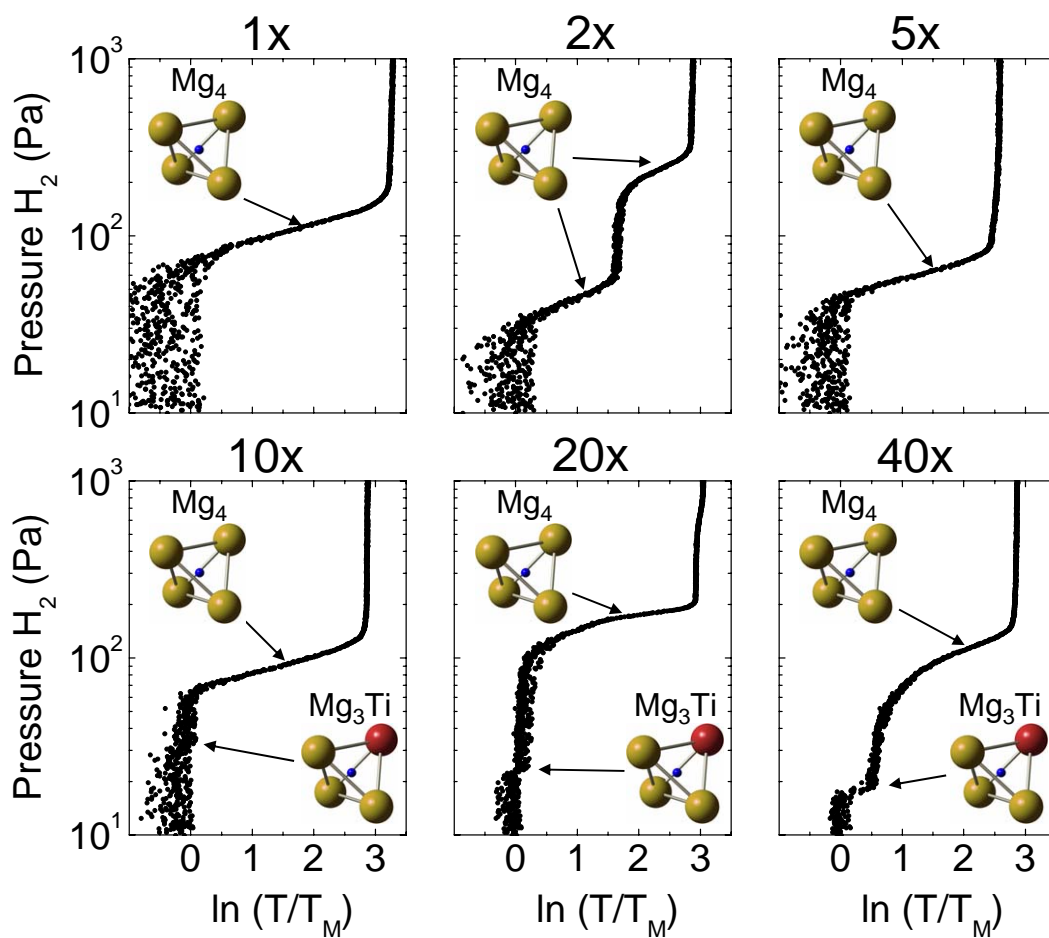


Figure 4.17: Loading Pressure-Transmission-Isotherms measured by hydrogenography at 333 K for the Mg/Ti multilayers covered with 10 nm of Pd.

clamping of the top Pd layer [52]. The same effect, together with the “scissor” property of Ti [52], is responsible for the double plateau observed for the 2x sample, Ti(10 nm)Mg(20 nm)Ti(10 nm)Mg(20 nm)Pd(10 nm): the bottom Mg layer (lower plateau) is sandwiched between two Ti layers and it is therefore quasifree [53], while the top one (higher plateau) is in contact with the Pd cover and feels its elastic constraint, therefore loading at higher hydrogen pressures. Following the same line of reasoning one would expect for the 5x sample to find two plateaus: a plateau at low pressure, build up by the bottom 4 Mg layers sandwiched between Ti and a plateau at higher pressure, coming from the top Mg layer in contact with Pd. The top plateau however is not visible due to the fact that the uppermost Mg layer is only 5 nm thick and therefore completely alloyed to Pd. In the 10x 20x and 40x the plateau pressure slightly increases with respect to the 5x sample. A possible explanation for such behavior is that in the 10x, 20x and 40x samples the individual Mg layers are very thin (4, 2 and 1 nm, respectively) and surface energy might provide a relevant contribution to the enthalpy of hydride formation [132]. Another effect that might play a role is the fact that in these samples the Ti layers (2, 1 and 0.5 nm) might not be thick enough to form perfectly closed films: the Mg layers would therefore not be completely shielded from the clamping effect of the top Pd cover. For the 40x sample a sloping plateau similar to the one measured for a co-deposited $\text{Mg}_{0.6}\text{Ti}_{0.4}$ alloy is observed [12], suggesting that the microstructure of this sample is closer to a mixed alloy than to a well defined multilayer.

It is noteworthy that for the 10x, 20x and 40x samples a small plateau appears at very low hydrogen pressures. The width of this plateau is proportional to the number of Mg/Ti interfaces present in the multilayers. We interpret these plateaus as originating from hydrogen atoms populating the interstitial sites located at the Mg/Ti interfaces: in the metallic films the hydrogen atoms are located in interstitial tetrahedral sites, inside the Mg layers these are Mg_4 sites but, crossing the Mg/Ti interfaces, there will also be Mg_3Ti , Mg_2Ti_2 , MgTi_3 and Ti_4 sites. Since the formation enthalpy of TiH_2 is smaller than the one of MgH_2 , the substitution of one (or more) Mg atoms with Ti in a tetrahedral site will lower the absorption energy and the site will be populated at lower hydrogen pressures [50]. As can be seen in Fig. 4.12, a similar small plateau at the beginning of the hydrogenation process is also observed when measuring the film electrical resistance, while loading the 10x sample used in the XRR measurement. A comparison of Fig. 4.12 and Fig. 4.17 shows that, when loaded in the *in-situ* XRR setup, the 10x sample absorbs hydrogen at a higher pressure with respect to the loading in the hydrogenography optical setup. This is not surprising since, when measuring isotherms by hydrogenography, we want to obtain equilibrium curves and the pressure is increased very slowly in 20 hours. In the XRR setup on the other hand the loading was completed in 30 minutes and it is therefore not an equilibrium measurement. The

small step observed at ~ 230 Pa in the pressure-resistance-isotherm cannot be explained with simple thermodynamic considerations, but it could be related to the fact that the measurement is done in the kinetic regime, as such a step is not observed in the equilibrium isotherm obtained by hydrogenography.

Diffusion simulation of hydrogen cycling

While loading the multilayers in the XRD setup we exposed them to 1 bar of H_2 at room temperature, a pressure sufficient to hydrogenate both the Ti and the Mg layers. Nevertheless we observed an intermediate state in which only the Ti layers were loaded. Furthermore, upon exposure to air at room temperature hydrogen desorbs from the Mg layers but remains trapped in the Ti ones and the original metallic state can only be recovered by heating the samples up to 433 K. These loading and unloading sequences can be qualitatively explained by looking at the difference in thermodynamic properties of hydrogen absorption in Mg and Ti. Pasturel *et al.* [133] have already shown how the chemical potential of hydrogen in different transition metals (TM) can influence the hydrogen sorption kinetics in $\text{Mg}_2\text{Ni}/\text{TM}/\text{Pd}$ trilayers. Here we extend their model to a system with 7 layers, in order to account for the multiple repetitions typical of a multilayer. The model treats hydrogen dissolved in metals in the lattice-gas approximation, without including any H-H interaction. The chemical potential of hydrogen in a metal (M) is therefore written as:

$$\begin{aligned}\mu_{\text{H}}^{\text{M}}(c_{\text{M}}) &= \bar{H}_{\text{H}} - T\bar{S}_{\text{H}} \\ &= \bar{H}_{\text{H}} - T(\bar{S}_{\text{conf.}} + \bar{S}_{\text{vibr.}})\end{aligned}\quad (4.4)$$

\bar{H}_{H} and \bar{S}_{H} are the partial molar enthalpy and entropy of hydrogen in metals, respectively. The configurational contribution to the entropy, $\bar{S}_{\text{conf.}}$, is proportional to $\ln[c_{\text{M}}/(1 - c_{\text{M}})]$, where c_{M} is the hydrogen concentration in the metal. This term takes care that hydrogen atoms obey Fermi-Dirac statistics in the host metallic lattice, due to the single occupation of interstitial sites. In most metals the vibrational term, $\bar{S}_{\text{vibr.}}$, is small at moderate temperatures and can be neglected, with the significant exception of Pd ($\bar{S}_{\text{vibr.}} \approx 19.2 \text{ JK}^{-1}(\text{mol H})^{-1}$ at 298 K) [134].

Each iteration of the model consists of two steps. First, the concentration within each layer is updated according to the diffusion equation. Subsequently, we impose the equality of chemical potential at the interface between two materials by changing the concentrations at the sites adjacent to the interface such that the chemical potential is made equal on both sites, while keeping the *total* amount of hydrogen atoms unchanged. Note that the equality in chemical potentials at the interfaces does not imply the equality of hydrogen concentrations in the adjacent surfaces of the two layers. Instead of using the experimental values of the hydrogen pressure and the enthalpies and entropies

of hydrogen absorption in Mg, Ti and Pd we define the following dimensionless parameters:

$$\begin{aligned}
e_{\text{H}} &= \frac{1}{2} \ln \frac{p_{\text{H}_2}}{p^0} \\
e_{\text{M}} &= \frac{\mu_{\text{H}}^{\text{M}} - \frac{1}{2}\mu_{\text{H}_2}^0}{RT} \\
&= \frac{\bar{H}_{\text{H}} - T\bar{S}_{\text{H}} - \frac{1}{2}H_{\text{H}_2}^0 + \frac{1}{2}TS_{\text{H}_2}^0}{RT} \\
&= \frac{(\bar{H}_{\text{H}} - \frac{1}{2}H_{\text{H}_2}^0) - T(\bar{S}_{\text{H}} - \frac{1}{2}S_{\text{H}_2}^0)}{RT} \\
&= \frac{\Delta H_{\text{M}}}{RT} - \frac{\Delta S_{\text{M}}^0}{R} \tag{4.5}
\end{aligned}$$

where $p^0 = 10^5$ Pa, ΔS_{M}^0 is the entropy of hydride formation which, except for Pd ($\Delta S_{\text{Pd}}^0 = -48.7 \text{ JK}^{-1}(\text{mol H})^{-1}$), is taken equal to the entropy of hydrogen gas at standard pressure ($\Delta S_{\text{M}}^0 \approx -\frac{1}{2}S_{\text{H}_2}^0 = -65 \text{ JK}^{-1}(\text{mol H})^{-1}$) and ΔH_{M} is the enthalpy of hydride formation: $\Delta H_{\text{Pd}} = -20.5 \text{ kJ}(\text{mol H})^{-1}$ [135], $\Delta H_{\text{Mg}} = -37.2 \text{ kJ}(\text{mol H})^{-1}$ [125], $\Delta H_{\text{Ti}} = -65 \text{ kJ}(\text{mol H})^{-1}$ [101]. Substituting these values in eq. 4.5 and taking $T = 333$ K, we obtain: $e_{\text{Pd}} = -1.5$, $e_{\text{Mg}} = -5.6$ and $e_{\text{Ti}} = -15.6$.

In Fig. 4.18, we simulate the loading and unloading behavior of a multilayer made of 3 Ti/Mg repetitions and covered with a Pd layer, in which the Mg layers are twice as thick as the Pd and Ti ones: $3x[\text{Ti}(z)\text{Mg}(2z)]\text{Pd}(z)$. In order to highlight only the effect of the chemical potential, we assume that the hydrogen diffusion coefficient is the same for all the materials. The loading pressure is taken as 10^5 Pa ($e_{\text{H}} = 0$) and the unloading pressure is taken negative enough in order to allow desorption from all the layers ($e_{\text{H}} = -20$). Upon exposure to 10^5 Pa of H_2 the Pd and Ti layers and the uppermost Mg layer load very quickly, while the Mg layers “sandwiched” between Ti absorb hydrogen more slowly, effectively producing a transient intermediate TiH_2/Mg multilayer. This is due to the fact that at the beginning of the loading process, when the hydrogen concentration is low everywhere, Ti acts as a hydrogen sink due to its lower enthalpy of hydride formation, effectively sucking hydrogen atoms lying at the Ti/Mg interfaces. When the Ti layers are almost full the logarithmic entropic term in eq. 4.4 dominates over the energetic term and Mg layers start to absorb hydrogen. Upon unloading the effect is opposite: at the beginning the hydrogen concentration is very high everywhere and hydrogen atoms remain trapped in the Ti layers until the adjacent Mg layers are “empty” enough to equilibrate the chemical potentials. When desorption starts in the Ti layers, however, the hydrogen concentration in the Mg layers is so low that the total flux of hydrogen atoms through Mg (which is proportional to the gradient in concentration) is minimal, resulting in a very slow hydrogen desorption. In Fig. 4.18 we also show that increasing the temperature of the

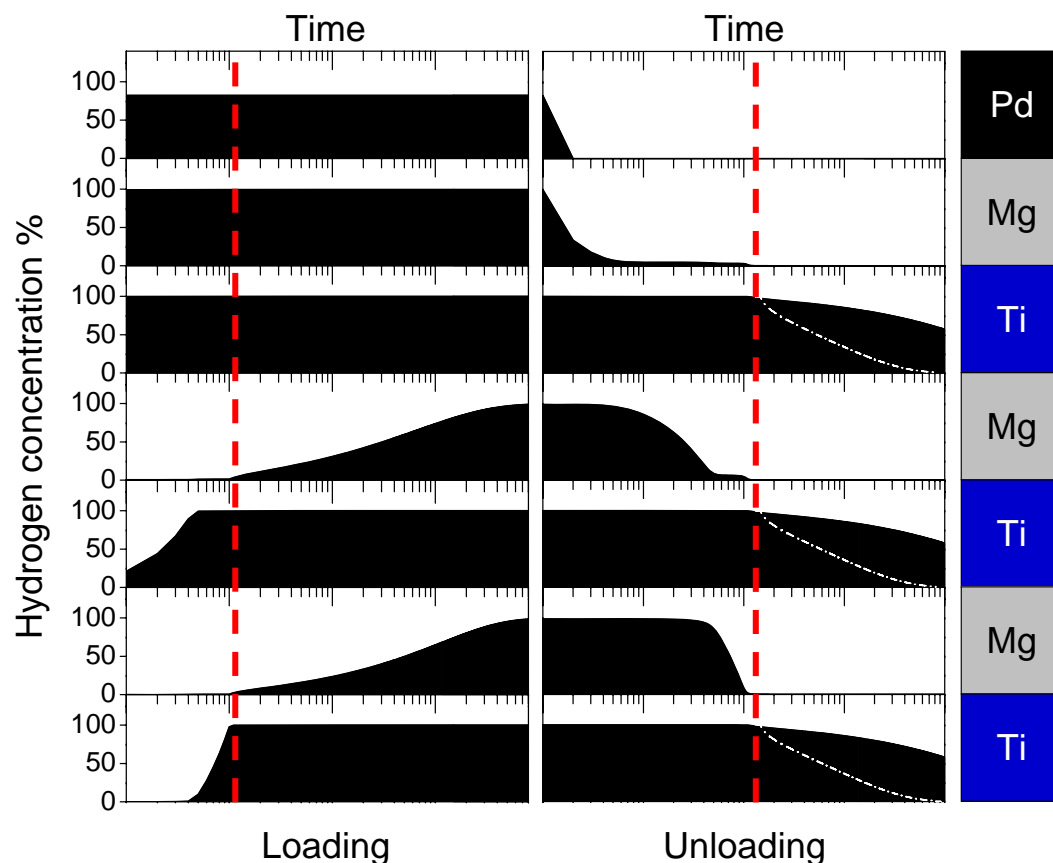


Figure 4.18: Simulated time evolution (in logarithmic scale) of the hydrogen concentration in each layer of a $3x[\text{Ti}(z)\text{Mg}(2z)]\text{Pd}(z)$ sample, upon hydrogen absorption ($e_{\text{H}} = 0$) and desorption ($e_{\text{H}} = -20$) at room temperature. The vertical dashed lines represent the intermediate states, observed experimentally both upon loading and unloading, in which only the Ti layers are hydrogenated. The white dash-dot lines are the simulated desorption rate from the Ti layers at 433 K.

system to 433 K enhances the rate of hydrogen desorption from the Ti layers (white dash-dot lines). With these simple simulations we can therefore give a qualitative interpretation of the persistence of hydrogen in the Ti layers, both upon loading and unloading, as observed experimentally.

4.2.4 Conclusions

We have prepared several Pd-capped Mg/Ti multilayers with various periodicities by means of magnetron sputtering. The deposited samples have lattice parameters in the z direction close to their nominal bulk values and low interfacial roughnesses. Partial structural coherence exists at the Mg/Ti interfaces in the as-deposited state but it is reduced upon hydrogen absorption and desorption. The hydrogen loading sequence, as confirmed by XRD, XRR and optical spectroscopy, agrees with what is expected from thermodynamic considerations on the enthalpies of formation of magnesium and titanium hydrides: Mg/Ti \rightarrow Mg/TiH₂ \rightarrow MgH₂/TiH₂. Hydrogen absorption in both the Ti and Mg layers leads to large expansions in the vertical out-of-plane direction, well beyond the elastic regime, indicating that massive material pile up, due to plastic deformations and creation of defects, has to take place. Upon dehydrogenation hydrogen is kinetically trapped in the Ti layers. Complete desorption only occurs upon exposure to air at 433 K leading to the original metallic layered structure, with a shorter coherence length. Magnesium hydride in a Mg/Ti multilayer with period Λ as small as 6 nm, retains its standard tetragonal structure, suggesting that the occurrence of a cubic hydrogenated phase, as observed in partially segregated Mg _{y} Ti_{1- y} ($y < 0.87$) thin films [50, 48], can only be stabilized by a very fine dispersion of Mg-rich and Ti-rich domains. Pressure-optical Transmission-Isotherms measured by hydrogenography, can be interpreted on the basis of the clamping effect on thin Mg films due to the adjacent layers [52, 53] and, possibly, on the surface energy differences between the metallic and hydrogenated states of ultra thin Mg films. A simple diffusion model allows us to reproduce both the loading and unloading sequences measured experimentally.

Chapter 5

Mg sandwiches: destabilization through elastic constraints

5.1 Introduction

Since their discovery in 1996 by Huiberts *et al.* [11] switchable mirrors have been covered by thin protective layers (typically made of Pd), to catalyze H₂ absorption in the film and prevent their oxidation. Due to the low solubility of hydrogen in Pd, the cap-layer's influence on the thermodynamic properties of switchable mirrors was always considered to be negligible [136] and never studied in detail.

In the present chapter we show that the presence of a Pd cap-layer does have a significant effect on the equilibrium hydrogen pressure of a thin Mg film. Thanks to the formation of a Mg-Pd alloy at the Mg/Pd interface, palladium acts as a clamping agent for the magnesium underneath, effectively increasing the hydrogen pressure at which MgH₂ is formed. The elastic nature of this effect derives from the long-range H-H interaction existing in coherent metals (see Section 1.1) and is confirmed by measurements of hydrogen absorption isotherms in Pd-capped Mg films with various thicknesses. A simple elastic model, whose details are presented in Appendix C, allows us to quantitatively reproduce the observed thickness dependence of the equilibrium hydrogen pressure. As expected, a similar destabilization effect is observed in Ni-capped Mg films, since nickel, like palladium, is miscible with Mg.

On the contrary, Mg films covered with immiscible elements, such as Ti, Nb and V, exhibit a hydrogen equilibrium pressure similar to the one observed in bulk Mg, effectively behaving like quasifree samples. In these cases the positive enthalpy of mixing of Mg and the cap layer metal leads to very poor adhesion at the Mg/cap interfaces. No changes in the hydrogen equilibrium pressure are observed for Pd-capped Ti/Mg/Ti trilayers, with magnesium thicknesses varying between 10 and 40 nm, indicating the absence of any elastic or surface energy contributions. The presence of a Ti layer between Mg and Pd has also a strong effect in the structural stability of the films and in their kinetics of hydrogen absorption and desorption, by suppressing the formation of Mg-Pd

alloy at the Mg/Pd interface. Such intermixing at the Mg/Pd interface lowers the rate of hydrogen desorption and is responsible for the aging of the samples upon subsequent hydrogenation/dehydrogenation cycles.

These findings, besides shedding a new light on the physics of metal hydrides, are also interesting from the point of view of their application. Tuning the thermodynamics of hydrogen absorption in metal hydrides is nowadays one of the key targets in the search for a suitable hydrogen storage system. The possibility of controlling the equilibrium hydrogen pressure by elastic means opens the possibility of new strategies to tackle this fundamental problem. The elastic model developed for thin films (essentially bi-dimensional systems) can be extended to 3D systems and predicts even stronger destabilization for small Mg nanoparticles surrounded by a skin of hard material. Furthermore the presence of multiple plateaus in the loading isotherms of Mg-based multilayers suggest their application as tunable hydrogen detectors and hydrogen sensors.

In Section 5.2 we describe the discovery of the strong clamping effect in capped Mg films, by measuring hydrogen absorption isotherms on thin Mg layers covered with various elements. We then develop an elastic model that allows us to interpret the dependence of the equilibrium hydrogen pressure on the Mg film's thickness.

Section 5.3 shows the thermodynamic and kinetic effects arising upon insertion of a Ti layer between Mg and Pd. By comparison with the results obtained for Pd-capped Mg films, we demonstrate how the formation of Mg-Pd alloy at the Mg/Pd interface is responsible of both increasing the hydrogen equilibrium pressure and reducing the hydrogen desorption kinetics.

5.2 Destabilization of the Mg-H system through elastic constraints

Abstract – We tune the thermodynamics of hydrogen absorption in Mg by means of elastic clamping. The loading isotherms measured by hydrogenography show that Mg films covered with Mg-alloy-forming elements, such as Pd and Ni, have hydrogen plateau pressures more than two orders of magnitude higher than bulk Mg at the same temperature. An elastic model allows us to interpret the Mg thickness dependence of the hydrogen plateau pressure. Our results suggest an alternative route for the development of new hydrogen storage materials with optimized thermodynamic properties.

5.2.1 Introduction

Hydrogen is an attractive energy carrier for a future sustainable energy system. Compact hydrogen storage is however still a scientific and technological challenge [137]. Storage of molecular hydrogen, both gaseous and liquid, requires high pressures or very low temperatures and is thus not energy efficient. An alternative is to store atomic hydrogen in metal or complex hydrides. Storage in metal-hydrides allows, in principle, to achieve high volumetric and gravimetric densities and to reversibly operate at room temperature and atmospheric pressure. However there are thermodynamic and kinetic limitations associated with the chemical reactions involved in hydrogen absorption and desorption.

An optimal metal-hydride system has a hydrogen equilibrium pressure of 1 bar at room temperature. Due to weight constraints the interest of the scientific community has turned to lightweight hydride-forming elements such as Li, B, Na, Mg and Al. Mg can store up to 7.6 mass% of hydrogen, forming the ionic MgH_2 compound, but shows poor kinetics of hydrogen absorption/desorption and a hydrogen equilibrium pressure of 1 bar at the far too high temperature of 573 K. The absorption and desorption kinetics can be enhanced by reducing the size of the Mg grains via ball milling [138] hence shortening the hydrogen diffusion length, or by addition of proper catalysts [139]. Many efforts are currently dedicated to modifying the thermodynamics of the Mg-H system in order to promote hydrogen dissociation at lower temperatures. Some destabilization has been observed upon reduction of particle size [140] and alloying of Mg with other elements [141, 12], although this generally implies a reduction in the total hydrogen storage capacity. Theoretical works suggest the possibility to reduce the hydrogen desorption temperature in both MgH_2 nanoparticles with grain size smaller than ~ 1.3 nm [142] and in MgH_2 layers with thicknesses below 10 unit cells [143].

In this letter we show that the thermodynamic stability of the Mg-H system can be drastically modified via elastic constraints. This is a direct consequence of the long range H-H interaction in metals [8, 6]. In a metal with elastically free surfaces two hydrogen atoms feel an effective attractive interaction, while in a sample clamped on all sides the interaction becomes repulsive. Clamping can thus be used to tune the equilibrium hydrogen pressure to the levels required for specific applications. To prove the validity of our approach we prepared two series of capped Mg thin films: 1) to explore the role of chemical binding we deposited Mg thin films capped with various transition metals, differing in their affinities towards magnesium and in their hydrogen solubilities: Ni, Pd, Ti, Nb and V; 2) in order to study the thickness dependence of the elastic effect we prepared a series of Pd-capped Mg films of different thicknesses. The effect of clamping is strongly dependent on the chemical nature of the transition metal used as a cap-layer and will be interpreted with a simple elastic model. By choosing the appropriate sample geometry we are able to

increase the hydrogen plateau pressure more than 200 times with respect to bulk Mg.

5.2.2 Experimental details

Hydrogen absorption in our samples is measured by means of optical spectroscopy and Hydrogenography [12], a novel technique that allows to measure Pressure-Optical Transmission-Isotherms (PTI's). In a PTI the amount of light transmitted by a thin film is measured as a function of increasing pressure at constant temperature: when the metallic Mg films load with hydrogen the Mg-MgH₂ metal-insulator transition leads to an abrupt increase in the amount of transmitted light. From the Beer-Lambert law, $\ln(T/T_M) \propto c_H d$, the logarithm of the optical transmission, T , normalized for the transmission of the film in its metallic state, T_M , is proportional to the hydrogen concentration in the film, c_H and to the film thickness, d (see Appendix B). Measuring PTI's is therefore in all respects equivalent to measure standard Pressure-Composition-Isotherms [13]. The films used in this study are deposited in a UHV chamber ($p < 10^{-6}$ Pa) by RF/DC magnetron sputtering on glass and quartz substrates. All films are covered with Pd to prevent oxidation and catalyze hydrogen absorption. Optical reflection spectra are measured in a PerkinElmer Lambda 900 diffraction grating spectrometer, with energy range between 0.5 and 6.5 eV, during (de)hydrogenation at room temperature and H₂ pressures up to 10⁵ Pa. PTI's are recorded in an optical cell that allows to vary the hydrogen pressure from 10⁻¹ to 10⁶ Pa at constant temperatures, between 313 and 573 K. Further details on the hydrogenography experimental setup can be found in Ref. [12].

5.2.3 Results and discussion

In Fig. 5.1 the PTI of a 2x[Ti(10nm)Mg(20nm)] film covered with 10 nm of Pd is shown. In the pressure and temperature ranges explored Pd and Ni do not load with hydrogen. Ti, Nb and V layers on the contrary load at the beginning of the pressure ramp but, due to the metallic nature of their hydrides, produce very small optical effects compared to Mg. The observed plateaus are therefore only due to the formation of MgH₂ upon hydrogen absorption. The isotherm shown in Fig. 5.1 exhibits two clear and distinct plateaus of similar width. Since the width of the plateau is proportional to the thickness of the material the two plateaus must originate from the two distinct Mg layers. Furthermore, to obtain such a well defined double-plateau we have to assume that the two Mg layers are elastically disconnected [144] and have different site energies for hydrogen absorption. To prove these hypotheses we measure the optical reflection of the 2x[Ti(10nm)Mg(20nm)]Pd(20nm) sample deposited on quartz, while slowly increasing the hydrogen pressure. Optical spectra are measured through the transparent quartz substrate at near-normal incidence. In Fig.

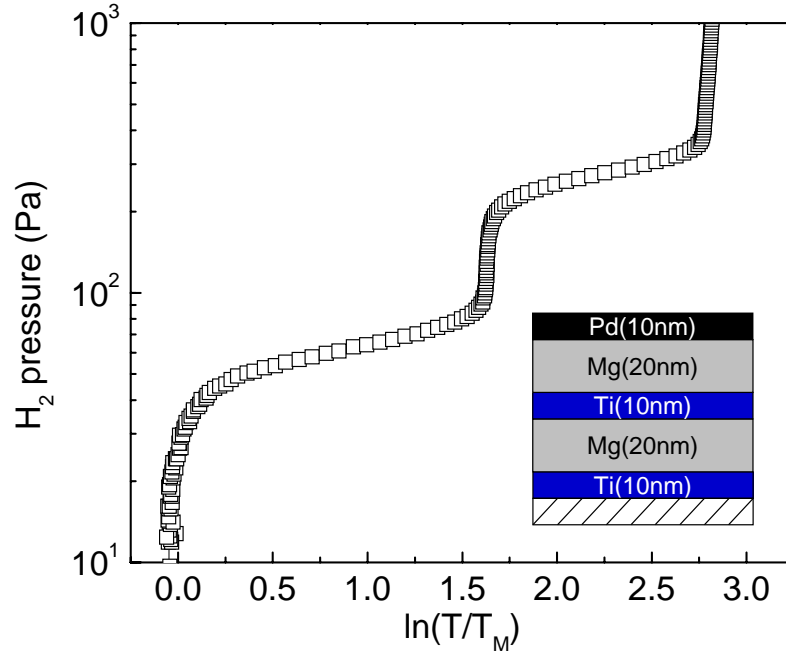


Figure 5.1: Loading PTI measured at 333 K for a $2x[\text{Ti}(10\text{nm})\text{Mg}(20\text{nm})]\text{Pd}(10\text{nm})$ sample deposited on glass. In the inset a cartoon of the sample geometry: glass-substrate/Ti/Mg/Ti/Mg/Pd.

5.2a the measured spectra are shown for three different steps of loading: 1) as-deposited metallic sample, 2) at intermediate loading and 3) fully loaded sample. The calculated spectra shown in Fig. 5.2b are generated with SCOUT [131] by taking into account the volume expansion occurring upon hydrogenation of Mg and Ti and including a rough interface between the quartz substrate and the first Ti layer. In the simulation the intermediate step is due to the complete loading of one of the two Mg layers while the other remains metallic. Comparison with the experimental spectra shows unambiguously that the Mg layer sandwiched between two Ti layers absorbs hydrogen at a lower pressure than the one capped with Pd. This is rather counterintuitive since the “Ti-sandwiched Mg” lies on the bottom of the sample and hydrogen has to diffuse through the top Mg layer, which remains in the diluted α phase, in order to reach the bottom one. For this mechanism to take place the two Mg layers have to differ with respect to their thermodynamic properties and they must be elastically disconnected by the presence of the Ti layer in between. This remarkable behavior is the result of the following H loading sequence. Already at very low H_2 pressures Ti forms TiH_2 . The consequent 25% volume expansion, together with the fact that Mg and Ti are immiscible, leads to reduced strains at the Mg/ TiH_2 interfaces. The Ti-sandwiched Mg layer is then effectively elastically disconnected from the surrounding. However, since Pd alloys

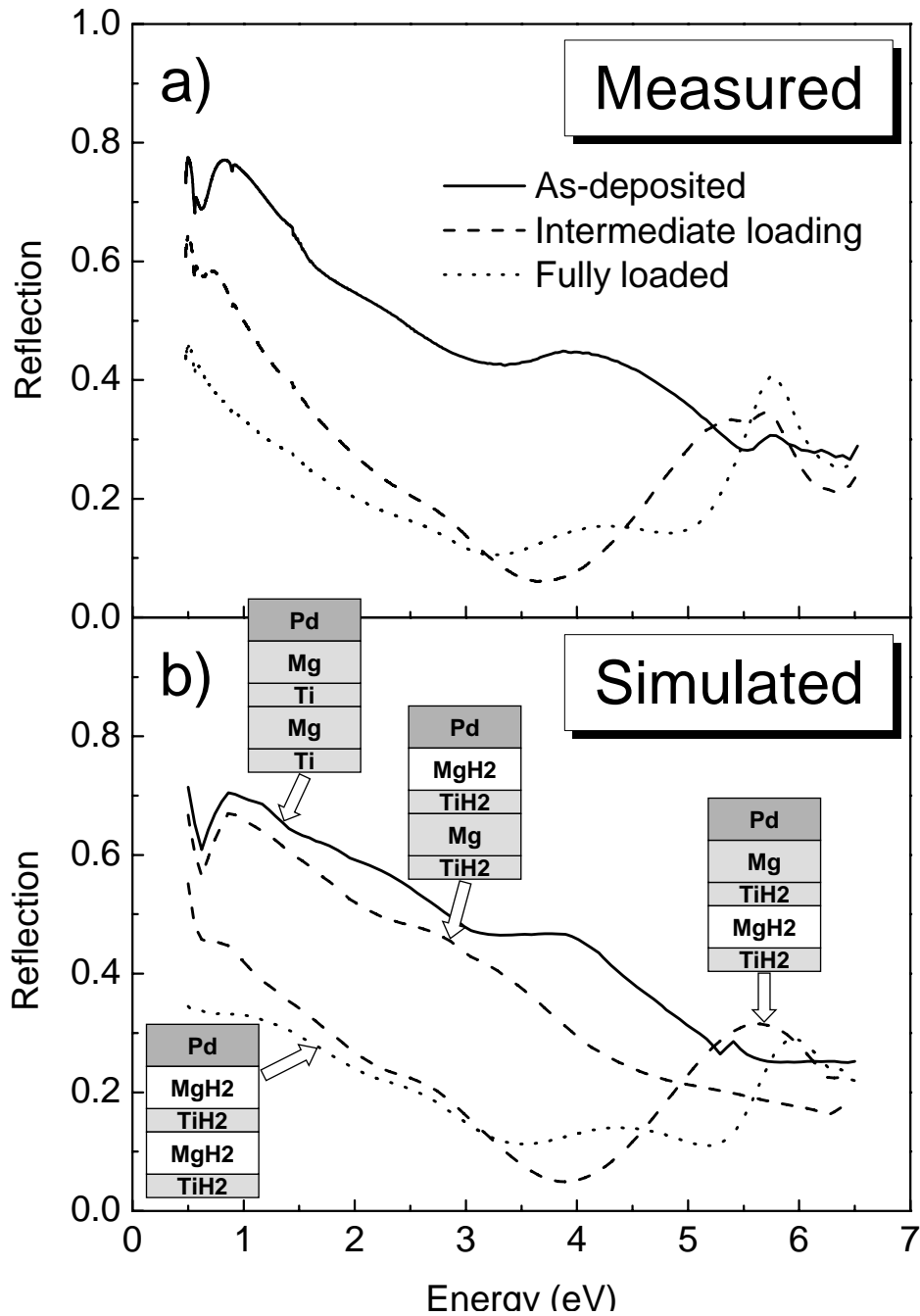


Figure 5.2: Measured (a) and simulated (b) optical reflection measured through the quartz substrate for a $2x[\text{Ti}(10\text{nm})\text{Mg}(20\text{nm})]$ film covered with 20 nm of Pd at different stages of loading. In the simulations two possible states are taken into account for the intermediate loading: the “loading from top” and “loading from bottom”. The dielectric functions of Ti, Mg, TiH_2 , MgH_2 and Pd used in the simulations are taken from Ref. [60], [145], [38], [146] and [60] respectively.

with Mg and loads at higher pressures, this reasoning is not applicable to the Ti-Mg-Pd block. When the top Mg layer expands upon H absorption it feels the Pd elastic constraint, resulting in a higher hydride formation enthalpy and consequently in a higher plateau pressure. To demonstrate the validity of this interpretation we considered two series of samples: a) Mg thin films capped with different transition metals, and b) Pd-capped Mg thin film with different thicknesses. Fig. 5.3 shows the PTI's for 5 different samples with the following geometry: Ti(10nm)Mg(20nm)X(10nm)Pd(10nm) with X = Ni, Pd, Ti, Nb and V. Due to the presence of a Ti layer between Mg and the substrate we

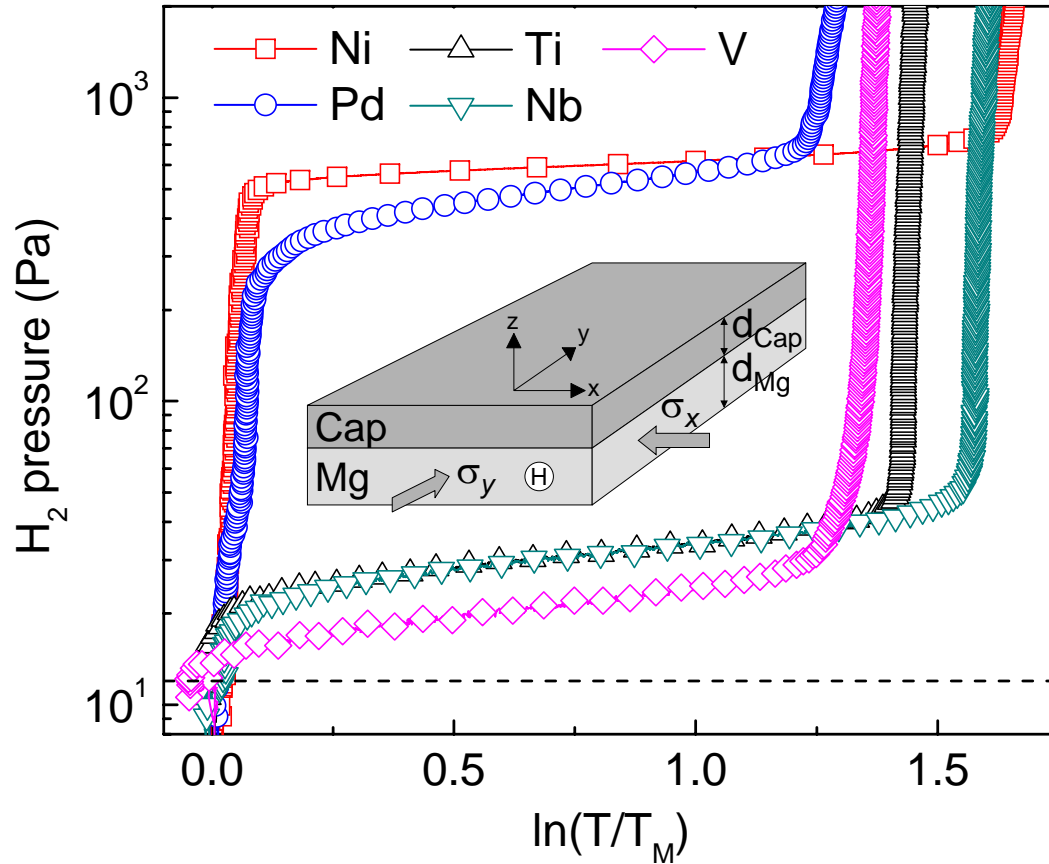


Figure 5.3: Effect of cap-layer: PTI's measured at 333 K for Ti(10nm)Mg(20nm)X(10nm)Pd(10nm) samples deposited on glass with X = Ni, Pd, Ti, Nb and V. The dashed line is the pressure at which coexistence of α and β phases begins to appear upon hydrogen absorption in bulk Mg [118]. In the inset: schematic visualization of the elastic model used to interpret the data.

can assume that the only clamping effect is due to the top Pd layer. Clearly two behaviors are distinguishable: 1) Mg alloy forming elements such as Ni and Pd have a strong effect on the thermodynamic properties of Mg, leading to a much higher plateau pressure than the one measured for Mg films of equal thickness capped with Ti, Nb and V; 2) the latter elements, which are immis-

cible with Mg, effectively behave like “scissors” and lead to “quasi-free” Mg layers with elastically disconnected interfaces. Assuming that the origin of the destabilization observed is only elastic in nature, we can build a simple model consisting of two layers - a Mg and a cap-layer - glued to each other as shown in the inset in Fig. 5.3: hydrogen atoms absorbed by the Mg layer isotropically expand the lattice of the metallic host, while the Mg feels a compressive stress in the x and y directions (σ_x and σ_y) due to the cap layer. In the z direction there is no stress built up by the clamping but we have to take into account the strain along the z direction due to the Poisson’s ratio, ν . The two layers are in vacuum and no effect of the substrate is taken into account, basically assuming that the bottom Ti layer is a perfect scissor. By taking into account only elastic constraints we can calculate the effective volume expansion of the Mg layer upon hydrogen absorption. Furthermore, the enthalpy of hydride formation has a simple volume dependence through the bulk modulus, B [9]: $d\Delta H/d \ln V = -B_{\text{Mg}} V_{\text{H}}$, where V_{H} is the partial molar volume of hydrogen in Mg. We can then derive an expression for the plateau pressure of the capped magnesium layer, Mg^* , with respect to free bulk magnesium, Mg^0 :

$$\ln \left(\frac{p^*}{p^0} \right) = \frac{E_{\text{Mg}}}{\tilde{E}} \left[1 - \nu_{\text{Mg}} + (1 - \nu_{\text{Cap}}) \frac{E_{\text{Mg}}}{E_{\text{Cap}}} \frac{d_{\text{Mg}}}{d_{\text{Cap}}} \right]^{-1} \quad (5.1)$$

where $\tilde{E} = \frac{9}{4} RT V_{\text{Mg}} / V_{\text{H}}^2$, V_{Mg} is the molar volume of Mg and $E = 3B(1 - 2\nu)$ is the Young’s modulus (details of the derivation can be found in Appendix C). The equation can also be rewritten as $[\ln(p^*/p^0)]^{-1} = I + S d_{\text{Mg}}$ with

$$I = \frac{\tilde{E}}{E_{\text{Mg}}} (1 - \nu_{\text{Mg}}), \quad S = \frac{\tilde{E}}{E_{\text{Cap}}} (1 - \nu_{\text{Cap}}) \frac{1}{d_{\text{Cap}}} \quad (5.2)$$

According to the model the equilibrium pressure for the capped Mg has a straightforward dependence on the thickness of the Mg layer, d_{Mg} . Fig. 5.4 shows the PTI’s for 5 samples with different Mg thicknesses: Ti(10nm)Mg(z nm)Pd(40nm), with $z = 10, 15, 20, 30$ and 40 nm. Two effects are clearly visible: a) the width of the plateau, w , is proportional to d_{Mg} as expected from the Beer-Lambert law, b) the plateau pressure decreases with increasing Mg thickness as predicted by the model. A 10 nm thick Mg film has an equilibrium hydrogen pressure of $2.8 \cdot 10^3$ Pa at 333 K, more than 200 times higher than bulk Mg at the same temperature ($p_{333 \text{ K}}^0 = 12$ Pa [118]). The plateau width is measured by dividing each isotherm into three regions: the solid solution (α phase) before the plateau, the coexistence region ($\alpha + \beta$ phases) and the fully hydrogenated region (β phase) after the plateau and fitting each part with a straight line: the width is then given by the distance, in units of $\ln(T/T_{\text{M}})$, between the intersection points. With the same geometrical construction we obtain the equilibrium pressure, as the pressure in the middle of the plateau. Ideally one would expect $w \rightarrow 0$ for $d_{\text{Mg}} \rightarrow 0$,

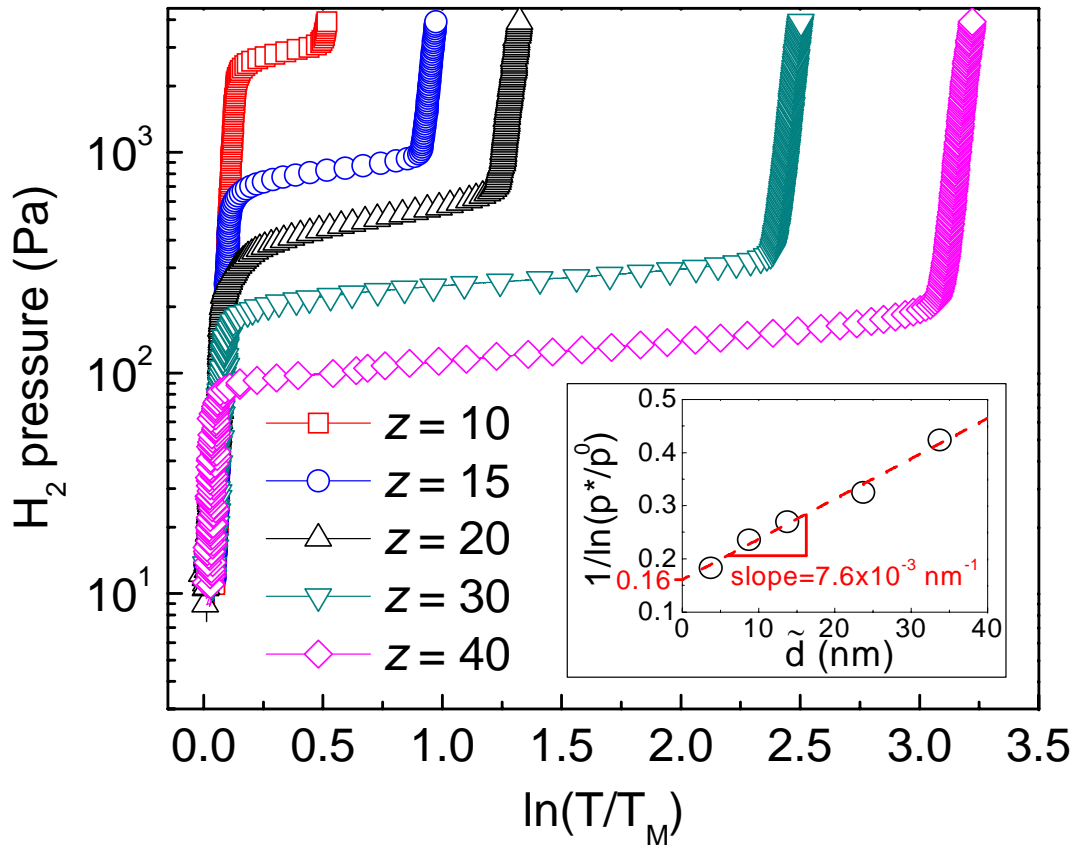


Figure 5.4: Effect of Mg thickness: PTI's measured at 333 K for Ti(10nm)Mg(z nm)Pd(40nm) samples deposited on glass with $z = 10, 15, 20, 30$ and 40 nm. In the inset: Mg thickness dependence of the equilibrium pressure. The dashed line is a linear fit to the points.

however, although the plateau width is found to be proportional to the Mg thickness, a linear fit shows a relation of the type $w = A(d_{\text{Mg}} - d_0)$, with $d_0 = 6$ nm. The presence of an intercept indicates that the total amount of Mg undergoing a phase transition to MgH_2 is thinner than expected and that we can assume for all samples that ~ 6 nm of Mg are “lost” due to alloying with the top Pd layer. In the comparison with the model we will therefore take into account an effective Mg thickness $\tilde{d} = d_{\text{Mg}} - d_0$. The formation of an interfacial Mg-Pd alloy is directly responsible for the strong clamping effect observed and is consistent with the difference in width observed in the two plateaus of Fig. 5.1, corresponding exactly to 6 nm. The inset in Fig. 5.4 shows the thickness dependence of the plateau pressure of Pd-capped Mg layers: plotting $[\ln(p^*/p^0)]^{-1}$ versus the effective Mg thickness we find a linear dependence as predicted by the model, with intercept $I = 0.16$ and slope $S = 7.6 \cdot 10^{-3} \text{ nm}^{-1}$. Substituting into equations 5.2 the literature values for the structural parameters of Mg, Pd and H ($V_{\text{Mg}} = 13.97 \text{ cm}^3/\text{mol}$, $V_{\text{H}} = 2.24 \text{ cm}^3/\text{mol}^*$, $\nu_{\text{Mg}} = 0.29$, $\nu_{\text{Pd}} = 0.39$, $E_{\text{Mg}} = 45.2 \text{ GPa}$, $E_{\text{Pd}} = 126 \text{ GPa}$) and taking $T = 333 \text{ K}$ and $d_{\text{Pd}} = 40 \text{ nm}$, we obtain the theoretical values $I_{\text{th}} = 0.27$ and $S_{\text{th}} = 2.1 \cdot 10^{-3} \text{ nm}^{-1}$. The agreement between experiment and theory is surprising when considering the strong approximations made in the model: no substrate is taken into account, the only interaction is elastic, hence neglecting surface energy contributions, and the layers are assumed to behave as perfect elastic bodies. The rather large S value obtained from the fit can be explained considering the alloying effect taking place at the Mg/Pd interface and assuming that only a fraction of ~ 10 out of 40 nm of Pd has a significant clamping effect on the Mg underneath. The discrepancy in the I values could reflect the fact that we consider the Young’s modulus of metallic Mg: taking into account MgH_2 , which is stiffer than Mg, would lead to a closer agreement between experiment and theory. The elastic model developed for a double-layer can be easily extended to 3D Mg nanoparticles embedded in a skin of hard material. Assuming Mg particles of 10 nm of diameter and a skin of 2 nm thickness, the model predicts an increase in hydrogen equilibrium pressure of more than 2000 times with respect to bulk Mg at the same temperature. The effect of clamping described in the present work is not only important in the perspective of hydrogen storage applications, but it is crucial in understanding the thermodynamics of all hydrogen-absorbing capped thin films, from switchable mirrors [11] to electrode materials for batteries [35], hydrogen detectors [23] multilayers and superlattices [147].

5.2.4 Conclusions

In conclusion we have shown the possibility to tailor the thermodynamics of a metal-hydrogen system by means of elastic constraints. Thin films of Mg

*Assuming 32% volume expansion upon hydrogenation of Mg.

are used as a model metal-hydrogen system. Elements immiscible with Mg behave like scissors, while Mg-alloy-forming elements exert a clamping effect that leads to huge increases in hydrogen equilibrium pressures. Clamping arises as a consequence of alloying between Mg and the top layer and its effects can be understood on the basis of a simple elastic model. The possibility to tune the thermodynamics of a metal-hydrogen system by elastic means offers attractive new possibilities for compact hydrogen storage.

5.3 Quasifree Mg-H thin films

Abstract – The thermodynamics of hydrogen absorption in Pd-capped Mg films are strongly dependent on the magnesium thickness. In the present work we suppress such dependency by inserting a thin Ti layer between Mg and Pd. By means of optical measurements we show that the surface energy contribution to the destabilization of MgH_2 is negligible. The inserted Ti layer prevents Mg-Pd alloy formation at the Mg/Pd interface, leading to quasi-free Mg films and enhancing the kinetics of hydrogen desorption. Our observations are important for the development of thin film devices.

5.3.1 Introduction

The thermodynamic and kinetic properties of metal-hydrides (MH) need to be drastically improved to make them a viable solution for hydrogen storage. Thanks to its relatively high volumetric and gravimetric capacities and its low cost magnesium hydride has been proposed as an excellent hydrogen storage system [137]. However, the kinetics of hydrogen uptake and release in magnesium are poor and the thermal stability of its hydride, MgH_2 , is too high. For practical applications in fact, assuming that the only relevant entropic contribution is due to the entropy loss of gaseous hydrogen, an ideal hydrogen storage system should have an enthalpy of hydride formation of about -40 kJ/molH_2 , in order to release hydrogen at a pressure of 10^5 Pa at room temperature. The formation of MgH_2 , however, releases 74.4 kJ/molH_2 , leading to an equilibrium pressure of 10^5 Pa at $\sim 300 \text{ }^\circ\text{C}$. Tuning the thermodynamics of hydrogen absorption in Mg has so far been achieved by means of proper doping [12, 141], although this generally results in a reduction of the material's storage capacity. Some destabilization upon reduction of the Mg particle size has also been observed experimentally [140] and predicted theoretically [142, 143]. In our group we have recently demonstrated the possibility of tuning the thermodynamics of hydrogen absorption in Mg thin films by means of elastic clamping [52]. By "sandwiching" thin Mg films between layers of elements which form stable alloys with Mg (such as Pd or Ni), we were able to increase the equilibrium pressure of hydrogen absorption by more than two orders of magnitude with respect to pure Mg in bulk. This destabilization is of elastic nature and it originates from the formation of Mg-Pd (or Mg-Ni) alloy at the interface between the two elements. On the contrary, Mg films sandwiched between layers of elements which are immiscible with Mg (such as Ti, Nb and V) do not feel significant elastic clamping. In the present work we compare the absorption isotherms already obtained for "Pd-capped" Mg films of different thicknesses, in which the elastic clamping has a significant effect, with layers of identical thickness but in which the Pd/Mg interface has been removed by the insertion of a thin layer of Ti, which we will call "Ti-buffer" samples.

5.3.2 Experimental details

The samples are deposited in a UHV system (base pressure of 10^{-6} Pa) by DC/RF magnetron sputtering of Mg (99.95%), Ti (99.999%) and Pd (99.98%) targets in argon atmosphere, on transparent substrates kept at room temperature. The films are covered with Pd to prevent oxidation and promote hydrogen dissociation and absorption. In all the samples discussed in the present work a 10 nm layer of Ti is deposited before Mg in order to reduce clamping effects from the substrate [52]. Hydrogen loading isotherms are measured at 333 K by means of Hydrogenography [12], an optical technique in which

the amount of light transmitted through a thin film is continuously monitored while slowly increasing the hydrogen pressure at constant temperature. The output of a hydrogenography experiment is therefore a Pressure-optical Transmission-Isotherm (PTI). A PTI is equivalent to a standard Pressure-Composition-Isotherm (PCI) [13], thanks to the Beer-Lambert law, according to which the logarithm of the optical transmission, normalized to the transmission of the film in its metallic state, is proportional to the hydrogen concentration in the film, c_H , times the film's thickness, d . Thus, $\ln(T/T_M) \propto c_H \cdot d$. In a PTI the width of the pressure plateau, indicating the magnitude of the optical change occurring in the film upon hydrogen absorption, is therefore directly proportional to the film's thickness.

5.3.3 Results and discussion

Figure 5.5a shows the isotherms obtained at 333 K for Ti-buffer samples, together with the results already obtained for Pd-capped ones [52]. The samples have the following geometries: Ti-buffer = substrate / Ti(10 nm) / Mg(z nm) / Ti(10 nm) / Pd(40 nm), Pd-capped = substrate / Ti(10 nm) / Mg(z nm) / Pd(40 nm), with $z = 10, 20, 30$ and 40 nm in both cases. The dashed line in Fig. 5.5a represents the pressure at which the MgH₂ phase begins to nucleate in thick, bulk-like Mg layers [118]. The insertion of a Ti layer drastically reduces the equilibrium pressure, leading to “quasi-free” Mg. The equilibrium pressure of the Ti-buffered films is independent on the thickness of the Mg layers, indicating that surface energy effects, which would produce a thickness dependence similar to the one observed for the Pd-capped samples, are negligible [132]. The plateaus shown in Fig. 5.5a, corresponding to the regions of the isotherms at almost constant pressure, have widths, w , expressed in terms of optical transmission and proportional to the nominal thickness of the Mg films, d_{Mg} . In Pd-capped samples we found a relation of the type $w = A(d_{Mg} - d_0)$, with $d_0 \approx 6$ nm [52]. These “missing” 6 nm are due to the formation of Mg-Pd alloy at the Mg/Pd interface. Figure 5.5b shows the thickness dependence of the plateau width for both the Pd-capped [52] and the Ti-buffer samples. Although the nominal thickness of the Pd-capped and Ti-buffer samples is the same, the plateau width of the former ones is constantly larger: the presence of a Ti layer between Mg and Pd leads to a smaller d_0 , indicating either a reduction of interalloying or a smaller roughness at the Mg/Cap interface. A flatter interface in the Ti-buffer samples is reasonable, considering that Mg and Ti are thermodynamically immiscible, while Mg and Pd form stable intermetallic compounds for a wide range of compositions. Fig. 5.6 shows the PTIs for 4 subsequent hydrogen loadings of a 20 nm thick Mg layer, both in the Pd-capped = Ti(10 nm)Mg(20 nm)Pd(40 nm) and Ti-buffer = Ti(10 nm)Mg(20 nm)Ti(10 nm)Pd(40 nm) geometries. The plateau width of the Pd-capped sample shrinks upon cycling indicating that

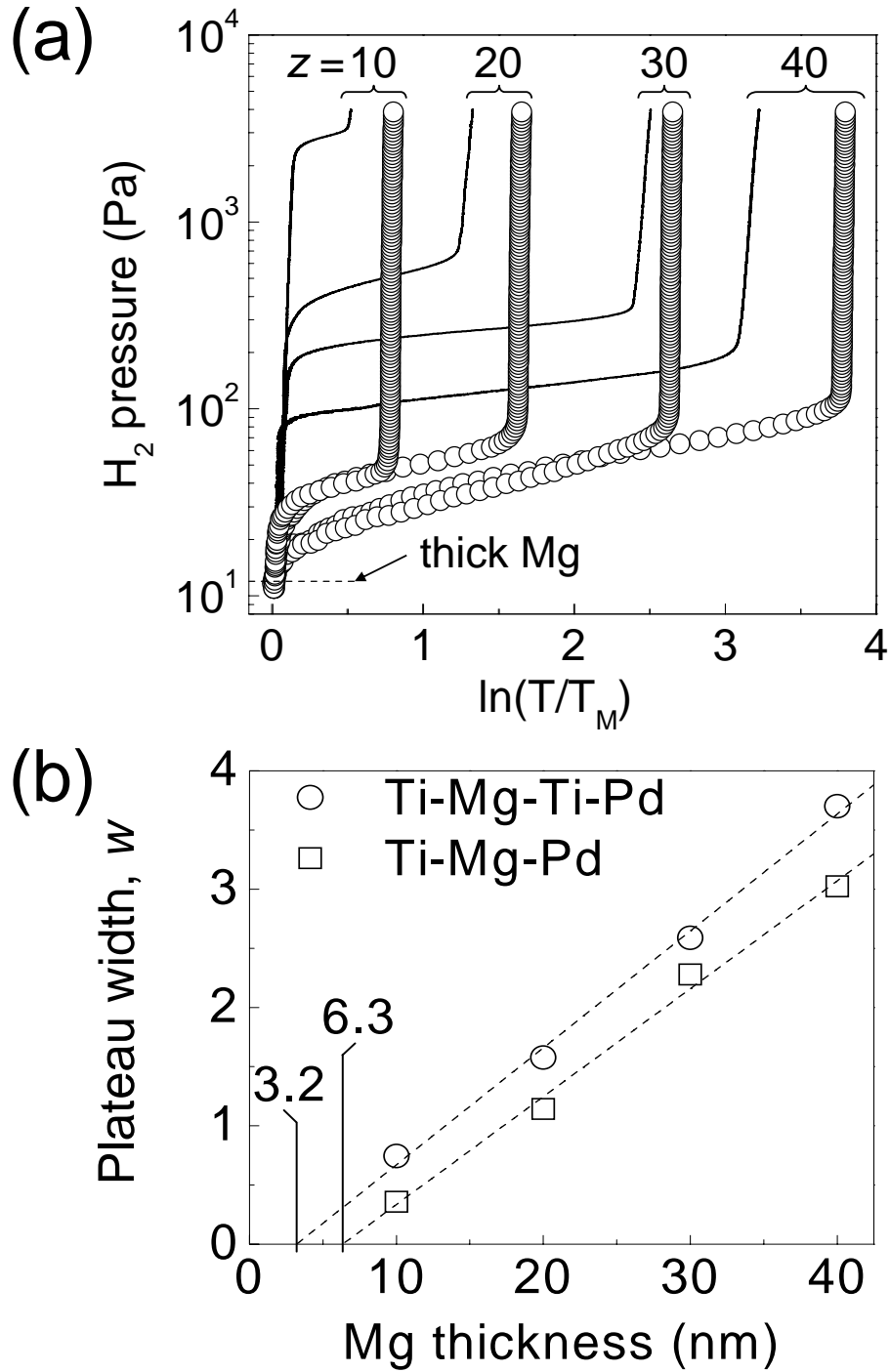


Figure 5.5: Effect of a Ti buffer layer on the thermodynamic properties of Mg thin films. (a) PTI's measured at 333 K for (lines) "Pd-capped" Ti(10 nm)Mg(z nm)Pd(40 nm) samples, as already published in [52] and (symbols) "Ti-buffer" Ti(10 nm)Mg(z nm)Ti(10 nm)Pd(40 nm) samples. The Mg thicknesses are in both cases $z = 10, 20, 30$ and 40 nm. (b) Thickness dependence of the plateau width, w , expressed in optical transmission, of Pd-capped and Ti-buffer samples.

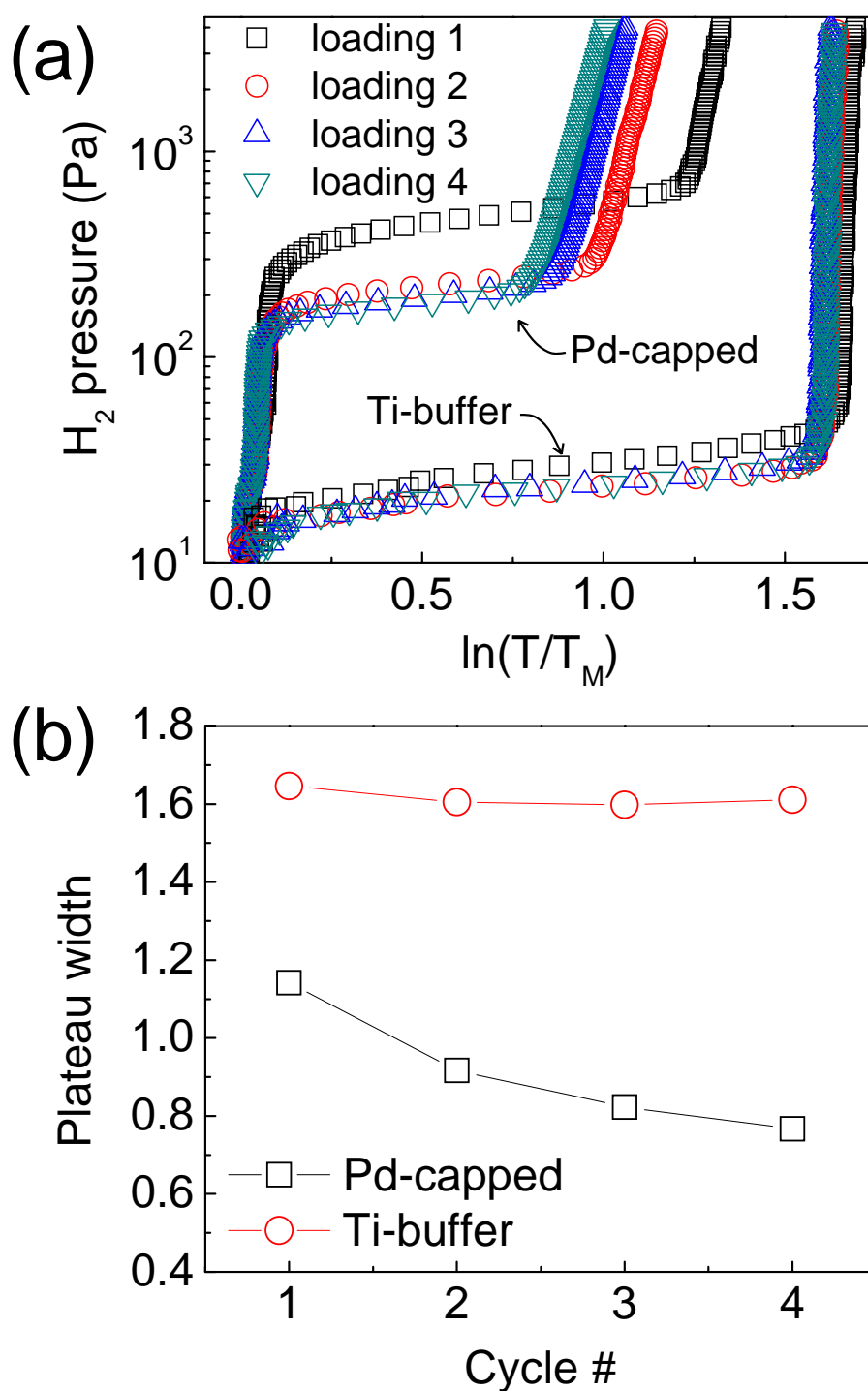


Figure 5.6: (a) PTIs of 20 nm thick Mg films both in the Pd-capped (top bundle of curves) and Ti-buffer (bottom bundle) geometries, for the first 4 hydrogenation cycles at 333 K. Note that the plateau pressures for all the cycles, except the first one, remain unchanged. (b) Evolution of the plateau width upon cycling.

the alloying between Mg and Pd, triggered by the absorption of hydrogen, continues even after the first hydrogen absorption. On the contrary in the Ti-buffer sample the Ti layer acts as a blocking barrier for atomic diffusion, preventing the formation of Mg-Pd alloy and resulting in pressure plateaus of practically constant width. The decrease in plateau pressure observed for the Pd-capped sample between the first and second cycle is most likely due to the partial release of stresses generated by the Pd clamping. Such relaxation is in fact absent in the Ti-buffer sample. In Fig. 5.7 we show the loading isotherms measured on a Mg sample deposited in the following way: 10 nm of Ti are deposited on a 3 inch wide glass wafer, then 20 nm of Mg are added on top of Ti, subsequently 2 nm of Ti are deposited with the use of a mask only on certain regions of the wafer in order to write “H₂”, finally 40 nm of Pd are added to protect the film from oxidation (Fig. 5.7a). With this sample architecture we are able to compare the behavior of a Pd-capped and a Ti-buffer Mg film, in the same specimen and under identical experimental conditions. When exposed to increasing hydrogen pressures at 333 K the film exhibits the following loading sequence (Fig. 5.7b): 1) for hydrogen pressures $p_{\text{H}_2} < 40$ Pa the film is everywhere metallic and no light is transmitted through it; 2) for $40 < p_{\text{H}_2} < 150$ Pa the regions of the sample containing a Ti-buffer layer load completely, forming the transparent MgH₂, while the Pd-capped regions remain metallic; 3) for $p_{\text{H}_2} > 150$ Pa also the Pd-capped regions form the hydride and the sample becomes completely transparent. The plateau width for the loading isotherms of the Ti-buffer areas in Fig. 5.7b is wider than for the Pd-capped regions. This indicates that Mg-Pd alloy has been significantly formed only in the latter. A Ti layer as thin as 2 nm is apparently thick enough to prevent Mg-Pd alloy formation and to produce remarkably different thermodynamic properties. The presence of a Ti-buffer layer also induces different kinetics of hydrogen desorption, as shown in Fig. 5.7c. When the sample is exposed to oxygen in a 20%O₂/Ar mixture at 333 K, the Ti-buffer regions unload much faster than the Pd-capped ones. This kinetic effect is on one end due to the absence of Mg-Pd alloy at the Mg/Pd interface. Doping Mg with Pd, in fact, enhances the kinetics of hydrogen absorption, but the desorption rates for these alloys are very low [75]. On the other hand it is well-known [133] that a hydrogen absorbing material (M) covered with a transition metal (TM) exhibits a fast unloading rate when the enthalpies of hydride formation for the two materials are such that: $\Delta H_{\text{TM}} < \Delta H_{\text{M}} < 0$. In our samples Mg covered with Ti ($\Delta H_{\text{Ti}} = -130$ kJ/molH₂ < $\Delta H_{\text{Mg}} = -74.4$ kJ/molH₂) shows indeed faster kinetics than Mg covered with Pd ($\Delta H_{\text{Pd}} = -38$ kJ/molH₂ > $\Delta H_{\text{Mg}} = -74.4$ kJ/molH₂).

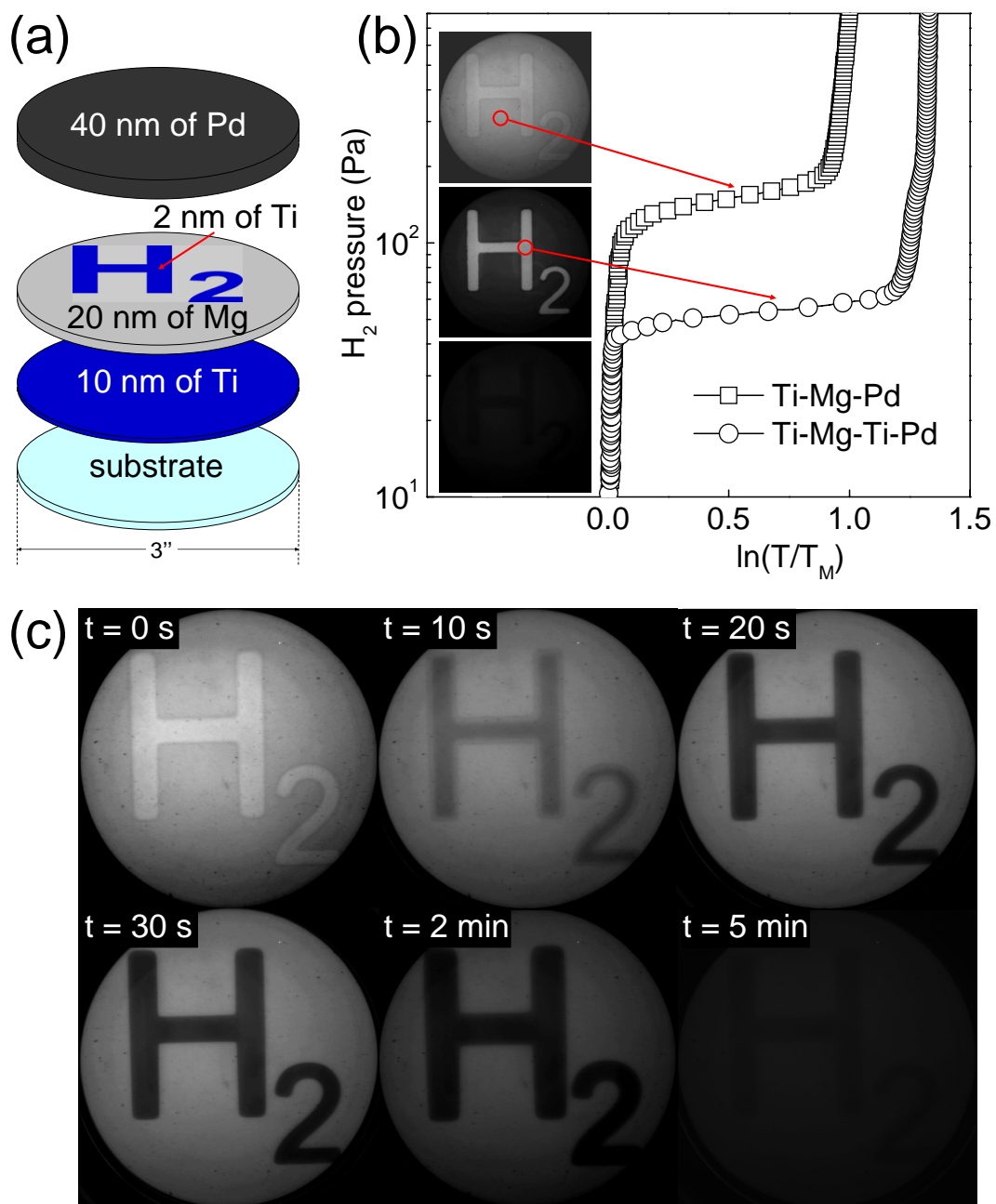


Figure 5.7: Mg sample deposited on a glass wafer and partially covered with a 2 nm thin Ti layer. (a) Sketch of the sample architecture. (b) PTIs measured during loading at 333 K. (c) Unloading sequence of the same sample when exposed to 10^5 Pa of 20% O_2 /Ar mixture at 333 K.

5.3.4 Conclusions

In conclusion we have shown that it is possible to dramatically change the thermodynamic properties of a thin metallic film by means of very little changes in the architecture of the samples. Surface energy effects are to be ruled out as a possible source of destabilization in clamped Mg films. The insertion of a buffer layer suppresses the formation of Mg-Pd alloy at the Mg/Pd interface. This effect is responsible for the enhanced cycling stability and improved performances reported for buffer-layer-inserted switchable mirrors [148, 149, 150]. Our results provide insights into the microstructural, thermodynamic and kinetic aspects of Pd-capped hydrogen-absorbing thin films used in technological applications, such as switchable mirrors [11] and optical hydrogen sensors [23].

Chapter 6

Energy Outlook

According to the “PhD Comics” author Jorge Cham, a Ph.D. thesis should end with two chapters: “*Stuff you’re supposed to be doing now*” and “*Make stuff up*”. For space reasons I will collapse them into one *stuff*... The aim is to give the reader an idea of the research that I am presently carrying out and that might be further developed in the future, starting from the findings discussed in this thesis.

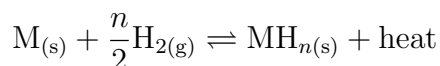
6.1 Introduction

In 2008, between 80 and 90 percent of the energy consumed globally was provided by fossil fuels (mainly oil, coal and natural gas). Fossil fuels are non-renewable resources and, although some controversy exists on the timescale of their depletion, their reserves are being rapidly consumed by an ever increasing global energy demand. It is clear that a major challenge in the coming years will be to develop radically new energy technologies capable of diminishing the world’s dependence on fossil fuels in the long run. Great expectations in this respect are placed upon renewable energy sources such as hydropower, geothermal, solar, wind and tide, which have the advantage of being “naturally replenished”.

In order to undertake such an energy paradigm shift we have to tackle some fundamental and technological issues related to the large scale applicability of renewable energy sources. A major concern is their intermittency: solar energy can only be captured during daylight, wind does not blow constantly, tides have specific cycle periods, just to mention a few examples. The problem of discontinuous delivery calls for a practical, safe and efficient way of storing energy. Hydrogen (H_2) has been proposed as a potential candidate both as energy storage material and as energy vector for mobile applications, thanks to an energy density *per mass unit* three times larger than gasoline and to its clean combustion process, the only exhaust product being water. A major obstacle to its applicability, however, is its low density: in order to achieve sufficient energy densities *per volume unit*, hydrogen has to be liquified at 20 K or compressed to 400 bar. Alternatively, hydrogen can be absorbed into

compounds such as metal- and complex-hydrides where, at room temperature and 1 bar of pressure, it reaches densities 2 times larger than pure liquid H₂.

The ability of some metals to absorb large amounts of hydrogen is known since the 19th century. The absorption reaction is generally exothermic and can be written as



The heat released by the absorption process is a key parameter to take into account, as it is the heat which has to be provided to the metal-hydride to desorb hydrogen. In mobile application, where metal-hydrides are used in combination with a fuel cell, a hydrogen storage system should be capable of releasing 1 bar of hydrogen at room temperature. Unfortunately there is no hydrogen absorbing material with such optimum thermodynamic properties, combined with fast kinetics of hydrogen uptake and release and high hydrogen densities (both per unit mass and per unit volume). It is for this reason that scientists are trying to modify (“tune”) the thermodynamics of hydrogen absorption in metals. Several approaches, such as alloying and nano-structuring, are currently taken into consideration.

In Chapter 5 we have seen that covering a thin Mg film with a Pd cap layer generates an elastic clamping that dramatically influences the thermodynamics of hydrogen absorption. Such an effect is highly desirable, but in order to be technologically viable many open questions need yet to be answered:

- *Is it possible to generalize the effect observed in a bi-dimensional thin film to a 3D nanoparticle?*
- *Is it possible to obtain similar clamping with different (cheaper, lighter) materials than palladium?*
- *Is there any other phenomenon, such as surface energy and quantum size effects, playing a significant role at the explored nanometer scale?*
- *Is the observed elastic effect altering the desorption isotherm as well as the absorption one? Is the loading-unloading hysteresis affected?*
- *Given the safety issues related to a possible “hydrogen economy” and the importance of a safe and reliable hydrogen detection system, is it possible to exploit the elastic clamping effect in advanced optical hydrogen sensors?*

In the following sections we briefly describe the research currently ongoing in our laboratory in some of these areas.

6.2 Elastic clamping in 3D

The elastic model developed for a bilayer in Appendix C can be extended to a three-dimensional system such as a spherical particle. Assuming perfect elastic behavior, a Mg nanoparticle with a radius of 10 nm, covered with a “skin” of MgO of 1.7 nm would have an equilibrium hydrogen pressure ~ 2000 times higher than bulk Mg at the same temperature [151]. This theoretical prediction has not yet been verified, but Mg nanoparticles covered with a MgO layer have been prepared by gas phase synthesis [152, 153, 154] and the study of their hydrogen absorption thermodynamics is currently under way.

Alternative methods to obtain 3D confinement include the deposition of Mg thin films onto patterned substrates and the encapsulation of Mg nanoparticles into nanoporous scaffolds. The inclusion of Mg into the pores of a scaffold has been successfully obtained both by infiltration of molten magnesium into nanoporous carbon [155, 156] and by infiltration of dibutylmagnesium into a carbon aerogel scaffold [157]. Although these systems have been characterized with respect to their hydrogen sorption properties, our studies suggest that the elastic influence of the scaffolds, which has not yet been taken into account, might play a dominant role and could be used to optimize the performances of these materials.

6.3 New materials

Due to the high costs of Pd, its use as a clamping agent is not optimal in the perspective of a potential commercial application. Furthermore, palladium is a heavy element and significantly reduces the gravimetric density of hydrogen in a Pd-capped Mg layer. We therefore began to study various materials, capable of clamping magnesium and permeable to hydrogen. Promising results have so far been obtained with Mg/Al multilayers. Aluminum is much lighter and cheaper than palladium and forms stable compounds with magnesium, suggesting that clamping effects might arise at Mg/Al interfaces due to the alloying of the two elements.

We studied the hydrogenation properties of Mg/Al multilayers with the following geometries: $8x[\text{Al}(z \text{ nm})\text{Mg}(5 \text{ nm})]/\text{Al}(z \text{ nm})/\text{Pd}(10 \text{ nm})$, with $z = 0.5, 1.0$ and 1.5 nm . The reflection and transmission spectra of the as-deposited and hydrogenated states can only be interpreted assuming strong intermixing of Mg and Al at the Mg/Al interfaces. Fig. 6.1 shows the loading isotherms measured on the Mg/Al multilayers at 333 K. As predicted by the clamping model, the plateau pressure strongly depends on the Al thickness z : the thicker the Al layers the higher the equilibrium pressure for hydride formation.

Although further investigations are needed to study the reversibility and the kinetics of hydrogen absorption in such multilayers, these results demonstrate that it is possible to “destabilize” the formation of MgH_2 , without sig-

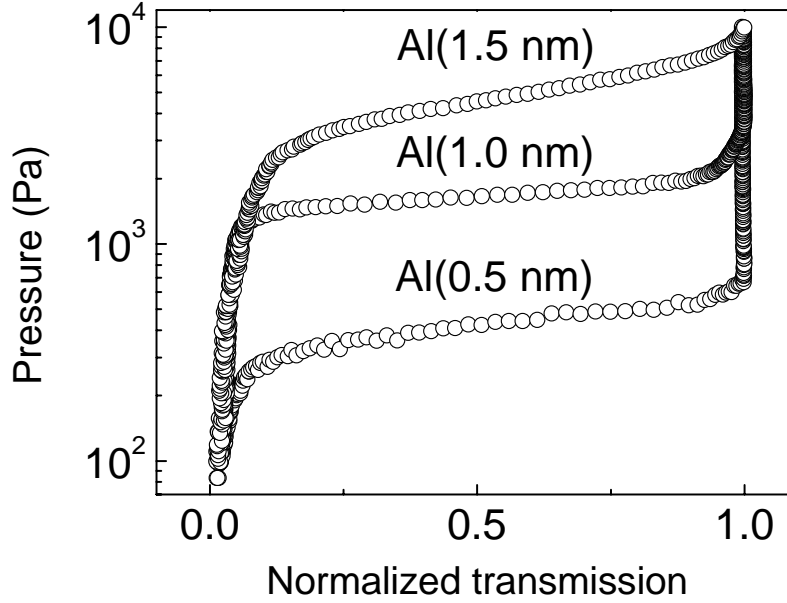


Figure 6.1: Loading isotherms measured at 333 K on Pd-capped Mg/Al multilayers with 8 bilayer repetitions, Mg thicknesses of 5 nm and Al thicknesses of 0.5, 1.0 and 1.5 nm.

nificantly affecting the storage capacity of magnesium.

6.4 Surface energy

According to the elastic model developed to explain the clamping effect of a cap layer [52], the plateau pressure of a clamped film, p^* , depends on the film thickness d as:

$$\ln p^* \propto \frac{1}{a + b \cdot d}$$

A similar dependence is expected for surface energy contributions in nanostructured metal hydrides [132, 158, 159]. A thin film of a metal M feels a surface energy contribution to the free energy of hydride formation of the type:

$$\Delta G(r)_{\text{surf}} = \frac{2V_M E_{M \rightarrow \text{MH}_2}(\gamma, r)}{d}$$

where V_M is the molar volume, d is the film thickness and $E_{M \rightarrow \text{MH}_2}(\gamma, r)$ is the difference in surface energy between the metal and the hydride, adjusted by the change in volume. Up to now such destabilization failed to be detected experimentally due to the very small effects involved: for metallic Mg nanoparticles, significant contributions are expected only for radii smaller than 10 nm [132]. However, in our study on Mg/Ti multilayers presented in Chapter 4, we have observed an increase in the plateau pressure for Mg thicknesses smaller

than 20 nm, which could not be directly attributed to elastic effects and could instead originate from surface energy contributions (see Fig. 6.2). By playing

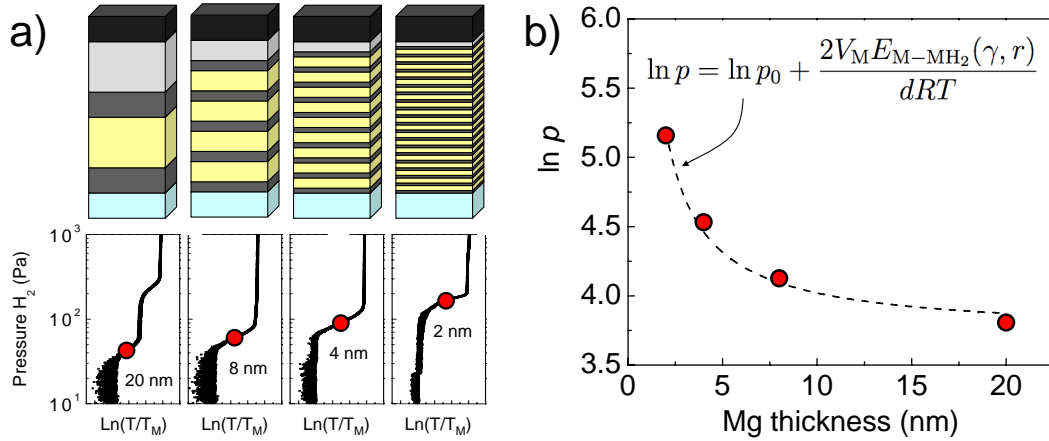


Figure 6.2: a) Rearrangement of Fig. 4.17. The red dots indicate the loading pressure of the Ti-sandwiched Mg layers. b) Equilibrium pressure of the Ti-sandwiched Mg layers as a function of the magnesium thickness. The dashed line is a fit to the data using the equation including surface energy contribution, with $p_0 = 40$ Pa and $E_{M-MH_2}(\gamma, r) = 0.24$ J/m².

with the geometries of Mg/Ti multilayers we therefore expect to be able to give a first reliable experimental proof of surface energy effects in metal hydrides.

The use of a thin film approach to investigate the role of surface energy contributions at the nanoscale could also be beneficial for the study of new Li-ion batteries based on nanoscale lithium intercalation compounds. In these systems, in fact, surface and interface effects seem to play a crucial role in determining the voltage profile during battery charging [160].

6.5 From optical hydrogen detectors to optical hydrogen sensors

An optical thin film hydrogen detector is a device that makes use of the changes in optical appearance occurring upon hydrogenation of a switchable mirror. In 2007 Slaman and co-workers reported on the implementation of a Pd-capped Mg-Ti thin film, as a sensing layer deposited on top of an optical fiber: when exposed to H₂ the Mg-Ti film absorbs hydrogen and switches from a reflecting to an absorbing state, changing the amount of light reflected in the optical fiber.

This is, however, a “binary” device, which only detects whether or not the H₂ pressure is higher than the equilibrium pressure of the switchable mirror, without giving further indications on the gas concentration in the atmosphere. In order to go from an optical hydrogen detector to an optical hydrogen sensor,

we need therefore a system whose optical response is directly proportional or at least a smooth and monotonous function of the hydrogen concentration.

The possibility to tune the equilibrium hydrogen pressure of magnesium by means of elastic clamping triggered the idea of using multilayered Mg-based films as advanced hydrogen sensing systems. If the equilibrium hydrogen pressure depends on the elastic constraints, by piling up many Mg films with different clamping, one can hope to produce a layered film whose optical response varies as a function of hydrogen pressure.

In Chapter 5 we have already seen an example of a two-step hydrogen sensor: the hydrogen loading isotherm of a Ti/Mg/Ti/Mg/Pd film has two distinct plateaus, corresponding to the hydrogenation of the two Mg layers at different pressures (see Fig. 5.1). The Mg layers show different thermodynamics because of the clamping effect of Pd on the top layer. By extending the same reasoning it is possible, by proper choice of the sample geometry, to obtain a system with three different optical responses in three different pressure regimes. In Fig. 6.3 we show the hydrogen loading isotherm of a sample with 3 Mg layers sandwiched respectively between two Ti layers (bottom), between a Ti and a Ni layer (middle) and between two Ni layers (top). The isotherm

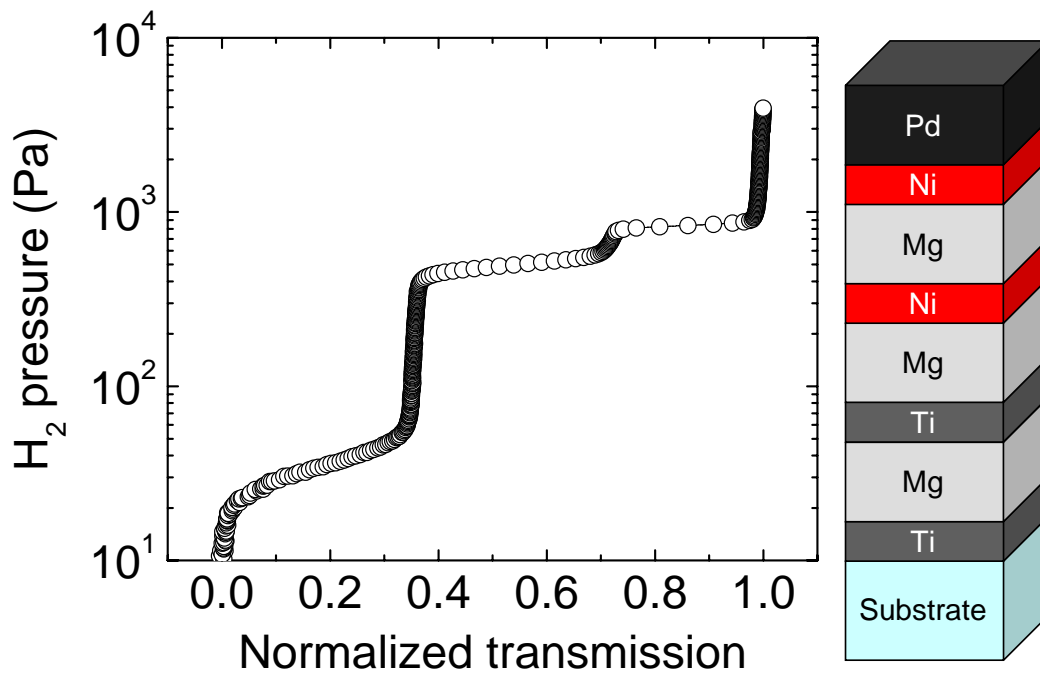


Figure 6.3: Loading isotherms measured at 333 K on a Pd-capped film with the geometry shown on the right of the plot. All the layers are 10 nm thick except for the Mg layers that are 20 nm thick.

shows three plateaus at three different hydrogen pressures, as a result of the differential clamping felt by each of the Mg layers. The bottom Mg layer loads

at the lowest pressure, being sandwiched between Ti layers, which do not exert any significant elastic constraint. The middle Mg feels the elastic constraint of one Ni layer and therefore loads at higher pressures and the top Mg layer is clamped on both sides and loads at an even higher pressure.

Although in this film the optical changes occur in transmission, it is possible to engineer a sample to be used on top of an optical fiber, whose response is maximized in reflection. In Fig. 6.4 we show the simulated optical reflection for a multilayer equivalent to the one shown in Fig. 6.3, but with varying thicknesses of the Mg layers. The reflection is calculated assuming light shining from the substrate side. The wavelength of commonly used and cheap LED is ~ 635 nm, corresponding to ~ 1.95 eV. As can be seen by the intersection of the vertical dashed line (centered at 1.95 eV) with the spectra in the four hydrogenation states, the amount of reflection of the sample can be taken as a clear indication of the number of Mg layers loaded and therefore of the surrounding hydrogen pressure.

6.6 Conclusions

Thanks to the recent advances in materials processing and synthesis, scientists can nowadays produce a cornucopia of *very small* structures (thin films, nanoparticles, nanotubes, nanowires, nanosprings, nanocrystals, nanoshells, etc.) with a remarkable control of their geometries. The physical properties of these materials dramatically differ from their large scale analogs. As we have seen in Chapter 5, for example, the clamping effect in thin Mg layers could only be observed at magnesium thicknesses smaller than ~ 50 nm, 2000 times thinner than an average human hair. Similarly, the surface energy effects of metal hydrides predicted by theory become relevant for particle sizes (film thicknesses) of few nanometers, only a *handful* of atoms. In metal hydrides these size effects are even more relevant, thanks to the peculiar long-range elastic interaction between hydrogen atoms dissolved in the metallic lattice. Such interaction is influenced by the shape and the dimensions of the metallic sample and can have a strong influence on the hydrogen sorption properties of materials.

The research presented in this final chapter aims at making a decisive step towards what might seem like a paradox: exploiting the hydrogen storage characteristics of *very small* objects in the perspective of *large scale* applications.

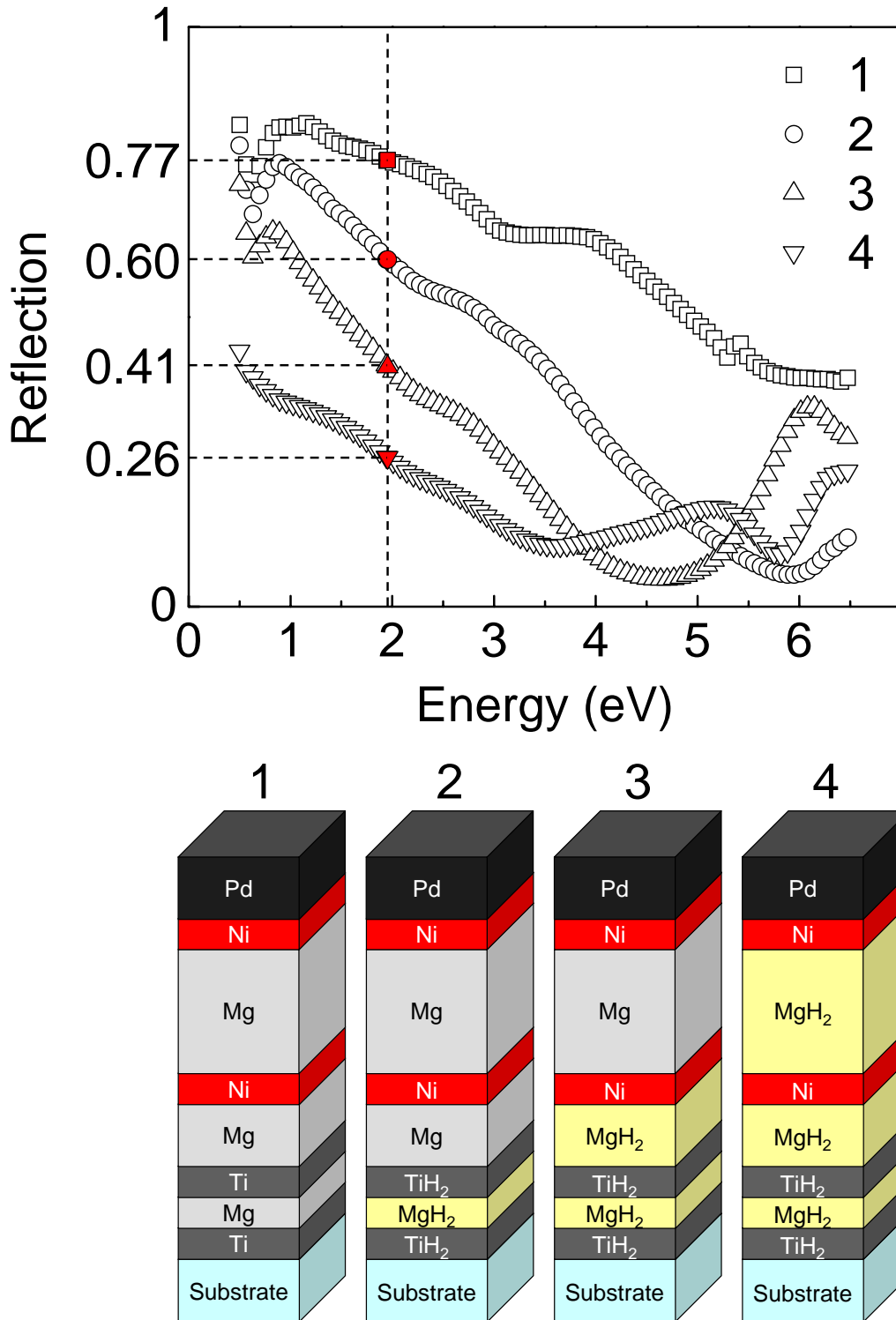


Figure 6.4: Simulated optical reflection, measured from the substrate side, for a multilayer as depicted in the cartoons, at 4 different stages of hydrogenations. The Ti and Ni layers are 5 nm thick, the Pd is 10 nm thick and the Mg layers are 5 (bottom), 10 (middle) and 20 (top) nm thick.

Appendices

Appendix A

Chemical short-range order

In section 1.5 we have introduced the concept of chemical short-range order. The definition we gave of the CSRO parameter “ s ” in eq. 1.3 was handy for our discussion, as it included quantities that are directly measurable by EXAFS. In the present Appendix we will show an equivalent and somewhat more rigorous way of defining the CSRO parameter and we will also give two examples of the possible influence of the chemical short-range order, on the transport properties of Mg-Ti thin films.

Let us consider a binary alloy A_xB_{1-x} in two dimensions. We can model it as a square matrix with side \sqrt{N} : the total amount of atoms is N and each atom has 4 nearest neighbors ($n_c = 4$), so that the total number of bonds, if the alloy is large enough to rule out surface effects, is $2N$, Fig. A.1. The

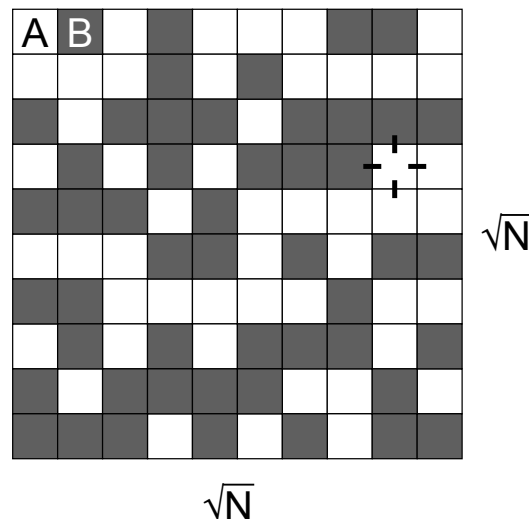


Figure A.1: Schematic representation of a bi-dimensional binary alloy.

probability of finding an A atom is of course $P_A = x$ and for a B atom is $P_B = 1 - x$. We define the chemical short-range order “ σ ” by writing the

probability of finding an A atom next to another A atom [105]:

$$P_{A/A} = x + \sigma(1 - x) \quad (\text{A.1})$$

Following the above definition, the probability of finding an A-A bond is

$$P_{AA} = P_A \cdot P_{A/A} = x[x + \sigma(1 - x)] \quad (\text{A.2})$$

and the total number of A-A bonds is

$$N_{AA} = 2N \cdot P_{AA} = 2Nx[x + \sigma(1 - x)] \quad (\text{A.3})$$

We show now that the two definitions in eq. 1.3 and A.1 are equivalent. Equation 1.3 can be rewritten as

$$s = 1 - \frac{n_{BA}}{n_c \cdot x} \cdot \frac{(1 - x)N}{(1 - x)N} = 1 - \frac{N_{BA}}{4xN(1 - x)} \quad (\text{A.4})$$

where N_{BA} is the total number of B-A bonds in the alloy and it is given by the product of the number of B-A bonds per B atom (n_{BA}) times the total number of B atoms ($(1 - x)N$). From eq. A.4 follows:

$$N_{BA} = 4xN(1 - x)(1 - s) \quad (\text{A.5})$$

The total number of bonds in the alloy is

$$2N = N_{BA} + N_{BB} + N_{AA} \quad (\text{A.6})$$

The number of B-B bonds is given by:

$$\begin{aligned} N_{BB} &= \frac{1}{2} [4(1 - x)N - N_{BA}] \\ &= \frac{1}{2} [4(1 - x)N - 4xN(1 - x)(1 - s)] \\ &= 2(1 - x)N [1 - x(1 - s)] \end{aligned} \quad (\text{A.7})$$

where the factor 1/2 is to avoid double counting. From eq. A.6 the total number of A-A bonds is

$$\begin{aligned} N_{AA} &= 2N - N_{BA} - N_{BB} \\ N_{AA} &= 2N - 4xN(1 - x)(1 - s) - 2(1 - x)N[1 - x(1 - s)] \\ N_{AA} &= 2Nx[x + s(1 - x)] \end{aligned} \quad (\text{A.8})$$

From eq. A.3 and A.8 we have $s = \sigma$ (Q.E.D).

The concept of chemical short-range order is crucial to understand the optical, structural and electrical properties of Mg-Ti thin films. In these metastable

alloys the Mg and Ti atoms are distributed along the sites of the hexagonal crystal lattice with a certain degree of chemical short-range order, leading to the coexistence of structurally coherent Mg-rich and Ti-rich regions. The intriguing spinodal-like microstructure triggers the question whether there might be percolation phenomena in the transport properties of these alloys. In the following two sections we briefly show that, although further investigations are necessary, both the electrical resistivity and the hydrogen diffusion properties of thin Mg-Ti films present unusual characteristics which might originate from a non-trivial microstructure.

CSRO and electrical resistivity?

The hydrogenated state of a 200 nm $\text{Mg}_{0.7}\text{Ti}_{0.3}$ film covered with 1 nm of Pd exhibits neither a metallic ($\rho \propto T$) nor a semiconducting ($\ln \rho \propto 1/T$) behavior: as shown in Fig. 3.4 the in-plane electrical resistivity decreases with the logarithm of the temperature ($\rho \propto -\ln T$). In Fig. A.2 we show the temperature dependence of the electrical resistivity of a 200 nm thick $\text{Mg}_{0.7}\text{Ti}_{0.3}$ film covered with 1 nm of Pd at different stages of hydrogenation. By using

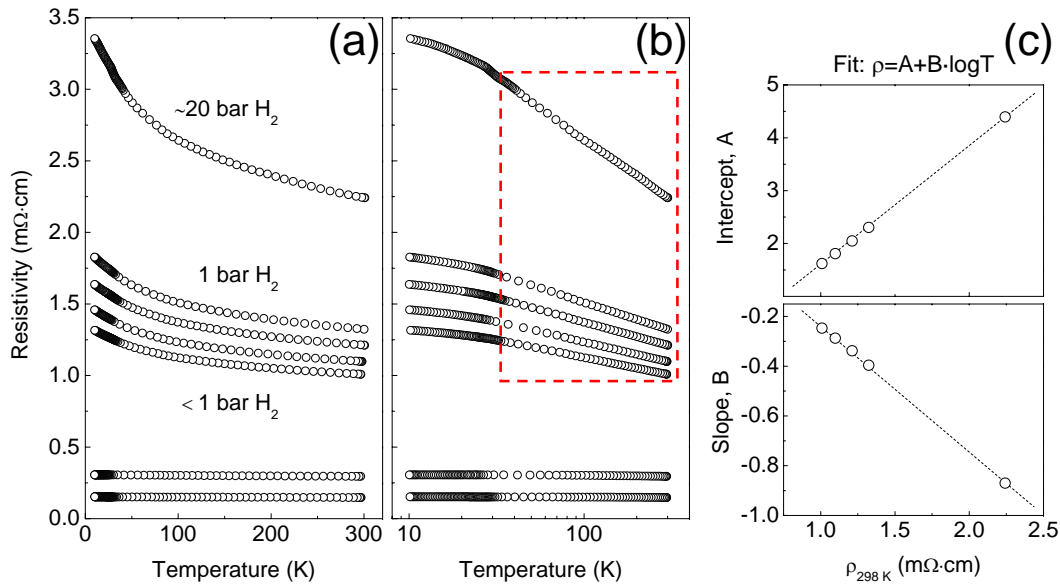


Figure A.2: (a) Temperature dependence of the in-plane electrical resistivity of a 200 nm thick $\text{Mg}_{0.7}\text{Ti}_{0.3}$ film covered with 1 nm of Pd, with varying hydrogen content. (b) Same as (a) but with a logarithmic x -axis. The dashed rectangle indicates the curves and the regions on which a linear fit is performed. (c) Intercept and slope parameters used in the linear fit of the curves in figure (b), plotted as a function of the resistivity at room temperature. The dashed lines are a guide to the eye.

only 1 nm of Pd it is possible to hydrogenate the sample, but dehydrogenation is extremely slow: in each cooling experiment the sample is loaded in hydrogen

atmosphere up to a certain hydrogen concentration, monitored by the electrical resistivity, then H_2 is replaced by He and the sample is cooled down to 10 K.

A logarithmic temperature dependence has already been observed in a few other systems, such as granular niobium nitride cermets [78], $Nd_{2-x}Ce_xCuO_{4-y}$ pellets [161], granular 3D Al-Ge films [162] and $YH_{3-\delta}$ thin films [79]. In 2003 Efetov and Tschersich [163] triggered by the results on granular 3D Al-Ge films, published a theoretical calculation of the electronic properties of granular materials (for a review see the work of Beloborodov *et al.* [164]). Their study shows that for a highly connected dispersion of metallic grains the electrical *conductivity* has a logarithmic dependence on temperature. In many experiments, including ours, however, the logarithmic dependence is found for the electrical *resistivity*, a phenomenon which is still without explanation*.

Nevertheless, it seems that such a peculiar temperature dependence of the resistivity must be connected with a certain degree of granularity of the material and, in the hydrogenated state of our Mg-Ti thin films, we have indeed coexistence of metallic TiH_2 and insulating MgH_2 domains. The increase in resistivity upon cooling might be related to a reduced tunneling probability between conducting regions separated by an insulating matrix [165].

The straightforward dependence of the fit parameters on the resistivity measured at room temperature is also intriguing, being the resistivity directly proportional to hydrogen concentration: Fig. A.2c shows that there must be a very simple relation, and possibly a simple theory, between the hydrogen content and the temperature dependence of the resistivity.

In order to correlate the “logT” dependence to the granular microstructure of the Mg-Ti thin films, a more extensive study, well beyond the scope of the present thesis, is needed. The investigation should focus on the electrical behavior of samples with various compositions and chemical short-range order parameters. The chemical short-range order could be tuned by changing the substrate temperature during the films deposition. An alternative method is to measure the out-of-plane resistivity of hydrogenated Mg/Ti multilayers with various periodicities: in this way the tunneling distance between conducting TiH_2 layers is simply given by the thickness of the MgH_2 layers.

CSRO and hydrogen diffusion?

Understanding the diffusion properties of hydrogen in Mg-Ti thin films is important for application of these materials as hydrogen storage media in batteries [35], as sensing layers in optical hydrogen sensors [23] and as smart coatings for solar collectors [21, 22]. The advantage of switchable mirrors lies

*The discrepancy between the theory, predicting a logarithmic divergence of the conductivity, and many experiments showing a logarithmic divergence of the resistivity, is also acknowledged by Beloborodov and co-workers [164]. However, their incredible conclusion is that “A more careful experimental study might clarify this question”... As the economist Robert S. Goldfarb puts it “if the data do not fit the theory, too bad for the data”.

in the possibility of studying hydrogen diffusion phenomena by optical means [166, 167]. In order to study hydrogen diffusion in Mg-Ti thin films we monitor the change in optical appearance between the reflecting metallic state and the black absorbing hydrogenated state. Although it is known that Ti-doping enhances the kinetics of hydrogen absorption we find that, beyond a certain Ti concentration its effects become deleterious, effectively reducing hydrogen diffusion through the material. A tentative explanation of this threshold could be given in the framework of percolation theory.

$\text{Mg}_y\text{Ti}_{1-y}$ films with a thickness of 100 nm are deposited in a UHV chamber (base pressure $< 10^{-6}$ Pa) by RF/DC Ar magnetron sputtering on glass substrates at room temperature. All the films are half-covered with 100 nm of Pd, to catalyze hydrogen absorption. The area of the sample which is not covered by Pd does not uptake hydrogen and is covered by a thin oxide layer. The film composition is measured by means of X-Ray Diffraction (XRD), making use of the linear relation existing between lattice spacing and Ti atomic concentration in $\text{Mg}_y\text{Ti}_{1-y}$ thin film alloys [38]. Diffraction patterns of films deposited on Si(111) substrates are measured in a Bruker D8 Discover diffractometer equipped with a two-dimensional detector. The diffusion measurements are performed in a loading cell connected to a gas flow controller and equipped with a transparent window. The cell is placed under an optical microscope (Olympus BX60F5) with a 3CCD camera (SONY DXC-950P) for image recording and it is flushed with Ar at 353 K for 1 hour before loading with hydrogen. During the diffusion experiment the cell is flushed with 8% H_2 in Ar at atmospheric pressure and 353 K. Upon hydrogen injection the Pd-covered part of the sample loads in few seconds while the “naked” Mg-Ti alloy remains metallic. Hydrogen then diffuses towards the metallic part of the sample and the diffusion process is measured by following the change in optical appearance of the sample in reflection mode. A LabVIEW software allows to control both the gas flow and the images acquisition. The temperature of the sample is controlled by a Pt100 thermocouple in direct contact with its surface. Good thermal contact between the sample and the thermocouple is achieved by use of a thermal contact paste and the temperature is maintained constant with an accuracy of 0.1 degree. A cartoon of the films geometry and the measurement concept is shown in Fig. A.3a.

A typical diffusion experiment consists of 20 hours of measurement with an acquisition rate of 1 frame/minute. The images are then analyzed in a Matlab-based software which allows to average over a wide area of the sample and to achieve very high signal-to-noise ratios. Three images collected at different times from a $\text{Mg}_{0.7}\text{Ti}_{0.3}$ sample measured at 353 K are shown in Fig. A.3b, together with their corresponding intensity profiles. In order to measure the distance traveled by the hydrogen front we applied several image analysis algorithms and found that the most reliable procedure is to measure the width of the hydrogenated (black) sample at a certain fixed percentage, α , of the

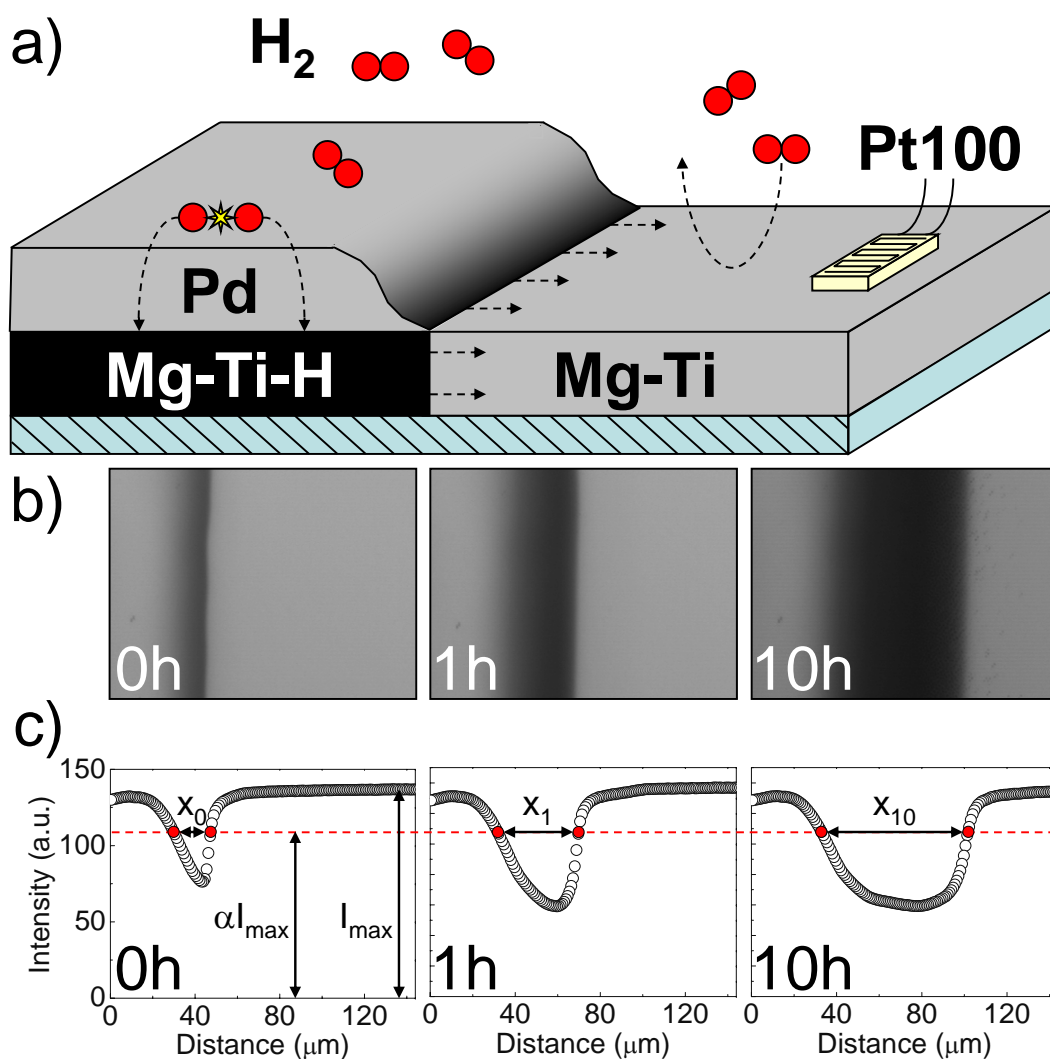


Figure A.3: a) Schematic experiment design: after being absorbed in the Mg-Ti alloy covered with Pd, hydrogen diffuses in the metallic part of the sample. The change in reflectance upon hydrogenation is followed optically with a microscope. b) Optical microscope images of a $\text{Mg}_{0.7}\text{Ti}_{0.3}$ alloy just after introduction of hydrogen in the cell (left) and after 1 (center) and 10 hours (right). c) Intensity profiles for the images in Fig. A.3b.

maximum intensity value (see dashed line in Fig. A.3b). If w_t is the width of the black area at time t , we find experimentally that the position of the hydrogen diffusion front x_f is given by

$$x_f = w_t - w_0 = \sqrt{K(t - t_0)} \quad (\text{A.9})$$

In Fig. A.4 the width w of the black hydrogenated sample is plotted as a function of time for a $\text{Mg}_{0.7}\text{Ti}_{0.3}$ sample. Fitting the data with eq. A.9 gives us three fit parameters: the width offset (w_0), the time offset (t_0) and the hydrogen front mobility (K). In the fit we neglect the first hour of measurements to remove the transient effect of increase in hydrogen partial pressure, which occurs at the beginning of the diffusion experiment when switching from pure Ar flow to H_2/Ar mixture.

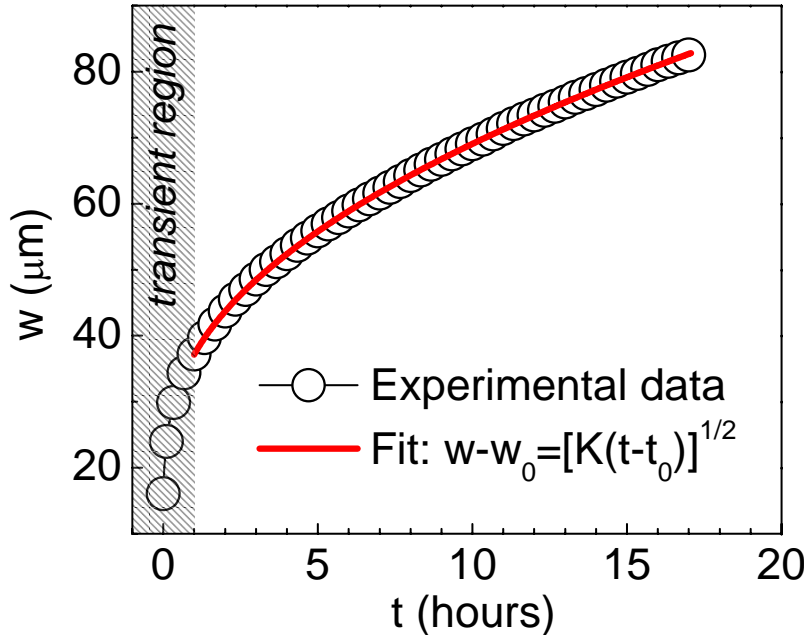


Figure A.4: Time dependence of the experimental (circles) and fitted (line) width w of the black hydrogenated area for a $\text{Mg}_{0.7}\text{Ti}_{0.3}$ alloy. The grey area at the beginning of the diffusion process is the transient region neglected in the fit. Only 4% of the experimental data points are shown.

In Fig. A.5 the composition dependence of the fitted hydrogen front mobility K is shown for all the measured Mg-Ti alloys. As expected [21] increasing Ti concentration enhances hydrogen diffusion in the $\text{Mg}_y\text{Ti}_{1-y}$ alloy. The effect of Ti is to stabilize the formation of a cubic $\text{Mg}_y\text{Ti}_{1-y}\text{H}_x$ hydride rather than the usual tetragonal MgH_2 , therefore enhancing the kinetics of hydrogen motion in the alloy. Rather surprisingly, however, the hydrogen mobility appears to have a sudden decrease for $y < 0.65$. The presence of this diffusion barrier is intriguing and our hypothesis is that it might originate from a

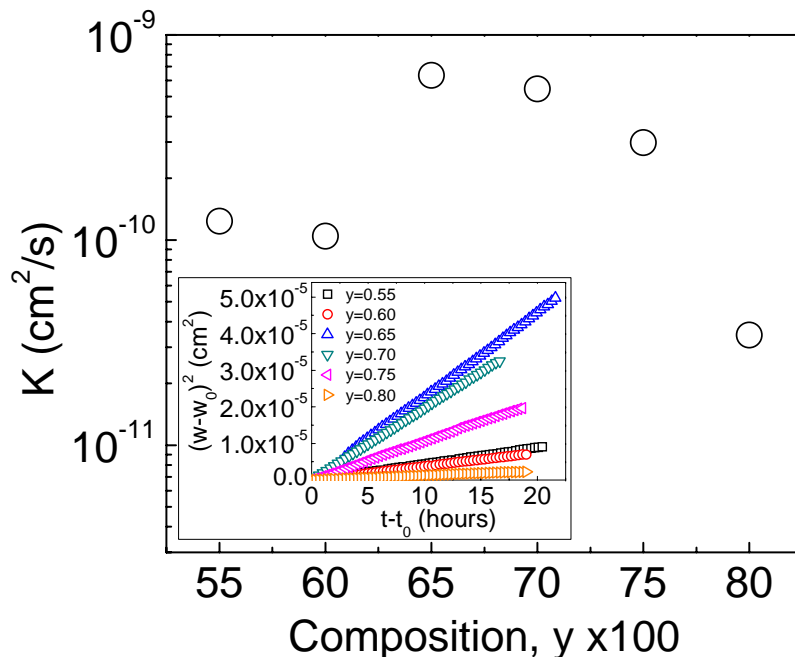


Figure A.5: Composition dependence of the hydrogen front mobility, K , for $\text{Mg}_y\text{Ti}_{1-y}$ alloys with $y = 0.55, 0.60, 0.65, 0.70, 0.75,$ and 0.8 . Inset: w^2 VS t plots for all the compositions explored, where the linear relation is a “footprint” of diffusion.

percolation threshold, due to the differential hydrogen affinity of Mg and Ti. As a tentative mechanism we assume that a hydrogen atom, diffusing through the interstitial sites of the alloy, is irreversibly trapped in Ti sites and is only allowed to move on Mg sites. This is justified by the lower enthalpy of hydride formation reported in literature for Ti ($-70 \text{ kJ}(\text{mol H})^{-1}$) with respect to Mg ($-37 \text{ kJ}(\text{mol H})^{-1}$) and by experimental evidence showing that, when loading Mg-Ti thin films, a fraction of hydrogen atoms remains trapped into the alloy as a result of irreversible bonding with Ti atoms [38, 35, 36]. The site percolation thresholds for a 2D square lattice and a 3D cubic lattice are ~ 0.6 and ~ 0.3 , respectively [168], suggesting that the observed diffusion threshold at about 0.6 might be due to the reduced dimensionality of the thin films. At the moment, however, we cannot exclude different diffusion mechanisms or influences coming from the preferential oxidation of the Ti-rich alloys and further investigation is needed to clarify these findings.

Appendix B

Beer-Lambert Law

Given the layered structure of many of our samples let us consider a Pd-capped Mg/Ti multilayer, $Nx[\text{Ti}(z)\text{Mg}(2z)]$. From the Beer-Lambert law, we have:

$$T_M = (T_{\text{Ti}}T_{\text{Mg}})^N T_{\text{Pd}} = (e^{-zN\alpha_{\text{Ti}}}e^{-2zN\alpha_{\text{Mg}}}) T_{\text{Pd}} \quad (\text{B.1})$$

where α_{Ti} and α_{Mg} are the absorption coefficients of Ti and Mg, respectively. In these samples the optical change occurring upon hydrogenation in the Ti and Pd films is negligible: at the pressures and temperatures explored in the present thesis Pd does not hydrogenate and Ti forms a metallic TiH_2 hydride ($\alpha_{\text{TiH}_2} \approx \alpha_{\text{Ti}}$). During loading Ti layers hydrogenate at very low hydrogen pressures without contributing significantly to the total optical change in the multilayer; at higher pressures however Mg begins to absorb a lot of hydrogen and, if we neglect the small optical changes occurring in the diluted α phase, when a fraction χ of Mg is fully hydrogenated we have:

$$\begin{aligned} T &= (T_{\text{TiH}_2}T_{\chi\text{MgH}_2}T_{(1-\chi)\text{Mg}})^N T_{\text{Pd}} \approx \\ &\approx (T_{\text{Ti}}T_{\chi\text{MgH}_2}T_{(1-\chi)\text{Mg}})^N T_{\text{Pd}} \\ &= N (e^{-zN\alpha_{\text{Ti}}}e^{-2zN\chi(1+\delta_z)\alpha_{\text{MgH}_2}}e^{-2zN(1-\chi)\alpha_{\text{Mg}}}) T_{\text{Pd}} \end{aligned} \quad (\text{B.2})$$

where the term $(1 + \delta_z)$ accounts for the thickness expansion occurring upon hydrogen absorption in Mg. The logarithm of the relative increase in optical transmission is then given by:

$$\ln \frac{T}{T_M} = 2zN [\chi\alpha_{\text{Mg}} - (1 + \delta_z)\alpha_{\text{MgH}_2}] \quad (\text{B.3})$$

MgH_2 , however, is an insulator with a very large optical band gap of 5.6 eV [19] and, in first approximation, we can assume that it is completely transparent to the light used in a hydrogenography experiment ($1.1 < \hbar\omega < 3.3$ eV [12]). Thus we take $\alpha_{\text{MgH}_2} \approx 0$ and Eq. B.3 reduces to:

$$\ln \frac{T}{T_M} = 2zN\chi\alpha_{\text{Mg}} \quad (\text{B.4})$$

The quantity $\ln T/T_M$ is directly proportional to the total Mg thickness ($2zN$) and to the fraction χ of MgH_2 in the multilayer. We can therefore directly relate the Pressure-Optical transmission-Isotherms (PTIs) obtained by hydrogenography, in which we plot the hydrogen pressure versus $\ln T/T_M$, to the standard Pressure-Composition-Isotherms (PCIs) measured for metal hydrides [13].

Appendix C

Elastic clamping model

Fundamental Equations

Young's modulus (E) is a measure of the stiffness of an isotropic elastic material

$$E = \frac{\sigma}{\varepsilon}$$

where σ is the stress in units of pressure and ε is the strain. For an isotropic material, the deformation in the direction of one axis produces deformations along the other axes. It is thus possible to generalize Hooke's Law for three dimensions:

$$\varepsilon^x = \frac{1}{E} [\sigma^x - \nu (\sigma^y + \sigma^z)]$$

$$\varepsilon^y = \frac{1}{E} [\sigma^y - \nu (\sigma^x + \sigma^z)]$$

$$\varepsilon^z = \frac{1}{E} [\sigma^z - \nu (\sigma^x + \sigma^y)]$$

where ν is the Poisson ratio. By definition all the tensile strains and stresses are positive and all the compressive ones are negative.

Hydrogen absorption in M

When hydrogen is absorbed in a metal M it induces an isotropic volume expansion given by:

$$\frac{\Delta V}{V} \approx 3 \frac{\Delta L}{L} = 3\varepsilon_H$$

If we assume the strain induced by hydrogen to be proportional to the hydrogen concentration c we can write:

$$\varepsilon_H = \alpha c$$

$$\frac{\Delta V}{V} = 3\alpha c$$

Clamping effects

In the x and y directions the stresses are built up so that S, the clamping layer, is expanded and M, the hydrogen-absorbing layer, is compressed (see Figure C.1). In the z direction there is no stress built up by the clamping between S

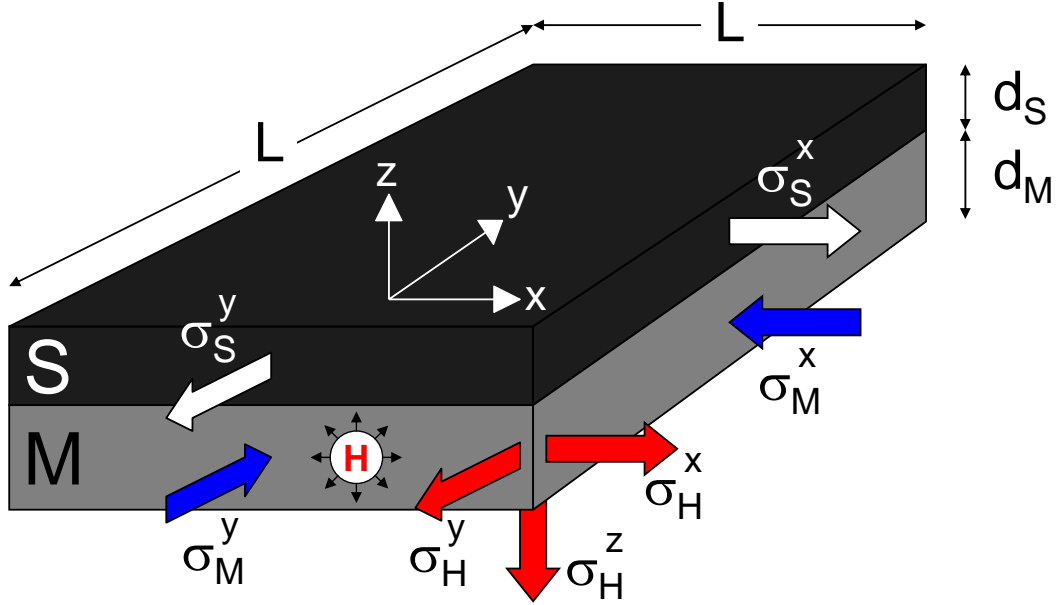


Figure C.1: Scheme of the strain components for two layers glued together, where the bottom layer, M, is capable of absorbing hydrogen.

and M: $\sigma_S^z = \sigma_M^z = 0$, but we have to take into account the strain along the z direction due to the Poisson ratio. In the xy plane the stresses are identical in the two in-plane directions: $\sigma_S^x = \sigma_S^y = \sigma_S$ and $\sigma_M^x = \sigma_M^y = \sigma_M$. Hence:

$$\varepsilon_S^x = \varepsilon_S^y = \frac{1}{E_S} [\sigma_S^x - \nu_S (\sigma_S^y + \overset{0}{\sigma_S^z})] = \frac{1}{E_S} (\sigma_S^x - \nu_S \sigma_S^y) = \frac{1}{E_S} \sigma_S (1 - \nu_S)$$

$$\varepsilon_M^x = \varepsilon_M^y = \frac{1}{E_M} [\sigma_M^x - \nu_M (\sigma_M^y + \overset{0}{\sigma_M^z})] = \frac{1}{E_M} (\sigma_M^x - \nu_M \sigma_M^y) = \frac{1}{E_M} \sigma_M (1 - \nu_M)$$

For simplicity we rewrite these two equations as follows:

$$\varepsilon_S = \frac{1}{E_S} \sigma_S (1 - \nu_S) \quad (\text{C.1})$$

$$\varepsilon_M = \frac{1}{E_M} \sigma_M (1 - \nu_M) \quad (\text{C.2})$$

In the z direction the M layer feels a tensile strain due to compression in the xy plane:

$$\varepsilon_M^z = \frac{1}{E_M} \left[\overset{0}{\sigma_M^z} - \nu_M (\sigma_M^x + \sigma_M^y) \right] = -\frac{1}{E_M} \nu_M (\sigma_M^x + \sigma_M^y)$$

which we rewrite

$$\varepsilon_M^z = -\frac{\nu_M}{E_M} 2\sigma_M \quad (\text{C.3})$$

Note that σ_M , being a compressive stress, is negative and the strain in the vertical direction ε_M^z is then positive.

Coupled strain in the xy plane

Since we assume that the two layers are glued to each other, the net displacements of the two layers in the xy plane must be equal. This means that the displacement of the M layer, given by the sum of the compressive strain due to clamping and the tensile strain due to hydrogen absorption, must be equal to the displacement on the S layer due only to clamping:

$$\varepsilon_H + \varepsilon_M = \varepsilon_S \quad (\text{C.4})$$

where, again, $\varepsilon_H = \varepsilon_H^{x,y}$, $\varepsilon_M = \varepsilon_M^{x,y}$, $\varepsilon_S = \varepsilon_S^{x,y}$. Note that ε_M , being a compressive strain, is negative.

Mechanical equilibrium

Furthermore the force acting on the M layer in the xy plane must be equal and opposite to the force acting on the S layer:

$$\sigma_M^{x,y} d_M L = -\sigma_S^{x,y} d_S L$$

or simply

$$\sigma_M d_M L = -\sigma_S d_S L$$

and

$$\sigma_S = -\sigma_M \frac{d_M}{d_S} \quad (\text{C.5})$$

By substituting equation C.5 in equation C.1 we obtain:

$$\varepsilon_S = -\frac{1}{E_S} \sigma_M (1 - \nu_S) \frac{d_M}{d_S} \quad (\text{C.6})$$

Substituting equations C.2 and C.6 into equation C.4 we obtain:

$$\sigma_M = \sigma_M^{x,y} = -\frac{\varepsilon_H}{1 - \nu_M} \cdot \frac{E_M}{\left(1 + \frac{E_M d_M}{E_S d_S} \frac{1 - \nu_S}{1 - \nu_M}\right)} \quad (\text{C.7})$$

Expansion of M

Substituting equation C.7 into equation C.3 gives:

$$\varepsilon_M^z = \frac{2\nu_M}{1 - \nu_M} \frac{1}{\left(1 + \frac{E_M d_M}{E_S d_S} \frac{1 - \nu_S}{1 - \nu_M}\right)} \cdot \varepsilon_H$$

In the xy plane the M layer feels the effect of both clamping from the S layer and the expansion due to hydrogen absorption. The total expansion in the xy plane is therefore:

$$\begin{aligned} \varepsilon_{M,tot}^{x,y} &= \varepsilon_{M,tot} = \varepsilon_H + \varepsilon_M = \varepsilon_H + \frac{1}{E_M} \sigma_M (1 - \nu_M) \\ &= \varepsilon_H \left[1 - \frac{1}{\left(1 + \frac{E_M d_M}{E_S d_S} \frac{1 - \nu_S}{1 - \nu_M}\right)} \right] \end{aligned} \quad (C.8)$$

The total volume expansion of the M layer can then be written:

$$\begin{aligned} \frac{\Delta V}{V} &= 3\varepsilon_H + \varepsilon_M^x + \varepsilon_M^y + \varepsilon_M^z \\ &= 3\varepsilon_H + 2\varepsilon_M^{x,y} + \varepsilon_M^z \\ &= 3\varepsilon_H + 2\varepsilon_M + \varepsilon_M^z \\ &= \varepsilon_H + 2(\varepsilon_H + \varepsilon_M) + \varepsilon_M^z \\ &= \varepsilon_H + 2\varepsilon_{M,tot}^{x,y} + \varepsilon_M^z \\ &= \varepsilon_H + 2\varepsilon_H \left[1 - \frac{1}{\left(1 + \frac{E_M d_M}{E_S d_S} \frac{1 - \nu_S}{1 - \nu_M}\right)} \right] + \frac{2\nu_M}{1 - \nu_M} \frac{1}{\left(1 + \frac{E_M d_M}{E_S d_S} \frac{1 - \nu_S}{1 - \nu_M}\right)} \varepsilon_H \\ &= 2\varepsilon_H \left[\frac{1}{2} + 1 - \frac{1}{(\dots)} + \frac{\nu_M}{1 - \nu_M} \frac{1}{(\dots)} \right] \\ &= 3\varepsilon_H \left[1 - \frac{2}{3} \cdot \frac{1 - 2\nu_M}{1 - \nu_M} \cdot \frac{1}{\left(1 + \frac{E_M d_M}{E_S d_S} \frac{1 - \nu_S}{1 - \nu_M}\right)} \right] \end{aligned} \quad (C.9)$$

Note that if the S layer (the clamping one) is very thick or very rigid ($d_S \gg d_M$ or $E_S \gg E_M$) the volume expansion reduces to:

$$\frac{\Delta V}{V} = 3\varepsilon_H \left[\frac{1 + \nu_M}{3(1 - \nu_M)} \right]$$

Enthalpy change

The volume dependence of the enthalpy of hydride formation is given by

$$\frac{d\Delta H_M}{d \ln V} = -B_M V_H \quad (C.10)$$

where V_H is the partial molar volume of hydrogen. We can therefore write:

$$\begin{aligned}
\delta\Delta H_M &= \Delta H_{M,sandwiched} - \Delta H_{M,free} \\
&= B_M V_H \left(\left. \frac{\Delta V}{V} \right|_{free} - \left. \frac{\Delta V}{V} \right|_{sandwiched} \right) \\
&= 3\varepsilon_H B_M V_H \left[\frac{2}{3} \cdot \frac{1 - 2\nu_M}{1 - \nu_M} \cdot \frac{1}{\left(1 + \frac{E_M}{E_S} \frac{d_M}{d_S} \frac{1 - \nu_S}{1 - \nu_M}\right)} \right] \quad (C.11)
\end{aligned}$$

From the van't Hoff equation, using the subscript “*f*” for “free” and “*s*” for “sandwiched”, we have:

$$\begin{aligned}
\frac{1}{2} \ln p_f &= \frac{\Delta H_f}{RT} - \frac{\Delta S^0}{R} \\
\frac{1}{2} \ln p_s &= \frac{\Delta H_s}{RT} - \frac{\Delta S^0}{R} = \frac{\Delta H_f + \delta\Delta H_M}{RT} - \frac{\Delta S^0}{R} \\
\frac{1}{2} \ln \left(\frac{p_s}{p_f} \right) &= \frac{\delta\Delta H_M}{RT} \\
\frac{p_s}{p_f} &= \exp \left(2 \frac{\delta\Delta H_M}{RT} \right) \quad (C.12)
\end{aligned}$$

where enthalpies are expressed in J/molH.

Substituting equation C.11 in C.12 we obtain finally:

$$\frac{p_s}{p_f} = \exp \left\{ 2 \frac{3\varepsilon_H B_M V_H}{RT} \left[\frac{2}{3} \cdot \frac{1 - 2\nu_M}{1 - \nu_M} \cdot \frac{1}{\left(1 + \frac{E_M}{E_S} \frac{d_M}{d_S} \frac{1 - \nu_S}{1 - \nu_M}\right)} \right] \right\} \quad (C.13)$$

which is equivalent to Eq. 5.1 of Section 5.2.

A useful expression is obtained for the logarithm $\ln p_s/p_f$:

$$\left[\ln \left(\frac{p_s}{p_f} \right) \right]^{-1} = I + S \frac{d_M}{d_S} \quad (C.14)$$

with

$$I = \frac{\tilde{E}}{E_M} (1 - \nu_M) \quad (C.15)$$

and

$$S = \frac{\tilde{E}}{E_S} (1 - \nu_S) \quad (C.16)$$

where $\tilde{E} = \frac{3}{4} RT V_M / V_H^2$ and we have used the following relations: $E = 3B(1 - 2\nu)$ and $3\varepsilon_H = \frac{V_H}{V_M}$.

Bibliography

- [1] News Feature. Electricity without carbon. *Nature*, 454:816–823, 2008.
- [2] A. Züttel, A. Borgschulte, and L. Schlapbach, editors. *Hydrogen as a future energy carrier*. Wiley-VCH, Weinheim, 2008.
- [3] A. Züttel. Materials for hydrogen storage. *Mat. Today*, 6:24–33, 2003.
- [4] G. Alefeld. Wasserstoff in Metallen als Beispiel für ein Gittergas mit Phasenumwandlungen. *Phys. Stat. Sol.*, 32:67, 1969.
- [5] G. Alefeld. Phase-transitions of hydrogen in metals due to elastic interaction. *Ber. Bunsenges. Phys. Chem.*, 76:746–755, 1972.
- [6] H. Wagner and H. Horner. Elastic interaction and the phase transition in coherent metal-hydrogen systems. *Adv. Phys.*, 23:587–637, 1974.
- [7] G. Alefeld and J. Völkl, editors. *Hydrogen in Metals I-II*, volume 28 of *Topics in Applied Physics*. Springer, Berlin, 1978.
- [8] H. Zabel and H. Peisl. Sample-shape-dependent phase transition of hydrogen in niobium. *Phys. Rev. Lett.*, 42:511, 1979.
- [9] R. Griessen and R. Feenstra. Volume changes during hydrogen absorption in metals. *J. Phys. F: Met. Phys.*, 15:1013–1019, 1985.
- [10] C. Langhammer, I. Zorić, B. Kasemo, and B. M. Clemens. Hydrogen storage in Pd nanodisks characterized with a novel nanoplasmonic sensing scheme. *Nano Lett.*, 7:3122–3127, 2007.
- [11] J. N. Huiberts, R. Griessen, J. H. Rector, R. J. Wijngaarden, J. P. Dekker, D. G. de Groot, and N. J. Koeman. Yttrium and lanthanum hydride films with switchable optical properties. *Nature*, 380:231, 1996.
- [12] R. Gremaud, C. Broedersz, D. M. Borsa, A. Borgschulte, Ph. Mauron, H. Schreuders, J. H. Rector, B. Dam, and R. Griessen. Hydrogenography: an optical combinatorial method to find new light-weight hydrogen storage materials. *Adv. Mater.*, 19:2813, 2007.

- [13] R. Gremaud, M. Slaman, H. Schreuders, B. Dam, and R. Griessen. An optical method to determine the thermodynamics of hydrogen absorption and desorption in metals. *Appl. Phys. Lett.*, 91:231916, 2007.
- [14] B. Dam, R. Gremaud, C. Broedersz, and R. Griessen. Combinatorial thin film methods for the search of new lightweight metal hydrides. *Scr. Mater.*, 56:853–858, 2007.
- [15] P. van der Sluis, M. Ouwerkerk, and P. A. Duine. Optical switches based on magnesium lanthanide alloy hydrides. *Appl. Phys. Lett.*, 70:3356–3358, 1997.
- [16] T. J. Richardson, J. L. Slack, R. D. Armitage, R. Kostecki, B. Farangis, and M. D. Rubin. Switchable mirrors based on nickel-magnesium films. *Appl. Phys. Lett.*, 78:3047–3049, 2001.
- [17] W. Lohstroh, R. J. Westerwaal, B. Noheda, S. Enache, I. A. M. E. Giebels, B. Dam, and R. Griessen. Self-organized layered hydrogenation in black Mg_2NiH_x switchable mirrors. *Phys. Rev. Lett.*, 93:197404, 2004.
- [18] M. Pasturel, M. Slaman, D. M. Borsa, H. Schreuders, B. Dam, R. Griessen, W. Lohstroh, and A. Borgschulte. Stabilized switchable “black state” in $\text{Mg}_2\text{NiH}_4/\text{Ti}/\text{Pd}$ thin films for optical hydrogen sensing. *Appl. Phys. Lett.*, 89:021913, 2006.
- [19] I. A. M. E. Giebels, J. Isidorsson, and R. Griessen. Highly absorbing, black Mg and rare-earth-Mg switchable mirrors. *Phys. Rev. B*, 69:205111, 2004.
- [20] D. M. Borsa, W. Lohstroh, R. Gremaud, J. H. Rector, B. Dam, R. J. Wijngaarden, and R. Griessen. Critical composition dependence of the hydrogenation of $\text{Mg}_{2\pm\delta}\text{Ni}$ thin films. *J. Alloys Compd.*, 428:34–39, 2007.
- [21] D. M. Borsa, A. Baldi, M. Pasturel, H. Schreuders, B. Dam, R. Griessen, P. Vermeulen, and P. H. L. Notten. Mg-Ti-H thin films for smart solar collectors. *Appl. Phys. Lett.*, 88:241910, 2006.
- [22] A. Baldi, D.M. Borsa, H. Schreuders, J.H. Rector, T. Atmakidis, M. Bakker, H.A. Zondag, W.G.J. van Helden, B. Dam, and R. Griessen. Mg-Ti-H thin films as switchable solar absorbers. *Int. J. Hydrogen Energy*, 33:3188–3192, 2008.
- [23] M. Slaman, B. Dam, M. Pasturel, D. M. Borsa, H. Schreuders, J. H. Rector, and R. Griessen. Fiber optic hydrogen detectors containing Mg-based metal hydrides. *Sens. Actuators B*, 123:538–545, 2007.

- [24] B. Dam, R. Griessen, W. Lohstroh, M. Pasturel, and M. Slaman. Optical switching device, 2006. Patent, Pub. No.: WO/2007/049965.
- [25] B. Dam, H. Schreuders, M. Slaman, and M. Pasturel. Protective coating for metal-hydride based devices, 2007. Patent, Pub. No.: WO/2007/126313.
- [26] J. R. Howell and R. B. Bannerot. Optimum solar collector operation for maximizing cycle work output. *Sol. Energy*, 19:149–153, 1977.
- [27] A. Remhof, B. Hjörvarsson, R. Griessen, I. A. M. E. Giebels, and B. Dam. Hydrogen functionalized materials. In A. Züttel, A. Borgschulte, and L. Schlapbach, editors, *Hydrogen as a future energy carrier*. Wiley-VCH, Weinheim, 2008.
- [28] C. G. Granqvist. *Handbook of inorganic electrochromic materials*. Elsevier, Amsterdam, 1995.
- [29] P. R. Somani and S. Radhakrishnan. Electrochromic materials and devices: present and future. *Mater. Chem. Phys.*, 77:117133, 2002.
- [30] V. M. M. Mercier and P. van der Sluis. Toward solid-state switchable mirrors using a zirconium oxide proton conductor. *Sol. State Ionics.*, 145:17–24, 2001.
- [31] P. van der Sluis and V. M. M. Mercier. Solid state Gd-Mg electrochromic devices with ZrO_2H_x electrolyte. *Electrochim. Acta*, 46:2167–2171, 2001.
- [32] Y. Yamada, K. Tajima, S. Bao, M. Okada, and K. Yoshimura. Toward solid-state switchable mirror devices using magnesium-rich magnesium-nickel alloy thin films. *Jpn. J. Appl. Phys.*, 46:5168–5171, 2007.
- [33] F. R. de Boer, R. Boom, W. C. M. Mattens, A. R. Miedema, and A. K. Niessen. *Cohesion in Metals: Transition Metal Alloys*. North-Holland Physics, Amsterdam, 1988.
- [34] T. Mitchell, S. Diplas, P. Tsakirooulos, J. F. Watts, and J. A. D. Matthew. Study of alloying behaviour in metastable Mg-Ti solid solutions using Auger parameter measurements and charge-transfer calculations. *Philos. Mag. A*, 82:841, 2002.
- [35] R. A. H. Niessen and P. H. L. Notten. Electrochemical hydrogen storage characteristics of thin film MgX (X = Sc, Ti, V, Cr) compounds. *Electrochem. Solid-State Lett.*, 8:A534–A538, 2005.
- [36] P. Vermeulen, R. A. H. Niessen, and P. H. L. Notten. Hydrogen storage in metastable Mg_yTi_{1-y} thin films. *Electrochem. Commun.*, 8:27–32, 2006.

- [37] P. Vermeulen, R. A. H. Niessen, D. M. Borsa, B. Dam, R. Griessen, and P. H. L. Notten. Effect of the deposition technique on the metallurgy and hydrogen storage characteristics of metastable $\text{Mg}_y\text{Ti}_{1-y}$ thin films. *Electrochem. Solid-State Lett.*, 9:A520–A523, 2006.
- [38] D. M. Borsa, R. Gremaud, A. Baldi, H. Schreuders, J. H. Rector, B. Kooij, P. Vermeulen, P. H. L. Notten, B. Dam, and R. Griessen. Structural, optical, and electrical properties of $\text{Mg}_y\text{Ti}_{1-y}\text{H}_x$ thin films. *Phys. Rev. B*, 75:205408, 2007.
- [39] G. Liang and R. Schulz. Synthesis of Mg-Ti alloy by mechanical alloying. *J. Mater. Sci.*, 38:1179–1184, 2003.
- [40] D. G. Nagengast, A. T. M. van Gogh, E. S. Kooij, B. Dam, and R. Griessen. Contrast enhancement of rare-earth switchable mirrors through microscopic shutter effect. *Appl. Phys. Lett.*, 75:2050–2052, 1999.
- [41] M. Di Vece, S. J. M. Zevenhuizen, and J. J. Kelly. Optical switching properties from isotherms of Gd and GdMg hydride mirrors. *Appl. Phys. Lett.*, 81:1213, 2002.
- [42] M. Di Vece, A. M. J. van der Eerden, J. A. van Bokhoven, S. Lemaux, J. J. Kelly, and D. C. Koningsberger. X-ray absorption fine structure study of the structural and electronic properties of the GdMg hydride switchable mirror. *Phys. Rev. B*, 67:035430, 2003.
- [43] M. Gonzalez-Silveira, R. Gremaud, A. Baldi, H. Schreuders, B. Dam, and R. Griessen. Effect of H-induced microstructural changes on pressure-optical transmission isotherms for Mg-V thin films. submitted, 2010.
- [44] E. Ma. Alloys created between immiscible elements. *Prog. Mater. Sci.*, 50:413–509, 2005.
- [45] D. C. Koningsberger and R. Prins. *X-ray absorption: Principles, applications, techniques of EXAFS, SEXAFS and XANES*. John Wiley and Sons Inc., New York, NY, 1987.
- [46] B. E. Warren, B. L. Averbach, and B. W. Roberts. Atomic size effect in the x-ray scattering by alloys. *J. Appl. Phys.*, 22:1493, 1951.
- [47] J. H. He and E. Ma. Nanoscale phase separation and local icosahedral order in amorphous alloys of immiscible elements. *Phys. Rev. B*, 64:144206, 2001.

- [48] A. Baldi, R. Gremaud, D. M. Borsa, C. P. Baldé, A. M. J. van der Eerden, G. L. Kruijtzter, P. E. de Jongh, B. Dam, and R. Griessen. Nanoscale composition modulations in $\text{Mg}_y\text{Ti}_{1-y}\text{H}_x$ thin film alloys for hydrogen storage. *Int. J. Hydrogen Energy*, 34:1450–1457, 2009.
- [49] M. Slaman, B. Dam, H. Schreuders, and R. Griessen. Optimization of Mg-based fiber optic hydrogen detectors by alloying the catalyst. *Int. J. Hydrogen Energy*, 33:1084–1089, 2008.
- [50] R. Gremaud, A. Baldi, M. Gonzalez-Silveira, B. Dam, and R. Griessen. Chemical short-range order in $\text{Mg}_y\text{Ti}_{1-y}\text{H}_x$ thin films probed by hydrogenography. *Phys Rev. B*, 77:144204, 2008.
- [51] A. Baldi, G. K. Pálsson, M. Gonzalez-Silveira, M. Slaman, H. Schreuders, J. H. Rector, G. Krishnan, B. J. Kooi, G. S. Walker, M. W. Fay, B. Hjörvarsson, R. J. Wijngaarden, B. Dam, and R. Griessen. Mg/Ti multilayers: Structural, optical and hydrogen absorption properties. <http://arxiv.org/abs/0911.5666>, 2009.
- [52] A. Baldi, M. Gonzalez-Silveira, V. Palmisano, B. Dam, and R. Griessen. Destabilization of the Mg-H system through elastic constraints. *Phys. Rev. Lett.*, 102:226102, 2009.
- [53] A. Baldi, V. Palmisano, M. Gonzalez-Silveira, Y. Pivak, M. Slaman, B. Dam, and R. Griessen. Quasifree Mg-H thin films. *Appl. Phys. Lett.*, 95:071903, 2009.
- [54] T. J. Richardson, J. L. Slack, B. Farangis, and M. D. Rubin. Mixed metal films with switchable optical properties. *Appl. Phys. Lett.*, 80:1341–1351, 2002.
- [55] J. L. M. van Mechelen, B. Noheda, W. Lohstroh, R. J. Westerwaal, J. H. Rector, B. Dam, and R. Griessen. Mg-Ni-H film as selective coatings: Tunable reflectance by layered hydrogenation. *Appl. Phys. Lett.*, 84:3651–3653, 2004.
- [56] D. Kyoï, T. Sato, E. Rönnebro, N. Kitamura, A. Uedac, M. Ito, S. Katsuyama, S. Hara, D. Noreus, and T. Sakai. A new ternary magnesium titanium hydride Mg_7TiH_x with hydrogen desorption properties better than both binary magnesium and titanium hydrides. *J. Alloys Compd.*, 372:213–217, 2004.
- [57] B. Farangis, P. Nachimuthu, T. J. Richardson, J. L. Slack, B. K. Meyer, R. C. C. Perera, and M. Rubin. Structural and electronic properties of magnesium-3D transition metal switchable mirrors. *Solid State Ionics*, 165:309–314, 2003.

- [58] T. J. Richardson, B. Farangis, J. L. Slack, P. Nachimuthu, R. Pereira, N. Tamura, and M. Rubin. X-ray absorption spectroscopy of transition metal-magnesium hydride thin films. *J. Alloys Compd.*, 356-357:204–207, 2003.
- [59] M. Born and E. Wolf. *Principles of Optics*. University Press, Cambridge, 1980.
- [60] E. D. Palik. *Handbook of Optical Constants of Solids*. Academic Press, San Diego, 1998.
- [61] S. Shuxi and E. Wäckelgård. Optimization of solar absorbing three-layers coatings. *Sol. Energy Mater. Sol. Cells*, 90:243, 2006.
- [62] J. Isidorsson, I. A. M. E. Giebels, R. Griessen, and M. Di. Vece. Tunable reflectance Mg-Ni-H films. *Appl. Phys. Lett.*, 80:2305–2307, 2002.
- [63] S. Zhao, C.-G. Ribbing, and E. Wäckelgård. New method to optimize a solar absorber graded film profile. *Sol. Energy*, 78:125–130, 2005.
- [64] J. Chen, Z. Yan, L. Chen, and B. Andresen. Efficiency bound of a solar-driven stirling heat engine system. *Int. J. Energy. Res.*, 22:805–812, 1998.
- [65] D. W. de Vries. *Design of a photovoltaic/thermal combi panel*. PhD thesis, Eindhoven University of Technology, 1998.
- [66] H. A. Zondag, D. W. de Vries, W. G. J. van Helden, R. J. C. van Zolingen, and A. A. van Steenhoven. The yield of different combined PV-thermal collector designs. *Sol. Energy*, 74:253–269, 2003.
- [67] L. Vegard. Die Konstitution der Mischkristalle und die Raumflung der Atome. *Z. Phys.*, 5:17, 1921.
- [68] D. A. G. Bruggeman. Berechnung verschiedener physikalischer Konstanten von heterogenen Substanzen. II. Dielektrizitätskonstanten und Leitfähigkeiten von Vielkristallen der nichtregulären Systeme. *Ann. Phys.*, 417:645 – 672, 1936.
- [69] J. C. Maxwell-Garnett. Colours in metal glasses and in metal films. *Trans. R. Soc. London*, 203:385420, 1904.
- [70] J. H. He, H. W. Sheng, P. J. Schilling, C.-L. Chien, and E. Ma. Amorphous structures in the immiscible Ag-Ni system. *Phys. Rev. Lett.*, 86(13):2826–2829, 2001.

- [71] J. H. He, H. W. Sheng, J. S. Lin, P. J. Schilling, R. C. Tittsworth, and E. Ma. Homogeneity of a supersaturated solid solution. *Phys. Rev. Lett.*, 89(12):125507, 2002.
- [72] A. Borgschulte, R. J. Westerwaal, J. H. Rector, H. Schreuders, B. Dam, and R. Griessen. Catalytic activity of noble metals promoting hydrogen uptake. *J. of Catalysis*, 239:263–271, 2006.
- [73] L. J. van der Pauw. A method of measuring specific resistivity and hall-effect of discs of arbitrary shape. *Philips Res. Repts.*, 13:1–9, 1958.
- [74] E. S. Kooij, A. T. M. van Gogh, and R. Griessen. In situ resistivity measurements and optical transmission and reflection spectroscopy of electrochemically loaded switchable YH_x films. *J. Electrochem. Soc.*, 143:3348, 1999.
- [75] M. Pasturel, M. Slaman, H. Schreuders, J. H. Rector, D. M. Borsa, B. Dam, and R. Griessen. Hydrogen absorption kinetics and optical properties of Pd-doped Mg thin films. *J. Appl. Phys.*, 100:023515, 2006.
- [76] S. J. van der Molen, D. G. Nagengast, A. T. M. van Gogh, J. Kalkman, E. S. Kooij, J. H. Rector, and R. Griessen. Insulating fcc $\text{YH}_{3-\delta}$ stabilized by MgH_2 . *Phys. Rev. B*, 63:235116, 2001.
- [77] W. Lohstroh, R. J. Westerwaal, J. L. M. van Mechelen, H. Schreuders, B. Dam, and R. Griessen. The dielectric function of Mg_yNiH_x thin films ($2 \leq y \leq 10$). *J. Alloys Compd.*, 430:13–18, 2006.
- [78] R. W. Simon, B. J. Dalrymple, D. VanVechten, W. W. Fuller, and S. A. Wolf. Transport measurements in granular niobium nitride cermet films. *Phys. Rev. B*, 36:1962, 1987.
- [79] J. N. Huiberts, R. Griessen, R. J. Wijngaarden, M. Kremers, and C. VanHaesendonck. Logarithmic divergence of the electrical resistivity in the metal hydride $\text{YH}_{3-\delta}$. *Phys Rev. Lett.*, 79:3724–3727, 1997.
- [80] J. P. Bastide, B. Bonnetot, J. M. Letoffe, and P. Claudy. Polymorphism of magnesium hydride under high pressure. *Mater. Res. Bull.*, 15:1215–1224, 1980.
- [81] C. Michaelsen. On the structure and homogeneity of solid solutions: the limits of conventional x-ray diffraction. *Philos. Mag. A*, 72(3):813–828, 1995.
- [82] A. Pundt and C. Michaelsen. APFIM study of the compositional inhomogeneity of sputtered Co-Cr magnetic thin film. *Appl. Surf. Sci.*, 87-88:264–270, 1995.

- [83] S. Er, D. Tiwari, G. A. de Wijs, and G. Brocks. Tunable hydrogen storage in magnesium-transition metal compounds: First-principles calculations. *Phys. Rev. B*, 79:024105, 2009.
- [84] P. Vajeeston, P. Ravindran, A. Kjekhus, and H. Fjellvåg. Pressure-induced structural transitions in MgH_2 . *Phys. Rev. Lett.*, 89:175506, 2002.
- [85] T. Klassen, U. Herr, and R. S. Averbach. Ball milling of systems with positive heat of mixing: Effect of temperature in Ag-Cu. *Acta Mater.*, 45:2921–2930, 1997.
- [86] A. R. Yavari, P. J. Desr, and T. Benameur. Mechanically driven alloying of immiscible elements. *Phys. Rev. Lett.*, 68:2235 – 2238, 1992.
- [87] G. Veltl, B. Scholz, and H.-D. Kunze. Amorphization of Cu-Ta alloys by mechanical alloying. *Mater. Sci. Eng.*, A134:1410–1413, 1991.
- [88] A. R. Yavari and P. J. Desr. Thermodynamics and kinetics of amorphisation during mechanical alloying. *Mater. Sci. Forum*, 88-90:43–50, 1992.
- [89] H. J. Fecht, E. Hellstern, Z. Fu, and W. L. Johnson. Nanocrystalline metals and compounds by high energy ball milling. *Metall. Trans. A*, 21A:2333, 1990.
- [90] C. Gente, M. Oehring, and R. Bormann. Formation of thermodynamically unstable solid solutions in the Cu-Co system by mechanical alloying. *Phys. Rev. B*, 48:13244–13252, 1993.
- [91] W.P. Kalisvaart, R.A.H. Niessen, and P.H.L. Notten. Electrochemical hydrogen storage in MgSc alloys: A comparative study between thin films and bulk materials. *J. Mater. Res.*, 22:1640, 2007.
- [92] M. Vaarkamp, J. C. Linders, and D. C. Koningsberger. A new method for parameterization of phase shift and backscattering amplitude. *Physica B*, 208-209:159–160, 1995.
- [93] J. W. Cook Jr. and D. E. Sayers. Criteria for automatic x-ray absorption fine structure background removal. *J. Appl. Phys.*, 52:5024–5031, 1981.
- [94] D. C. Koningsberger, B. L. Mojet, G. E. van Dorssen, and D. E. Ramaker. XAFS spectroscopy; fundamental principles and data analysis. *Topics in Catalysis*, 10:143–155, 2000.
- [95] E. A. Stern. Number of relevant independent points in x-ray-absorption fine-structures spectra. *Phys. Rev. B*, 48:9825, 1993.

- [96] G. G. Li, F. Bridges, and C. H. Booth. X-ray-absorption fine-structure standards: A comparison of experiment and theory. *Phys. Rev. B*, 52:6332, 1995.
- [97] I. A. M. E. Giebels. *PhD Thesis*. PhD thesis, VU University Amsterdam, 2004. ISBN 90-9018547-X.
- [98] M. S. Conradi, M.P. Mendenhall, T. M. Ivancic, E. A. Carl, C. D. Browning, P. H. L. Notten, W. P. Kalisvaart, P. C. M. M. Magusin, R. C. Bowman Jr, S. J. Hwang, and N. L. Adolphi. NMR to determine rates of motion and structures in metal-hydrides. *J. Alloys Compd.*, 446-447:499–503, 2007.
- [99] M. J. van Setten, S. Er, G. Brocks, R. A. de Groot, and G. A. de Wijs. First-principles study of the optical properties of $\text{Mg}_x\text{Ti}_{1-x}\text{H}_2$. *Phys. Rev. B*, 79:125117, 2009.
- [100] A. Borgschulte, R. J. Westerwaal, J. H. Rector, B. Dam, and R. Griessen. Hydrogen sorption mechanism of oxidized nickel clusters. *Appl. Phys. Lett.*, 85:4884–4886, 2004.
- [101] F. D. Manchester, editor. *Phase Diagrams of Binary Hydrogen Alloys*. ASM International, Materials Park, OH 44073-0002, 2000.
- [102] J. R. Lacher. A theoretical formula for the solubility of hydrogen in palladium. *Proc. R. Soc. London, Ser. A*, 161:525–545, 1937.
- [103] R. Griessen, A. Driessen, and D. G. de Groot. Search for new metal-hydrogen systems for hydrogen storage. *JLCM*, 103:235, 1984.
- [104] H. Hemmes, E. Salomons, R. Griessen, P. Sanger, and A. Driessen. Lattice-gas model for the formation of palladium-silver hydrides at pressures up to 100 GPa. *Phys. Rev. B*, 39:10606 – 10613, 1989.
- [105] R. C. Brouwer, J. Rector, N. Koeman, and R. Griessen. Hydrogen as a local probe: Diffusion and short-range order in $\text{Ti}_{1-y}\text{V}_y$ alloys. *Phys. Rev. B*, 40:3546–3559, 1989.
- [106] R. C. Brouwer, J. Rector, N. Koeman, and R. Griessen. Heat of solution and site energies of hydrogen in disordered transition-metal alloys. *Phys. Rev. B*, 40:1481–1494, 1989.
- [107] S. Froyen and C. Herring. Distribution of interatomic spacings in random alloys. *J. Appl. Phys.*, 52:7165, 1981.

- [108] T. Flanagan and J. Oates. Thermodynamics of intermetallic compound-hydrogen systems. In *Hydrogen in intermetallic compounds I*, Topics in Applied Physics, Vol. 63. Springer-Verlag, New York, 1988. Edited by L. Schlapbach.
- [109] J. D. Eshelby. The determination of the elastic field of an ellipsoidal inclusion, and related problems. *Proc. R. Soc. London, Ser. A*, 241:376–396, 1957.
- [110] H. Wagner. Elastic interaction and phase transition in coherent metal-hydrogen alloys. In *Hydrogen in Metals I*, Topics in Applied Physics, Vol. 28. Springer-Verlag, Berlin, 1978. Edited by G. Alefeld and J. Völkl.
- [111] W. Lohstroh, R. J. Westerwaal, J. L. M. van Mechelen, C. Chacon, E. Johansson, B. Dam, and R. Griessen. Structural and optical properties of Mg_2NiH_x switchable mirrors upon hydrogen loading. *Phys. Rev. B.*, 70:165411, 2004.
- [112] K. A. Gschneider Jr. Physical properties and interrelationships of metallic and semimetallic elements. *Solid State Phys.*, 16:275–426, 1964.
- [113] R. Yu and P. K. Lam. Electronic and structural properties of MgH_2 . *Phys. Rev. B*, 37:8730 – 8737, 1988.
- [114] W. Wolf and P. Herzig. First-principles investigations of transition metal dihydrides, TH_2 : T = Sc, Ti, V, Y, Zr, Nb; energetics and chemical bonding. *J. Phys.: Condens. Matter*, 12:45354551, 2000.
- [115] R. B. Schwarz and A. G. Khachatryan. Thermodynamics of open two-phase systems with coherent interfaces. *Phys. Rev. Lett.*, 74:2523 – 2526, 1995.
- [116] R. B. Schwarz and A. G. Khachatryan. Thermodynamics of open two-phase systems with coherent interfaces: Application to metal-hydrogen systems. *Acta Mater.*, 54:313–323, 2006.
- [117] G. Song, M. Geitz, A. Abromeit, and H. Zabel. Solubility isotherms of hydrogen in epitaxial Nb(110) films. *Phys. Rev. B.*, 54:14093, 1996.
- [118] A. Krozer and B. Kasemo. Hydrogen uptake by Pd-coated Mg: Absorption-decomposition isotherms and uptake kinetics. *J. Less Common Metals*, 160:323–342, 1990.
- [119] S. Bao, K. Tajima, Y. Yamada, M. Okada, and K. Yoshimura. Magnesiumtitanium alloy thin-film switchable mirrors. *Sol. Energy Mater. Sol. Cells*, 92:224–227, 2008.

- [120] G. K. Pálsson, A. R. Rennie, and B. Hjörvarsson. Examination of the reliability of x-ray techniques for determining hydrogen-induced volume changes. *Phys. Rev. B*, 78:104118, 2008.
- [121] B. Y. Jin and J. B. Ketterson. Artificial metallic superlattices. *Adv. Phys.*, 38:189–366, 1989.
- [122] E. E. Fullerton, I. K. Schuller, H. Vanderstraeten, and Y. Bruynseraede. Structural refinement of superlattices from x-ray diffraction. *Phys. Rev. B*, 45:9292–9310, 1992.
- [123] M. Björck and G. Andersson. Genx: an extensible x-ray reflectivity refinement program utilizing differential evolution. *J. Appl. Cryst.*, 40:1174–1178, 2007.
- [124] B. K. Agarwal. *X-Ray Spectroscopy: An Introduction*. Springer-Verlag New York, LLC, 1991.
- [125] J. F. Stampfer, C. E. Holley, and J. F. Suttle. The magnesium-hydrogen system. *J. Am. Chem. Soc.*, 82:3504–3508, 1960.
- [126] M. Ito, D. Setoyama, J. Matsunaga, H. Muta, K. Kurosaki, M. Uno, and S. Yamanaka. Electrical and thermal properties of titanium hydrides. *J. Alloys Compd.*, 420:25–28, 2006.
- [127] U. Laudahn, A. Pundt, M. Bicker, U. v. Hülsen, U. Geyer, T. Wagner, and R. Kirchheim. Hydrogen-induced stress in nb single layers. *J. Alloys Compd.*, 293-295:490–494, 1999.
- [128] D. E. Savage, J. Kleiner, N. Schimke, Y.-H. Phang, T. Jankowski, J. Jacobs, R. Kariotis, and M. G. Lagally. Determination of roughness correlations in multilayer films for x-ray mirrors. *J. Appl. Phys.*, 69:1411–1424, 1991.
- [129] H. Zabel. X-ray and neutron reflectivity analysis of thin-films and superlattices. *Appl. Phys. A*, 58:159–168, 1994.
- [130] A. Borgschulte, R. J. Westerwaal, J. H. Rector, B. Dam, R. Griessen, and J. Schoenes. Effect of the strong metal-support interaction on hydrogen sorption kinetics of pd-capped switchable mirrors. *Phys. Rev. B*, 70:155414, 2004.
- [131] W. Theiss. *SCOUT Thin Film Analysis Software Handbook, Hard and Software*. Aachen, 2000. www.mtheiss.com.
- [132] V. Berube, G. Chen, and M. S. Dresselhaus. Impact of nanostructuring on the enthalpy of formation of metal hydrides. *Int. J. Hydrogen Energy*, 33:4122–4131, 2008.

- [133] M. Pasturel, R. J. Wijngaarden, W. Lohstroh, H. Schreuders, M. Slaman, B. Dam, and R. Griessen. Influence of the chemical potential on the hydrogen sorption kinetics of Mg₂Ni/TM/Pd (TM = transition metal) trilayers. *Chem. Mater.*, 19:624–633, 2007.
- [134] R. Gremaud. *Hydrogenography. A thin film optical combinatorial study of hydrogen storage materials*. PhD thesis, VU University Amsterdam, 2008. ISBN/EAN 978-90-9023439-7 (available at: <http://dare.uvu.vu.nl/handle/1871/12914>).
- [135] H. Frieske and E. Wicke. Magnetic susceptibility and equilibrium diagram of pdh_n. *Berichte der Bunsen-Gesellschaft*, 77:48–52, 1973.
- [136] H. Zabel and B. Hjoörvarsson. Hydrogen in thin films and multilayers. In V. A. Goltsov, editor, *Progress in Hydrogen Treatment of Materials*. Donetsk State Technical University, Donetsk, 2001.
- [137] L. Schlapbach and A. Züttel. Hydrogen-storage materials for mobile applications. *Nature*, 414:353–358, 2001.
- [138] A. Zaluska, L. Zaluski, and J. O. Ström-Olsen. Nanocrystalline magnesium for hydrogen storage. *J. Alloys Compd.*, 288:217–225, 1999.
- [139] W. Oelerich, T. Klassen, and R. Bormann. Metal oxides as catalysts for improved hydrogen sorption in nanocrystalline Mg-based materials. *J. Alloys Compd.*, 315:237–242, 2001.
- [140] R.A. Varin, T. Czujko, Ch. Chiu, and Z. Wronski. Particle size effects on the desorption properties of nanostructured magnesium dihydride (MgH₂) synthesized by controlled reactive mechanical milling (CRMM). *J. Alloys Compd.*, 424:356–364, 2006.
- [141] J. J. Vajo, F. Mertens, C. C. Ahn, R. C. Bowman, and B. Fultz. Altering hydrogen storage properties by hydride destabilization through alloy formation: LiH and MgH₂ destabilized with Si. *J. Phys. Chem. B*, 108:13977–13983, 2004.
- [142] R. Wagemans, J. H. van Lenthe, P. E. de Jong, A. J. van Dillen, and K. P. de Jong. Hydrogen storage in magnesium clusters: Quantum chemical study. *J. Am. Chem. Soc.*, 127:16675, 2005.
- [143] J.J. Liang. Theoretical insight on tailoring energetics of Mg hydrogen absorption/desorption through nano-engineering. *Appl. Phys. A*, 80:173178, 2005.
- [144] H. Peisl. *Topics in Applied Physics: Hydrogen in Metals I*. Springer, Berlin, 1978. edited by G. Alefeld and J. Völkl.

- [145] R. Machorro, J. M. Siqueiros, and S. Wang. Optical properties of Mg, from UV to IR, using ellipsometry and reflectometry. *Thin Solid Films*, 269:1–5, 1995.
- [146] J. Isidorsson, I. A. M. E. Giebels, H. Arwin, and R. Griessen. Optical properties of MgH₂ measured *in situ* by ellipsometry and spectrophotometry. *Phys. Rev. B*, 68:115112, 2003.
- [147] G. Andersson, B. Hjörvarsson, and P. Isberg. Influence of compressive biaxial strain on the hydrogen uptake of ultrathin single-crystal vanadium layers. *Physical Review B*, 55:1774, 1997.
- [148] A. T. M. van Gogh, S. J. van der Molen, J. W. J. Kerssemakers, N. J. Koeman, and R. Griessen. Performance enhancement of metal-hydride switchable mirrors using Pd/AlO_x composite cap layers. *Appl. Phys. Lett.*, 77:815–817, 2000.
- [149] J. L. Slack, J. C. W. Locke, S. W. Song, J. Ona, and T. J. Richardson. Metal hydride switchable mirrors: Factors influencing dynamic range and stability. *Sol. Energy Mater. Sol. Cells*, 90:485–490, 2006.
- [150] S. Bao, Y. Yamada, M. Okada, and K. Yoshimura. Titanium-buffer-layer-inserted switchable mirror based on MgNi alloy thin film. *Jpn. J. Appl. Phys.*, 45:L588–L590, 2006.
- [151] Y. Pivak and R. Griessen. Elastic clamping in 3D. private communication.
- [152] L. Pasquini, E. Callini, E. Piscopiello, A. Montone, M. Vittori Antisari, and E. Bonetti. Metal-hydride transformation kinetics in Mg nanoparticles. *Appl. Phys. Lett.*, 94:041918, 2009.
- [153] E. Callini, L. Pasquini, E. Piscopiello, A. Montone, M. Vittori Antisari, and E. Bonetti. Hydrogen sorption in Pd-decorated MgMgO core-shell nanoparticles. *Appl. Phys. Lett.*, 94:221905, 2009.
- [154] G. Krishnan, B. .J. Kooi, G. Palasantzas, J. Th. M. De Hosson, Y. Pivak, and B. Dam. Thermal stability of gas phase magnesium nanoparticles towards hydrogen storage. *J. Appl. Phys.*, accepted for publication, 2010.
- [155] P. E. de Jongh, R. W. P. Wagemans, T. M. Eggenhuisen, B. S. Dauvillier, P. B. Radstake, J. D. Meeldijk, J. W. Geus, and K. P. de Jong. The preparation of carbon-supported magnesium nanoparticles using melt infiltration. *Chem. Mater.*, 19:6052–6057, 2007.

- [156] R. Wagemans, K. De Jong, P. E. De Jongh, and B. S. Dauvillier. Process for preparing composites comprising carbon and magnesium for hydrogen storage, 2008. European Patent Application EP1876252.
- [157] S. Zhang, A. F. Gross, S. L. Van Atta, M. Lopez, P. Liu, C. C. Ahn, J. J. Vajo, and C. M. Jensen. The synthesis and hydrogen storage properties of a MgH₂ incorporated carbon aerogel scaffold. *Nanotechnology*, 20:204027, 2009.
- [158] M. Fichtner. Properties of nanoscale metal hydrides. *Nanotechnology*, 20:204009, 2009.
- [159] K. C. Kim, B. Dai, J. K. Johnson, and D. S. Sholl. Assessing nanoparticle size effects on metal hydride thermodynamics using the Wulff construction. *Nanotechnology*, 20:204001, 2009.
- [160] M. Wagemaker, F. M. Mulder, and A. Van der Ven. The role of surface and interface energy on phase stability of nanosized insertion compounds. *Adv. Mater.*, 21:1–7, 2009.
- [161] V. Radhakrishnan, C. K. Subramaniam, V. Sankaranarayanan, G. V. Subba Rao, and R. Srinivasan. Logarithmic temperature dependence of the resistivity of Nd_{2-x}Ce_xCuO_{4-y}. *Physica C*, 167:53–58, 1990.
- [162] A. Gerber, A. Milner, G. Deutscher, M. Karpovsky, and A. Gladkikh. Insulator-superconductor transition in 3D granular Al-Ge films. *Phys. Rev. Lett.*, 78:4277–4280, 1997.
- [163] K. B. Efetov and A. Tschersich. Coulomb effects in granular materials at not very low temperatures. *Phys. Rev. B*, 67:174205, 2003.
- [164] I. S. Beloborodov, A. V. Lopatin, V. M. Vinokur, and K. B. Efetov. Granular electronic systems. *Rev. Mod. Phys.*, 79:469, 2007.
- [165] I. S. Beloborodov, K. B. Efetov, A. V. Lopatin, and V. M. Vinokur. Transport properties of granular metals at low temperatures. *Phys. Rev. Lett.*, 91:246801–1, 2003.
- [166] F. J. A. den Broeder, S. J. van der Molen, M. Kremers, J. N. Huiberts, D. G. Nagengast, A. T. M. van Gogh, W. H. Huisman, N. J. Koeman, B. Dam, J. H. Rector, S. Plota, M. Haaksma, R. M. N. Hanzen, R. M. Jungblut, P. A. Duine, and R. Griessen. Visualization of hydrogen migration in solids using switchable mirrors. *Nature*, 394:656–658, 1998.
- [167] A. Remhof, S. J. van der Molen, A. Antosik, A. Dobrowolska, N. J. Koeman, and R. Griessen. Switchable mirrors for visualization and control of hydrogen diffusion in transition metals. *Phys. Rev. B*, 66:020101, 2002.

-
- [168] S. Galam and A. Mauger. Universal formulas for percolation thresholds.
Phys. Rev. E, 53:2177–2181, 1996.

Summary

Since their discovery in 1996, switchable mirrors have attracted great interest both for their intriguing physics and for their technological application. A switchable mirror is a thin metallic film, typically deposited on a transparent substrate and therefore mirror-like, which is capable of reversibly changing its optical appearance upon absorption of hydrogen.

The first mirrors were made of rare-earth metals and had a yellowish transparent hydrogenated state. Subsequently Mg-rare-earth and Mg-transition metals mirrors were shown to have improved transparency of the hydrogenated state and much smaller costs. Intriguingly, while loaded with hydrogen some of these mirrors showed a dark, light-absorbing, intermediate state. This “black state” is destroyed upon full hydrogenation and it is due to non-trivial mechanisms of nucleation and growth of the hydride phase.

The possibility to switch a thin film from a light-reflecting to a light-absorbing state, however, suggested their application as smart covers for solar collectors and as highly sensitive optical hydrogen detectors.

At the beginning of the present thesis we therefore searched for suitable materials, that would hopefully show a good optical reflection in the metallic state and a dark appearance in the hydrogenated state. To our great surprise, thin films of co-sputtered Mg and Ti showed the desired characteristics: the black appearance of the hydrogenated state is not destroyed upon full hydrogenation, but it is a final, stable, reversible state of the metal hydride. Furthermore the hydrogen absorption and desorption transitions occur within few seconds, suggesting the application of Mg-Ti alloys as novel hydrogen storage materials.

The physical origin of the optical black state in Mg-Ti thin film alloys is difficult to interpret. In order to understand it we investigated the microstructure of these films, by combining structural, electrical and optical data. Although some hypothesis could already be made, a clear picture was only obtained by probing the local distribution of the Mg and Ti atoms within the alloy’s crystal structure. This was done by combining extended x-ray absorption fine structure (EXAFS) data with a modeling of the absorption isotherms, as measured with Hydrogenography. The results showed that, although the average crystal structure resembles the one expected for a perfectly mixed alloy, magnesium and titanium atoms are distributed with a small degree of chemical short-range order. Such a peculiar microstructure originates from the positive enthalpy of

mixing of magnesium and titanium: during the films deposition Mg and Ti atoms are rapidly cooled on the substrate and, although they would naturally tend to segregate, the rapid quenching freezes the alloy structure into a crystalline “metastable” fine dispersion of Mg-rich and Ti-rich nano-domains.

The technological significance of this discovery can only be understood by considering that, when loaded with hydrogen, most immiscible binary alloys containing magnesium (Mg-V, Mg-Sc, Mg-Y, Mg-La, Mg-Ce, Mg-Gd) undergo a severe segregation into their constituent elements. Mg-Ti alloys, on the other hand, are structurally reversible for several cycles of hydrogen absorption and desorption. We have therefore proven that it is possible to synthesize new lightweight hydrogen absorbing materials, beyond the limits imposed by thermodynamic equilibrium.

The exceptional reversibility observed in Mg-Ti thin film alloys can be understood on the basis of the “spinodal-like” microstructure, composed of Mg-rich and Ti-rich coherently bound domains, together with what could be called *an accident of nature*: upon exposure to increasing hydrogen pressures the Ti-rich domains absorb hydrogen, while Mg-rich parts remain in the metallic phase. This is due to the lower (more negative) enthalpy of hydride formation of TiH_2 with respect to MgH_2 . At higher hydrogen pressures also the Mg domains are hydrogenated and the films become black. The *accident* is that the molar volume of Mg and TiH_2 are almost identical: in the intermediate state, when only Ti-rich areas are loaded with hydrogen, the system is in a structurally stable situation composed of Mg-rich and TiH_2 -rich domains with (almost) identical volumes, which prevents the segregation observed in other binary Mg-based alloys.

In order to further investigate the role of chemical segregation and structural coherence in Mg-Ti alloys we artificially engineered one dimensional chemical short-range order by depositing Mg/Ti multilayers with various periodicities. Surprisingly, notwithstanding the large lattice mismatch between Mg and Ti, we obtained multilayers with good crystal quality and partially coherent Mg/Ti interfaces. Upon hydrogenation the Ti layers absorb hydrogen before the Mg ones, as expected from a thermodynamic perspective and confirmed with a simple diffusion model. X-ray reflectometry measurements indicate that hydrogen absorption induces a large out-of-plane expansion of both Mg and Ti, well beyond the elastic limits. This has great consequences on the nature of the Mg/Ti interfaces, which must lose their structural integrity and lead to quasi decoupled layers of Mg and Ti.

The effect of “broken” Mg/Ti interfaces is particularly intriguing when looking at the loading isotherms of Mg-based multilayers. What we observed experimentally is that Mg films as thin as 20 nm, when “sandwiched” between Ti layers, exhibit loading pressures similar to the ones expected for bulk magnesium. On the contrary, when sandwiched between elements such as palladium and nickel, magnesium loads at much higher pressures. After studying many

different sample geometries we proposed that a significant increase of hydrogen loading pressure is observed when Mg is adjacent to an element which forms a stable alloy with it (such as Pd and Ni), while immiscible elements (such as Ti, Nb and V) induce a bulk-like quasifree behavior. The Mg-alloy-forming elements have the ability to clamp the Mg layers, inducing elastic stresses during the hydrogen absorption process. By taking into account the long-ranged elastic interaction between two hydrogen atoms dissolved into a metallic lattice, we developed a simple elastic model for the elastic response of a bilayer. The model qualitatively reproduces the variations in hydrogen loading pressures observed experimentally in Pd-capped Mg layers with various thicknesses.

Our observations show that it is possible to *tune* the thermodynamics of hydrogen absorption in Mg thin films by means of elastic clamping. The same model developed for a bilayer predicts an even larger increase of hydrogen equilibrium pressures for 3D magnesium nanoparticles covered with a clamping hard skin. Although Mg has a high gravimetric and volumetric capacity of hydrogen storage at a very low cost, its use as hydrogen storage material is hindered by its poor kinetic and thermodynamic properties. Magnesium hydride is too stable for practical applications, with a hydrogen equilibrium pressure of less than a millibar at room temperature. Increasing the equilibrium pressure of such a material is therefore highly desirable in the perspective of an efficient use of hydrogen as an energy carrier.

Furthermore, the possibility to tune the hydrogen equilibrium pressure of a Mg thin film, combined with the optical changes occurring upon the hydrogenation of magnesium, opens the possibility of using Mg-based multilayers in multistep optical detectors, with good sensitivities in a wide range of hydrogen pressures.

Samenvatting

Sinds hun ontdekking in 1996 hebben schakelbare spiegels een grote belangstelling gewekt, zowel vanwege hun intrigerende fysica als hun mogelijke toepassing. Een schakelbare spiegel is een dunne metaalfilm die op een transparant substraat wordt gedeponerd en waarvan het optische gedrag bij ab- en desorptie van waterstof omkeerbaar verandert. De eerste spiegels werden gemaakt van zeldzame aard metalen en vertoonden een gele, transparante toestand na beladen met waterstof. Vervolgens bleken legeringen met het goedkope Mg te leiden tot schakelbare spiegels met een veel betere transparantie in de gehydrogeneerde toestand. Intrigerend is dat sommige van deze spiegels een donkere, licht-absorberende intermediaire toestand vertonen. Deze toestand verdwijnt bij volledige hydrogenering en is toe te schrijven aan een ongebruikelijk mechanisme van nucleatie en groei van de hydridefase. De mogelijkheid om een dunne film van een licht-reflecterende naar een licht-absorberende toestand te schakelen, suggereerde hun toepassing als smart covers voor zonnecollectoren en als detectielaag voor optische waterstofsensoren.

Daarom zijn wij allereerst op zoek gegaan naar geschikte materialen met een zo groot mogelijk contrast in de optische reflectie tussen de metallische en de zwarte toestand. Dit vonden we in een film die gemaakt is door tegelijkertijd Mg en Ti te sputteren. Echter, in dit geval verdwijnt de zwarte toestand bij volledige belading niet, maar het blijkt juist de finale, stabiele, omkeerbare toestand te zijn van het volledig beladen metaalhydride. Deze optische overgang vindt binnen enkele seconden plaats, wat de toepassing van deze Mg-Ti legeringen nog aantrekkelijker maakt.

De fysische oorsprong van de optische zwarte toestand in Mg-Ti dunne filmlegeringen is moeilijk te interpreteren. Een duidelijk beeld kon pas worden verkregen uit de lokale distributie van Mg en Ti binnen de kristalstructuur van de legering. Uit *X-Ray Absorption Fine Structure* (EXAFS) analyse bleek dat, hoewel de gemiddelde kristalstructuur op die van een volkomen gemengde legering lijkt, de magnesium en titanium atomen op kleine schaal een zekere chemische orde bezitten.

Deze bijzondere microstructuur komt voort uit de positieve mengenthalpie van titanium in magnesium: tijdens de depositie van de films koelen de Mg en Ti atomen op het substraat snel af en dit leidt ertoe dat, hoewel men macroscopische segregatie zou verwachten, zich een metastabiele verdeling van

kristallijne Ti-rijke nano-domeinen in een Mg matrix vormt.

De technologische betekenis van deze ontdekking kan slechts begrepen worden door te beseffen dat de meeste niet-mengbare binaire legeringen van magnesium (Mg-V, Mg-Sc, Mg-Y, Mg-La, Mg-Ce, Mg-Gd) zich bij beladen scheiden in hun constituërende elementen. De Mg-Ti legeringen daarentegen zijn structureel omkeerbaar gebleken, zelfs na honderden waterstofbeladingscycli. Hieruit blijkt dat het mogelijk is om nieuwe, lichtgewicht, waterstof absorberende materialen samen te stellen, voorbij de grenzen die door thermodynamisch evenwicht worden opgelegd.

De uitzonderlijke omkeerbaarheid die we in Mg-Ti dunne filmlegeringen waarnemen, is te begrijpen op basis van de spinodale microstructuur: Ti-rijke nano-domeinen die coherent gekoppeld zijn aan de Mg-matrix, gecombineerd met wat een ongeval van de natuur zou kunnen worden genoemd. Bij blootstelling aan stijgende waterstofdruk, absorberen de Ti-rijke domeinen waterstof, terwijl de Mg-rijke delen in de metaalfase blijven. Dit is toe te schrijven aan de lagere (meer negatieve) enthalpie van hydridevorming van TiH_2 in vergelijking tot MgH_2 . Bij een hogere waterstofdruk worden ook de Mg domeinen gehydrogeneerd en worden de films zwart. Het ongeval is dat het molaire volume van Mg en TiH_2 vrijwel identiek is: in de intermediaire toestand, wanneer slechts de Ti-rijke gebieden met waterstof worden beladen, is het systeem daardoor in een structureel stabiele situatie. Dit verhindert de segregatie die in andere binaire op Mg-gebaseerde legeringen wordt waargenomen.

Om de rol van de chemische segregatie en de structurele coherentie in Mg-Ti legeringen verder te onderzoeken, hebben we wij kunstmatig n-dimensionale, chemisch geordende structuren gemaakt door Mg/Ti multilagen met diverse periodiciteiten te deponeren. Tot onze verrassing - gezien de grote roostermismatch tussen Mg en Ti - verkregen wij multilagen met een goede kristalkwaliteit en gedeeltelijk coherente interfaces tussen Mg en Ti. Weer vinden we dat bij hydrogenering eerst de Ti-lagen waterstof absorberen, zoals we konden voorspellen op basis van een eenvoudig, op diffusie gebaseerd verspreidingsmodel en rekening houdend met de thermodynamische verschillen tussen beide elementen. Röntgenmetingen wijzen erop dat de waterstofabsorptie een grote roosterexpansie veroorzaakt van zowel Mg als Ti, ver voorbij de elastische grenzen. Dit heeft grote gevolgen op de aard van de Mg/Ti interfaces, die hun structurele integriteit verliezen wat tot quasi ontkoppelde lagen van Mg en Ti leidt. Het effect van deze ontkoppelde Mg/Ti interfaces is bijzonder intrigerend wanneer men kijkt naar de Mg-beladingsisothermen in deze multilagen.

We vinden voor films bestaande uit 20 nm Mg ingesloten tussen Ti, evenwichtsdrukken gelijkend op die van bulk magnesium. Daarentegen laadt magnesium bij een veel hogere druk, wanneer de laag geklemd is tussen palladium of nikkel. Na bestudering van het beladingsgedrag van diverse stapelingen concluderen wij dat een significante verhoging van de waterstofevenwichtsdruk optreedt, indien Mg omgeven wordt door elementen waarmee het een stabiele

legering vormt (zoals Pd en Ni). Bestaan de omringende lagen uit elementen die niet met Mg mengbaar zijn (zoals Ti, Nb en V), dan zien we een op de bulk gelijkende evenwichtsdruk. Legeringvormende elementen zijn elastisch gekoppeld aan de Mg-lagen, waardoor deze lagen onder spanning komen te staan bij beladen met waterstof. Rekening houdend met de lange afstand interactie tussen waterstofatomen in de vaste stof, ontwikkelden wij een eenvoudig model voor de elastische interactie tussen twee lagen. Het model reproduceert kwalitatief de variaties in de waterstofbeladingsdruk zoals die experimenteel in de Pd-Mg lagen wordt waargenomen. Onze observaties tonen aan dat het mogelijk is om de thermodynamica van waterstofabsorptie in dunne films van Mg te modifieren door middel van elastische koppeling. Op basis van hetzelfde model verwachten we een nog grotere verhoging van de waterstof evenwichtsdruk in een systeem van 3D magnesium nanodeeltjes voorzien van een in-elastische, waterstofdoorlatende schil.

Hoewel met Mg een hoge gravimetrische en volumetrische capaciteit van waterstofopslag tegen zeer lage kosten gerealiseerd kan worden, belemmeren zijn slechte kinetische en thermodynamische eigenschappen het gebruik ervan. Magnesiumhydride is normaliter te stabiel voor praktische toepassingen, gegeven een waterstofevenwichtsdruk van minder dan een millibar bij kamertemperatuur. Het verhogen van de evenwichtsdruk van een dergelijk materiaal is daarom hoogst wenselijk in het perspectief van een efficiënt gebruik van waterstof als energiedrager. De mogelijkheid om de waterstofevenwichtsdruk van een dunne Mg film te veranderen gecombineerd met de optisch veranderingen die optreden bij beladen, biedt voorts de mogelijkheid een optische waterstofsensor te maken met een groot drukbereik.

List of Publications

1. D. M. Borsa, A. Baldi, M. Pasturel, H. Schreuders, B. Dam, R. Griessen, P. Vermeulen and P. H. L. Notten
Mg-Ti-H thin films for smart solar collectors
Appl. Phys. Lett. **88**, 241910 (2006).
2. A. Baldi, F. Di Pascasio and D. Gozzi
H₂ cold plasma on Pd/H system at low hydrogen pressure
Appl. Phys. Lett. **89**, 051918 (2006).
3. D. M. Borsa, R. Gremaud, A. Baldi, H. Schreuders, J. Rector, B. Kooi, P. Vermeulen, P. H. L. Notten, B. Dam and R. Griessen
Structural, optical and electrical properties of Mg-Ti-H thin films
Phys. Rev. B **75**, 205408 (2007).
4. A. Baldi, D. M. Borsa, H. Schreuders, J. H. Rector, T. Atmakidis, M. Bakker, H. A. Zondag, W. G. J. van Helden, B. Dam and R. Griessen
Mg-Ti-H thin films as switchable solar absorbers
Int. J. Hydrogen Energy **33**, 3188-3192 (2008).
5. R. Gremaud, A. Baldi, M. Gonzalez-Silveira, B. Dam and R. Griessen
Chemical short-range order and lattice deformations in Mg_yTi_{1-y}H_x thin films probed by hydrogenography
Phys. Rev. B **77**, 144204 (2008).
6. A. Baldi, R. Gremaud, D. M. Borsa, C. P. Baldé, A. M. J. van der Eerden, G. L. Kruijtzter, P. E. de Jongh, B. Dam and R. Griessen
Nanoscale composition modulations in Mg_yTi_{1-y}H_x thin film alloys for hydrogen storage
Int. J. Hydrogen Energy **34**, 1450-1457 (2009).
7. A. Baldi, M. Gonzalez-Silveira, V. Palmisano, B. Dam and R. Griessen
Destabilization of the Mg-H system through elastic constraints
Phys. Rev. Lett. **102**, 226102 (2009).
8. A. Baldi, V. Palmisano, M. Gonzalez-Silveira, Y. Pivak, M. Slaman, H. Schreuders, B. Dam and R. Griessen

Quasifree Mg-H thin films

Appl. Phys. Lett. **95**, 071903 (2009).

9. A. Baldi, G. K. Pálsson, M. Gonzalez-Silveira, M. Slaman, H. Schreuders, J. H. Rector, G. Krishnan, B. J. Kooi, G. S. Walker, M. W. Fay, B. Hjörvarsson, R. J. Wijngaarden, B. Dam and R. Griessen
Mg/Ti multilayers: Structural, optical and hydrogen absorption properties
Submitted for publication (<http://arxiv.org/abs/0911.5666>).
10. M. Gonzalez-Silveira, R. Gremaud, A. Baldi, H. Schreuders, B. Dam and R. Griessen
Effect of H-induced microstructural changes on pressure-optical transmission isotherms for Mg-V thin films
Submitted for publication.
11. H. Leegwater, H. Schut, W. Egger, A. Baldi, B. Dam, and S. W. H. Eijt
Di-vacancies and the hydrogenation of Mg-Ti films with short range chemical order
Submitted for publication
12. A. Baldi, F. Claessen, S. de Man, M. Gonzalez-Silveira, M. Slaman, H. Schreuders, J. H. Rector, B. Dam and R. Griessen
Optical study of hydrogen diffusion in Mg-Ti-H thin films
In preparation.
13. S. de Man, M. Gonzalez-Silveira, A. Baldi, D. Visser and R. Griessen
Combinatorial search of intrinsic high hydrogen permeability membrane materials
In preparation.
14. V. Palmisano, A. Baldi, M. Slaman, H. Schreuders, B. Dam and R. Griessen
From optical hydrogen detectors to optical hydrogen sensors
In preparation.

Acknowledgements

My first, most passionate and largest THANKS! goes to my wife, Valentina, simply for being her beautiful self and, most importantly, for being it here, next to me. I would have not been able to finish this work without your constant support and love. You and Lorenzo are my home.

If, after reading the thesis, you think that magnesium and titanium are a very *odd couple*, it means you haven't met my supervisors! To Ronald and Bernard, for almost exactly opposite reasons, goes all my gratitude. To Ronald, for teaching me that the main objective of a Ph.D. is to grow as a physicist and to Bernard, for teaching me that the main objective of a Ph.D. is to grow as a person. To Ronald, for pushing me into the fundamental physical aspects of our research and to Bernard, for making me think about the possible technological applications of our findings. To Ronald, for asking me to dug deep and to Bernard, for reminding me to fly high. To both of you, for investing in me your time and energy and passion.

A heartfelt thanks goes to the *Fantastic Four* technicians of the condensed matter physics group, who have patiently heard me misspell their names for more than four years: Ermanno-Herman, Giovanni-Jan, Cirillo-Kier and Martino-buongiorno-Martin. A thesis is not large enough to list all your superpowers...

Of course I could not miss to thank all the group members that contributed in making life at the VU so special: Marta (and David and Alba and the fish paella, of course), Roberto-Robin (colleague and flatmate), Stefano-Sven (my spare brain, probably the only one working properly), Leonardo-Lennard (the most italian dutch), Dana (who taught me literally everything at the beginning), Davide (first, but definitely not last, italian of the group), the polar bear Eugenio-Yevheniy, Chase, the untranslatable Rinke, Claudia, Gregorio-Grzegorz, Pasquale-Dhwajal, Adriano-Audrius, Diana and Kinga, Ciro-Cédric, Felice-Felix, Giovanna-Jonna, Cristiano-Christiaan, Daniele-Dennis, Tommaso-Tim, Lorenzo-Ioris, Eugenio-Yuji, Iolanda-Yolanda, Vincenzo-Vincent and all the rest, past and present, that I am forgetting at the moment... I would also like to thank very much Kees and Gunnar, for teaching me two new experimental techniques but, most importantly, for being friends before than colleagues.

Thanks to my Little Italy: Vasco-the-president-Molini (who taught me what friendship is all about and whose friendship I am most proud of) and Alies and Sanna, Andrea-spacchiamotutto-Candelli (our *maestro di vita*) and Anne, Valerio-parmisano-Palmisano (the Dr. Jekyll and Mr. Hyde), Matteo-trucido-Filippi (the social convention buster), Matteo-colonnello-Tondini (the newborn radical), Giuseppe-Giuhshepneh-appibirdai-Nicoletti and, in random order, Cosimo, Ciantal-Chantal, Eduardo, Gabbiana-Fabiana, Marco e Pasquale, Eva e Carlo, Priscilla, Marco J, Donnamarino-Beatrice, Giovanni e Marianna, Francesco e Viola, Laura e Ilaria, tutti gli Alter/Natives passati e futuri. A most felt thanks flies to reach our beloved Enrico, we miss your smile, your kindness and your enthusiasm (by the way, Soma says “hi!”).

Infine, dopo aver ringraziato la mia Little Italy, vorrei ringraziare la mia Grande Italia. A tutti coloro che mi hanno supportato e sopportato negli anni passati (mamma e Alex, papà e Milena, Emanuele, nonna Rosanna e le tribù di cugini/zii/nipoti Baldi e Negri, Patty e i suoi *bambini*, Roberto, nonna Anna e gli zii di Vale, gli amici, in ordine sparso: Alessandro, Alfredo, Valerio, Baronca, Franz, Gabriele, Guido, Bradipo e Michela, Sardo e Giulia, Giulia e Luca, Marzia e Armando, Massi e Giuliana, Sasà e Valentina, la Tanga, Valeria, Elena) e che (spero) continueranno a farlo in quelli futuri, un grazie di cuore!

Grazie in particolar modo a mia madre e mio padre, ai quali spero con questo lavoro di aver regalato una piccola soddisfazione, pur consapevole che mai un figlio potrà ripagare tutto il bene ricevuto dai genitori.

Curriculum Vitae



Andrea Baldi was born on 22 October 1979 in Rome, Italy. In 1998, he graduated in the scientific high school Istituto Pio XII in Rome. In 2005, he received his master degree *cum laude* in Chemistry from the University of Rome "La Sapienza", with a thesis on the hydrogen absorption properties of Pd wires exposed to hydrogen plasmas, in the chemical physics group of prof. Daniele Gozzi. From September 2005 to November 2009 he has been a PhD student at the VU University Amsterdam in the condensed matter physics group, under the supervision of prof.dr. R.P. Griessen and prof.dr. B. Dam. From November 2009 to January 2010 he has been a postdoctoral researcher in the same group. During his period in Amsterdam he studied the hydrogen sorption properties of Mg-based thin films and multilayers, with a special focus on the effects of stress and surface energy on the thermodynamic properties of very thin layers. Since February 2010 he is a postdoctoral researcher in the Chemical Engineering department of the Delft University of Technology, in the Materials for Energy Conversion and Storage (MECS) group of prof.dr. B. Dam.